STOCHASTIC MODELING OF DRIVEN TRANSPORT PROCESSES: ANALYSES AND SIMULATIONS

A Thesis Submitted
in Partial Fulfilment of the Requirements
for the Degree of

Doctor of Philosophy

by

ANKITA GUPTA

Under the Guidance of

Dr. Arvind Kumar Gupta

DEPARTMENT OF MATHEMATICS
INDIAN INSTITUTE OF TECHNOLOGY ROPAR

JANUARY, 2024

Ankita Gupta: *Stochastic Modeling of Driven Transport Processes: Analyses and Simulations*
Copyright ©2024, Indian Institute of Technology Ropar
All Rights Reserved

To my family
for their endless love, patience and support

Declaration of Originality

I hereby declare that the work which is being presented in the thesis entitled **STOCHASTIC MODELING OF DRIVEN TRANSPORT PROCESSES: ANALYSES AND SIMULATIONS** has been solely authored by me. It presents the result of my own independent investigation/research conducted during the time period from January, 2019 to January, 2024 under the supervision of **Dr. Arvind Kumar Gupta**, Associate Professor, Department of Mathematics, Indian Institute of Technology Ropar. To the best of my knowledge, it is an original work, both in terms of research content and narrative, and has not been submitted or accepted elsewhere, in part or in full, for the award of any degree, diploma, fellowship, associateship, or similar title of any university or institution. Further, due credit has been attributed to the relevant state-of-the-art and collaborations (if any) with appropriate citations and acknowledgments, in line with established ethical norms and practices. I also declare that any idea/data/fact/source stated in my thesis has not been fabricated/ falsified/ misrepresented. All the principles of academic honesty and integrity have been followed. I fully understand that if the thesis is found to be unoriginal, fabricated, or plagiarized, the Institute reserves the right to withdraw the thesis from its archive and revoke the associated Degree conferred. Additionally, the Institute also reserves the right to appraise all concerned sections of society of the matter for their information and necessary action (if any). If accepted, I hereby consent for my thesis to be available online in the Institute's Open Access repository, inter-library loan, and the title & abstract to be made available to outside organizations.

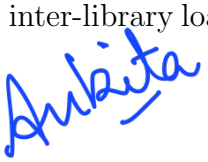

Signature

Name: Ankita Gupta
Entry Number: 2018MAZ0006
Program: PhD
Department: Mathematics
Indian Institute of Technology Ropar
Rupnagar, Punjab 140001

Date: April 2, 2024

Acknowledgement

I would like to express my heartfelt appreciation to those individuals who have contributed to the completion of this thesis. First and foremost, I would like to thank my supervisor 'Dr. Arvind Kumar Gupta' for providing his constant support and motivation through my journey. He not only assisted me academically but also listened to my personal struggles, encouraging me to stay strong, maintain a positive mindset, and focus on the future. He even pushed me to try out different things like sports, travel, or enjoying evenings with my colleagues. Under his guidance, I've learned to push my limits, handle multiple tasks, and greatly improved my presentation skills. His words, "Everyone is working fine, but only a few can find their way to great achievements," have served as a constant reminder for me to strive harder and reach for excellence.

I acknowledge the tireless dedication of my doctoral committee: Dr. Subhash Chandra Martha, Dr. Partha Sharathi Dutta, Dr. Madeti Prabhakar, and Prof. Navin Kumar who have continuously evaluated my progress and provided invaluable guidance. I would also like to thank Mr. Neeraj, our senior lab assistant, and Ms. Jaspreet, the office staff, for their assistance throughout the years. I express my gratitude to the Department of Mathematics at IIT Ropar for offering me a warm and supportive atmosphere, along with the essential laboratory facilities and resources essential for conducting my research as well as financial support for presenting in several conferences. Equally significant, I am extremely thankful to CSIR (File No. 09/1005(0023)/2018-EMR-I) for financial support and for providing all the essential resources needed for my research.

I will be forever thankful to my dear friends for their continuous support and companionship throughout this journey, making challenges more manageable and moments of joy more memorable. A special place in my heart belongs to Bipasha, whose seniority and collaborative spirit have provided me with invaluable support and guidance. I extend special thanks to my colleague, Himanshu, for supporting me academically, emotionally, and mentally. His encouragement was particularly valuable during difficult moments when continuing further seemed difficult. I am thankful to my friends Amrendra, Taran, Piyush, Riya, Nazim and Sadanand for their contribution through meaningful discussions and our enjoyable moments together. I also want to extend my thanks to Dr. Riya for being a patient listener to all my nonsense and for our pleasant evening walks by the canal. I appreciate Sonam, Niharika, Aditi, Sahil, Nikhil, Monika, Vikash, Surya and my other lab members for their assistance and time. Last but not the least, I would like to thank my junior Ashish and my colleague Swati, for their priceless care, affection, and support.

Lastly, a big applause for my family. My sister, who convinced my father to let me

pursue PhD. Mom, my pillar of strength, who showed me how to keep going and find happiness in every little thing. Dad, my silent supporter, who stood by me without expecting anything in return. And my brother, always there to lend a hand, no matter how busy. Their love and support are what made this journey achievable.

In addition to all the above people, I express my gratitude to God for bestowing upon me Acharyat Prashant ji-a spiritual guide who lights my way, fosters clarity in my thoughts, and empowers me with strength through each guiding word.

A sincere thank you
to all of you for your meaningful
contributions to this work.

Certificate

This is to certify that the thesis entitled **Stochastic Modeling of Driven Transport Processes: Analyses and Simulations**, submitted by **Ankita Gupta (2018MAZ0006)** for the award of the degree of **Doctor of Philosophy** of Indian Institute of Technology Ropar, is a record of bonafide research work carried out under my guidance and supervision. To the best of my knowledge and belief, the work presented in this thesis is original and has not been submitted, either in part or full, for the award of any other degree, diploma, fellowship, associateship or similar title of any university or institution.

In my opinion, the thesis has reached the standard fulfilling the requirements of the regulations relating to the Degree.

Signature

Dr. Arvind Kumar Gupta
Department of Mathematics
Indian Institute of Technology Ropar
Rupnagar, Punjab 140001
Date: April 2, 2024

Lay Summary

In our everyday lives, the way things move– be it cars on the road or substances within our bodies– plays a crucial role in shaping our experiences. Understanding and optimizing these systems is like holding the key to a smoother, more efficient world. In this study, we explore the importance of modeling transport systems, ranging from vehicles on the road to biological processes, and how the totally asymmetric simple exclusion process (TASEP) serves as a vital tool in this pursuit.

Imagine your daily commute or a package being delivered across town. Modeling vehicular transport systems allows researchers to simulate and study traffic flow, predict congestion, and find ways to make transportation more efficient. On a broader scale, similar modeling principles can be applied to biological transport systems, such as the movement of molecules within cells or the flow of blood in our circulatory systems. These biological processes share surprising similarities with vehicular traffic, making them intriguing subjects for study.

TASEP emerges as versatile modeling tool that enables the simulation of entity movements, whether it be cars navigating roads or particles within a biological system. Through this model, researchers acquire valuable insights into the dynamics of these systems, allowing them to discern patterns and discover avenues for enhancing efficiency.

To make these models more pertinent to real-world situations, we have tried to integrate diverse and realistic features. This involves incorporating factors such as traffic lights, road conditions, and driver behaviors specifically tailored for vehicular transport models. Biological transport involves mimicking adaptive behaviors and incorporating characteristics inspired by the complexity of living systems. These enhancements aim to create simulations that mirror the intricacies of real-world scenarios, allowing us to refine strategies for optimizing transport in diverse contexts.

In essence, the modeling of transport systems through TASEP which involve random motion of particles, enriched with realistic features, is a journey toward a better, more efficient world. Whether it's making your daily commute smoother or understanding how substances move within living organisms, these models pave the way for innovative solutions that can enhance transportation systems and improve the way things flow in our interconnected world.

Abstract

Transportation is a fundamental aspect of human and biological systems, serving as the mechanism for the movement of people, goods, and organisms from one place to another. Its significance lies in its ability to connect diverse locations, assist in economic growth, cultural exchange, and ecological balance. In biological systems, intricate mechanisms such as motor proteins traveling along microtubules play a crucial role in cellular transport, ensuring the proper distribution of essential molecules within cells. On a macroscopic scale, vehicular traffic and pedestrian flow are essential components of urban life, influencing the efficiency and livability of cities. The coordinated movement of ants, exemplifying collective behavior, showcases how transportation is vital for the survival and thriving of social organisms. Therefore, it is important to investigate the collective motion of the entities involved, by employing a mathematical model, with the objective of explaining the complex dynamics that characterize their interactions.

Over the years, a discrete lattice gas model, namely totally asymmetric simple exclusion process (TASEP), has emerged as a paradigmatic model, which is often adopted to study the non-equilibrium stochastic motion of various physical and biological transport processes. Treating entities such as vehicles, motor proteins, and ants as particles, this model aptly captures their unidirectional movement along the respective track by representing them with discrete lattice structures. Considering the numerous scenarios involving systems with open boundaries, the terminal points of the lattice are linked to boundary reservoirs and the dynamics of the particles are governed by simple Poisson process. To provide a sound theoretical framework, mean-field theory and its variants are adopted which neglects all the correlations between neighbouring particles. A notable consistency between mean-field predictions and Monte Carlo simulations is observed, affirming the theoretical predictions of the stationary properties.

In this thesis, we contribute to a thorough understanding of collective behaviour of particles by incorporating various realistic features. The first part is inspired by the motion of a limited number of motor proteins like kinesin and dynein in opposite directions on a microtubules. In particular, we examine the influence of individual particle constraints on both species in a one-dimensional bidirectional transport model. The stationary properties of the system is regulated by the entry-exit rates of the species as well as the occupancy of the respective reservoir. Continuing our exploration in bidirectional transport, further we analyze an exclusion model resembling the structure of a roundabout.

The second part broadens a single-lane model to a two-lane TASEP by introducing diverse elements such as stochastic blockages at each site, the existence of narrow entrances, reservoir crowding, or inter-lane coupling. These incorporated features

emulate various scenarios found in both intracellular transport and vehicular traffic. Initially, our focus is on a system characterized by narrow two-lane entrances, where defects can stochastically bind and unbind within a resource-constrained environment. Despite the inherent complexity, we are able to derive theoretical expressions for stationary properties through the usage of mean-field theory. Furthermore, we explore a resource-limited, two-lane coupled model where simple mean-field methods prove inadequate for obtaining explicit solutions. To conduct a thorough analysis of this challenging problem, we utilize vertical cluster mean-field in conjunction with singular-perturbation technique.

The last part of the thesis centers around the attachment and detachment dynamics of motor proteins on complex structure of microtubules, known as the Langmuir kinetics. Initially, a network junction model is investigated under conditions of infinite resources, followed by an examination under finite resource constraints.

Overall, the objective of this work is to utilize mathematical modeling as a tool to attain a deep comprehension of the complexities that may emerge in a transport system where particles undergo random motion.

Keywords: Driven diffusive systems; Stochastic transport; Exclusion process; Monte Carlo simulations; Mean-field approximation; Langmuir kinetics; Singular perturbation technique; Steady-state.

Contents

Declaration v

Acknowledgement vii

Certificate ix

Lay Summary xi

Abstract xiii

List of Figures xix

List of Tables xxix

1 Introduction 1

1.1 Non-equilibrium systems . . . 2
1.2 Driven diffusive systems . . . 3
1.2.1 Transport phenomena . . . 3
1.3 Totally Asymmetric Simple Exclusion Process: A lattice-gas model . . . 6
1.4 Mathematical treatment: Master equations . . . 8
1.4.1 Theoretical methods . . . 9
1.4.2 Stochastic simulations . . . 10
1.4.3 Approximate method: Mean-field theory . . . 11
1.5 Extensions of the TASEP model . . . 16
1.5.1 Stochastic attachment-detachment . . . 16
1.5.2 Bidirectional flow . . . 17
1.5.3 Impact of narrow entrances . . . 19
1.5.4 Role of limited resources . . . 20
1.5.5 Dynamic disorder . . . 21
1.5.6 Coupled TASEPs . . . 22
1.6 Aims and objectives . . . 22
1.7 Outline of the thesis . . . 24

2 Interplay of two reservoirs in a bidirectional transport system 27

2.1 Motivation and background . . . 27
2.2 Model description and theoretical framework . . . 28
2.3 Existence of phases . . . 32

2.3.1 Symmetric phases . . . 33
2.3.2 Asymmetric phases . . . 34
2.4 Results and discussion . . . 36
2.4.1 Symmetric filling factor ($\mu_+ = \mu_-$) . . . 36
2.4.1.1 Spontaneous symmetry-breaking phenomenon (SSB) . . . 38
2.4.1.2 Shock dynamics . . . 39
2.4.1.3 Finite-size effect on asymmetric phases . . . 41
2.4.2 Asymmetric filling factors ($\mu_+ \neq \mu_-$) . . . 42
2.4.2.1 Stationary properties: Impact of μ_+ . . . 43
2.4.2.2 Stationary properties: Impact of μ_- . . . 45
2.5 Swapping rate of two-species other than 1 . . . 48
2.6 Summary and conclusion . . . 50
2.7 Appendix: Symmetric phases . . . 52
2.8 Appendix: Asymmetric phases . . . 53
2.9 Appendix: Numerical Scheme . . . 56

3 Exclusion processes on a roundabout traffic model with constrained resources 59
3.1 Motivation and background . . . 59
3.2 Model . . . 60
3.3 Master equations and mean-field analysis . . . 62
3.3.1 Dynamics of lanes P and Q . . . 64
3.3.2 Dynamics of bridge lanes . . . 66
3.3.3 Boundary dynamics . . . 66
3.4 Analytic predictions . . . 67
3.4.1 Symmetric phases . . . 68
3.4.2 Asymmetric phases . . . 68
3.5 Results: analysis and implications . . . 69
3.5.1 Role of filling factor . . . 70
3.5.2 Shock dynamics . . . 73
3.5.3 Back-and-forth transitions . . . 76
3.5.4 Finite-size effect . . . 78
3.6 Conclusion . . . 79
3.7 Appendix: Symmetric phases . . . 80
3.8 Appendix: Asymmetric phases . . . 82
3.8.1 Discarded phases . . . 88

4 Reservoir crowding in a dynamic disordered bidirectional system with narrow entrances **89**
4.1 Motivation and background . . . 89
4.2 Stochastic model with dynamic defects . . . 90
4.3 Theoretical analysis: Master equations . . . 94
4.3.1 Particle density evolution . . . 94
4.3.2 Defect density evolution . . . 95
4.3.3 Discrete to continuum mean-field equations . . . 95
4.4 Mean-field theory . . . 99
4.5 Feasible phases . . . 100
4.5.1 Symmetrical phases . . . 100
4.5.2 Asymmetrical phases . . . 102
4.6 Results and discussions . . . 104
4.6.1 Effect of reservoir crowding . . . 105
4.6.2 Back and forth transition . . . 107
4.6.3 Spontaneous symmetry-breaking . . . 109
4.6.4 Size-scaling dependencies of phases . . . 110
4.6.5 Influence of defects . . . 110
4.7 Conclusion . . . 113

5 Competition for resources in an exclusion model with biased lane-changing mechanism **115**
5.1 Introduction . . . 115
5.2 Description of the model . . . 116
5.3 Theoretical approach . . . 118
5.3.1 Continuum limit . . . 118
5.4 Bulk solution . . . 120
5.4.1 Numerical technique . . . 120
5.4.2 Cluster mean-field theory . . . 120
5.4.2.1 Zero particle current in lane A: (ZC_0/Q) . . . 123
5.4.2.2 Zero particle current in lane B: (P/ZC_1) . . . 125
5.4.2.3 Other phases . . . 127
5.5 Inner-solution: Boundary layer analysis . . . 128
5.6 Results and discussion . . . 131
5.6.1 Stationary phase diagrams . . . 132
5.6.2 Shock dynamics and phase transitions . . . 134
5.6.2.1 Upward unsynchronized shock . . . 134
5.6.2.2 Downward synchronized shock . . . 136
5.7 Summary and conclusion . . . 137

6 Particle creation and annihilation in an exclusion process on network 139
6.1 Motivation and background . . . 139
6.2 Network model . . . 140
6.3 Theoretical description . . . 141
6.4 Unconserved $V(m:n)$ network of TASEP . . . 143
6.5 Results and discussions . . . 149
6.5.1 Equal number of segments: $m = n$ . . . 149
6.5.2 Unequal incoming and outgoing segments: $m \neq n$ . . . 152
6.6 Conclusion . . . 155

7 Non-equilibrium processes in an unconserved network model with limited resources 157
7.1 Introduction . . . 157
7.2 Model and dynamic rules . . . 158
7.3 Single-lane TASEP-LK with limited resources . . . 159
7.3.1 Transient solution . . . 161
7.3.2 Steady-state solution . . . 161
7.4 Network model . . . 163
7.4.1 $Kz \neq 1$ . . . 164
7.4.2 $Kz = 1$ . . . 166
7.5 Results and discussions . . . 166
7.5.1 Equal number of lanes in both the subsystems $(m = n)$ . . . 166
7.5.2 Number of lanes in both the subsystems are different $(m \neq n)$ . . . 169
7.6 Conclusion . . . 172
7.7 Appendix A . . . 173
7.7.1 $Kz = 1$ . . . 174
7.7.2 $Kz \neq 1$ . . . 175
7.7.3 Explicit solution . . . 176
7.7.4 Implicit solution . . . 177
7.8 Appendix B . . . 177

8 Conclusion and future outlook 179
8.1 Summary of the results . . . 179
8.2 Future scope . . . 181

References 183

List of Publications 198

List of Figures

1.1 Classification of the systems in statistical mechanics. 2

1.2 (a) Vehicular traffic on road and (b) collective motion of ants. 4

1.3 Mechanism of Adenosine triphosphate (ATP) hydrolysis: a motor head attaches to the microtubule, with the trailing head positioned behind. Upon ATP binding, the neck linker undergoes stiffening, propelling the trailing head forward to the subsequent binding site. After ATP hydrolysis in the now trailing head, converting it to Adenosine diphosphate (ADP) and phosphate (P_i), the head detaches from the track. This cycle persists, with each ATP hydrolysis correlating with a single forward step in the process [1]. 5

1.4 Schematic representation of exclusion process with two types of boundary conditions: (a) periodic and (b) open. 7

1.5 A flow chart for conducting Monte Carlo simulations for random-sequential updating rule. Here, 'r' represents a uniformly distributed random number between 0 and 1. The variable 'i' ($1 \leq i \leq L$) corresponds to a site on the lattice. After repeating the above process for a sufficient time, the initial approximately 5% steps are disregarded to establish the steady-state. The average lattice density is then computed by taking the time average over an interval of $10L$. . 11

1.6 (a) Fundamental diagram representing the current-density relation. (b) Phase diagram for open TASEP system in the $\alpha - \beta$ plane. The solid red line, representing $\alpha = \beta$, signifies a first-order transition line, whereas the dashed blue lines represent second-order transitions. Insets show a typical density profile in the corresponding region. Symbols represent the simulation results. 14

1.7 Schematic representation of TASEP with LK. The entry rate of a particle through the first site is α and the exit rate from the last site is β. Attachment/detachment of a particle occurs with rate ω_a/ω_d. 17

1.8 (a) Sketch of a bidirectional TASEP model featuring two particle species, represented by red triangles (moving from left to right) and green circles (hopping from right to left) travelling unidirectionally while adhering to the exclusion principle. Two distinct species swap their respective positions upon meeting head-on. 18

1.9 Phase diagram for: (a) bidirectional TASEP model on one lane and (b) two-lane model featuring narrow entrances, with infinite resources. . . . 18

1.10 Illustration of a two-lane bidirectional exclusion model with narrow entrances. The two types of particle species are denoted by red and green circles. Arrows indicate allowed transitions while crosses depict prohibited movements. 19

1.11 Sketch of an open TASEP model with constrained resources. The variables α^{eff} and β^{eff} give the effective entrance and exit rates of the particles, respectively. 21

2.1 Schematic diagram for a bidirectional transport model comprised of a lattice connected to two reservoirs, each accommodating particles of a single-species only. Blue (+) and red (−) circles denote two oppositely directed particles travelling from left to right and right to left, respectively. The entrance rates of the two-particle species are given by α_+ and α_-, which are controlled by the occupancy of the corresponding reservoirs. The exit rates for both the particles are β. Two particles of distinct kinds are permitted to swap their positions with a rate s if they encounter each other on neighbouring sites. 29

2.2 Stationary phase diagrams for (a) $\mu = 0.3$, (b) $\mu = 0.9$, (c) $\mu = 1.1$, and (d) $\mu = 100$. Symmetric phases are represented by white regions, while the coloured regions denote asymmetric phases. Red symbols correspond to Monte Carlo simulation results. The L/L phase remains confined to a curve and acts as a boundary separating H/L (or S/L) and LD/LD phases, displaying a first-order phase transition taking average current as the order parameter. The size of the system is taken to be 1500. . . 37

2.3 Particle density histogram for (a) L/L and (b) H/L phases with the parameters $(\alpha, \beta, \mu) = (1, 0.1, 0.3)$ and $(2, 0.1, 1.5)$, respectively. Insets show the two-dimensional contour plot. 38

2.4 Plot of currents: (a) $(J_+ + J_-)/2$, $|J_+ - J_-|$, J_+, and J_-, and (b)$(J_+ + J_-)/2$ vs β for $\alpha = 3$ and $\mu = 1.1$. Inset in (b) displays a discontinuity in $(J_+ + J_-)/2$ near $\beta \approx 0.326$. Solid lines represent theoretical results and symbols refer to Monte Carlo simulations. 39

2.5 (a), (b) Position and height of the shock with respect to β for $\mu = 1.1$ and $\alpha = 0.1,\ 1,\ 3$. (c) Density profiles for fixed $\alpha = 1$ and $\beta = 0.1,\ 0.2,\ 0.25$ with $\mu = 1.1$. (d), (e) Position and height of the shock with respect to α for $\mu = 1.1$ and $\beta = 0.1,\ 0.2,\ 0.3$. (f) Density profiles for fixed $\beta = 0.2$ and $\alpha = 0.5,\ 1,\ 2$ with $\mu = 1.1$. (g) Effective entrance rates with respect to μ for $\alpha = 2$ and $\beta = 0.1$. (h) Density profiles for $\alpha = 2$ and $\beta = 0.1$ for $\mu = 0.5,\ 0.8,\ 1.1$. (i) Position of the shock with respect to μ for $\alpha = 2,\ 20$ and $\beta = 0.1$. Inset shows the change in position of the shock with respect to μ for $\alpha = 20$ and $\beta = 0.1$. In all figures, solid lines represent theoretical results and symbols correspond to Monte Carlo simulations. The size of the lattice is taken to be 3000. 40

2.6 (a) Effect of finite lattice length L on the S/L profile for fixed $(\alpha, \beta, \mu) = (1, 0.2, 1.1)$ and varied values of L. (b) Region width (Δ) of low-low density (L/L) phase with respect to β for fixed $\alpha = 0.5$ and $\mu = 0.5$. The solid curve is a guide to the eye with best-fit polynomial for the discrete simulation data (shown by red markers) until $L \approx 5000$. 42

2.7 Stationary phase diagrams for: (a) $\mu_+ = 1$ and (b) $\mu_+ = 20$ with $\mu_- = 0.3$. Solid lines represent theoretical results and symbols correspond to Monte Carlo simulations. The length of the lattice is 1500. 43

2.8 Stationary phase diagrams for: (a) $\mu_+ = 0.98$, (b) $\mu_+ = 1.5$ and (c) $\mu_+ = 15$ with $\mu_- = 0.9$. Solid lines represent theoretical results and symbols correspond to Monte Carlo simulations. The length of the lattice is set to 1500. 44

2.9 Position of the shock vs (a) μ_+ with $\mu_- = 0.3$, (b) β with $\mu_+ = 1$, $\mu_- = 0.3$, and (c) α with $\mu_+ = 1$, $\mu_- = 0.3$. The rest of the parameter values are mentioned in the respective figures. Inset in (a) shows the change in x_w with respect to μ_+ which is almost linear. Inset in (b) is a zoomed figure for smaller values of β. In all figures, solid lines represent theoretical results and symbols correspond to Monte Carlo simulations. The length of the lattice is set to 1500. 45

2.10 Stationary phase diagrams for: (a) $\mu_- = 0.3$, (b) $\mu_- = 0.5$, and (c) $\mu_- = 0.54$ with $\mu_+ = 0.55$. Solid lines represent theoretical results and symbols correspond to Monte Carlo simulations. The length of the lattice is taken to be 1500. 46

2.11 (a) Effective entrance rate α_{-}^{eff} with respect to μ_{-} for $\mu_{+} = 0.55$, $\alpha = 15$, $\beta = 0.8$. (b) Particle density ρ_{-} with respect to α for distinct values of β. (c) Density profiles of the negative species for different values of β, $\alpha = 3$, $\mu_{+} = 1$, $\mu_{-} = 0.3$. The rest of the parameter values are mentioned in the respective figures. In all figures, solid lines represent theoretical results and symbols correspond to Monte Carlo simulations. The length of the lattice is taken to be 1500. 47

2.12 Different dynamic regions based on the filling factors μ_{+} and μ_{-}. Eleven distinct regions numbered I to XI, have phase regimes that are qualitatively different. Table (2.2) provides a tabular description of the phase regimes that can exist in each of these different regions. In the table, a phase that does not exist is indicated by empty entries. 48

2.13 Density profiles for (a) H/L, (b) L/L, (c) S/L phases, (d) LD/LD, and (e) MC/MC with (α, β, μ) =(2,0.2,10),(2,0.315,1.1), $(1, 0.1, 0.3)$, $(1, 0.5, 0.9)$, $(3.5, 0.8, 1.1)$ with symmetric filling factors, and (f) M/M phase with $(\alpha, \beta, \mu_{+}, \mu_{-}) = (4.5, 0.8, 15, 0.9)$. The lattice length is taken to be 1500. Red and blue solid lines are mean-field results for (+) and (−) particles, respectively while filled markers correspond to Monte Carlo simulations. 49

2.14 (a) Density profile of the two-particle species for $\alpha = 0.7$, $\beta = 1$, $\mu_{-} = \mu_{+} = 1.1$, and $s = 0.8$ obtained using mean-field theory. Dashed lines correspond to solution obtained with initial condition $\rho_{+} = \rho_{-} = 0.4$, dotted line is plotted for initial condition $\rho_{+} = \rho_{-} = 0.7$, and symbols correspond to Monte Carlo simulations. (b) Density profile of the two-particle species for $\alpha = 0.5$, $\beta = 0.2$, $\mu_{+} = \mu_{-} = 1.1$, and $s = 0.8$. Solid lines represent mean-field results and symbols correspond to Monte Carlo simulations. 50

3.1 Model depiction in a diagrammatic form. Arrows indicate transitions that are permitted. Prohibited transitions are indicated by red crossed arrows. The two distinct species of particles progressing from left to right and right to left are represented by (+) and (−) symbols, respectively. . 61

3.2 Representation of the proposed model with the fictitious defined entrance and exit rates through each lane required for analytical treatment. . . . 64

3.3 Stationary phase diagrams for different values of μ: (a) $\mu = 0.1$, (b) $\mu = 0.45$, (c) $\mu = 0.6$, (d) $\mu = 0.7$, (e) $\mu = 1.5$ and (f) $\mu \to \infty$. Solid lines represent theoretical findings while red circles denote Monte Carlo simulation results. The blue dashed curves indicate the L-L-L/L-L-L phase. The phases L-L-L/L-L-L, L-L-S/L-L-L, L-L-H/L-L-L, L-S-H/L-L-L, and L-H-H/L-L-L, all converge in a narrow region which is presented by black squares in panels (d) and (e). 69

3.4 Phase transitions exhibited for $\mu = 0.8$ and $\beta = 1$ for varying values of α. The system evolves from LD-LD-LD/LD-LD-LD $\to$ LD-SP-LD/ LD-SP-LD $\to$ SP-HD-LD/SP-HD-LD. Since in the symmetric phase, the density profiles for the two species are identical, we plot the density profile only for the positive species. Solid lines give mean-field results while symbols correspond to Monte Carlo simulations. The shaded region for $x \in [1, 2]$ represents the bridge lane. 73

3.5 Phase transitions with respect to β for fixed values of the other parameters as $\alpha = 2$, and $\mu = 0.6$ representing evolution of the system from S-H-H/L-L-L $\to$ L-S-H/L-L-L $\to$ L-L-S/L-L-L $\to$ L-L-L/L-L-L $\to$ LD-LD-LD/LD-LD-LD. (a) and (b) shows the density profile for the (+) and the (-) species, respectively. Solid lines give mean-field results while symbols correspond to Monte Carlo simulations. The shaded region for $x \in [1, 2]$ represents the bridge lanes. The dotted arrow indicates the direction of increasing β. 74

3.6 Dynamics of the phase involving shock for $\mu = 0.7$, $\alpha = 12$ and different values of β. (a) $\to$ (b) $\to$ (c) $\to$ (d) $\to$ (e) $\to$ (f) gives the order of the phase transition. Solid lines give mean-field results while symbols correspond to Monte Carlo simulations. The shaded region for $x \in [1, 2]$ represents the bridge lanes. 75

3.7 (a) Density profiles displaying back-and-forth transition for $\mu = 0.7$ and $\alpha = 4$ with $\beta = 0.05$ (S-H-H/L-L-L), 0.2 (H-H-H/L-L-L) and 0.3 (S-H-H/L-L-L). (b) Effective entry-exit rates and the position of shock x_w (given by Eq. (3.31)) of the positive particles for lane P for fixed $\mu = 0.7$ and $\alpha = 4$. Solid lines denote theoretical results and round symbols show Monte Carlo simulation results. 76

3.8 (a) Variation of region width Δ of L-L-L/L-L-L phase with increasing β for fixed $\alpha = 0.4$ and $\mu = 0.45$ obtained through simulations. (b) Variation of phase boundary separating LD-SP-LD/LD-SP-LD region from SP-HD-LD/SP-HD-LD region for $\beta = 0.9$ and $\mu = 0.8$. The MCs results (symbols) approach the boundary obtained through a theoretical framework (dotted line) for larger values of L. 78

4.1 (a) A schematic of the two-lane TASEP with narrow entrances and dynamic defects competing for finite resources is shown. Particles (Defects) are depicted by circles (squares). Arrows represent allowed transitions, while crosses indicate prohibited ones. The effective injection and removal rates of the particles are denoted as $\widetilde{\alpha}^*$, and $\widetilde{\beta}$ respectively. (b) Narrow entrance implementation: For a particle to enter a lane, both the target site and the exit site of the other lane must be empty, and particle interactions are limited to the boundaries. (c) Dynamic behaviour of defects: Binding occurs with rate $\widetilde{k_+}$, while unbinding happens with the constant rate k_-. 92

4.2 Stationary phase diagram for: (a) $\mu_p = 0.3$, (b) $\mu_p = 0.49$, (c) $\mu_p = 0.5$, (d) $\mu_p = 0.8$, (e) $\mu_p = 2$, and (f) $\mu_p = 50$ with $c = 1$. White regions represent symmetric phases, while coloured regions indicate asymmetric phases. The red symbols correspond to results from Monte Carlo simulations and solid lines are theoretical findings. 105

4.3 Possible phase transitions observed in the system with increasing values of μ_p. The values C_i indicate critical values of μ_p at which difference phases appear and disappear. In particular, $C_1 \approx 0.31$, $C_2 \approx 0.43$, $C_3 \approx 0.5$, and $C_4 \approx 50$. In the shaded region $\mu_p \in (C_3, C_4)$, all the seven phases persists in the system. 107

4.4 (a) Density profile for $(\alpha, c, \mu_p) = (7, 1, 0.45)$ and different values of β. (b) Effective entrance rate (α_A^{eff}) , effective exit rate $(\widetilde{\beta})$ and the position of the shock (x_w) with respect to β for $(\alpha, c, \mu_p) = (7, 1, 0.45)$. Lines denote theoretical findings while symbols correspond to simulation results. . . 108

4.5 Particle density histogram plotted through Monte Carlo simulations for (a) LD/LD, (b) MC/MC, (c) H/L, and (d) S/L phases. The parameters are $(\alpha, \beta, \mu_p) = (3, 1, 0.49)$, $(3, 4, 2), (1, 0.5, 2)$, and $(2, 0.2, 0.3)$ in (a–d) with $c = 1$. 109

4.6 Finite-size effect on density profile of (a) shock in S/L phase for $(\alpha, \beta, \mu_p) = (0.5, 0.5, 0.5)$ and (b) MC/MC phase for $(\alpha, \beta, \mu_p) = (4, 1.5, 0.8)$. (c) Variation of region width Δ of L/L phase with increasing lane length L for fixed $\alpha = 1$ and $\mu_p = 0.5$. 110

4.7 Plot for the defect density and the scaling factor 'c' vs the filling factor μ_d with $k_+ = k_- = 1, p_d = 0.1$, and $\mu_p = 0.8$. Solid lines depict theoretical findings whereas symbols denote Monte Carlo simulation results. 111

4.8 Variation in the phase boundaries between different values with increasing values of μ_d and $k_+ = k_- = 1, p_d = 0.1, \mu_p = 0.8$ for: (a) $\alpha = 1$ and (b) $\alpha = 5$. Solid lines depict theoretical findings whereas symbols denote Monte Carlo simulation results. 112

5.1 Illustration of the two-lane exclusion model with open boundaries. Lane A functions as a feeder lane, while lane B serves as an absorber lane. Arrows represent permissible transitions, while crosses indicate restricted transitions. The variables α^* and β represent the entry and exit rates, respectively. 116

5.2 (a) Possible states of a vertical cluster in the two-lane system. (b)Feasible transitions in a vertical cluster. (i) $P_{10}P_{01}$, (ii) $P_{10}P_{00}$, (iii) P_{10}, (iv) $P_{11}P_{00}$, (v) $P_{11}P_{10}$, and (vi) $P_{11}P_{01}$. 121

5.3 Phase diagrams for stationary states for different values of μ: (a) $\mu = 0.1$, (b) $\mu = 0.4$, (c) $\mu = 0.5$, (d) $\mu = 0.6$, (e) $\mu = 0.9$, (f) $\mu = 1$, (g) $\mu = 1.5$, (h) $\mu = 3$, and (i) $\mu \to \infty$. Each diagram delineates both bulk and surface transitions, categorized through boundary layer analysis. Solid lines denote bulk transitions, while dashed (thick red) lines describe surface transitions. M designates the Meissner phase phase corresponding to MC-ZC_0/ZC_1-MC phase which is independent of the boundary parameters. 133

5.4 (a) Density profiles of particles in lane A with $\alpha = 2$, $\mu = 0.4$, and $\beta = 0.01,\ 0.05,\ 0.1,\ 0.15$, and $\beta = 0.24$. (b) Position and height of the shock in ZC_0/S phase with respect to β for fixed $\alpha = 2$ and $\mu = 0.4$. The variable $\Delta = 1 - \beta - \alpha^{eff}$ gives the height of the shock. Symbols describe Monte Carlo results, while solid/dashed/dotted lines correspond to theoretical findings. 135

5.5 (a) Density profiles of particles in lane A with $\beta = 0.2$, $\mu = 0.4$, and $\alpha = 0.1,\ 0.2,\ 1$, and $\beta = 8$. (b) Position and height of the shock in ZC_0/S phase with respect to α for fixed $\beta = 0.2$ and $\mu = 0.4$. The variable $\Delta = 1 - \beta - \alpha^{eff}$ gives the height of the shock. Symbols describe Monte Carlo results, while solid/dashed/dotted lines correspond to theoretical findings. 136

5.6 (a) Density Profile and (b) position as well as the height of the shock in LD-ZC_0/ZC_1-HD phase for fixed $(\mu, \beta) = (1, 0.4)$. The variable $\Delta = \beta$ gives the height of the shock. Symbols describe Monte Carlo results, while solid/dashed lines correspond to theoretical findings. 137

5.7 (a) Density Profile and (b) position as well as the height of the shock in LD-ZC_0/ZC_1-HD phase for fixed $(\mu, \alpha) = (1, 0.8)$ and different values of β. The variable Δ gives the height of the shock. Symbols describe Monte Carlo results, while solid/dashed lines correspond to theoretical findings. 137

6.1 Schematic demonstration of the model where m incoming segments and n outgoing segments are connected via a junction. The particle can enter the first vacant site of incoming segments with rate α and exit from the last site of outgoing segments with rate β. To the right, the zoomed version of a segment is shown where attachment(detachment) of particles can occur in the bulk of each segment with rate $\omega_A/(\omega_D)$. . . 141

6.2 Stationary phase diagrams for different value of Ω: (a) $\Omega = 0$, (b) $\Omega = 0.1$, (c) $\Omega = 0.25$, and (d) $\Omega = 0.5$ for $m = n = 2$. Note that, the phase diagrams as well as the density profiles will remain unaffected for any values of m $(n = m)$. The phase transformations are continuous for boundaries between all observed phases. Solid blue lines represent theoretical results and dotted red symbols correspond to Monte Carlo simulation. 150

6.3 Density profiles for different value of Ω when $m = n = 2$. The vertical line at $x = 1$ shows the position of the junction. 151

6.4 Stationary phase diagrams for different value of Ω: (a) $\Omega = 0$, (b) $\Omega = 0.1$, (c) $\Omega = 1 - \frac{\sqrt{3}}{2}$, (d) $\Omega = \frac{1}{2}\left(1 - \frac{1}{\sqrt{2}}\right)$, (e) $\Omega = \frac{1}{2\sqrt{2}}$, (f) $\Omega = 0.42$, (g) $\Omega = 0.5$, and (h) $\Omega = \frac{1}{2}\left(1 + \frac{1}{\sqrt{2}}\right)$ for $m = 2$ and $n = 1$. The phase transformations are continuous for boundaries between all observed phases. Solid blue lines represents theoretical results and dotted red symbols correspond to Monte Carlo simulation. 153

7.1 Illustration of $m \times n$ network model with LK. Arrows (crosses) indicate the allowed (prohibited) hopping. Here, α^{eff} and β correspond to injection and removal rates whereas ω_A^{eff} and ω_D are attachment and detachment rates, respectively. 158

7.2 Stationary phase diagrams for different value of μ: (a) $\mu = 0.2$, (b) $\mu = 0.75$, (c) $\mu = 2.5$, and (d) $\mu = 200$ for $m = n$, $K = 1$ and $\Omega_D = 0.1$. Note that, the phase diagrams will remain unaffected for any values of m, $(m = n)$. Green solid/dotted lines represent mean-field results and red symbols correspond to the Monte Carlo simulations. The subscripts 'l' and 'r' signify the presence of a boundary layer forming in the density profile at the left and the right end respectively. M represents the Meissner phase where the bulk density is independent of the boundary parameters. . . 168

7.3 Stationary phase diagrams for different value of μ: (a) $\mu = 0.33$, (b) $\mu = 0.67$, and (c) $\mu = 3.33$ for $m = 2, n = 1$, $K = 1$ and $\Omega_D = 0.1$. Dotted green line denotes LD:HD phase. Green solid/dotted lines represent mean-field results and red symbols correspond to the Monte Carlo simulations. The subscripts 'l' and 'r' signify the presence of a boundary layer forming in the density profile at the left and the right end, respectively. M represents the Meissner phase where the bulk density is independent of the boundary parameters. 169

7.4 Stationary phase diagrams for different value of μ: (a) $\mu = 0.33$, (b) $\mu = 0.67$, (c) $\mu = 1$, and (d) $\mu = 3.33$ for $m = 2, n = 1$, $K = 3$ and $\Omega_D = 0.01$. Dashed green line denotes LD:HD phase. Green solid/dashed lines represent mean-field results and red symbols correspond to Monte Carlo simulations. The subscripts 'l' and 'r' signify the presence of a boundary layer forming in the density profile at the left and the right end respectively. M represents a region where the bulk density is independent of the boundary parameters. 171

7.5 Typical density profiles for $m = n$, $K = 1$, $\Omega_D = 0.1$ ((a)-(c) with $\mu = 2.5$ and (d)-(j) with $\mu = 200$), $m = 2$, $n = 1$, $K = 1$, $\Omega_D = 0.1$ ((k)-(m) with $\mu = 1$) and $m = 2$, $n = 1$, $K = 3$, $\Omega_D = 0.01$ ((n)-(o) with $\mu = 1$). Solid blue curves and red symbols denote mean-field and Monte Carlo simulations respectively. 178

List of Tables

1.1 Summary of the bulk and boundary densities, conditions of existence of distinct stationary phases for the simplest version of TASEP model. The bulk density of the lane is denoted by ρ and the density at boundary sites $i = 1(L)$ is signified as $\rho^1(\rho^L)$. J represents the corresponding steady-state current due to the flow of particles. 15

2.1 Summary of the existential conditions, effective entrance rates, shock position, and the reservoir quotients for the possible symmetric as well as asymmetric phases for the proposed model. LD/LD and MC/MC represent symmetric phases while H/L, M/L, S/L, and M/M correspond to asymmetric phases. The notations $\alpha_{\pm}^{eff}$ and $r_{\pm}$, respectively denote the effective entrance rates and the reservoir quotients for the two-particle species, whereas x_w gives the position of shock in the S/L phase. 35

2.2 The phases that exist in eleven different possible phase regions of the bidirectional system. The empty entries denote the phase that does not exist in the corresponding region. 48

4.1 Summary of the results for the particle densities, existence conditions and reservoir density of a reservoir crowding featured dynamically disordered one-dimensional lane with L sites. Here, ρ^1, ρ^{bulk}, and ρ^L give the particle density at entry site, bulk, and exit site, respectively. The position of the shock is denoted by x_w, the filling factor by μ and the scaling factor by 'c'. Also, u is the unit step function. 100

6.1 Summary of the results for one-dimensional open TASEP coupled with LK. 143

6.2 Phases with LD to LD (LD $\rightarrow$ LD) transition at the junction. 146

6.3 Phases with HD to HD (HD $\rightarrow$ HD) transition at the junction. 147

6.4 Phases with LD to MC (LD$\rightarrow$MC) transition at the junction for $m > n$. 147

6.5 Phases with HD to MC (HD$\rightarrow$MC) transition at the junction for $m > n$. 148

6.6 Phases with MC to MC (MC $\rightarrow$ MC) transition at the junction. 148

6.7 The possible phase transitions that can occur across the junction for different values of m and n. 155

Chapter 1

Introduction

Statistical mechanics, an invaluable and versatile tool, seamlessly integrates principles and methodologies of statistics to navigate through complex systems characterized by an immense number of particles. These systems cover a range of scenarios, including vehicular traffic flow [2], pedestrian dynamics [3], behaviour of group of ants [4], intracellular transport in biological processes [5], and protein synthesis [6], and numerous other scenarios. The primary goal is to anticipate and elucidate the measurable properties inherent in macroscopic structures by probing the properties and behaviours of the microscopic elements constituting the arrangement. For instance, within the realm of statistical mechanics, thermal energy takes on the definition of the potential within atomic particles in displaced states, while temperature becomes a significant measure reflecting how energy is distributed within these particles.

Operating on a microscopic scale, the theoretical framework of statistical mechanics aims to understand and predict the macroscopic behavior of physical systems. By utilizing statistical methods, it bridges the gap between the microscopic properties of individual particles (atoms, molecules, etc.) and the macroscopic observables (temperature, pressure, etc.), analyzing the collective behavior of large ensembles of particles. Therefore, while it deals with microscopic entities and their interactions, its aim is to describe and predict macroscopic phenomena, making it primarily a microscopic approach with implications for macroscopic observations. In 1902, Josiah Willard Gibbs [7] meticulously formulated the mathematical framework and fundamental principles of statistical mechanics. The contributions of James Clerk Maxwell and Ludwig E. Boltzmann [8] subsequently enhanced this groundwork, particularly in the realm of thermodynamics. The amalgamation of statistical principles and mechanics not only offers a comprehensive framework for understanding a broad spectrum of phenomena but also establishes a crucial connection between the microscopic and macroscopic realms. The combined endeavours of Gibbs, Maxwell, and Boltzmann in the early twentieth century established the bedrock for this transformative approach, shaping a discipline that continues to play a central role in predicting and interpreting the dynamic properties of complex transport systems across various domains.

1.1 Non-equilibrium systems

In a general context, we can sort the behaviour of multi-particle systems into two primary categories: (i) systems that are in or near equilibrium and (ii) systems that are significantly distant from equilibrium. Figure (1.1) illustrates the classification of systems in statistical mechanics. Within the first category, internal stability in isolation defines equilibrium within systems. A system is deemed close to equilibrium if it promptly returns to its balanced state after experiencing a minor perturbation. It is important to acknowledge that while they are often conceptualized as idealized, they may still interact with the environment. However, the defining characteristic is that these interactions reach a steady state where macroscopic observables remain constant over time. Additionally, these systems typically experience forces, but the net force acting on the system is generally zero, resulting in a state of balance or equilibrium. The comprehensive research conducted by Gibbs and Boltzmann has led to the development of a unified theory that offers a thorough understanding of such systems [9]. By utilizing Onsager's theory along with linear response theory, one can elucidate the characteristics of these systems [8,10].

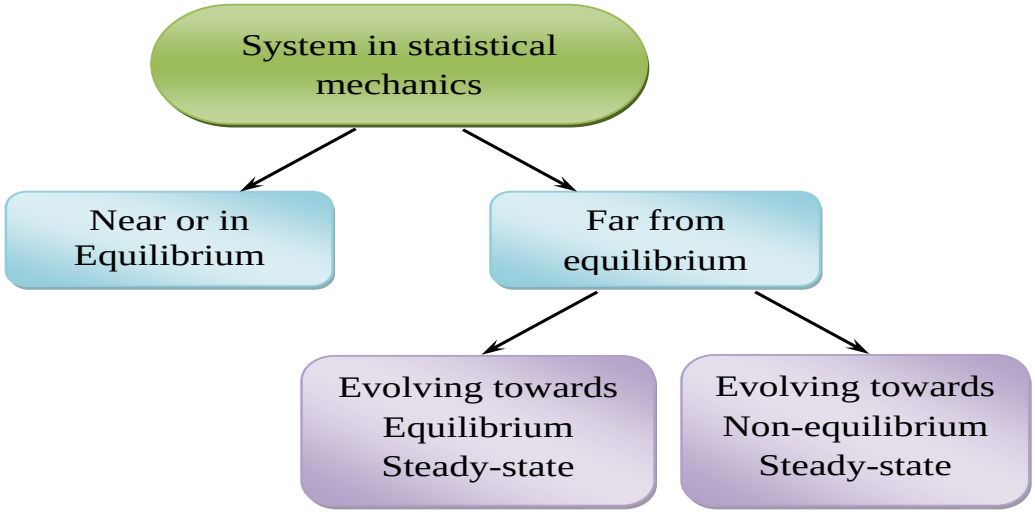

Figure 1.1: Classification of the systems in statistical mechanics.

Contrastingly, several real-life systems exist that interact dynamically with their environment, experiencing a non-zero net driving force. In systems far from equilibrium, a constant non-zero current is sustained, frequently leading to a non-equilibrium steady-state that challenges the applicability of Onsager's theory. This steady-state condition involves a continuous flow, such as heat flux or motion, without any change in their properties over time. Examples of such non-equilibrium systems abound in various phenomena, including vehicular traffic flow, transport processes in biological systems, epidemic spreading, behaviour of groups of ants, gel electrophoresis, protein

synthesis, pedestrian flow, flight of birds, and the floating progression of fish. While the steady-state represents a relatively simpler scenario within the broader category of non-equilibrium systems, it remains beyond the descriptive scope of the probability distribution outlined by Boltzmann and Gibbs. Despite recent efforts, we remain significantly distant from ascertaining whether the development of a comprehensive general theory for steady-state is feasible, let alone subjecting it to further scrutiny [11,12]. The lack of understanding regarding steady-states in systems operating outside of equilibrium propels the scientific community to explore the realms of non-equilibrium statistical mechanics. This exploration aims to delve deeply enough to uncover previously unknown physical phenomena through thorough investigation.

1.2 Driven diffusive systems

In the expansive domain of non-equilibrium physics, driven diffusive systems represent a distinctive class of systems that continually gain or lose energy from or to an external field. This characteristic ensures that the system is consistently in a non-equilibrium state, and the condition of detailed balance is not maintained. However, a pairwise balance condition guides the system toward achieving a non-equilibrium steady-state, where the system halts its evolution over time, maintaining a constant current.

The continuous movement of active agents is enforced by introducing a drive that influences the direction of their motion. In certain models such as vehicular traffic, particle motion is initiated by external fields, earning the designation of 'field-driven particles'. Conversely, in systems like pedestrian flow and cellular biological transport, particles move under internal driving forces and are termed 'self-driven particles'. These diffusive systems often hold greater significance in real-world physical and biological stochastic transport mechanisms, a topic further discussed in upcoming sections.

1.2.1 Transport phenomena

Here, we try to explain certain transport mechanisms that serve as a motivation for the thesis. It is crucial to underscore that this study goes beyond the limitations set by these particular phenomena discussed below.

- **Vehicular traffic.**

  Effective vehicular traffic management is a critical aspect of urban planning and transportation infrastructure (Fig. (1.2a)). As cities continue to grow and traffic congestion becomes a pressing issue, the need for efficient and innovative traffic management strategies becomes paramount. Vehicular traffic management

involves the application of various measures and technologies to regulate the flow of traffic, enhance safety, and minimize congestion. This includes the implementation of intelligent transportation systems, traffic signal optimization, dynamic traffic modeling, and the use of real-time data analytics. Furthermore, sustainable practices, such as the promotion of public transportation and the integration of smart traffic solutions, play a pivotal role in achieving comprehensive traffic management goals. By adopting a holistic approach that combines technology, data-driven insights, and sustainable urban planning, vehicular traffic management aims to create safer, more efficient, and environmentally friendly transportation systems in developing urban areas [13].

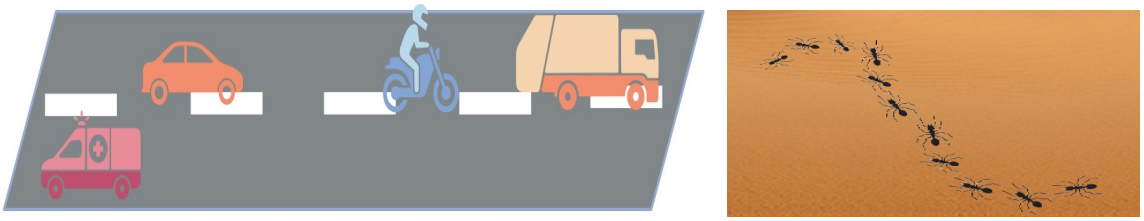

(a) (b)

Figure 1.2: (a) Vehicular traffic on road and (b) collective motion of ants.

- **Ant Trails.** Ants (Fig. (1.2b)) showcase remarkable efficiency in navigating their environment, whether foraging for food or managing various tasks, exhibiting complex communication and organization. The formation of trails, optimization of routes, and coordination of movements highlight decentralized decision-making processes among ants. Their transport is vital for ecosystem functioning, biodiversity, nutrient cycling, and pest control, making ants ecologically significant contributors to various ecosystems.

- **Intracellular transport by motor proteins.** The cell, recognized as the fundamental building block of life, operates as the cornerstone for both the structure and function of all living organisms. Within the intricate framework of cellular anatomy, organelles play a pivotal role by executing one or more vital tasks, each dependent on progressive microscopic processes. These operations, fueled by a steady energy supply, manifest as robust out-of-equilibrium systems. Sustaining cell functionality necessitates the active transportation of essential ingredients across diverse intracellular locations. However, due to the densely packed composition and micro-level intricacies, diffusion alone cannot accomplish these operations. Microtubules (MTs), the stiffest cytoskeleton filaments, form a network within the cell, providing tracks for the long-distance intracellular transport of cargos such as lipid droplets, endosomes, mitochondria, proteins, and viruses [14]. The coordinated

motions along these pathways of microtubules guarantee the accurate delivery of cellular components to designated intracellular locations.

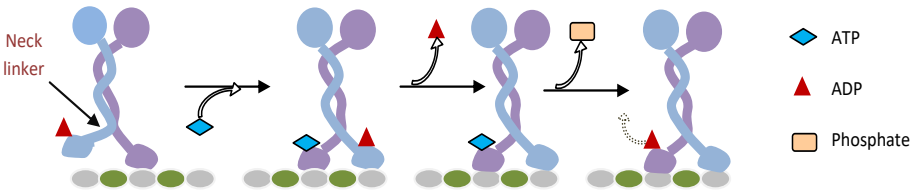

Figure 1.3: Mechanism of Adenosine triphosphate (ATP) hydrolysis: a motor head attaches to the microtubule, with the trailing head positioned behind. Upon ATP binding, the neck linker undergoes stiffening, propelling the trailing head forward to the subsequent binding site. After ATP hydrolysis in the now trailing head, converting it to Adenosine diphosphate (ADP) and phosphate (P_i), the head detaches from the track. This cycle persists, with each ATP hydrolysis correlating with a single forward step in the process [1].

Microtubules, characterized by their stiff nature and intricate association and disassociation progression, consist of polymers with fundamental subunits, tubulins, forming protofilaments that assemble into helical cylinders. These microtubules serve as the primary tracks for intracellular transport, with their polar nature dictated by the tubulin subunits. Motor proteins, specifically from the kinesin and dynein families, play a pivotal role in this transport system. These cytoskeleton motors move along polar microtubules, utilizing the potential from ATP hydrolysis to facilitate forward stepping along the filament [15,16] as shown in Fig. (1.3). Kinesins predominantly progress towards the microtubule's plus end, away from the nucleus, while dyneins move towards the minus end, towards the nucleus, resulting in a bidirectional flow. The collective behaviour of these motor proteins is crucial for understanding the complex dynamics of cellular transport, with disruptions in this system contributing to various diseases, including Alzheimer's, neurodegenerative disorders, and polycystic kidney diseases [15]. A thorough examination of the unified dynamics of motor proteins offers a valuable understanding of the complex cellular transport system and its importance for the overall health of the cell.

- **Pedestrian Flow.** This involves the movement of individuals in public spaces, such as streets, sidewalks, and public transit hubs. Various factors influence pedestrian transport, including crowd dynamics, pedestrian density, environmental conditions, and architectural features. Studying pedestrian flow helps identify patterns, bottlenecks, and potential hazards, aiding in the development of efficient crowd management strategies.

1.3 Totally Asymmetric Simple Exclusion Process: A lattice-gas model

In this section, we will explore the approach used to analyze the characteristics of the stationary states in non-equilibrium stochastic transport systems. The inherent randomness in non-equilibrium transport processes implies that their prolonged behaviour is unaffected by the starting conditions. Additionally, the intricacy of studying these phenomena is heightened by the involvement of a substantial number of particles in the system. To tackle this complexity, we have employed a stochastic model based on the population dynamics, effectively managing both the stochastic nature and the abundance of particles. This technique allows us to capture a comprehensive macroscopic representation of the system under investigation.

Such systems are mainly studied using lattice-gas models [17] which were introduced by Katz, Lebowitz, and Spohn [18]. At first glance, the terms 'lattice' and 'gas' may seem contradictory, as a lattice is a defining characteristic of a crystalline solid, and there is no actual lattice in the gaseous phase of matter. The concept of a lattice gas, however, involves discretizing continuous space into a regular array of cells. These cells, restricted to hosting only one particle at a time, collectively form a discrete lattice. At any given moment, a fraction of these lattice sites are occupied by particles, contributing to the dynamic nature of the system.

The Totally Asymmetric Simple Exclusion Process (TASEP) stands out as a special class of lattice-gas model, gaining widespread recognition in recent decades. It has established itself as an exemplary model, particularly well-suited for the study of non-equilibrium stochastic transport systems, hence, earning the designation as 'mother of all traffic models'. This model was first introduced by Macdonald in 1968 to study the kinetics of biopolymerization [19] (the motion of a ribosome along a piece of mRNA during translation), which involves the diffusion of biological entities along a one-dimensional path. Specifically, this model focuses on examining the coordinated actions of dynamic entities, commonly referred to as particles, as they advance unidirectionally along a one-dimensional lattice. Generally, the particles transverse from left to right while adhering to the hard-core exclusion principle, which ensures that a lattice site cannot accommodate more than one particle at a time. Since its first incarnation, these models have been utilized to enhance our comprehension of molecular transport processes across several fields [20–22]. Widely recognized as stochastic models, they have undergone extensive scrutiny and application in exploring various transport phenomena including vehicular traffic [23], dynamics of motor proteins [24], protein synthesis [6], pedestrian flow [25], gel electrophoresis [26], modeling of ant trails [5], etc.

The stationary behaviour of the model is strongly influenced by the incorporated boundary conditions, typically falling into two categories: (i) periodic/closed and (ii) open boundary conditions [27,28]. In closed TASEPs, as a particle traverses the lattice and reaches the last site, it jumps to the first site if unoccupied, creating a ring-like structure, as illustrated in Fig. (1.4a). Under these boundary conditions, the preservation of particle count within the system leads to a stationary state characterized by translational invariance. Consequently, a single phase occurs, controlled by both the number of sites and particles in the system.

On the contrary, in the presence of open boundary conditions (see Fig. (1.4b)), the arrival and departure of the particles from the extreme ends of the lattice disrupts the conservation of the overall particle count in the system. In this case, the system reveals various counter-intuitive non-equilibrium phenomena such as localized shock formation, phase transitions, phase separations, symmetry-breaking, etc [27–34]. The central focus of this thesis lies in the exploration of open TASEP. Consequently, let's initiate the discussion by scrutinizing the governing dynamics and identifying key features of the simplest version of the open TASEP model. The open model adheres to the following rules:

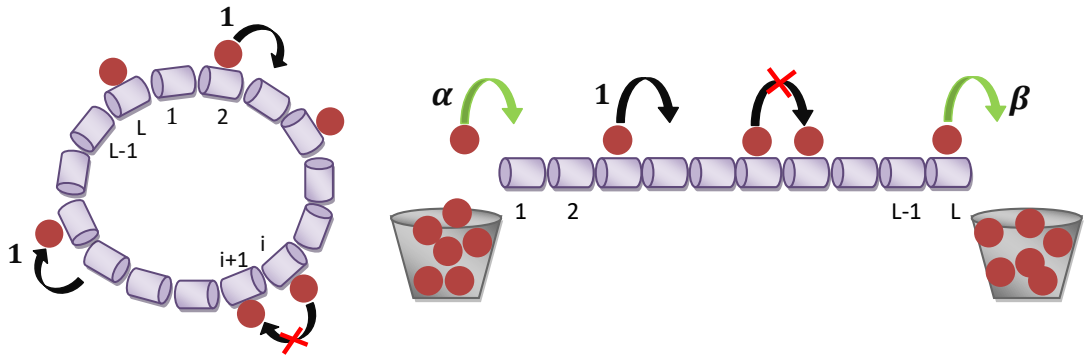

(a) (b)

Figure 1.4: Schematic representation of exclusion process with two types of boundary conditions: (a) periodic and (b) open.

- Particles undergo diffusion on a one-dimensional lattice having L number of sites.
- Each lattice site is either vacant or contains at most one particle, adhering to the hard-core exclusion principle, which stipulates that simultaneous occupation by two or more particles of a single site is prohibited. Moreover, this principle is followed along the whole lattice.
- A particle is injected into the lattice through the first site with rate α, provided the target site is empty.

- The particle moves in a unidirectional manner across the lattice, typically from left to right, with a predetermined hopping rate that is set at 1.
- Finally, a particle upon reaching the Lth site escapes into the environment with an exit rate of β.

Another crucial element in modeling stochastic transport processes is the updating procedure, which should properly represent the dynamics of the system under consideration. These rules have a critical impact on the system at a macroscopic level, while the microscopic kinetics remain unchanged. The TASEP model has been broadly investigated by four main classes of updating rule, namely, sub-lattice parallel update, ordered sequential update, parallel update and random-sequential update [35]. The parallel updating procedure is a discrete-time updating rule, which effectively mimics the dynamics of vehicular traffic and pedestrian flow. However, the random-sequential rule is a continuous-time updating procedure that is well suited for biological transport processes.

In this thesis, our attention will be dedicated to the TASEP model and its extensions involving open boundary conditions and a random-sequential updating procedure. The upcoming sections will thoroughly explore the mathematical framework of open TASEP, emphasizing significant results.

1.4 Mathematical treatment: Master equations

In non-equilibrium systems, a master equation serves as a mathematical tool to delineate the temporal changes in the probability distribution of a system as it experiences random transitions between distinct states. Unlike equilibrium systems, non-equilibrium systems lack detailed balance, signifying that transition rates between different states are not necessarily equal in both directions. Additionally, the Markovian property is a prerequisite, meaning the occurrence of a state solely depends on its immediate predecessor, implying the absence of memory effects.

Let the symbols τ and τ' designate two different microscopic states (distinct configurations) within the system, both of which fall within a specified state space, denoted as S. If $\omega(\tau' \to \tau)$ denotes the transition rates from state τ' to τ and $P(\tau', t)$ represents the probability for the system to be in configuration τ', then the time evolution of the probability $P(\tau, t)$ to find the system in configuration τ is governed by the master equation expressed as

$$\frac{\partial P(\tau,t)}{\partial t} = \underbrace{\sum_{\tau' \neq \tau} \omega(\tau' \to \tau) P(\tau', t)}_{Gain} - \underbrace{\sum_{\tau' \neq \tau} \omega(\tau \to \tau') P(\tau, t)}_{Loss}. \tag{1.1}$$

In Eq. (1.1), the initial term on the right-hand side represents the possible ways of transitioning from configuration τ' to τ, while the subsequent term concerns the probability of leaving the configuration τ. Typically, in the studied model, the transition rates ω are presumed to be constant over time and are deduced from the system's dynamics. Our primary focus lies in the steady-state properties of the system, and these can be determined by solving $\frac{\partial P(\tau,t)}{\partial t} = 0$ which leads to

$$\sum_{\tau' \neq \tau} \omega\left(\tau' \to \tau\right) P\left(\tau'\right) - \sum_{\tau' \neq \tau} \omega\left(\tau \to \tau'\right) P(\tau) = 0. \tag{1.2}$$

The aforementioned expression provides a necessary condition for a system to reach a steady-state. A potential solution to this equation is given by

$$\omega\left(\tau' \to \tau\right) P\left(\tau'\right) = \omega\left(\tau \to \tau'\right) P\left(\tau\right). \tag{1.3}$$

It implies that the system adheres to the detailed balance condition, signifying a state where transition probabilities achieve an equilibrium.

In the context of stochastic processes and master equations, the steady-state distribution that emerges from detailed balance conditions often resembles the Boltzmann distribution. When the detailed balance is satisfied, the ratio of probabilities $P\left(\tau'\right)/P\left(\tau\right)$ becomes proportional to the ratio of transition rates $\omega\left(\tau \to \tau'\right)/\omega\left(\tau' \to \tau\right)$, which closely resembles the exponential term in the Boltzmann distribution.

In the following sections, we delve into a comprehensive exploration of appropriate methodologies employed for analyzing the model. Our emphasis is on elucidating how the stationary properties of the system with the random updating rule are influenced by the open boundary conditions .

1.4.1 Theoretical methods

The one-dimensional exclusion process with a random-sequential updating rule is an extensively researched model in the field of statistical physics. Various methods have been applied to scrutinize and find solutions for this model. Here are some exact techniques employed in the study of TASEP.

1. Recursion: Utilizing a recursion relation, this approach precisely calculates expressions for density and current through a complex generating function method, as detailed in Ref. [31]. Furthermore, it can be extended to compute higher-order correlation functions.

2. Matrix-Product Ansatz: This approach entails expressing configuration weights as a product of non-commuting matrices, facilitating the derivation of precise expressions

for density and current [32]. The methodology is inspired by the quantum inverse scattering method.

3. Bethe Ansatz: In this approach, the process begins by defining the Hamiltonian, expressing it using creation and annihilation operators, and suggesting a trial wave function that adheres to the system's symmetries [36]. The next crucial step is to enforce the Bethe Ansatz equations, which are derived by requiring the wave function to be an eigenstate of the Hamiltonian. Solving these equations produces the Bethe roots, which characterize the eigenstates of the system. These roots are then employed to compute particle densities and currents, providing precise solutions for particular parameter configurations within the model.

The aforementioned methods involve complex, lengthy and time-consuming calculations, rendering them quite challenging. Furthermore, adapting these methods beyond the basic model to analyze diverse models that feature more realistic processes, as we will explore in the subsequent sections, poses a substantial difficulty. Initially, we elucidate the simulation techniques utilized, followed by a theoretical method that yields exact results.

1.4.2 Stochastic simulations

Monte Carlo simulations, named after the Monaco casino, use random sampling to model and analyze complex systems. This computational technique approximates mathematical results and evaluates system behaviour, especially when analytical solutions are challenging. By performing numerous random experiments, it provides statistical estimates in fields like physics, finance, and engineering. Widely applied for probability, optimization, and numerical integration problems, Monte Carlo simulations [37] offer valuable insights into complex systems' behaviour, with accuracy depending on the number of iterations performed.

In this thesis, we have verified our theoretical findings through Monte Carlo simulations employing random sequential update rules, which are better suited for studying intracellular transport systems. We illustrate the procedure for performing Monte Carlo simulations for a single-lane TASEP in Fig. (1.5)

In addition to this, we have utilized the Gillespie algorithm [38] (akin to kinetic Monte Carlo), introduced by Joseph H. Gillespie in 1976. For a given system state, the algorithm identifies all potential sites for a successful move, computes their kinetic rates, and sums them up. The event probability is then determined by weighing each rate against the total rate. The time until the next event is calculated as $\Delta t = -ln(r)/(\text{sum of all kinetic rates})$, where r is a random number generated from a uniform distribution between 0 and 1. The lists are updated accordingly, and the

process is iterated until 10^9 number of events have occurred. To ensure the system reaches a steady state, the initial 5% of these events are excluded.

Now, we delineate a frequently utilized theoretical approach to obtain stationary solutions for the TASEP model. This method offers several advantages: (i) It is straightforward to implement mathematically. (ii) It yields exact solutions. (iii) It has demonstrated effectiveness, particularly when dealing with an enhanced system complexity.

1.4.3 Approximate method: Mean-field theory

In this section, we briefly explore the steady-state solution of the model using simple mean-field theory (MFT), demonstrating a strong agreement between the obtained solution and Monte Carlo simulations.

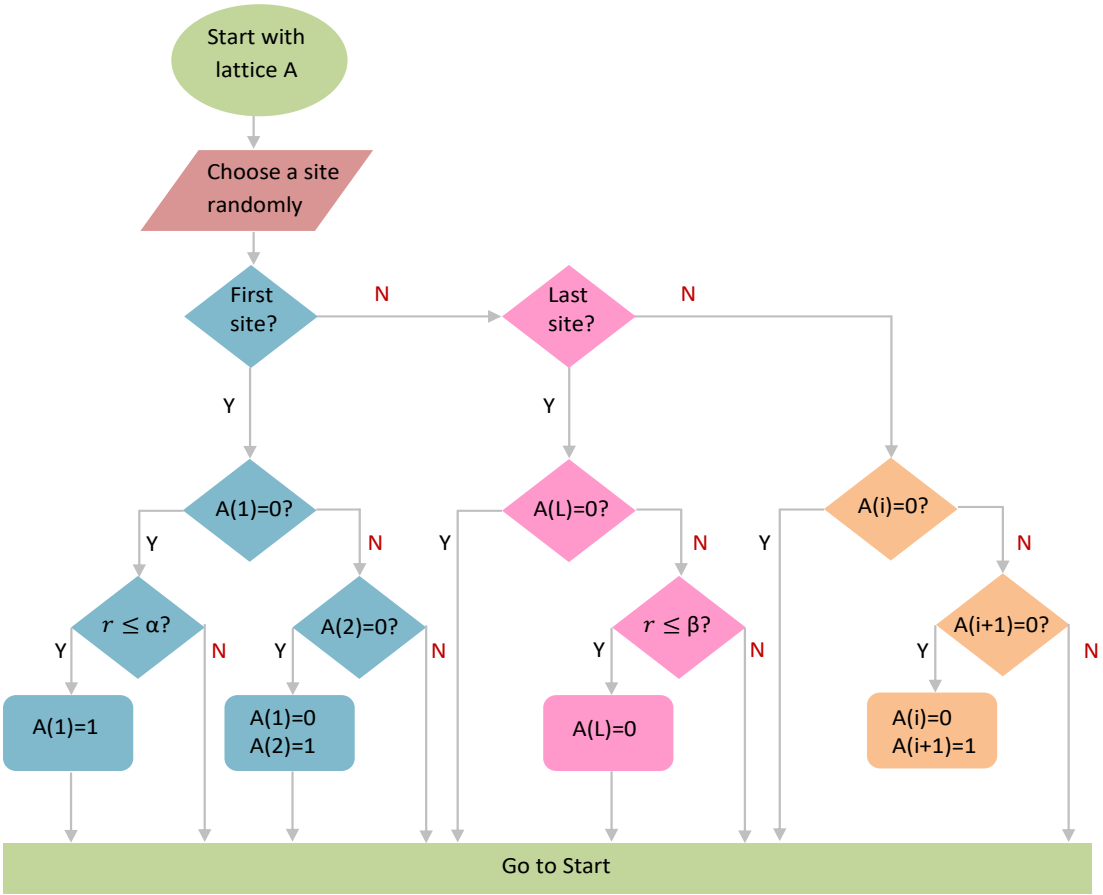

Figure 1.5: A flow chart for conducting Monte Carlo simulations for random-sequential updating rule. Here, 'r' represents a uniformly distributed random number between 0 and 1. The variable 'i' ($1 \leq i \leq L$) corresponds to a site on the lattice. After repeating the above process for a sufficient time, the initial approximately 5% steps are disregarded to establish the steady-state. The average lattice density is then computed by taking the time average over an interval of $10L$.

Let us use a binary variable denoted by τ_i, $i \in \{1, 2, \ldots, L\}$ to express the occupancy

status of individual sites on the discrete lattice. Each τ_i is defined as:

$$\tau_i = \begin{cases} 1, & \text{if site } i \text{ is occupied by a particle,} \\ 0, & \text{if site } i \text{ is empty.} \end{cases}$$

Thus, the configuration of the system at any time t is denoted by $\tau(t) = (\tau_1(t), \tau_2(t), \ldots, \tau_L(t))$.

For any given initial configuration $\tau(0) = (\tau_1(0), \tau_2(0), \ldots, \tau_L(0))$, we can derive master equations governing the time evolution of the average occupancy of the bulk sites $1 < i < L$, during an elementary time interval dt, given by

$$\frac{d\langle\tau_i\rangle}{dt} = \langle\tau_{i-1}(1-\tau_i)\rangle - \langle\tau_i(1-\tau_{i+1})\rangle \tag{1.4}$$

where $\langle\ldots\rangle$ depicts the statistical average. The above equation characterizes the variation in particle density at the ith site as the difference between the average influx and out-flux of particles to and from that particular site. At the boundary sites $i = 1$ and L, particle densities evolve as

$$\frac{d\langle\tau_1\rangle}{dt} = \alpha\langle 1-\tau_1\rangle - \langle\tau_1(1-\tau_2)\rangle, \tag{1.5}$$

$$\frac{d\langle\tau_L\rangle}{dt} = \langle\tau_{L-1}(1-\tau_L)\rangle - \beta\langle\tau_L\rangle. \tag{1.6}$$

The incorporation of open boundary conditions is denoted by the initial term on the right-hand side of Eq. (1.5), indicating the introduction of a particle on the lattice at a rate of α. The subsequent term on the right-hand side in Eq. (1.6) corresponds to the departure of a particle from the lattice at a rate of β. In the case of periodic boundary conditions, the master equation given by Eq. (1.4) is adjusted such that for $i = 1$, $\tau_{i-1} = \tau_L$, and for $i = L$, τ_{i+1} is replaced with τ_1.

.It is apparent that the Eqs. (1.4), (1.5), and (1.6) mentioned above include two-point correlators, rendering them intractable to handle in the current form. Therefore, a natural approach is to decompose the correlator function into the product of individual averages, a method known as the mean-field approximation [31]. Originally proposed by Pierre Curie [39], this approach has been applied to solve models akin to TASEP, where exact solutions were elusive for steady-state conditions. The core concept of the mean-field approximation is to focus on a single particle instead of considering many particles collectively. In essence, it simplifies a many-body system into a one-body system, facilitating the analysis of steady-state dynamics. The key principle of this theory is its neglect of correlations between the occupations of different sites. For a more in-depth understanding, interested readers can refer to Refs. [31,40].

Now, utilizing mean-field approximation, we factorize the two-point correlators by

using

$$\langle \tau_i \tau_j \rangle = \langle \tau_i \rangle \langle \tau_j \rangle , \quad \forall i, j \in \{1, 2, \ldots, L\}. \tag{1.7}$$

Certainly, the set of equations given by Eq. (1.4) constitutes a many-body problem, given its discrete nature. In case L is substantially large, dealing with a huge number of equations is difficult. Therefore, to simplify this many-body problem into a one-body problem, particularly in the continuum limit (thermodynamic limit), where L approaches infinity ($L \to \infty$), we employ coarse-graining on the discrete lattice with a lattice constant $\epsilon = 1/L$. Consequently, we re-scale both spatial and temporal variables as $x = i/L \in [0, 1]$ and $t = t/L$, respectively. Expressing the average particle density as $\langle \tau_i \rangle = \rho_i = \rho(x) \in [0, 1]$ and employing a Taylor series expansion on $\rho_{i\pm1}$ while retaining terms up to second-order derivatives, we obtain

$$\rho_{i\pm1} = \rho_i \pm \frac{1}{L}\frac{\partial \rho_i}{\partial x} + \mathcal{O}\left(\frac{1}{L^2}\right).$$

In the thermodynamic limit, the expansion outlined above transforms Eq. (1.4) into a well-known continuity equation [41,42] expressed as:

$$\frac{\partial \rho}{\partial t} + \frac{\partial J(\rho)}{\partial x} = 0. \tag{1.8}$$

Note that the subscript i has been omitted, as the lattice lacks any form of inhomogeneity. Here,

$$J(\rho) = \rho(1 - \rho) \tag{1.9}$$

represents the particle current, in the system. The subsequent analysis relies on the existence of this unique relationship denoted by $J(\rho)$, depicting the connection between current and particle density. Noteworthy characteristics of this particle-density relationship are outlined below.

- At a particle density of zero, indicating an absence of particles on the lattice, the particle flow is also zero.
- As the number of particles on the lattice gradually increases, both the density and particle current exhibit a gradual rise.
- The density eventually reaches the value $\rho_{max} = 0.5$, representing the scenario of maximum particle flow with $J_{max} = 0.25$.
- When the particle density reaches one, the lattice is fully packed, rendering any movement impossible; consequently, the current returns to a value of 0.

This relationship is visually represented by a parabolic curve, as illustrated in Fig. (1.6b) and is referred to as the fundamental diagram.

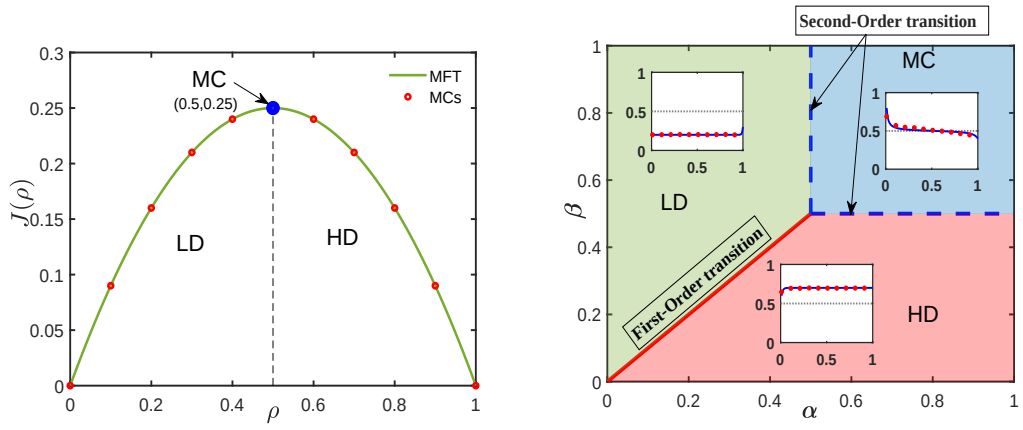

(a) (b)

Figure 1.6: (a) Fundamental diagram representing the current-density relation. (b) Phase diagram for open TASEP system in the $\alpha - \beta$ plane. The solid red line, representing $\alpha = \beta$, signifies a first-order transition line, whereas the dashed blue lines represent second-order transitions. Insets show a typical density profile in the corresponding region. Symbols represent the simulation results.

Since we are interested in attaining the steady-state solution for the system, we nullify the time derivative term by setting $\partial\rho/\partial t = 0$. This simplification transforms Eq. (1.8) into the following form:

$$(2\rho - 1)\frac{d\rho}{dx} = 0. \tag{1.10}$$

The corresponding boundary equations, as outlined in Eqs. (1.5) and (1.6), are then converted to:

$$\begin{aligned} \rho(0) &= \alpha, \\ \rho(1) &= 1 - \beta. \end{aligned} \tag{1.11}$$

Upon examination of Eqs. (1.10) and (1.11), it becomes evident that we are dealing with a first-order differential equation that must satisfy two boundary conditions, categorizing the problem as over-determined. The potential solutions to Eq. (1.10) are given by $\rho(x) = 0.5$ and $\rho(x) = k$ where k is a constant depending upon the boundary condition utilized. Hence, the stationary behaviour of the system is dictated by the parameters α and β that govern the boundaries [30,43].

The $\alpha - \beta$ parameter space reveals three distinct stationary solutions for particle densities (see Fig. (1.6)(b)). These solutions correspond to α, $1 - \beta$, and 0.5, denoted as the low density (LD), high density (HD), and maximal current (MC) phases, respectively. Now, we provide a summary of the properties associated with each phase.

1. **Low density (LD) phase.** The bulk density in this phase is entirely determined by the solution $\rho = \alpha$, and owing to the impact of the entry rate, this phase is referred

Phase	ρ^1	ρ	ρ^L	J	Phase region
Low density (LD)	α	α	$\frac{J}{\beta}$	$\alpha(1-\alpha)$	$\alpha < \min\{\beta, 0.5\}$
High density (HD)	$1-\frac{J}{\alpha}$	$1-\beta$	$1-\beta$	$\beta(1-\beta)$	$\beta < \min\{\alpha, 0.5\}$
Maximal current (MC)	$1-\frac{1}{4\alpha}$	0.5	$\frac{1}{4\beta}$	0.25	$0.5 < \min\{\alpha, \beta\}$

Table 1.1: Summary of the bulk and boundary densities, conditions of existence of distinct stationary phases for the simplest version of TASEP model. The bulk density of the lane is denoted by ρ and the density at boundary sites $i = 1(L)$ is signified as $\rho^1(\rho^L)$. J represents the corresponding steady-state current due to the flow of particles.

to as the entrance-dominated phase. The condition for the existence of this phase is straightforwardly expressed as $\alpha < \min\{\beta, 0.5\}$. This implies that the density in this phase remains below 0.5, earning it the designation of a low density phase. Moreover, it implies that the entry rate α consistently remains lower than the exit rate β, suggesting a likelihood of particles exiting the lattice at a faster pace than their entry.

2. **High density (HD) phase.** In this phase, the bulk density is defined by $\rho = 1-\beta$, which is governed by the exit rate, earning it the label of the exit-dominated phase. The criteria for its existence can be straightforwardly derived: $\beta < \min\{\alpha, 0.5\}$. The conditions $\beta < \alpha$ imply that particles enter more rapidly than they leave. Consequently, the accumulation of a significant number of particles on the lattice results in a density exceeding 0.5, classifying it as a high density phase.

3. **Maximal current (MC) phase.** Here, the density profile stabilizes at a constant value of 0.5, irrespective of the entry-exit rates. The existence of this phase requires $\min\{\alpha, \beta\} > 0.5$. Known as the maximal current phase, it is characterized by the current reaching its peak value of 0.25, aligning with the solution of $\frac{dJ}{d\rho} = 0$. Importantly, both α and β surpass 0.5, signifying swift entry and exit of particles from the lattice.

Based on the above results, a phase diagram can be drawn in the $\alpha - \beta$ parameter space, as illustrated in Fig. (1.6b), while a concise summary of the findings is outlined in Table (1.1).

A notable aspect of the one-dimensional exclusion model with open boundaries is the occurrence of boundary-induced phase transitions, a phenomenon absent in equilibrium systems.

1. **First-order transition.** On the boundary between the LD and HD phases, the equality of entry and exit rates creates a shock that delineates the low and high

density segments. This shock is non-localized and moves randomly throughout the lattice. The density undergoes a discontinuous variation across this transition line, leading to a first-order transition.

2. **Second-order transition.** In contrast, the transition from both the LD and HD phases to the MC phase, along the lines $\alpha = 0.5$ and $\beta = 0.5$ respectively, is characterized by a continuous change in both density and current. Hence, a second-order phase transition occurs in these cases.

We want to emphasize that although the mean-field approximation has shown its effectiveness in this thesis, it is not universally applicable in all situations. For instance, in the simple TASEP scenario with parallel updating [43], significant correlations between particles emerge, rendering the basic mean-field approximation inadequate. Similarly, when examining interactions between adjacent sites [103], the limitations of the simple mean-field approach become evident, necessitating the adoption of cluster mean-field methods.

1.5 Extensions of the TASEP model

The simple exclusion model serves as a well-established framework that offers valuable insights into the transport phenomena. Nevertheless, it falls short of comprehensively representing the complexities found in realistic transport systems. To address this limitation, substantial work has been devoted to extending the model by integrating essential features, including narrow entrances, coupled lattices, dynamic disorder, bidirectional transport, Langmuir kinetics, complex networks, finite resources, and more. In the following sections, we will provide a concise overview of each of these generalization, that are relevant to the problems addressed in this thesis.

1.5.1 Stochastic attachment-detachment

During intracellular transport, the processive motor proteins traversing along microtubules, frequently undergo binding and unbinding events between the cytoplasm and the filament. A similar situation can be witnessed in vehicular traffic, where vehicles can enter and exit highways using on/off ramps. To incorporate these attachment and detachment processes, the foundational TASEP model is modified to include the concept of Langmuir Kinetics (LK) [44]. Under this dynamics, the particles attach with a rate ω_a and detach with rate ω_d from the lattice, in addition to the unidirectional motion at a unit rate, as shown in Fig. (1.7). Consequently, the number of particles within the bulk is not conserved, therefore, it is also termed as non-conserving dynamics.

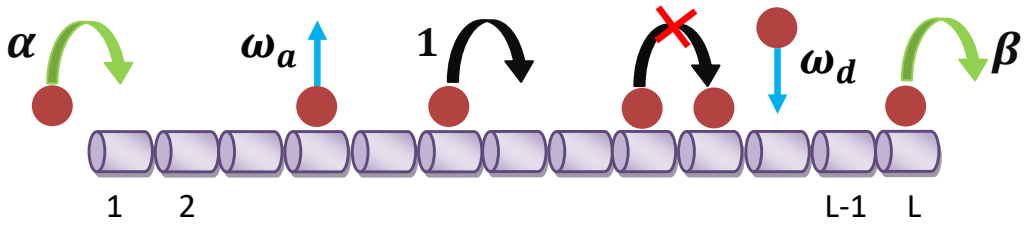

Figure 1.7: Schematic representation of TASEP with LK. The entry rate of a particle through the first site is α and the exit rate from the last site is β. Attachment/detachment of a particle occurs with rate ω_a/ω_d.

The categorization of TASEP as a non-equilibrium process sets it apart from LK, which is characterized as an equilibrium process. If we disregard the particle horizontal movement in the stochastic attachment and detachment process, the steady-state particle density is solely determined by the ratio of the kinetic rates, expressed as $\rho = K/(K+1)$, where $K = \omega_a/\omega_d$ represents the binding constant. As a result, it can be stated that this steady-state remains robust with respect to the boundary conditions and is primarily governed by bulk dynamics. In contrast, the simple exclusion model evolves into a stationary non-equilibrium state that maintains a finite conserved current within the bulk and is highly sensitive to alterations in boundary dynamics. To effectively capture the interplay between these two contrasting dynamics, the LK rates are re-scaled as $\Omega_a = \omega_a L$ and $\Omega_d = \omega_d L$ [45,46].

The inclusion of LK in TASEP, originally proposed to investigate a financial market issue [47], was subsequently applied to represent the dynamics of molecular motors [45,46,48]. The initial exploration in this direction centred on studying the consequences of detachment in a one-dimensional exclusion process model [48]. Later, it was expanded to encompass attachment dynamics, yielding several intriguing and noteworthy phenomena, such as localized shocks, space-dependent bulk currents, and phase separation [45,46]. These phenomena are not observable in isolated TASEP and LK processes. Moreover, the existence of these localized shocks contributes to a more intricate phase diagram compared to the simpler TASEP model.

1.5.2 Bidirectional flow

In a eukaryotic cell, the dynamic process of intracellular transport relies on the cooperation of two essential motor proteins, kinesin and dynein [49]. Kinesin predominantly propels cargo towards the plus end of microtubules, directing it towards the cell's periphery, while dynein, in contrast, moves cargo in the opposite direction, towards the cell's centre or minus end of microtubules [50]. This coordinated bidirectional movement ensures the precise delivery of organelles, vesicles, and other cellular components to their intended destinations. The balanced operation of kinesin

and dynein, often facilitated by regulatory proteins and adaptor molecules, plays a vital role in numerous cellular processes, supporting intracellular transport and cellular organization with remarkable precision and efficiency. Similarly in rural regions, single-lane roads are prevalent, enabling traffic flow in both directions, yet often insufficient for vehicles to overtake one another safely [5,51]. This serves as the groundwork for the investigation of minimal models in bidirectional transport, with a focus on the interaction between two distinct species and the collective mobility of these elements.

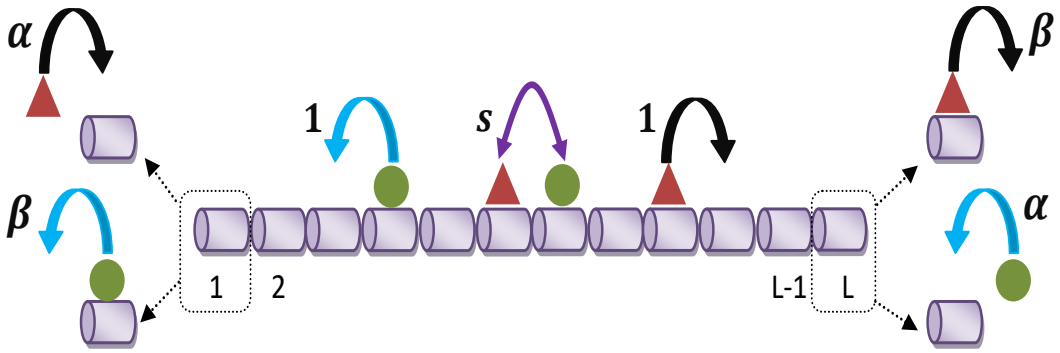

Figure 1.8: (a) Sketch of a bidirectional TASEP model featuring two particle species, represented by red triangles (moving from left to right) and green circles (hopping from right to left) travelling unidirectionally while adhering to the exclusion principle. Two distinct species swap their respective positions upon meeting head-on.

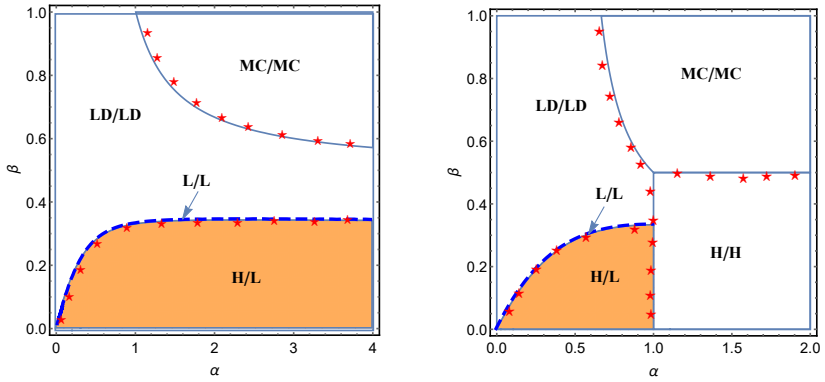

(a) (b)

Figure 1.9: Phase diagram for: (a) bidirectional TASEP model on one lane and (b) two-lane model featuring narrow entrances, with infinite resources.

In this direction, the 'bridge model' was the pioneer in emphasizing the steady-state properties of a system featuring two distinct particles navigating a single lattice [52]. The primary idea was to prevent particles from colliding by permitting them to swap positions whenever they encounter each other (see Fig. (1.8)). The phase diagram for a one-dimensional bidirectional lattice with infinite resources is depicted in Fig. (1.9b). It reveals two symmetric phases: MC/MC and LD/LD, as well as two asymmetric

phases: L/L and H/L. This illustrates phases with symmetry breaking, even under the symmetric conditions of the dynamic process for both particle types within a single channel. Such unexpected phenomenon is recognized as 'spontaneous symmetry breaking' [34,53]. Nonetheless, the precise understanding of this phenomenon still remains elusive. The transition to a state of broken symmetry continued to be a subject of debate on the model [54,55]. Subsequently, the investigation was expanded to a novel category of the bridge model that incorporated junctions [56], and to the examination of stochastic directional switching mechanisms and lane switching processes in a conserved TASEP multi-species model operating in two channels [57]. Many different generalizations of the bidirectional model have been investigated by including more complex dynamics such as resource scarcity [58], non-conserving dynamics [59], two-lane bidirectional transport with constraint entrances [60].

1.5.3 Impact of narrow entrances

Microtubules are comprised of polymer chains made up of fundamental subunits called α/β-tubulin, which naturally arrange themselves into protofilaments of diameter approximately 25nm along the microtubule's length [61]. Typically, twelve to fourteen of these protofilaments twist together, forming a helical cylinder that serves as a highway for long-distance intracellular transport, guided by molecular motors like kinesin and dynein [62]. However, this twisting arrangement introduces curvature to the microtubule, resulting in both circular and wavy pathways, which has been observed experimentally, indicating that the protofilaments take on curved shapes [63]. The bends found in protofilaments give rise to constraint passageways that function as links connecting the entry and exit points for multiple filaments [63]. Moreover, in vehicular traffic, the locations where traffic congestion delays or completely halts unrestricted directional movement, thereby obstructing bidirectional traffic flow, can also be regarded as a narrow entrance point.

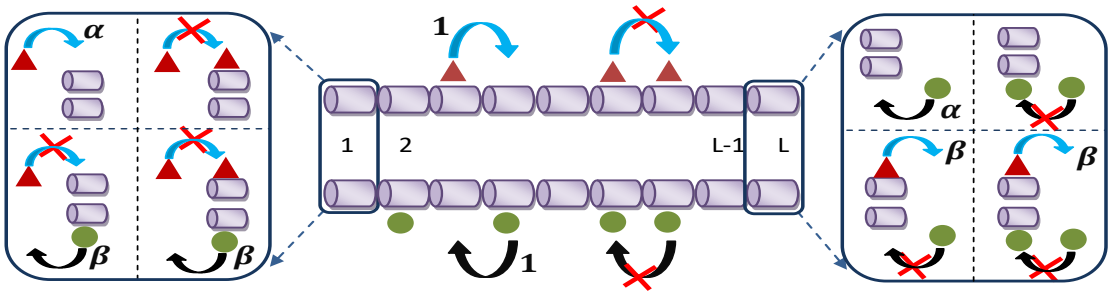

Figure 1.10: Illustration of a two-lane bidirectional exclusion model with narrow entrances. The two types of particle species are denoted by red and green circles. Arrows indicate allowed transitions while crosses depict prohibited movements.

These observations initiated the exploration of two-lane exclusion processes, which

entail the movement of two distinct particle species in opposing directions along separate lattices, where interactions occur exclusively at the lattice boundaries [60]. In this study, a system with two lanes and narrow entrances was examined, as depicted in Fig. (1.10). The particles are allowed to attach from an infinite reservoir to vacant entry sites on a lattice, provided that the corresponding site on another lattice is also unoccupied. Importantly, a particle could exit the lattice without being influenced by the presence or absence of a different type of particle at the corresponding site on the other lattice. In the bulk of the system, both types of particles moved in opposite directions at a unit rate. Since the particles only interacted at the boundaries, this system can be conceptualized as two independent single-lane Totally Asymmetric Simple Exclusion Processes (TASEPs) with particles moving in opposite directions. The corresponding phase diagram is depicted in Fig. (1.9b). While both systems can be seen as interactions between two independent lanes only at the boundaries, they differ significantly in terms of their stationary properties. This contrast is evident in Fig. (1.9), prompting the necessity to extend these models individually.

1.5.4 Role of limited resources

Numerous physical and biological occurrences, such as protein synthesis, motor protein movement, pedestrian flow, and vehicular traffic, involve competition for finite resources [64–67]. For instance, in protein synthesis, ribosomes play a crucial role in translating messenger RNA (mRNA) sequences into proteins, but their availability may be limited, especially during periods of rapid growth or stress, leading to competition among different mRNA molecules for these essential resources [68]. Transcription factors, which regulate gene transcription by binding to DNA sequences, can also face constraints, impacting the expression of target genes and creating competition for their binding sites. Generally, the entrance rate of particles is influenced by reservoir occupancy. However, a crowded reservoir not only increases particle entrance rates but may also impede their exit rates from lanes. This phenomenon is akin to the 'parking garage problem', where a crowded garage can slow down vehicle exits onto the road. Recent studies on a TASEP variant, termed 'reservoir crowding', consider the impact of reservoir occupancy on both entry and exit rates [58,69,70], effectively replicating real-world scenarios.

Figure (1.11) provides a visualization of a TASEP system with limited resources. If N_r represents the number of particles in the reservoir at a steady state, then in general scenarios, $\alpha^{eff} = \alpha f(N_r)$ and $\beta^{eff} = \beta$ [64]. In situations where the system experiences reservoir crowding, β^{eff} undergoes modification to $\beta g(N_r)$. The functions f and g represent increasing and decreasing functions of the reservoir density, respectively. In situations with finite resources, a localized shock phase emerges,

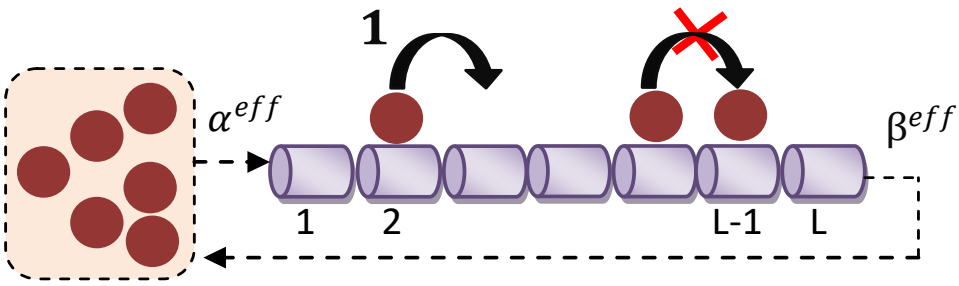

Figure 1.11: Sketch of an open TASEP model with constrained resources. The variables α^{eff} and β^{eff} give the effective entrance and exit rates of the particles, respectively.

covering a substantial portion of the phase plane and diminishing as particle resources increase [64]. Conversely, in the scenario of reservoir crowding, the shock phase continues to persist irrespective of the particle count in the system [69].

1.5.5 Dynamic disorder

Real-world transportation is often hampered by various physical or natural barriers that slow down or momentarily obstruct the regular flow of particles by causing jamming-like situations. Such situations can occur in microscopic scenarios, where the movement of RNA polymerase during gene transcription is hindered by regulatory proteins and structures bound to DNA [71] or in macroscopic traffic situations, where a defective vehicle or malfunctioning traffic light can lead to congestion on a busy road. Messenger-RNA (mRNA), which comprises of a sequence of codons, is synthesized during the transcription of DNA templates. Subsequently, it is decoded by transfer-RNA (tRNA) within the ribosome during the translation process to generate an amino acid chain. The speed of translation at each codon site is regulated by the specificity of the codon and the concentration of tRNA molecules that are freely diffusing. Interestingly, in many cases, the protein formed from amino acid chains or the aggregation of tRNA molecules can impede the movement of the motor proteins [15]. These impurities can be categorized into two types: static and dynamic, where static defects refer to fixed or immobile imperfections in a system that do not change over time. On the other hand, dynamic defects are imperfections in a system that can arise and disappear, affecting the system's behaviour and properties intermittently. A prime example of dynamic disorder can be observed in DNA transcription, where the DNA structure is highly dynamic, and transiently bound proteins hinder the transcription process [72]. Other examples include the periodic switching of traffic lights and defects that stochastically bind and unbind at specific sites [73,74].

1.5.6 Coupled TASEPs

Over the past few decades, there has been a noticeable increase in the inclination to extend single-dimensional models to coupled multi-lane systems, motivated by various real-world phenomena. In both vehicular traffic and biological transport, particles demonstrate the capability to adhere to or deviate from their prescribed routes in various systems [75,76]. Several instances from vehicular traffic illustrate such scenarios few of them are: (i) Accelerating on the entrance ramp, the driver seamlessly merges into highway traffic by changing lanes, skillfully finding a safe gap in the flow [77]. (ii) When faced with lane closure due to construction, drivers employ zipper merging, alternately merging from closing lanes into open ones. (iii) Faced with an obstacle or hazard in their current lane, drivers swiftly change lanes to steer clear of the impediment, be it road debris or a stalled vehicle [78]. Similarly, in biological transport, motor proteins can attach and detach from microtubules and cytoplasm, allowing for adaptability in their pathways [79]. Another example is seen in ants who optimize resource collection by metaphorically changing lanes on foraging trails, and adjust pheromone-guided paths based on the availability of food sources [80]. In all of these cases, the ability of particles to switch paths is influenced by the dynamic conditions they encounter.

In light of all these situations, numerous efforts have been made to adapt the exclusion model and explore particle dynamics, considering the particle configuration in neighbouring lanes as a significant factor. A theoretical framework employing vertical cluster mean-field is employed to analyze a two-channel model with symmetric and asymmetric coupling [81,82] or a combination of both [83–86]. The research findings indicate that robust asymmetric coupling results in seven stationary phases, the majority of which exhibit zero particle flux in one of the channels. However, under strong asymmetric coupling, the characteristics of the two lanes become nearly identical. Subsequently, various adaptations of the coupling model were introduced, integrating diverse dynamical rules, including coupling on anti-parallel lanes [87,88], multi-channel coupled system [89,90], periodic boundaries [91], and Langmuir kinetics [92–98]. Some of them also conducted a thorough examination of the system's stationary properties through a boundary layer analysis [96–98].

1.6 Aims and objectives

This thesis explores the steady-state properties of non-equilibrium stochastic transport processes, specifically focusing on systems propelled by diffusion. Our goal is to harness knowledge from a range of disciplines, including Mathematics, Statistics, Biology, and Physics, in order to characterize the dynamic properties inherent in these systems. The collective behaviour of these systems is replicated through various network

topologies, including single, multiple, or junction-type. To bring realistic dynamics into these systems, we include at least one dynamic element that operates in real-time, such as (i) stochastic association and disassociation of particles (referred to as Langmuir Kinetics), (ii) bidirectional flow, (iii) inclusion of obstacles, (iv) constrained entrances, and (v) limited resources. As a foundational approach, we employ a discrete stochastic Markov model TASEP, a paradigmatic framework commonly used to elucidate complex non-equilibrium transport phenomena.

The primary goal of examining the different variants is to scrutinize the stationary characteristics of the system. This involves analyzing key aspects such as particle density on the lattice, the flow of particles, and the phase diagrams within the realm defined by the governing parameters of the model's dynamics. The examination of these properties is conducted through a comprehensive approach that combines theoretical techniques, particularly mean-field theory, with stochastic simulations such as Monte Carlo technique (including the Gillespie algorithm). Outlined below are the main aims and objectives of this thesis.

- *To understand the phenomenon of spontaneous symmetry breaking (SSB) observed in one-dimensional bidirectional transport systems.* To pursue this objective, we intend to analyze the consequences of connecting the system to two reservoirs, each designated for particles of a single species. The motivation for this inquiry stems from the dynamic interplay of multiple species moving in opposite directions within various real-world transport processes.

- *To scrutinize the SSB phenomena in systems involving junctions.* Further continuing our investigation into the phenomenon of SSB, we turn our attention to the intricate dynamics of bidirectional particle flow within configurations resembling roundabouts in the vicinity of finite resources. The overarching goal is to construct a robust theoretical framework capable of effectively capturing and elucidating the crucial stationary properties inherent in this complex system.

- *Exploring the consequences of reservoir crowding on a two-lane narrow entrance system in a resource-limited environment, particularly in the presence of a dynamic defect.* The inspiration for addressing this problem arises from the finite availability of entities in real-world situations, affecting both entry and exit rates. Furthermore, the insufficient literature addressing generalized models that incorporate dynamic disorder contributes to the motivation behind this investigation.

- *Building a model to understand the lane switching dynamics of particles in multi-lane system.* Towards this aim, we intend to investigate a resource-constrained two-lane model with lane-changing mechanism. To the best of our knowledge, there is currently

no existing research that theoretically examines this model and provides a universal framework for traffic processes.

- *To obtain a framework for analyzing the dynamics of Langmuir kinetics on a junction-type topology.* Complex network behaviour is a common occurrence in biological transport phenomena, where numerous pathways merge at specific junctions and then diverge in different directions. Stimulated by these observations, as well as the association and disassociation of entities on these pathways, we aim to analyze two different variants of a single junction model. In the first model, the focus is on examining the network topology with Langmuir kinetics to study stationary properties in a context where particle resources are unlimited. In the subsequent model, a global constraint is introduced to restrict the overall number of particle resources.

1.7 Outline of the thesis

This thesis introduces various generalizations of TASEP-based models that have not been previously explored, examining them under diverse dynamical settings that emulate real-world transportation scenarios. We predominantly employ the mean-field approach for theoretical examination and conduct extensive Monte Carlo simulations to rigorously validate those findings. The work of the thesis is organized into eight chapters, with six main chapters (from Chapter 2 to 7) complemented by the introductory (Chapter 1) and conclusive chapter (Chapter 8). The following is a summary of the contents covered in each chapter.

Chapter 1: In this chapter, we concisely explore the basic introduction and motivation for this thesis. It includes a relevant literature survey that underscores the necessity to investigate more generalized models and their characteristics.

Chapter 2: Interplay of two reservoirs in a bidirectional transport system
In this chapter, driven by the interactions among multiple species in various real-world transport processes, we introduce a bidirectional totally asymmetric simple exclusion process. The system involves two finite particle reservoirs controlling the influx of particles moving in opposite directions, each representing a distinct species. To analyze the stationary characteristics of the system, such as densities and currents, we utilize a theoretical framework based on mean-field approximation. We aim to study the influence of individual species populations, quantified by the filling factor, taking into account both equal and unequal conditions. It is expected that the system will demonstrate spontaneous symmetry-breaking phenomena in case of equal filling

factors. But can we expect such phenomena, in case the filling factors for the two species differ?

Chapter 3: Exclusion processes on a roundabout traffic model with constrained resources

Inspired by the traffic dynamics observed at roundabouts, we investigate the impact of limited resources on the movement of two distinct particle types along bidirectional lanes connected by two bridges. Each bridge is dedicated exclusively to the transportation of a specific particle species. Utilizing a mean-field framework, we aim to establish a theoretical foundation for our findings, providing analytical insights into stationary properties for both symmetric and asymmetric phases. The central focus is on understanding the significant impact of resource constraints on the system's quantitative and qualitative behaviour, particularly in the context of the interplay between finite resources and bidirectional transport. Our comprehensive examination extends to investigating system phase transitions, including symmetry-breaking phenomena and shock dynamics.

Chapter 4: Reservoir crowding in a dynamic disordered bidirectional system with narrow entrances

To deal with the existence of imperfections in intricate processes such as vehicular traffic and intracellular transport, this chapter focuses on a dynamically disordered system comprising of two lanes with narrow entrances. Particle movement encounters hindrance due to defects that stochastically bind and unbind at each site. Global constraints on both the number of particles and defects are introduced. Notably, the particle reservoir experiences crowding, influencing particle entry-exit rates. The model is analyzed within a mean-field framework, to explore phenomena such as stationary phase diagrams, particle densities, and spontaneous symmetry breaking. Our aim is to thoroughly examine the role of various parameters, including defect binding/unbinding rates, particle entry-exit rates, particle hopping rates in the presence of defects, and the number of particles/defects.

Chapter 5: Competition for resources in an exclusion model with biased lane-changing mechanism

The content of this chapter highlights the significance of the lane-changing mechanism evident in diverse biological and transportation phenomena. The lateral motion of a particle decreases when there is an opportunity for changing lanes. This mechanism gives rise to vertical interactions among entities, underscoring the necessity to apply vertical cluster mean-field theory. Additionally, the extreme ends of the lanes are linked to a reservoir having finite capacity. Our main concern is to examine the

effects of the filling factor on the stationary properties of the system. The theoretical finding reports phases involving the synchronized as well as unsynchronized presence of domain wall in each lane. The results are validated through the Gillespie algorithm.

Chapter 6: Particle creation and annihilation in an exclusion process on networks

This chapter explores an open network junction model of the totally asymmetric simple exclusion process with bulk particle attachment and detachment. Using a mean-field approach, we theoretically derive stationary system properties such as particle density, phase transitions, and phase diagrams. We classify various stationary phases in the system according to the phase transitions happening across the junction. Our system dynamics encourage us to answer a few essential queries. (i) Does the number of segments regulate the stationary properties of the system? (ii) How do the association-dissociation rates govern the dynamics of the system?

Chapter 7: Non-equilibrium processes in an unconserved network model with limited resources

In this chapter, we revisit the distinctive network topology involving interconnected lanes through a junction, as previously defined in the preceding chapter. Here, the system is enhanced with the addition of a particle reservoir with limited capacity. Despite the considerable complexity involved, will the mean-field approximation prove to be an effective approach to obtain the system's stationary properties? We start by scrutinizing the time evolution of particle density is conducted with the aim of achieving a steady-state behaviour. Then, in the stationary state, our objective is to investigate the qualitative and quantitative behaviour of the system in both scenarios. This involves examining cases where the number of lanes before and after the junction is either equal or unequal.

Chapter 8: Conclusion and Future Work

In the concluding chapter, we offer a summary of the results deliberated in the preceding sections of this thesis. Furthermore, we present future directions to enhance our understanding of non-equilibrium traffic phenomena.

Chapter 2

Interplay of two reservoirs in a bidirectional transport system

In the preceding chapter, we thoroughly examined the fascinating non-trivial characteristics exhibited by the one-dimensional totally asymmetric simple exclusion process (TASEP) model. Motivated by the interplay of multiple species in several real world transport processes, in this chapter[1], we propose a bidirectional totally asymmetric simple exclusion process with finite particle reservoirs regulating the inflow of oppositely directed particles corresponding to two different species. The system's stationary characteristics, such as densities, currents, etc., are investigated using a theoretical framework based on mean-field approximation and are supported by extensive Monte Carlo simulations.

2.1 Motivation and background

As previously mentioned in the introduction, various efforts have been undertaken to extend the TASEP model from a single-species to a multi-particle system, involving two distinct species of particles traveling in opposite directions on a lattice. Contrary to the single-species model, these extensions have reported various cooperative phenomena, such as spontaneous symmetry-breaking (SSB) and phase separation [34,53,55,58,99–101]. For two different types of propelled particles on a linear path, the 'bridge model' was the first model to address the existence of the broken symmetry under analogous dynamical conditions [52]. While the mean-field approach confirms the persistence of one of the asymmetric phases (low-low density phase) to a narrow region, Monte Carlo simulations reveal that this phase may not prevail in the thermodynamic limit [54,55]. Later, this study was extended to analyze multi-species models comprised of two lanes where particles travel in opposite directions and interact only at the boundaries [100–102]. However, our understanding of the mechanisms of the SSB phenomenon is very limited [34,52–55,58,99–104].

The majority of the studied TASEP models with open boundaries explore the dynamics of the multi-species system equipped with infinite resources which are far

[1]The content of this chapter is published in: "Ankita Gupta, Bipasha Pal, Arvind Kumar Gupta. Interplay of reservoirs in a bidirectional system. *Physical Review E,* 107(3):034103, 2023"

from reality. Many realistic phenomena both physical and biological such as protein synthesis, movement of motor proteins, pedestrian flow, and vehicular traffic involve competition for limited resources on either single or multi-lane systems. In this direction, several variants of TASEPs have evolved where the entrance rate of the particles is regulated by the occupancy of the reservoir, which leads to an addition of localized shock in the density profile [10,64,66,102,105–116]. In a recent study, a bidirectional system coupled to a finite reservoir has been investigated where the exit rate is also affected by the presence of limited resources [58]. All the research available on such extensions have primarily focused on a global constraint on the total number of particles in the system. In a bidirectional system connected to a unified finite reservoir that can hold all the particles, the total occupancy of the reservoir determines the entrance rates of the particles. Circumstantially, a scenario could develop in which the reservoir contains no particle of a certain species and as the entry rates depend upon the total number of particles in the reservoir rather than that of individual species, the dynamics of the system then promote the entry of this species, which is absurd. Several intriguing characteristics could arise if the total particle number of individual species is regulated.

Instigated by the indispensable significance of several reservoirs in a transport process with multispecies systems, the present study examines the dynamics of two-particle species moving in opposite directions on a single lattice strategically coupled to two different reservoirs. Our purpose is to investigate the impact of constrained resources for both the species on the stationary properties and characterize its essential features. We attempt to provide a theoretical framework for the system by utilizing mean-field approximation for bidirectional flow on a lattice connected to two reservoirs, each accommodating particles of a single-species only. It is interesting to scrutinize the impact of constraints on resources available for each species on the stationary properties of the system such as the SSB phenomenon and phase separation. Specifically, we aim to address the following queries. (i) How does the presence of finite resources influence the bidirectional flow? (ii) How is the SSB phenomenon affected, when both the particle species are available in equal quantities? (iii) Does the SSB phenomenon still prevail in the case of different capacities of the two reservoirs? (iv) If not, what qualitative and quantitative differences arise in the complex system properties for these two different scenarios?

2.2 Model description and theoretical framework

We consider a one-dimensional lattice comprised of L sites identified as $i = 1, 2, \ldots, L$. The boundaries of the lattice are represented by the sites $i = 1$ and $i = L$,

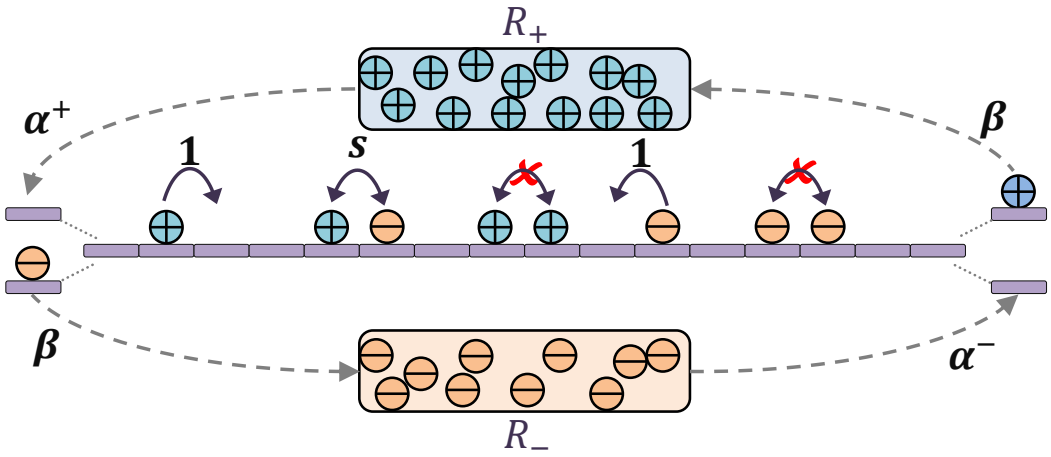

Figure 2.1: Schematic diagram for a bidirectional transport model comprised of a lattice connected to two reservoirs, each accommodating particles of a single-species only. Blue (+) and red (−) circles denote two oppositely directed particles travelling from left to right and right to left, respectively. The entrance rates of the two-particle species are given by α_+ and α_-, which are controlled by the occupancy of the corresponding reservoirs. The exit rates for both the particles are β. Two particles of distinct kinds are permitted to swap their positions with a rate s if they encounter each other on neighbouring sites.

whereas the remaining sites are referred to as bulk. Two species of particles denoted by the symbols (+) and (−) translocate on this lattice in opposite directions depicting the bidirectional flow as shown in Fig. (2.1). The particles interact via the hard-core exclusion principle which guarantees that not more than one particle occupies a single site. In particular, it is assumed that a (+) particle transverses from left to right, whereas a (−) particle hops in the reverse direction with a unit rate whenever the adjacent site is empty. If two different species of particles encounter each other on the lattice, they exchange their positions at a rate s, if the direction permits.

Furthermore, it is assumed that the lattice is connected to two finite reservoirs R_+ and R_- having no internal dynamics. The reservoir R_+ can accommodate only (+) particles, whereas the reservoir R_- solely sustains (−) particles. The total number of particles of an individual species is taken to be constant in our system. Specifically, N_{t_+} and N_{t_-} quantify the total number of (+) and (−) particles, respectively. A (+)/(−) particle from R_+/R_- enters the lattice through the site $i = 1/L$ if empty, with innate entry rate α, hops along the lattice and then escapes through the site $i = L/1$ with a removal rate β to rejoin the reservoir R_+/R_-.

As the lattice is coupled to two-particle reservoirs, the ingress rate of each species of the particle will no longer be constant; instead, it is regulated according to the number of particles in the associated reservoir. Also, a smaller number of particles in the reservoir implies lower entrance rates and enhanced content in the reservoir will lead to an increase in the entrance rates. Therefore, it is reasonable to modify the entrance

rate [110] of both species as

$$\alpha_+ = \alpha\frac{N_{r_+}}{N_{t_+}}, \qquad \alpha_- = \alpha\frac{N_{r_-}}{N_{t_-}}, \tag{2.1}$$

where N_{r_+}/N_{r_-} is the instantaneous number of $(+)/(-)$ particles in the reservoir R_+/R_-. Although the function we've selected is the simplest and most intuitive, there are infinite alternatives to choose from. Our selection is based on its analytical tractability. In different scenarios, while quantitative behaviors may differ, the qualitative nature of the system remains constant.

Clearly, $N_{r_+} \leq N_{t_+}$ and $N_{r_-} \leq N_{t_-}$ imply that the modified entrance rates remain confined between 0 and α. To scrutinize the effect of coupling the bidirectional transport to two reservoirs, we associate a parameter namely, the filling factor defined as $\mu_j = N_{t_j}/L,\ j \in \{(+),(-)\}$ to each reservoir. Additionally, we define the reservoir quotient as $r_j = N_{r_j}/L$.

To characterize the occupancy status of each site i, we designate two symbols denoted by τ_+^i and τ_-^i, which take binary value '1' in case the site is occupied by $(+)$ and $(-)$ particle, respectively and '0' otherwise. The master equations that govern the dynamics of both the particles in the bulk are given by

$$\frac{d\langle\tau_+^i\rangle}{dt} = J_+^{i-1,i} - J_+^{i,i+1}, \quad \frac{d\langle\tau_-^i\rangle}{dt} = J_-^{i+1,i} - J_-^{i,i-1}, \tag{2.2}$$

where $\langle\cdots\rangle$ represents the statistical average. The terms $J_+^{i-1,i}$ and $J_-^{i+1,i}$ represent the currents in the bulk arising due to $(+)$ and $(-)$ particles, expressed as

$$J_+^{i-1,i} = \langle\tau_+^{i-1}(1-\tau_-^i-\tau_+^i)\rangle + s\langle\tau_+^{i-1}\tau_-^i\rangle, \tag{2.3}$$
$$J_-^{i+1,i} = \langle\tau_-^{i+1}(1-\tau_-^i-\tau_+^i)\rangle + s\langle\tau_-^{i+1}\tau_+^i\rangle. \tag{2.4}$$

The first and the second terms on the right-hand sides of the above two equations correspond to the hopping of a particle to the adjacent vacant site and the interchange of the two-species of particles in the appropriate direction, respectively. It can be readily seen from Eqs. (2.3) and (2.4) that the two bulk current equations are decoupled for $s = 1$ and hence we consider only this case for further study. However, some insight about the scenarios when $s \neq 1$ is given in Section (2.5).

For $s = 1$, Eqs. (2.3) and (2.4) can be written in simplified form as

$$J_+^{i-1,i} = \langle\tau_+^{i-1}(1-\tau_+^i)\rangle,\ J_-^{i+1,i} = \langle\tau_-^{i+1}(1-\tau_-^i)\rangle, \tag{2.5}$$

which implies that a $(+)/(-)$ particle does not distinguish between a hole and a $(-)/(+)$ particle while moving forward. Similarly, the particle evolution equations

at the boundaries, $i = 1$ and $i = L$, can be written as

$$\frac{d\langle\tau_+^1\rangle}{dt} = J_+^{\text{enter}} - J_+^{1,2}, \quad \frac{d\langle\tau_+^L\rangle}{dt} = J_+^{L-1,L} - J_+^{\text{exit}}, \tag{2.6}$$

$$\frac{d\langle\tau_-^1\rangle}{dt} = J_-^{2,1} - J_-^{\text{exit}}, \quad \frac{d\langle\tau_-^L\rangle}{dt} = J_-^{\text{enter}} - J_-^{L,L-1}, \tag{2.7}$$

where

$$\begin{aligned} J_+^{\text{enter}} &= \alpha_+\langle(1-\tau_+^1-\tau_-^1)\rangle, \quad J_+^{\text{exit}} = \beta\langle\tau_+^L\rangle, \\ J_-^{\text{enter}} &= \alpha_-\langle(1-\tau_-^L-\tau_+^L)\rangle, \quad J_-^{\text{exit}} = \beta\langle\tau_-^1\rangle. \end{aligned} \tag{2.8}$$

Analyzing Eq. (2.2) along with Eqs. (2.6) and (2.7) in the present form are intractable due to the involvement of both one-point and two-point correlators. Therefore, a simple approach known as the mean-field approximation (MFT), which has been often used for mathematical treatment in the bidirectional model [34,53,58], is employed. This approximation ignores all kinds of correlations among the particles and the correlator functions are written as a product of individual occupancy numbers, i.e.,

$$\langle\tau_+^i\tau_+^k\rangle = \langle\tau_+^i\rangle\langle\tau_+^k\rangle, \quad \langle\tau_-^i\tau_-^k\rangle = \langle\tau_-^i\rangle\langle\tau_-^k\rangle, \tag{2.9}$$

where $i,\ k \in \{1, 2, \ldots, L-1, L\}$. Further, the mean-field densities at site i for particles of either kind are designated as $\rho_+^i = \langle\tau_+^i\rangle$ and $\rho_-^i = \langle\tau_-^i\rangle$. Likewise, the currents corresponding to both particles are written as

$$J_+^{i-1,i} = \rho_+^{i-1}(1-\rho_+^i), \quad J_-^{i+1,i} = \rho_-^{i+1}(1-\rho_-^i). \tag{2.10}$$

We coarse-grain the discrete lattice by introducing a quasi-continuous variable $x = i/L \in [0, 1]$ using the lattice constant $\epsilon = 1/L$ and re-scaling time as $t' = t/L$, in the thermodynamic limit. On expanding the mean-field densities in Eq. (2.2) in powers of ϵ and retaining the terms up to the second-order, we obtain

$$\frac{\partial\rho_\pm}{\partial t'} = \frac{\partial}{\partial x}\left(\frac{\epsilon}{2}\frac{\partial\rho_\pm}{\partial x} \mp \rho_\pm(1-\rho_\pm)\right). \tag{2.11}$$

Note that, based on the spatial homogeneity, the superscript i is dropped in the continuum limit. At steady-state, the above equation reduces to

$$\frac{\epsilon}{2}\frac{\partial^2\rho_\pm}{\partial x^2} \pm (2\rho_\pm - 1)\frac{\partial\rho_\pm}{\partial x} = 0. \tag{2.12}$$

In the limit $\epsilon \to 0$, this equation yields $(1-2\rho_\pm)\frac{\partial\rho_\pm}{\partial x} = 0$, i.e., $\frac{\partial J_\pm}{\partial x} = 0$, where $J_\pm$ gives

us the bulk current of each species of particle as

$$J_+ = \rho_+(1-\rho_+), \quad J_- = \rho_-(1-\rho_-). \tag{2.13}$$

Meanwhile, the boundary currents are expressed as

$$J_+^{\text{enter}} = \alpha_+(1-\rho_+^1-\rho_-^1), \quad J_+^{\text{exit}} = \beta\rho_+^L, \tag{2.14}$$

$$J_-^{\text{enter}} = \alpha_-(1-\rho_-^L-\rho_+^L), \quad J_-^{\text{exit}} = \beta\rho_-^1. \tag{2.15}$$

As evident from Eqs. (2.13), (2.14), and (2.15), the bulk currents of both species are decoupled and the particles of different kinds effectively interacts only at the boundaries by blocking the entry to particles of other type. Therefore, the system can be viewed as two-independent single-species TASEP models coupled only at the boundaries. So, it is reasonable to define the effective entrance rates α_+^{eff} and α_-^{eff} similar to Refs. [34,53] for the two-species of particles by exploiting the continuity of current in bulk and the boundaries of the lattice as

$$\alpha_+^{eff} = \frac{J_+}{\frac{J_+}{\alpha_+}+\frac{J_-}{\beta}}, \quad \alpha_-^{eff} = \frac{J_-}{\frac{J_-}{\alpha_-}+\frac{J_+}{\beta}}. \tag{2.16}$$

Due to the continuity of current in the bulk, $J_+ = J_+^{\text{enter}} = J_+^{\text{exit}}$ and $J_- = J_-^{\text{enter}} = J_-^{\text{exit}}$. Since the extreme ends of the lattice are coupled to two different finite reservoirs R_+ and R_-, we utilize the particle number conservation condition which gives

$$N_{t_+} = N_{r_+} + N_+, \quad N_{t_-} = N_{r_-} + N_-, \tag{2.17}$$

where N_+ and N_- denote the number of $(+)$ and $(-)$ particles on the lattice, respectively. The above equation can also be rewritten as

$$\mu_+ = r_+ + \int_0^1 \rho_+(x)\,dx, \quad \mu_- = r_- + \int_0^1 \rho_-(x)\,dx. \tag{2.18}$$

Now our objective will be to calculate the effective entrance rates $\alpha_\pm^{eff}$ and the particle densities by utilizing Eqs. (2.13), (2.14), and (2.15) along with Eq. (2.18). These explicitly obtained expressions for the effective rates will help to quantify the stationary properties of the system such as phase diagrams, density profiles, particle currents, and possible phase transitions.

2.3 Existence of phases

To explore the impact of coupling the bidirectional system to separate particle

reservoirs corresponding to each species, we study the dynamic properties of the system in the $\alpha - \beta$ parameter space and inspect all the stationary system properties such as density profiles, particle currents, and phase transitions. In literature, the one-dimensional TASEP model for open boundaries with parameters α and β has been reported to exhibit three stationary phases, namely low density (LD), high density (HD), and maximal current (MC) phase [32]. Incorporating constraints on the available resources induces an additional localized shock phase (SP) as a key feature [64,105]. Furthermore, it has been observed that the bidirectional TASEP model with unlimited resources exhibits symmetry-breaking phenomenon [34,53]. Such a model demonstrates two symmetric (i.e., low density (LD/LD) and maximal current (MC/MC) phase) and two asymmetric (i.e., low-low (L/L) and high-low (H/L) phase) phases. In the current model, if the restriction on the available resources is removed, we retrieve the findings for the model with an infinite number of particles [34,53].

Now, let us investigate the feasible stationary phases that might persist in the homogeneous bidirectional TASEP model with two finite particle reservoirs. To clarify, we denote a phase as A/B where A and B illustrate a phase manifest by the (+) and (−) particles, respectively. For the proposed model, each species can be found solely in one of the following four phases: low density, high density, maximal current, or shock. We classify the various phases as symmetric or asymmetric based on the nature of their observed stationary properties such as density profiles, effective entrance rates, and particle currents. It must be noted that we have used the symbol LD (L) for low density, HD (H) for high density, SP (S) for shock phase and MC (M) for maximal current phase to depict symmetric (asymmetric) phases.

2.3.1 Symmetric phases

Here, we address the occurrence of various symmetric phases and the desire to calculate the explicit effective rates, density profiles, and phase boundaries. For such phases, the two-species of particles have identical dynamics as well as stationary properties including effective entrance rates, densities, and currents. In particular, $\mu_+ = \mu_-$, $\alpha_+^{eff} = \alpha_-^{eff}$, $\rho_+ = \rho_-$, and $J_+ = J_-$. Under these circumstances, the effective entrance rates are reduced to

$$\alpha_+^{eff} = \frac{\alpha\beta r_+}{\beta\mu_+ + \alpha r_+}, \quad \alpha_-^{eff} = \frac{\alpha\beta r_-}{\beta\mu_- + \alpha r_-}, \tag{2.19}$$

and in addition, from Eq. (2.18), we acquire $r_+ = r_-$. For the sake of simplification, we designate the common effective entrance rate, filling factor, and reservoir quotient by α^{eff}, μ, and r, respectively. Our aim is to calculate the effective entrance rates by utilizing the particle conservation criteria to theoretically obtain the expressions for the

phase boundaries, shock position, and particle densities.

The system can be thought of as two independent single-species TASEP models coupled only at the boundaries, so each species can be found in one of four phases, namely LD, HD, MC, or SP. Keeping in mind the nature of the symmetric phases, only four phases are possible, namely LD/LD, HD/HD, MC/MC, and SP/SP. However, out of these, only two are feasible, specifically LD/LD and MC/MC. The other possibilities such as SP/SP and HD/HD can be discarded based on analytical arguments. Precisely, the HD/HD phase cannot exist as the total particle density cannot be greater than 1. In the case of the SP/SP phase, the constraint $\alpha^{eff} = \beta$ must be satisfied. However, this condition has no feasible solutions for any value of μ. A summary of the explicit expressions for the existential conditions, effective entrance rates, and the reservoir quotient is given in Table (2.1). The stationary properties such as particle density, bulk current, reservoir quotient, etc., in each symmetric phase, are detailed in Appendix (2.7).

2.3.2 Asymmetric phases

The symmetry of the system is affected by the localized interactions between the distinct particle species at the boundaries, leading to the SSB phenomenon when $\mu_+ = \mu_-$. In the case $\mu_+ \neq \mu_-$, only asymmetric phases exist where the stationary properties of the two-species of particles are generally different. Specifically, the densities of the $(+)$ and $(-)$ particles in the system are unequal i.e., $\rho_+ \neq \rho_-$, which leads to

$$\alpha_+^{eff} \neq \alpha_-^{eff}. \tag{2.20}$$

Each species can illustrate any of the four phases: low density, high density, shock, or maximal current phase leading to the total number of possible asymmetric phases displayed by the system being equal to $4^2 = 16$. Keeping in view that the total particle density is bounded above by 1, phases such as M/H, H/M, S/M, M/S, H/S, S/H, and H/H are discarded. In the case of S/S phase, effective entry rate must equate to the exit rate for each species, leading to $\alpha_+^{eff} = \beta$ and $\alpha_-^{eff} = \beta$. Consequently, this condition yields $\alpha_+^{eff} = \alpha_-^{eff}$, thereby contradicting the prerequisites for an asymmetric phase. As a result, the S/S phase is disregarded.

Now, to calculate the effective entrance rates for the remaining eight feasible phases, we need to determine the reservoir quotients by utilizing the particle number conservation for each species. These expressions will be further employed to obtain the phase boundaries, the position of shock, and the particle densities. Table (2.1) summarizes the existence criteria, effective entrance rates, the position of shock, and the reservoir quotients for each possible asymmetric phase. The theoretical computation

Phase	Phase region/ Shock position	$\alpha_{\pm}^{eff}$	$r_{\pm}$
LD/LD	$\alpha^{eff} < \min\{0.5, \beta\}$	$\mu - r$	$\frac{\alpha(\mu-\beta)-\beta\mu+\sqrt{4\alpha\beta\mu^2+(\alpha(\mu-\beta)-\beta\mu)^2}}{2\alpha}$
MC/MC	$0.5 < \min\{\alpha^{eff}, \beta\}$	$\frac{\alpha\beta(2\mu-1)}{2\mu(\alpha+\beta)-1}$	$\mu - 0.5$
H/L	$\beta < \min\{\alpha_{+}^{eff}, 0.5\}$,	$\alpha_{+}^{eff} = \frac{\alpha(\beta-1)\beta^2 r_+}{\alpha r_+(\alpha_-^{eff}-1)\alpha_-^{eff}+\beta^2\mu_+(\beta-1)}$	$r_+ = \mu_+ - (1-\beta)$
	$\alpha_{-}^{eff} < \min\{\beta, 0.5\}$	$\alpha_{-}^{eff} = \frac{\alpha r_- + \mu_- - \sqrt{(\alpha r_- + \mu_-)^2 - 4\alpha\beta\mu_- r_-}}{2\mu_-}$	$r_- = \frac{1}{2(\alpha+\mu_-)}\Big(\alpha(\mu_- - \beta) + \mu_-(2\mu_- - 1) + \sqrt{(\alpha(\mu_- - \beta) + \mu_-(2\mu_- - 1)^2 + 4(1-\mu_-)\mu_-^2(\alpha+\mu_-)}\Big)$
M/L	$0.5 < \min\{\alpha_{+}^{eff}, \beta\}$	$\alpha_{+}^{eff} = \frac{\beta\alpha r_+}{\beta\mu_+ + 4\alpha r_+ J_-}$	$r_+ = \mu_+ - 0.5$
	$\alpha_{-}^{eff} < \min\{\beta, 0.5\}$	$\alpha_{-}^{eff} = \frac{\beta(\mu_- + \alpha r_-)}{2\beta\mu_-}$	$r_- = \frac{1}{8\beta(\alpha+\mu_-)}\Big(\alpha(4\beta(\mu_- - 1)+1) + 4\beta\mu_-(2\mu_- - 1)$
		$-\frac{\sqrt{\beta(\alpha\mu_- r_- + \beta(\mu_- - \alpha r_-)^2)}}{2\beta\mu_-}$	$+\sqrt{(\alpha(1+4\beta(\mu_- - 1)) + 4\mu_-\beta(2\mu_- - 1))^2 - 64\beta^2(\mu_- - 1)\mu_-^2(\mu_- + \alpha))}\Big)$
S/L	$0 \le x_w \le 1$	$\alpha_{+}^{eff} = \frac{\beta\mu_+ + \alpha\beta r_+}{2\beta\mu_+}$	$r_+ = \frac{(\beta-1)\beta^2\mu_+}{\alpha\left(\alpha_-^{eff}(1-\alpha_-^{eff})+\beta(\beta-1)\right)}$
	$\alpha_{-}^{eff} < \min\{\beta, 0.5\}$	$-\frac{\sqrt{\beta\left(\beta(\mu_+ - \alpha r_+)^2 - 4(\alpha_-^{eff}-1)\alpha_-^{eff}\alpha\mu_+ r_+\right)}}{2\beta\mu_+}$	$r_- = \frac{1}{2(\alpha+\mu_-)}\Big(\alpha(\mu_- - \beta) + \mu_-(2\mu_- - 1)$
	$x_w = \frac{\beta+\mu_+ - r_+ - 1}{\alpha_+^{eff}+\beta-1}$	$\alpha_{-}^{eff} = \frac{\mu_- + \alpha r_- - \sqrt{(\mu_- + \alpha r_-)^2 - 4\alpha\beta\mu_- r_-}}{2\mu_-}$	$+\sqrt{\alpha^2(\beta-\mu_-)^2 + \mu_-^2 + 2\alpha\mu_-\Big(\beta + \mu_-(1-2\beta)\Big)}\Big)$
M/M	$0.5 < \min\{\alpha_{+}^{eff}, \beta\}$	$\alpha_{+}^{eff} = \frac{\alpha r_+}{\beta\mu_+ + \alpha r_+}$	$r_+ = \mu_+ - 0.5$
	$0.5 < \min\{\alpha_{-}^{eff}, \beta\}$	$\alpha_{-}^{eff} = \frac{\alpha r_-}{\beta\mu_- + \alpha r_-}$	$r_- = \mu_- - 0.5$

Table 2.1: Summary of the existential conditions, effective entrance rates, shock position, and the reservoir quotients for the possible symmetric as well as asymmetric phases for the proposed model. LD/LD and MC/MC represent symmetric phases while H/L, M/L, S/L, and M/M correspond to asymmetric phases. The notations $\alpha_{\pm}^{eff}$ and $r_{\pm}$, respectively denote the effective entrance rates and the reservoir quotients for the two-particle species, whereas x_w gives the position of shock in the S/L phase.

for the expressions of each phase in this category is explained in Appendix (2.8). We have obtained the explicit theoretical expressions for the stationary particle densities, phase boundaries, and reservoir quotients for feasible phases by employing a mean-field approach. Additionally, the steady-state particle densities can also be procured from Eq. (2.11) along with the boundary conditions given by Eqs. (2.14) and (2.15) numerically by utilizing a finite difference scheme outlined in Appendix (2.9). Although the approach is simple to use, the theoretical phase boundaries cannot be obtained through this method, making it difficult to conduct a thorough analysis of how different parameters, such as the filling factors, affect the stationary features of the system.

2.4 Results and discussion

In this section, we inquire about the effect of coupling the system with two finite reservoirs on the steady-state properties and obtain the phase diagrams for specific values of μ_+ and μ_- in the parameter space $\alpha - \beta$. We perceive both qualitative and quantitative changes in the topology of the phase diagram specifically in terms of symmetry-breaking for $\mu_+ = \mu_-$ and the emergence of other phases. The theoretical outcomes obtained in the previous section involve several approximations; therefore, to validate these results, we perform elementary Monte Carlo simulations (MCs) following the random-sequential update rule for $2 \times 10^7 L$ time steps. At each simulation step, a site is chosen randomly, upon which the dynamic rules described in Section (2.2) are implemented. The initial 5% of the time steps are scraped ensuring the system reaches a steady-state. We segregate our further analysis into two distinct categories: (i) when the filling factors are symmetric, $\mu_+ = \mu_-$ and (ii) when the filling factors are asymmetric, $\mu_+ \neq \mu_-$.

2.4.1 Symmetric filling factor ($\mu_+ = \mu_-$)

Motivated by the findings of a bidirectional TASEP model with a single infinite reservoir where symmetry-breaking phenomena have been observed, we wish to study a constrained system where the number of particles of both species is equal. To simplify, we prefer to refer to the common filling factors by μ. Initially, for a very small value of μ, the phase diagram is comprised of one symmetric phase namely LD/LD as presented in Fig. (2.2a) for $\mu = 0.3$. Despite the symmetry in the dynamic rates of both (+) and (−) particles, the system reveals two asymmetric phases: S/L and L/L. The stationary characteristics of the two-species vary in such phases. It is noteworthy to specify that a symmetry-breaking phenomenon is observed in the system even when the total number of particles of each species is much less. Moreover, the L/L phase remains confined to a curve forming a boundary separating the LD/LD and the S/L phase regions. No

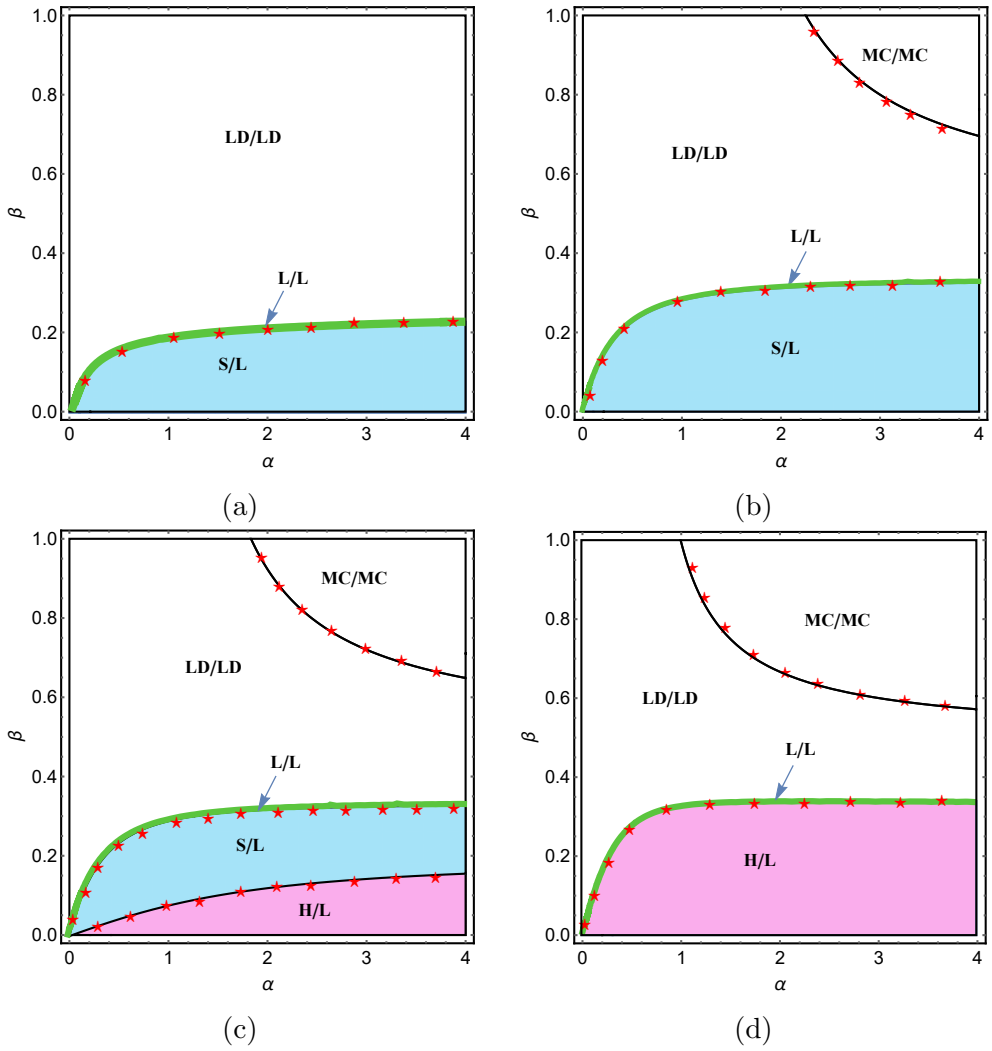

Figure 2.2: Stationary phase diagrams for (a) $\mu = 0.3$, (b) $\mu = 0.9$, (c) $\mu = 1.1$, and (d) $\mu = 100$. Symmetric phases are represented by white regions, while the coloured regions denote asymmetric phases. Red symbols correspond to Monte Carlo simulation results. The L/L phase remains confined to a curve and acts as a boundary separating H/L (or S/L) and LD/LD phases, displaying a first-order phase transition taking average current as the order parameter. The size of the system is taken to be 1500.

substantial changes are observed in the phase schema until $\mu = 0.5$, except for the expansion of the S/L and shrinkage in the LD/LD region. With the enhancement in μ from 0.5, another symmetric phase namely MC/MC appears in the phase diagram in addition to the previously existing phases, which is evident from Fig. (2.2b) for $\mu = 0.9$. This appearance of a symmetric maximal current phase after $\mu = 0.5$ is affirmed by Eqs. (2.31) and (2.32). At this stage, adequate particles are available to fill the lattice entirely and retain the MC/MC phase.

With the further advent in μ, no other symmetrical phase is observed. As soon as $\mu > 1$, an asymmetric phase precisely H/L enters the phase schema next to the S/L phase, resulting in the shrinkage of the later mentioned phase region (as prescribed in

Fig. (2.2c)). It can also be guaranteed from Eq. (2.36) that a necessary condition for the existence of H/L is $\mu > 1$. Further increasing the value of μ results in the expansion of the H/L phase region and, as $\mu \to \infty$, the S/L phase disappears altering the topology of the phase diagram both qualitatively and quantitatively. Note that, in the extreme case of $\mu \to \infty$, the rates α_+ and α_- approach the innate entrance rates, and the global limitation on the number of particles is bygone. As expected, the system behaves as a bidirectional two-species model with infinite resources where two symmetric phases, LD/LD, MC/MC, and two asymmetric phases, L/L and S/L persist [34,53]. Clearly, the number of observed phases in the stationary phase diagrams changes from $3 \to 4 \to 5 \to 4$ as μ increases, displaying a non-monotonic trend.

2.4.1.1 Spontaneous symmetry-breaking phenomenon (SSB)

One of the most remarkable features of a bidirectional system is the spontaneous symmetry-breaking phenomenon. To investigate this occurrence in detail through Monte Carlo simulations, we generate particle density histograms by continuously monitoring the instantaneous particle densities ρ_+ and ρ_- of the positive and the negative species. In simulations, considering a system size of $L = 1000$, initial 10^9 time steps are discarded and then we gather data for 9×10^9 time steps. If the peak in the density histogram distribution satisfies $\rho_+ = \rho_-$, the corresponding phase is labeled as symmetric otherwise, it is labeled as an asymmetric phase. Figure (2.3) shows the typical density histogram plots for L/L and H/L phases in the case of the symmetric filling factor with $(\alpha, \beta, \mu) = (1, 0.1, 0.3)$ and $(2, 0.1, 1.5)$, respectively. In the case of the L/L phase, Fig. (2.3a) demonstrates that a peak occurs for $\rho_+ < \rho_- < 0.5$, which means that the symmetry-breaking is observed. For the H/L phase, as anticipated, a peak with $\rho_+ > 0.5$ and $\rho_- < 0.5$ is obtained as shown in Fig. (2.3b).

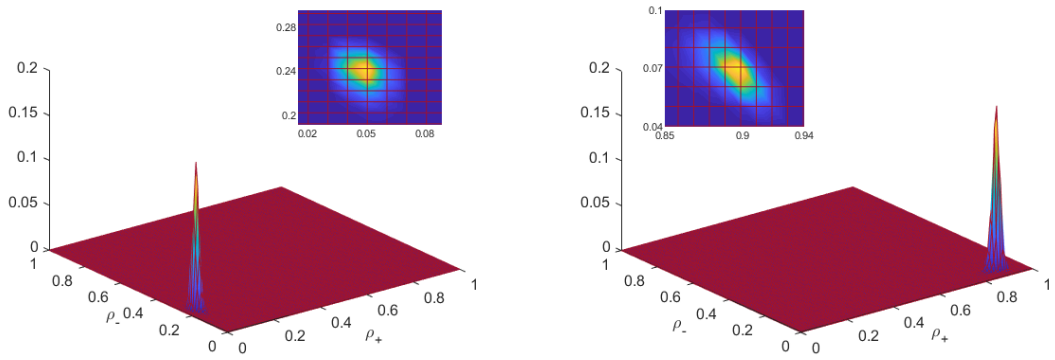

(a) (b)

Figure 2.3: Particle density histogram for (a) L/L and (b) H/L phases with the parameters $(\alpha, \beta, \mu) = (1, 0.1, 0.3)$ and $(2, 0.1, 1.5)$, respectively. Insets show the two-dimensional contour plot.

The SSB phenomenon can also be analyzed by inspecting the nature of the currents corresponding to the two-species of particles as well as the possible phase transitions for a chosen set of parameters. The currents J_+ and J_- when plotted with respect to β for $\alpha = 3$ with filling factor $\mu = 1.1$, as shown in Fig. (2.4a), display a sudden change at the value $\beta \approx 0.326$ after which they remain equal. To investigate this observation in detail, we further plot the value of the currents $(J_+ + J_-)/2$ and $|J_+ - J_-|$ for $\alpha = 3$ and $\mu = 1.1$. The average particle current in the system along the line $\alpha = 3$ also displays similar behaviour near the critical point $\beta \approx 0.326$ (see Fig. (2.4b)). This abrupt change is a consequence of the transition from symmetric to asymmetric phases. Moreover, the behaviour of $|J_+ - J_-|$ also changes at the point $\beta \approx 0.326$, after which it remains constant and takes the value zero, confirming the emergence of the symmetric phase. Note that the phase diagram for $\mu = 1.1$ given by Fig. (2.2c) illustrates a phase transition from asymmetric to symmetric phases as S/L $\rightarrow$ H/L $\rightarrow$ L/L $\rightarrow$ LD/LD $\rightarrow$ MC/MC as β varies. Further, when the particle currents for each species are individually analyzed, it can be noted that the current associated with the $(+)$ particles is greater than or equal to the current associated with the $(-)$ particles (see Fig. (2.4b)). Mathematically, the existential conditions given by Eqs. (2.36) and (2.41) of H/L and S/L phases, respectively, require the effective entrance rate of the negative species to remain lower than the exit rate implying that the current $J_- = \alpha_-^{eff}(1-\alpha_-^{eff})$ is less than the current $J_+ = \beta(1-\beta)$. Thus one can conclude that the transition from asymmetric phases to symmetric phases with respect to current is of the first-order.

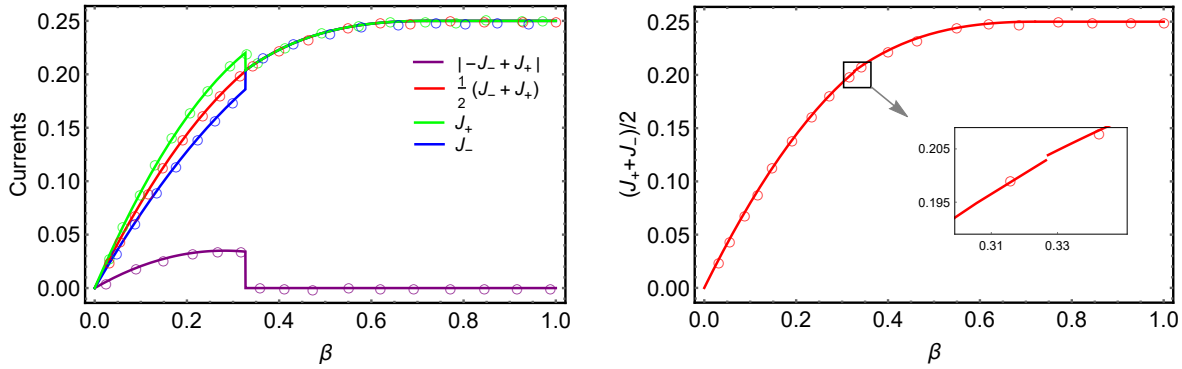

(a) (b)

Figure 2.4: Plot of currents: (a) $(J_+ + J_-)/2$, $|J_+ - J_-|$, J_+, and J_-, and (b)$(J_+ + J_-)/2$ vs β for $\alpha = 3$ and $\mu = 1.1$. Inset in (b) displays a discontinuity in $(J_+ + J_-)/2$ near $\beta \approx 0.326$. Solid lines represent theoretical results and symbols refer to Monte Carlo simulations.

2.4.1.2 Shock dynamics

We now discuss the features of the localized shock that appears in the density profile of the asymmetric S/L phase. In the thermodynamic limit, Eq. (2.11) reduces

to the continuity equation given by $\partial\rho_{\pm}/\partial t' \pm \partial J_{\pm}/\partial x = 0$ and the speed of shock for $(+)$ species is expressed as $s = \beta - \alpha_{+}^{eff}$. For the existence of shock, its speed in the corresponding lattice must be equal to zero. Using this condition, as well as the particle number conservation, the steady-state properties of the S/L phase have been thoroughly investigated and details are provided in Appendix (2.8).

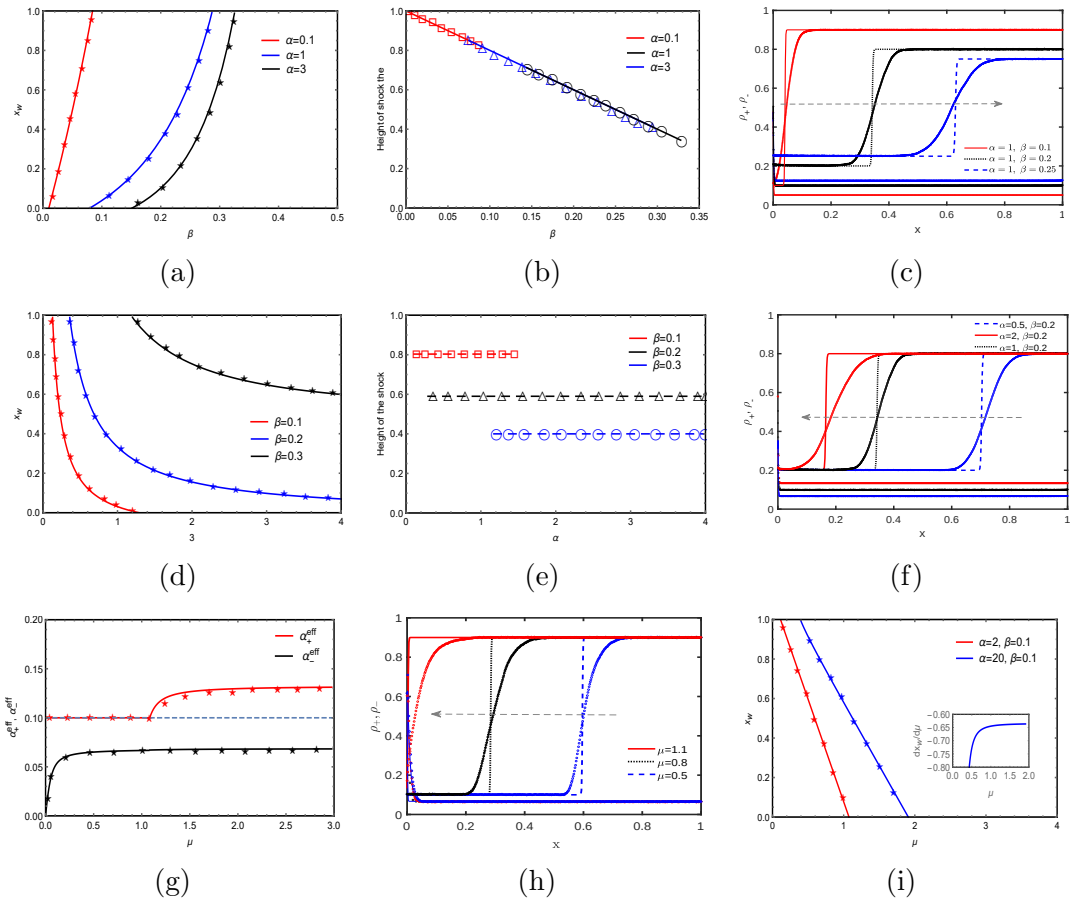

Figure 2.5: (a), (b) Position and height of the shock with respect to β for $\mu = 1.1$ and $\alpha = 0.1,\ 1,\ 3$. (c) Density profiles for fixed $\alpha = 1$ and $\beta = 0.1,\ 0.2,\ 0.25$ with $\mu = 1.1$. (d), (e) Position and height of the shock with respect to α for $\mu = 1.1$ and $\beta = 0.1,\ 0.2,\ 0.3$. (f) Density profiles for fixed $\beta = 0.2$ and $\alpha = 0.5,\ 1,\ 2$ with $\mu = 1.1$. (g) Effective entrance rates with respect to μ for $\alpha = 2$ and $\beta = 0.1$. (h) Density profiles for $\alpha = 2$ and $\beta = 0.1$ for $\mu = 0.5,\ 0.8,\ 1.1$. (i) Position of the shock with respect to μ for $\alpha = 2,\ 20$ and $\beta = 0.1$. Inset shows the change in position of the shock with respect to μ for $\alpha = 20$ and $\beta = 0.1$. In all figures, solid lines represent theoretical results and symbols correspond to Monte Carlo simulations. The size of the lattice is taken to be 3000.

Now, we focus on the propagation of shock with respect to the exit rate as well as the entry rate using the analytical expression of shock position given by Eq. (2.40), which is detailed in Appendix (2.8). From Figs. (2.5a) and (2.5c), one can observe that upon the variation of exit rate, the shock position changes continuously from 0 to 1. It means that, with an increase in β after a certain critical value, marking the phase

boundary S/L and H/L, the shock enters the lattice from the left end. Further increase in β shifts the shock towards the right until it attains the value corresponding to the phase boundary between S/L and L/L, beyond which the shock leaves the lattice. In this case, the non-zero shock height, which depends solely on β, decreases linearly (see Fig. (2.5b)). Similarly, upon varying the entry rate, the position of shock displays a shift from the right end towards the left end (see Figs. (2.5d) and (2.5f)). The height of this shock remains constant throughout the variation of entry rate due to dependence on β that remains fixed (see Fig. (2.5e)). Thus, if one considers the position and height of shock as order parameters, then the transitions are of second and first-order, respectively.

The localized shock appears as a consequence of finite resources; therefore, it is imperative to understand how the filling factor impacts the propagation of shock. In this regard, we choose a point from $\alpha - \beta$ space and analyze the impact of varying μ on the properties of shock. Due to the dependence of shock height only on β, one can readily conclude that it remains constant with respect to μ. This subsequently means that α_+^{eff} remains constant throughout the S/L phase. However, α_-^{eff} is found to increase. To support these analytical arguments, we have plotted the effective rates in Figs. (2.5g) and (2.5h). Moreover, from Fig. (2.5h) one can observe that the shock shifts towards the right end with respect to μ for constant (α, β) until it reaches the left end and finally leaves the lattices. This signifies the transition from the S/L to the H/L phase that appears as a consequence of the effective entry rate exceeding the exit rate for (+) species (see Fig. (2.5g)). To validate it mathematically, the effective rates for both the species have been calculated in the limit $\mu \to \infty$ and are given as

$$\alpha_+^{eff} \to \frac{2\alpha\beta^2(\beta-1)}{\alpha^3 + 2(\beta-1)\beta^2 - \alpha^2\big(2\beta - 1 + \sqrt{(1+\alpha)^2 - 4\beta\alpha}\big)}, \tag{2.21}$$

and

$$\alpha_-^{eff} \to \frac{1+\alpha-\sqrt{(1+\alpha)^2-4\alpha\beta}}{2}, \tag{2.22}$$

which satisfies the existential conditions for the H/L phase. Furthermore, the shift in position is predominantly linear for higher values of μ, which can be viewed from Fig. (2.5i) where the derivative approaches a linear profile with an increase in μ.

2.4.1.3 Finite-size effect on asymmetric phases

It has been observed in past studies that TASEP with symmetry-breaking phenomenon results in rigorous size-scaling dependencies [34,52]. So, to further analyze this effect of the finite lattice length L on the shock-low density phase in the proposed model, we have plotted the density profiles for a point $(\alpha, \beta) = (1, 0.2)$ chosen in the S/L region with $\mu = 1.1$ for different values of L [see Fig. (2.6a)]. As anticipated, the shock

profile is primarily sharpened by an increase in the value of L, while the underlying S/L phase remains intact. The other asymmetric phase, L/L, arises in the system even for a

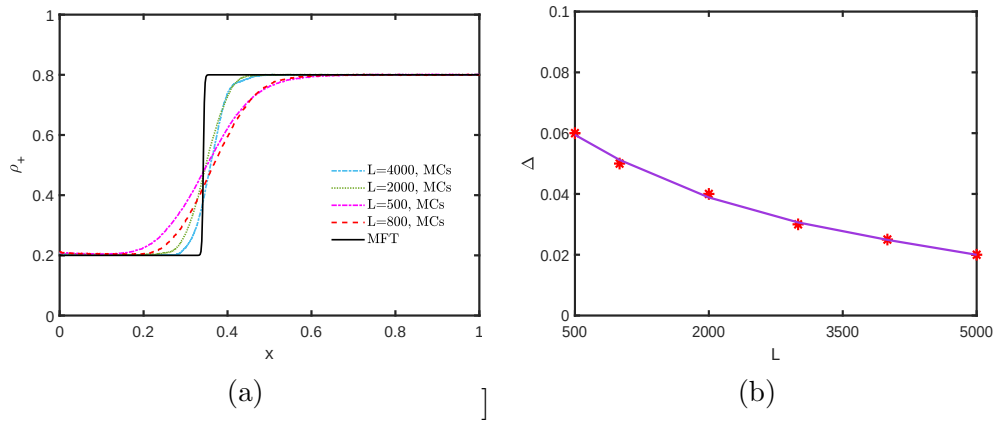

(a) (b)

Figure 2.6: (a) Effect of finite lattice length L on the S/L profile for fixed $(\alpha, \beta, \mu) = (1, 0.2, 1.1)$ and varied values of L. (b) Region width (Δ) of low-low density (L/L) phase with respect to β for fixed $\alpha = 0.5$ and $\mu = 0.5$. The solid curve is a guide to the eye with best-fit polynomial for the discrete simulation data (shown by red markers) until $L \approx 5000$.

relatively small number of particles of each species and persists for its higher value, as illustrated in Fig. (2.2). According to the mean-field approximation, this phase exists on a curve while simulations reveal that it appears for a considerable domain, as also reported earlier [55,100]. To study this effect of the system size on the L/L phase, we plot the region width (Δ) with respect to β for fixed $\alpha = 0.5$ and $\mu = 0.5$ in Fig. (2.6b). As observed from the figure, the region width Δ decreases with an increase in L and almost shrinks to a restricted range at $L \approx 5000$. We have plotted $\Delta(L)$ with best-fit polynomial as a guide to the eye for the discrete simulation data, in Fig. (2.6b). As expected, based on simulations, the L/L phase region exists for a significant range of β for smaller values of L, while for larger system size, it shrinks to a narrow region, thereby substantiating the theoretical observations in the thermodynamic limit.

2.4.2 Asymmetric filling factors ($\mu_+ \neq \mu_-$)

Now let us inquire into the bidirectional system when the filling factors corresponding to the two-species of particles are distinct. Even if both the particle species demonstrate the same phase, all their stationary properties cannot be equal, specifically, the particle density, and therefore there is no point in talking about the SSB phenomenon in this case. The difference in the filling factor forces the system to manifest only asymmetric phases. Without loss of generality, we choose to discuss the crucial properties such as the density profiles, phase diagrams, and phase transitions for the case when $\mu_+ > \mu_-$. The reverse scenario where $\mu_+ < \mu_-$ can be investigated

from the results attained for $\mu_+ > \mu_-$ by utilizing the transformations discussed at the end of this section.

To explore the impact of coupling the system with two different reservoirs on the stationary properties, we analyze our system in two distinct cases: (i) taking fixed small, intermediate, or large values of μ_-; simultaneously varying μ_+ and (ii) fixing μ_+ and changing values of μ_-.

2.4.2.1 Stationary properties: Impact of μ_+

Here, we aim to focus on the structural variations that occur in the phase diagram when μ_- is kept fixed and the filling factor corresponding to positive particles μ_+ changes. For the case when both the filling factors were equal, our discussion in Section (2.4.1) reveals that important topological changes were encountered in the phase diagram at critical points, $\mu = 0.5$ and 1. Therefore, we consider three different circumstances: $\mu_- \leq 0.5$, $0.5 < \mu_- \leq 1$, and $1 < \mu_-$. When the filling factor μ_-

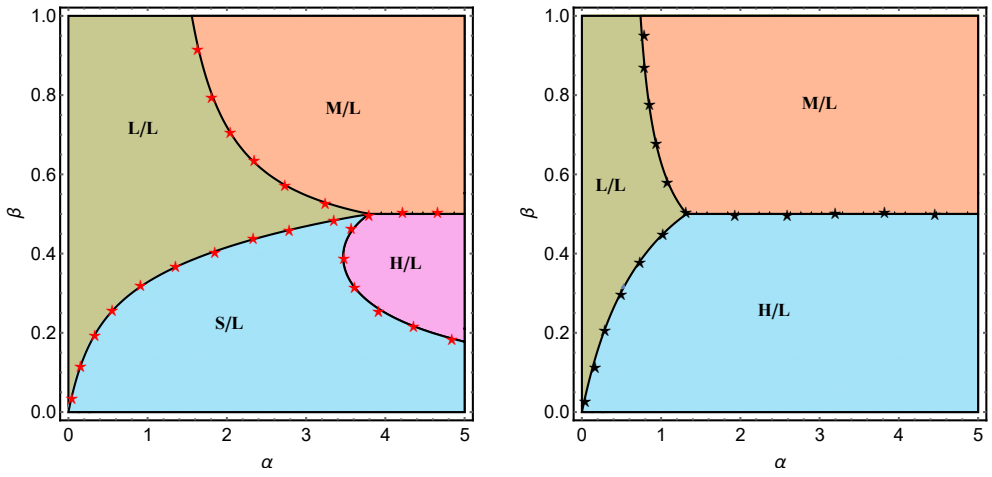

Figure 2.7: Stationary phase diagrams for: (a) $\mu_+ = 1$ and (b) $\mu_+ = 20$ with $\mu_- = 0.3$. Solid lines represent theoretical results and symbols correspond to Monte Carlo simulations. The length of the lattice is 1500.

is kept less than $\min\{0.5, \mu_+\}$, varying the other filling factor strongly influences the stationary phase diagram as presented in Figs. (2.2a) and (2.7) for $\mu_- = 0.3$. Initially when $\mu_+ = \mu_-$, three phases were observed comprising one symmetric (LD/LD) and two asymmetric phases (L/L and S/L). As soon as $\mu_+ \neq \mu_-$, the LD/LD phase disappears because the system no longer satisfies symmetric conditions for the rates. This phase is substituted by the asymmetric L/L phase where the particle densities of the two-species are dissimilar. The vanishing of the symmetric phases also indicates the termination of the SSB phenomena. As μ_+ increases beyond 0.5, two other phases, M/L and H/L, emerge in the phase schema; see Fig. (2.7a). On further increment in μ_+, the regions for

M/L and H/L grow in size. This expansion is attributed to the fact that with increasing μ_+, the particle flux of the positive species becomes larger while the flux of the negative species remains unaltered. As $\mu_+ \to \infty$, the S/L phase is no longer realized, along with H/L and M/L covering the majority of the phase diagram (see Fig. (2.7b)). Note that the number of phases with respect to μ_+ changes from three to four and then reduces to three, which depicts a non-monotonic trend.

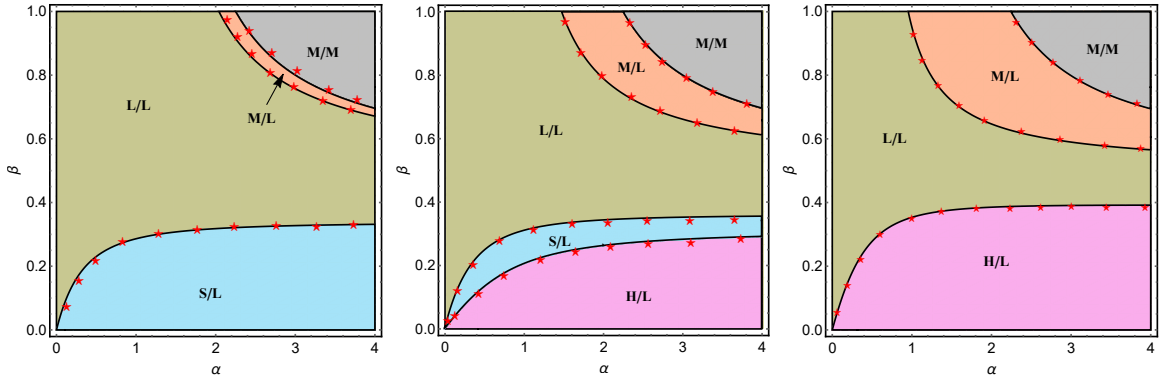

(a) (b) (c)

Figure 2.8: Stationary phase diagrams for: (a) $\mu_+ = 0.98$, (b) $\mu_+ = 1.5$ and (c) $\mu_+ = 15$ with $\mu_- = 0.9$. Solid lines represent theoretical results and symbols correspond to Monte Carlo simulations. The length of the lattice is set to 1500.

We now concentrate on the stationary properties of the system when μ_- satisfies $0.5 < \mu_- \leq \mu_+$. The outcomes of the theoretical analysis and Monte Carlo simulations are presented in Fig. (2.8) for $\mu_- = 0.9$ and different values of μ_+. There are four phases in the system for $\mu_+ = \mu_- = 0.9$ (see Fig. (2.2c)) among which LD/LD and MC/MC are the phases which are the most sensitive to the change in the value of μ_+. These phases are replaced with L/L and M/M phases for $\mu_+ \neq \mu_-$ along with the introduction of the maximal-low (M/L) region into the phase representation. The persistence of asymmetric maximal-low phase requires either one of μ_+ or μ_- must be greater than 0.5. The corresponding topological structure of the phase diagram is illustrated in Fig. (2.8a). It is important to note that though the bulk characteristics of the two-particle species are the same in both MC/MC and M/M phases, the particle densities are not equal at the boundaries. Specifically, the effective entrance rates are different in cases of M/M (as confirmed from Eq. (2.20)) implying that $\rho_+(0) \neq \rho_-(1)$. Now, as μ_+ increases, the H/L phase enters the phase diagram next to the S/L phase when $\mu_+ > 1$ (see Fig. (2.8b)). This critical point after which H/L appears in the phase schema is obtained from the condition that the existence of this phase requires $\alpha_+^{eff} > \beta$. It is compelling to mention that Fig. (2.8b) corresponds to a circumstance where the system experiences the maximum number of phases at steady-state. With further increasing μ_+, the M/L and H/L region expands followed by the shrinkage in L/L and S/L regions. Eventually, when $\mu_+ \to \infty$, the S/L phase disappears from the

phase structure as shown in Fig. (2.8b), with the system still displaying the other four stationary phases. In this case, initially, the number of phases displayed is 5, which reduces to 4, then further rises to 5, and finally decreases to 4.

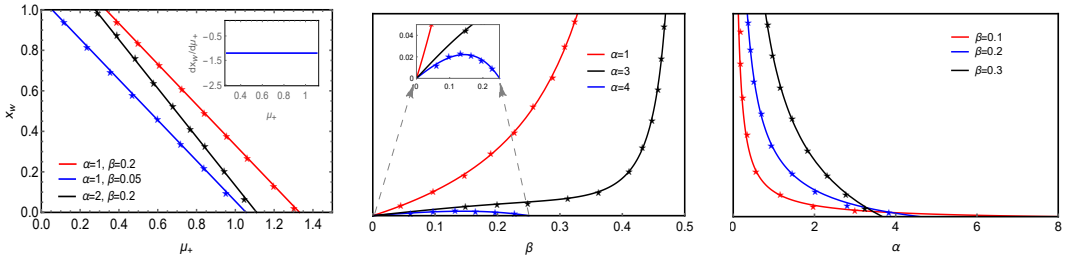

(a) (b) (c)

Figure 2.9: Position of the shock vs (a) μ_+ with $\mu_- = 0.3$, (b) β with $\mu_+ = 1$, $\mu_- = 0.3$, and (c) α with $\mu_+ = 1$, $\mu_- = 0.3$. The rest of the parameter values are mentioned in the respective figures. Inset in (a) shows the change in x_w with respect to μ_+ which is almost linear. Inset in (b) is a zoomed figure for smaller values of β. In all figures, solid lines represent theoretical results and symbols correspond to Monte Carlo simulations. The length of the lattice is set to 1500.

Upon comparison of the phase diagram in the present case with that of the symmetric filling factor, the nature of the S/L phase is expected to have distinct behaviour. One can readily observe that the shock may move towards either of the boundaries with respect to β depending upon the fixed α (see Fig. (2.9b)). However, with respect to α, the shock moves towards the left for any constant value of β (see Fig. (2.9c)). The shock height has a behaviour similar to the symmetric conditions and remains constant with the variation of α while other parameters are unchanged, whereas it decreases monotonically with respect to β, provided the remaining parameters are unaltered.

Finally, we intend to analyze how the filling factor μ_+ impacts the dynamics of the S/L phase for a fixed value of μ_-. Towards this direction, we have plotted Fig. (2.9a) which depicts the variation of shock position and its change (inset) with respect to μ_+. Clearly, the shock enters from the right end and leaves the lattice from the left end with respect to μ_+ for $\mu_- = 0.3$. One can readily conclude that the variation is almost linear revealing that the shock position is nearly proportional to the filling factor of the concerning species.

2.4.2.2 Stationary properties: Impact of μ_-

Now, let us focus on the properties of the system for fixed μ_+ and varying values of μ_- such that $\mu_+ > \mu_-$. When $\mu_+ < 0.5$, two phases are realized in the phase diagram namely L/L and S/L phases with the majority of the region covered by the L/L phase. One can see from Fig. (2.10a) that, for $\mu_- < 0.5 < \mu_+ = 0.55$, four asymmetric phases

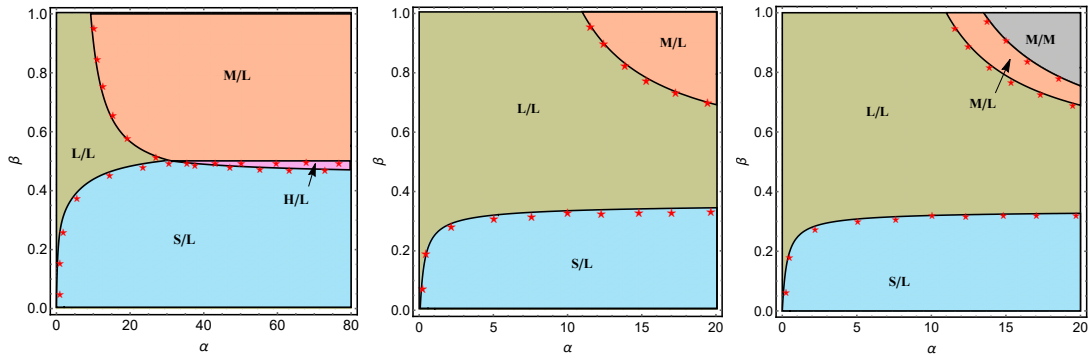

(a) (b) (c)

Figure 2.10: Stationary phase diagrams for: (a) $\mu_- = 0.3$, (b) $\mu_- = 0.5$, and (c) $\mu_- = 0.54$ with $\mu_+ = 0.55$. Solid lines represent theoretical results and symbols correspond to Monte Carlo simulations. The length of the lattice is taken to be 1500.

are displayed by the system (L/L, M/L, S/L, and H/L). As μ_- takes the value 0.5, the H/L phase disappears from the phase diagram along with the shrinkage of S/L and M/L regions as shown in Fig. (2.10b). This is because, with an increase in μ_-, enough negative particles are available in the system to hinder the movement of the positive particles. Mathematically, it is also affirmed by Eq. (2.36) that the H/L phase does not persist for $\mu_- = 0.5$. As soon as $\mu_- > 0.5$, the maximal-maximal (M/M) phase emerges in the phase diagram changing its topology qualitatively (see Fig. (2.10c)). It is noteworthy to mention here that when $\mu_+ > \mu_-$, the density of the positive particles always remains greater than that of the negative particles.

One of the major consequences of coupling the system with two-particle reservoirs having distinct filling factors is the appearance of the M/L phase in the phase diagram which has not been observed in previous studies [34,53]. For fixed α, β, and μ_+ chosen such that these parameters lie in the M/L region, we study the changes in the bulk densities for the two-particle species. In this phase, the positive particles manifest maximal current phase with a bulk density equal to 0.5 while the negative species depict an entrance-dominated phase with the bulk density given by Eq. (2.42). It can be noted that the value α_-^{eff} is entirely expressed in terms of α, β, and μ_-. As we plot the effective entrance rate α_-^{eff} against μ_- for $\alpha = 15$, $\beta = 0.8$, $\mu_+ = 0.55$, it can be observed that α_-^{eff} increases with increase in μ_- (see Fig. (2.11a)). Eventually, at the critical point $\mu_- = 0.55$, α_-^{eff} takes the value 0.5 indicating the termination of low density phase corresponding to the $(-)$ particles. Now, to focus on the variation in particle density corresponding to negative species with respect to change in both α and β, we plotted ρ_- vs α for different values of β in Fig. (2.11c). For fixed β, an increase in α enhances the inflow of negative species leading to an increase in the bulk density ρ_-. Similarly, upon varying the exit rate, the density corresponding to negative species increases with an increment in β (see Fig. (2.11b)).

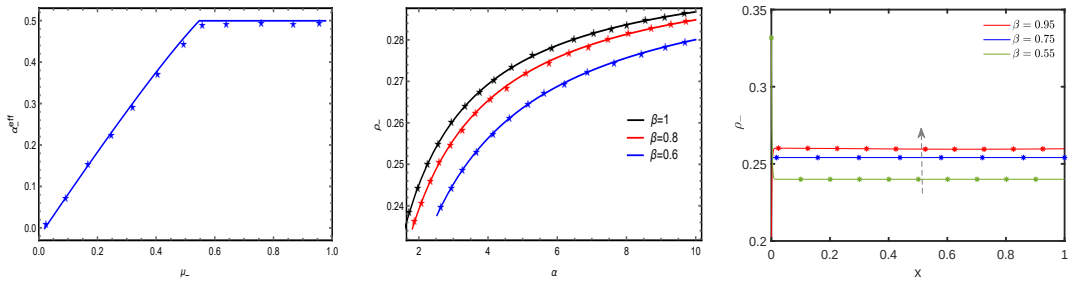

(a) (b) (c)

Figure 2.11: (a) Effective entrance rate α_-^{eff} with respect to μ_- for $\mu_+ = 0.55$, $\alpha = 15$, $\beta = 0.8$. (b) Particle density ρ_- with respect to α for distinct values of β. (c) Density profiles of the negative species for different values of β, $\alpha = 3$, $\mu_+ = 1$, $\mu_- = 0.3$. The rest of the parameter values are mentioned in the respective figures. In all figures, solid lines represent theoretical results and symbols correspond to Monte Carlo simulations. The length of the lattice is taken to be 1500.

Furthermore, it is necessary to point out the essential feature of the asymmetric M/M phase. Even though the bulk densities for both species in the M/M phase take the value 0.5, this phase is not identical to MC/MC, as in the former case the boundary densities corresponding to (+) and (−) particles are different. It is also evident from Eq. (2.45) that for $\mu_+ \neq \mu_-$,

$$\alpha_+^{eff} - \alpha_-^{eff} = \frac{\alpha\beta(\mu_+ - \mu_-)}{\prod_{j\in\{+,-\}}\Big(2\beta\mu_j + \alpha(2\mu_j - 1)\Big)} \neq 0. \tag{2.23}$$

In the above analysis, our discussion was focused on the case $\mu_+ \geq \mu_-$. The feasible phases, density profiles, and phase diagrams for the case when $\mu_+ < \mu_-$ can be obtained from the results acquired when $\mu_+ > \mu_-$ by the implementation of the following transformation:

$$\begin{gathered} \rho_+ \leftrightarrow \rho_- \\ \mu_+ \leftrightarrow \mu_- \\ \text{A/B phase} \leftrightarrow \text{B/A phase.} \end{gathered} \tag{2.24}$$

We summarize eleven possible distinct regimes identified for different filling factors in Fig. (2.12). Without loss of generality, for the case when $\mu_+ = \mu_-$, we have assumed that the particle density of positive particles is greater than that of the negative species, i.e., the system displays H/L and S/L phases along the line $\mu_+ = \mu_-$. The density profiles corresponding to different phases are shown in Fig. (2.13).

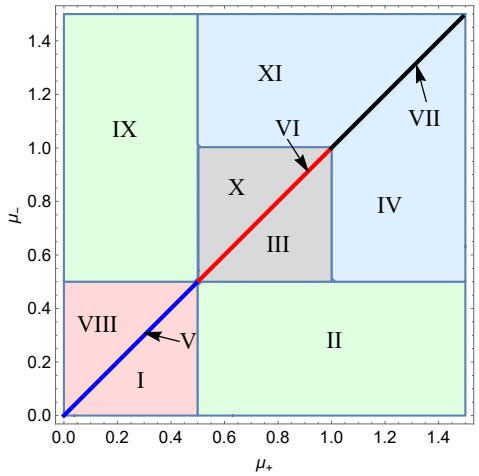

Figure 2.12: Different dynamic regions based on the filling factors μ_+ and μ_-. Eleven distinct regions numbered I to XI, have phase regimes that are qualitatively different. Table (2.2) provides a tabular description of the phase regimes that can exist in each of these different regions. In the table, a phase that does not exist is indicated by empty entries.

Phase	I	II	III	IV	V	VI	VII	VIII	IX	X	XI
S/L	✓	✓	✓	✓	✓	✓	✓				
H/L		✓		✓			✓				
M/L		✓	✓	✓							
MC/MC						✓	✓				
L/L	✓	✓	✓	✓	✓	✓	✓	✓	✓	✓	✓
LD/LD					✓	✓		✓			
M/M			✓	✓						✓	✓
L/M									✓	✓	✓
L/H									✓		✓
L/S								✓	✓	✓	✓

Table 2.2: The phases that exist in eleven different possible phase regions of the bidirectional system. The empty entries denote the phase that does not exist in the corresponding region.

2.5 Swapping rate of two-species other than 1

Our above investigation as well as previous studies [34,54], reveal that the predictions of the mean-field approximation are consistently supported by Monte Carlo simulations in the case of $s = 1$. Several attempts have been made focusing on the case when the exchange rate of the two-particle species if they encounter each other is not equal to 1 [34,117]. It is reasonable to anticipate that the mean-field technique will also perform admirably for the case of $s \neq 1$ as well. In this direction, if the mean-field approximation is employed on Eqs. (2.3) and (2.4), we obtain the bulk

currents corresponding to both the particle species as

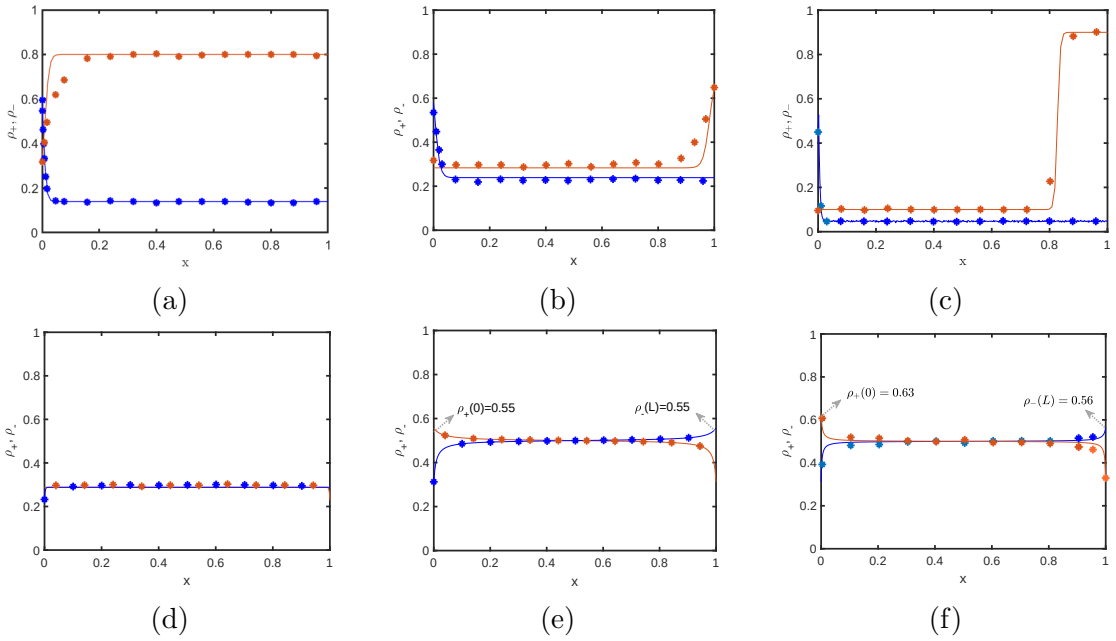

Figure 2.13: Density profiles for (a) H/L, (b) L/L, (c) S/L phases, (d) LD/LD, and (e) MC/MC with (α, β, μ) =(2,0.2,10),(2,0.315,1.1), $(1, 0.1, 0.3)$, $(1, 0.5, 0.9)$, $(3.5, 0.8, 1.1)$ with symmetric filling factors, and (f) M/M phase with $(\alpha, \beta, \mu_+, \mu_-) = (4.5, 0.8, 15, 0.9)$. The lattice length is taken to be 1500. Red and blue solid lines are mean-field results for (+) and (−) particles, respectively while filled markers correspond to Monte Carlo simulations.

$$\begin{aligned} J_+^{i-1,i} &= \rho_+^{i-1}(1-\rho_+^i-\rho_-^i) + s\rho_+^{i-1}\rho_-^i, \\ J_-^{i+1,i} &= \rho_-^{i+1}(1-\rho_-^i-\rho_+^i) + s\rho_-^{i+1}\rho_+^i. \end{aligned} \tag{2.25}$$

Applying a similar approach as discussed in Section (2.2), we use Taylor series expansion for $\rho^{i\pm1}$ and, retaining the terms up to second-order, the continuum equation obtained using a mean-field approach given by Eq. (2.25) reduces to

$$\begin{aligned} \frac{\partial \rho_\pm}{\partial t} = \frac{\partial}{\partial x}\left(\frac{\epsilon}{2}\frac{\partial \rho_\pm}{\partial x} \mp \rho_\pm(1-\rho_\pm)\right) &\pm (1-s)\left(\rho_+\frac{\partial \rho_-}{\partial x} + \rho_-\frac{\partial \rho_+}{\partial x}\right) \\ &\pm (1-s)\frac{\epsilon}{2}\left(\rho_+\frac{\partial^2 \rho_-}{\partial x^2} - \rho_-\frac{\partial^2 \rho_+}{\partial x^2}\right). \end{aligned} \tag{2.26}$$

This equation can be solved numerically by using a finite difference scheme which has been outlined in Appendix (2.9). It can be observed that this solution highly depends upon the initial densities of the two-species and does not match with the simulation results (see Fig. (2.14a)). While, in some cases, an agreement between simulations and mean-field results are remarkable (see Fig. (2.14b)). This depicts the failure of the mean-field theory in case the switching rate of the two-particle species is not equal to 1. The identical observation was also made previously in Ref. [34] for the case of an

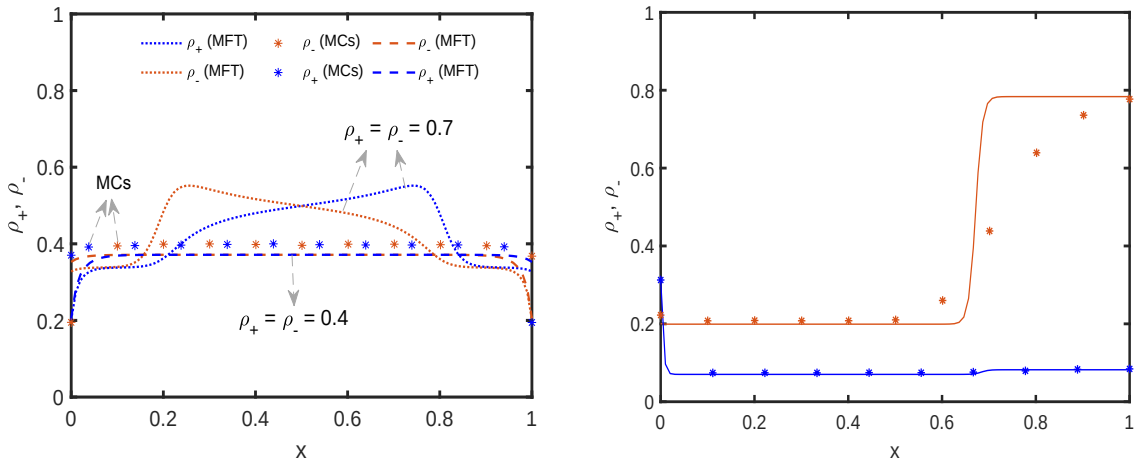

Figure 2.14: (a) Density profile of the two-particle species for $\alpha = 0.7$, $\beta = 1$, $\mu_- = \mu_+ = 1.1$, and $s = 0.8$ obtained using mean-field theory. Dashed lines correspond to solution obtained with initial condition $\rho_+ = \rho_- = 0.4$, dotted line is plotted for initial condition $\rho_+ = \rho_- = 0.7$, and symbols correspond to Monte Carlo simulations. (b) Density profile of the two-particle species for $\alpha = 0.5$, $\beta = 0.2$, $\mu_+ = \mu_- = 1.1$, and $s = 0.8$. Solid lines represent mean-field results and symbols correspond to Monte Carlo simulations.

infinite reservoir. Therefore, an alternate technique needs to be used to capture the system properties theoretically for $s \neq 1$, which will require further investigation.

2.6 Summary and conclusion

To summarize, we investigate a theoretical model that mimics the bidirectional movement of particles along a one-dimensional track, as is seen in the movement of cargo vesicles driven by motor proteins on microtubules and vehicular traffic on narrow roads. This model can be viewed as a two-species bidirectional totally asymmetric simple exclusion process with distinct finite particle reservoirs for each species. The entry of each particle species on the lattice is governed by the occupancy of the respective particle reservoir. The total number of particles for each species remains constant in the system and is characterized by the corresponding filling factor. Our model significantly differs from the previous studies where only one unified reservoir is taken into account. We theoretically examine the effect of the system dynamics on the crucial steady-state properties, such as phase diagrams, density profiles, phase boundaries, and phase transitions, in the framework of mean-field theory. All these theoretical outcomes are validated through extensive Monte Carlo simulations.

To study the impact of coupling the lattice to different finite reservoirs, we have explicitly considered two different scenarios: (i) the symmetric case when the filling factors for both species are equal and (ii) the asymmetric case where these factors

are different. In the former case, we observe a maximum of five stationary phases, two symmetric phases namely low density (LD/LD), maximal current phase (MC/MC), and three asymmetric phases: low-low density (L/L), shock-low density (S/L), and high-low density (H/L) phase. Despite the dynamics of the two-species being identical, symmetry breakdown is recorded in this case, which persists even for a very small magnitude of the filling factor. Further, particle density histograms are studied to examine the effect of this phenomenon through Monte Carlo simulation results. The S/L phase is an asymmetric phase that has not been previously obtained in bidirectional systems with infinite resources. The number of perceived phases in the phase diagram changes from $3 \to 4 \to 5 \to 4$ with increasing values of the common filling factor, which represents a non-monotonic trend.

For the case when the filling factors are unequal, a maximum of $4^2 = 16$ asymmetric phases can be observed in the system. Out of these, only eight phases are realized in the phase schema and the rest are discarded based on either physical or analytical arguments. Since, in this category, the two filling factors always remain different, the system cannot manifest a symmetric phase. The introduction of asymmetric filling factors leads to significant changes in the phase structure both quantitatively and qualitatively. A noteworthy feature of the phase diagrams is the presence of maximal-low (M/L) and maximal-maximal (M/M) phases which have not been detected in analogous systems with infinite resources. Even in this case, the variation in the number of phases in the phase diagram shows a non-monotonic trend.

For a deeper analysis of the S/L phase, we study the position and the height of the shock as well as the particle densities of both the species with respect to change in all the parameters: entry-exit rates and the filling factors. The exact number, dynamic characteristics, and region of various phases rely on the number of particles in each reservoir. We have identified the critical points where the appearance and disappearance of phases occur in the system.

It is important to note that the proposed model differs from the previous study [58] in several ways. Unlike the bidirectional system with reservoir crowding and a global constraint on the total number of particles in the system examined in the previous study, the current model imposes a global constraint on the number of resources of an individual species and regulates only the entrance rates based on the reservoir's capacity. Additionally, the present model introduces another feature: the M/L phase, which was not observed in Ref. [58]. All the phase boundaries in the present study exhibit a concave downward shape, in contrast to the convex upward trend, observed in the case of a unified reservoir [58].

2.7 Appendix: Symmetric phases

There are two feasible symmetric phases for which the explicit expressions for the phase boundaries, particle density, and the effective entrance rate α^{eff} can be theoretically computed by utilizing the framework presented in Sections (2.2) and (2.3.1). In all of these phases, the two-species of particles display identical stationary properties, which are examined in the following discussion.

- **Low density phase (LD/LD).** In this phase, both the species of the particles are in low density with bulk densities equal to α^{eff} and the current corresponding to both the particle species is equal to $J_+ = J_- = \alpha^{eff}(1-\alpha^{eff})$. As a result, Eq. (2.18) reduces to

$$\mu = r + \alpha^{eff}. \tag{2.27}$$

Upon solving Eqs. (2.19) and (2.27) along with the fact that $\alpha_+^{eff} = \alpha_-^{eff}$, the reservoir quotient is obtained as

$$r = \frac{1}{2\alpha}\left(\alpha(\mu-\beta) - \beta\mu + \sqrt{4\alpha\beta\mu^2 + (\alpha(\mu-\beta)-\beta\mu)^2}\right). \tag{2.28}$$

The existential conditions of this phase require the effective entrance to be less than 0.5 and β, which leads to

$$\min\{0.5,\ \beta\} > \frac{1}{2\alpha}\left(\alpha(\mu+\beta) + \beta\mu - \sqrt{4\alpha\beta\mu^2 + (\alpha(\mu-\beta)-\beta\mu)^2}\right). \tag{2.29}$$

Note that, in the limiting case of $\mu \to \infty$, α^{eff} is given by $\alpha\beta/(\alpha+\beta)$ which matches with the corresponding effective entry rate obtained for the LD/LD phase in the case of the bidirectional model with no restriction on the number of particles in the system [34].

- **Maximal current phase (MC/MC).** This case persists when both the particle species are individually in the MC phase with bulk densities 0.5 and bulk particle currents $J_+ = J_- = 0.25$. Such a phase is characterized by the following conditions:

$$\alpha^{eff} > 0.5, \quad \beta > 0.5. \tag{2.30}$$

Using Eq. (2.18), we have

$$r = \mu - 0.5, \tag{2.31}$$

which provides the existential conditions in the $\alpha - \beta$ plane as

$$\alpha > \frac{2\beta\mu}{(2\mu-1)(2\beta-1)}, \quad \beta > 0.5. \tag{2.32}$$

Further, it is evident from Eq. (2.31) that the MC/MC phase exists only when

$$\mu > 0.5. \tag{2.33}$$

For $\mu \to \infty$, Eq. (2.32) reduces to $\alpha > \frac{\beta}{2\beta-1}$ which is the condition for the MC/MC phase in the standard bidirectional TASEP with a common reservoir containing infinite resources [34].

2.8 Appendix: Asymmetric phases

In each of the asymmetric phases discussed below, first the effective entrance rates α_+^{eff} and α_-^{eff} are computed, which are then utilized to determine particle densities, the position of shock, and existential criteria in each phase.

- **High-low density phase (H/L)**. It is assumed that the (+) particles exhibit high density phase where density is greater than 0.5 and the (−) particles portray low density phase. Employing the expressions for currents given by Eq. (2.13), we attain $J_+ = \beta(1-\beta)$ and $J_- = \alpha_-^{eff}(1-\alpha_-^{eff})$. Substituting these into Eq. (2.16), the value of effective entrance rates is procured as

$$\begin{aligned} \alpha_-^{eff} &= \frac{1}{2\mu_-}\Big(\alpha r_- + \mu_- - \sqrt{(\alpha r_- + \mu_-)^2 - 4\alpha\beta\mu_- r_-}\Big), \\ \alpha_+^{eff} &= \frac{\alpha(\beta-1)\beta^2 r_+}{\alpha r_+(\alpha_-^{eff}-1)\alpha_-^{eff} + \beta^2\mu_+(\beta-1)}. \end{aligned} \tag{2.34}$$

Utilizing the particle number conservation given by Eq. (2.18) provides $\mu_+ = r_+ + 1 - \beta$ and $\mu_- = r_- + \alpha_-^{eff}$, which along with Eq. (2.34) gives the reservoir quotients as

$$\begin{aligned} r_+ &= \mu_+ - (1-\beta), \\ r_- &= \frac{1}{2(\alpha+\mu_-)}\Big(\alpha(\mu_- - \beta) + \mu_-(2\mu_- - 1)) \\ &\quad + \sqrt{\alpha(\mu_- - \beta) + \mu_-(2\mu_- - 1)^2 + 4(1-\mu_-)\mu_-^2(\alpha+\mu_-)}. \end{aligned} \tag{2.35}$$

These calculated values of the reservoir quotients can be replaced in Eq. (2.34) to obtain the effective entrance rates. The feasible region corresponding to this phase satisfies

$$\beta < \min\{\alpha_+^{eff}, 0.5\}, \quad \alpha_-^{eff} < \min\{\beta, 0.5\}, \tag{2.36}$$

along with the filling factors satisfying $\mu_+ \geq \mu_-$ and $\mu_+ > 0.5$. Moreover, the condition $\alpha_+^{eff} > \beta$ is satisfied only if $\mu_- < 0.5 < \mu_+$ or $(0.5 < \mu_-$ and $1 < \mu_+)$. It is worth pointing out that in case both the filling factors are equal, the SSB

phenomenon is observed. Moreover, all the stationary properties such as particle densities, reservoir quotients, and particle currents for the case of symmetric filling factors can be calculated by substituting $\mu_+ = \mu_- = \mu$ in all the above obtained expressions.

Clearly, when both $\mu_+ \to \infty$ and $\mu_- \to \infty$, the conditions for the existence of the H/L phase in a bidirectional system with an infinite particle reservoir is recovered [34].

- **Shock-low density phase (S/L)**. We presume that the (+) particles display a shock phase while the (−) particles are in low density phase. This phase persists when the boundary-controlling parameters ensure the following constraints:

$$\begin{aligned} J_+ = \beta(1-\beta) = \alpha_+^{eff}(1-\alpha_+^{eff}), \qquad J_- = \alpha_-^{eff}(1-\alpha_-^{eff}), \\ \int_0^1 \rho_+ \, dx = \int_0^{x_w} \alpha_+^{eff} \, dx + \int_{x_w}^1 (1-\beta) \, dx, \end{aligned} \tag{2.37}$$

where x_w is the position of shock in the density profile. The effective entrance rates for the particles can be retrieved from Eq. (2.16) as

$$\begin{aligned} \alpha_-^{eff} &= \frac{1}{2\mu_-}\Big(\mu_- + \alpha r_- - \sqrt{(\mu_- + \alpha r_-)^2 - 4\alpha\beta\mu_- r_-}\,\Big), \\ \alpha_+^{eff} &= \frac{\mu_+ + \alpha r_+}{2\mu_+} - \frac{\sqrt{\beta\big(\beta(\mu_+ - \alpha r_+)^2 - 4\alpha(\alpha_-^{eff}-1)\alpha_-^{eff}\mu_+ r_+}}{2\beta\mu_+}. \end{aligned} \tag{2.38}$$

Now we make use of Eq. (2.18) to calculate the reservoir quotient for (−) particles, which yields

$$\begin{aligned} r_- = \frac{1}{2(\alpha+\mu_-)}\Big(&\alpha(\mu_- - \beta) + \mu_-(2\mu_- - 1) \\ &+ \sqrt{\alpha^2(\beta-\mu_-)^2 + \mu_-^2 + 2\alpha\mu_-\big(\beta + \mu_-(1-2\beta)\big)}\Big). \end{aligned}$$

Since the existence of such a phase requires $\alpha_+^{eff} = \beta$, we have

$$r_+ = \frac{(\beta-1)\beta^2\mu_+}{\alpha\left(\alpha_-^{eff}(1-\alpha_-^{eff}) + \beta(\beta-1)\right)}. \tag{2.39}$$

The position of the shock can be procured by utilizing Eqs. (2.18) and (2.37) along with Eqs. (2.39) and (2.39), as

$$x_w = \frac{\beta + \mu_+ - r_+ - 1}{2\beta - 1}. \tag{2.40}$$

Finally, the boundary parameters must satisfy the following conditions for the S/L phase to exist:

$$0 \leq x_w \leq 1, \quad \alpha_-^{eff} < \min\{\beta, 0.5\}. \tag{2.41}$$

It must be noted that when $\mu_+ = \mu_-$, spontaneous symmetry-breaking is observed in the system and the corresponding results can be attained by replacing μ_+ and μ_- by μ in all the above expressions. Furthermore, this phase vanishes when both μ_+ and μ_- tend to ∞.

- **Maximal-low phase (M/L)**. In this phase, it is assumed that the (+) particles manifest maximal current with density given by 0.5, whereas the average particle density of (−) particles remains less than 0.5. Here, the particle currents are $J_+ = 0.25$, and $J_- = \alpha_-^{eff}(1-\alpha_-^{eff})$. These expressions when substituted in Eq. (2.16) and solved for the effective entrance rates provide

$$\begin{aligned} \alpha_-^{eff} &= \frac{1}{2\beta\mu_-}\Big(\beta(\mu_- + \alpha r_-) - \sqrt{\beta\left(\alpha\mu_- r_- + \beta(\mu_- - \alpha r_-)^2\right)}\Big) \\ \alpha_+^{eff} &= \frac{\beta\alpha r_+}{\beta\mu_+ + 4\alpha r_+ J_-}, \end{aligned} \tag{2.42}$$

and further α_+^{eff} can be calculated. Moreover, from Eqs. (2.18) and (2.42), we have

$$r_+ = \mu_+ - 0.5, \quad r_- = \frac{1}{8\beta(\alpha+\mu_-)}\left(X + \sqrt{X^2 - 64\beta^2(\mu_- - 1)\mu_-^2(\mu_- + \alpha)}\right),$$

where $X = \alpha\left(4\beta(\mu_- - 1) + 1\right) + 4\beta\mu_-(2\mu_- - 1)$. Using the above obtained expressions for the boundary parameters, the conditions of existence for this phase are framed as

$$\min\{\alpha_+^{eff}, \beta\} > 0.5 > \alpha_-^{eff}, \quad \mu_+ > \max\{\mu_-, 0.5\}. \tag{2.43}$$

- **Maximal-maximal phase (M/M).** All the stationary properties of this phase are similar to the MC/MC phase except the fact that here $\alpha_+^{eff} \neq \alpha_-^{eff}$, which further implies $\mu_+ \neq \mu_-$. In this phase, the reservoirs' quotients are given by $r_j = \mu_j - 0.5$ for $j \in \{+, -\}$. Since these quotients must be non-negative, the existential criteria for this phase are

$$\min\{\mu_+, \mu_-\} > 0.5, \quad \min\{\alpha_+^{eff}, \alpha_-^{eff}, \beta\} > 0.5, \tag{2.44}$$

where

$$\alpha_+^{eff} = \frac{\alpha r_+}{\beta\mu_+ + \alpha r_+}, \quad \alpha_-^{eff} = \frac{\alpha r_-}{\beta\mu_- + \alpha r_-}. \tag{2.45}$$

- **Low-low density phase (L/L).** This phase exists when the particle densities for

both species are entry dominated and remain less than 0.5. Such a phase exists when

$$\alpha_+^{eff} < \min\{\beta, 0.5\}, \quad \alpha_-^{eff} < \min\{\beta, 0.5\}. \tag{2.46}$$

The corresponding particle currents are expressed as

$$J_+ = \alpha_+^{eff}(1 - \alpha_+^{eff}), \quad J_- = \alpha_-^{eff}(1 - \alpha_-^{eff}). \tag{2.47}$$

Utilizing the fact that the particles are conserved along with $\rho_+ = \alpha_+^{eff}$ and $\rho_- = \alpha_-^{eff}$, we have

$$r_+ = \mu_+ - \alpha_+^{eff}, \quad r_- = \mu_- - \alpha_-^{eff}. \tag{2.48}$$

Solving Eq. (2.16) along with Eqs. (2.47) and (2.48), the effective entrance rates for both species can be obtained. In the case of symmetric filling factors, one can substitute $\mu_+ = \mu_- = \mu$ in all of the above expressions.

The existential conditions of the phases such as L/S, L/M, and L/H can be obtained by interchanging the roles of the parameters for the (+) and the (−) particles in S/L, M/L, and H/L phases, respectively.

2.9 Appendix: Numerical Scheme

In this section, we delineate a numerical approach to obtain the density profiles for the bidirectional system. Our system seems quite simple but it is difficult to solve second-order differential equations Eqs. (2.11) and (2.26) analytically. The term involving time is retained in the system and steady-state particle density for both the species is captured in the limit $t \to \infty$, where t is the total number of time steps to guarantee the occurrence of steady-state. The differential equation is discretized by choosing $\Delta x = 1/L$ and Δt is selected so that the stability criteria $\Delta t/\Delta x^2 \leq 1$ is maintained. Time and the space derivatives involved in the equation are replaced with forward and central difference formulas. Denoting the approximation to ρ_j at $(i\Delta x, n\Delta t)$ by $\rho_j^{i,n}$ for $j \in \{+, -\}$, we obtain the following equations:

$$\begin{aligned}\rho_+^{i,n+1} = \rho_+^{i,n} + \frac{\epsilon\Delta t}{2}(1-s)\rho_+^{i,n}\left(\frac{\rho_-^{i+1,n} - 2\rho_-^{i,n} + \rho_-^{i-1,n}}{\Delta x^2}\right) + \frac{\epsilon\Delta t}{2}\left(1 - (1-s)\rho_-^{i,n}\right) \\ \left(\frac{\rho_+^{i+1,n} - 2\rho_+^{i,n} + \rho_+^{i-1,n}}{\Delta x^2}\right) + \Delta t\left(2\rho_+^{i,n} - 1 + (1-s)\rho_-^{i,n}\right)\left(\frac{\rho_+^{i+1,n} - \rho_+^{i-1,n}}{2\Delta x}\right) \\ +\Delta t\ (1-s)\rho_-^{i,n}\left(\frac{\rho_-^{i+1,n} - \rho_-^{i-1,n}}{2\Delta x}\right),\end{aligned} \tag{2.49}$$

for the positive particles. Since the above equation is not valid for $i = 1$ and $i = L$ and both the species interact explicitly only at the boundaries, we cannot directly include boundary conditions in the above discretization. Instead, we utilize Eqs. (2.6) and (2.7), which can be written as

$$\rho_+^{1,n+1} = \rho_+^{1,n} + \Delta t\Big(\alpha\big(1 - \frac{\sum \rho_+^{i,n}}{L\mu_+}\big)(1 - \rho_+^{1,n} - \rho_-^{1,n}) - \rho_+^{1,n}(1 - \rho_+^{2,n} - \rho_-^{2,n}) - s\rho_+^{1,n}\rho_-^{2,n}\Big),$$
$$\rho_+^{L,n+1} = \rho_+^{L,n} + \Delta t\big(\rho_+^{L-1,n}(1 - \rho_+^{L,n} - \rho_-^{L,n}) + s\rho_+^{L-1,n}\rho_-^{L,n} - \beta\rho_+^{L,n}\big).$$

In the case of $s = 1$, Eq. (2.49) simplifies considerably and is given by

$$\rho_+^{i,n+1} = \rho_+^{i,n} + \frac{\epsilon\Delta t}{2\Delta x^2}\left(\rho_+^{i+1,n} - 2\rho_+^{i,n} + \rho_+^{i-1,n}\right) + \frac{\Delta t}{2\Delta x}\left(\rho_+^{i+1,n} - \rho_+^{i-1,n}\right)(2\rho_+^{i,n} - 1).$$

Similar equations can be written for the negative particles as well.

Chapter 3

Exclusion processes on a roundabout traffic model with constrained resources

In Chapter 2, we delved into bidirectional transport within a lattice confined to a single-lane and hosting a finite number of particles. A similar transport phenomenon is observed in network structures resembling roundabouts. This chapter[1] concentrates on exploring roundabout topologies with resource constraints, specifically highlighting scenarios where two distinct particle species move in opposite directions. To provide a theoretical ground for our findings, we employ a mean-field framework and successfully validate them through kinetic Monte Carlo simulations.

3.1 Motivation and background

Networks play a vital role in the realm of traffic flow, allowing for a deep understanding and effective management of the complex interactions and dynamics among diverse transportation components. The rising traffic demands have led to a significant expansion in the construction of new roads and the improvement of existing ones. An essential feature of these road networks is the creation of numerous points where different roads meet and cross paths with one another. In past decades, different topologies of networks have been modelled and analyzed to enhance traffic flow optimization, encompassing various aspects like movement at junctions, roundabouts, shortcuts, crossroads, traffic circles, multiple lanes, etc [99,102,103,118–126]. A variant investigates the stationary behaviour of a one-dimensional lane inserted with a double chain section in between [120,127–129]. In other words, a single-lane road acts as a feeder segment for two diverging branches that subsequently merge back into a single-lane. In this model, the unidirectional movement of particles is considered and the dynamics of the system are strongly characterized by the entrance rate of particles to the first single-lane and the exit rate from the second single-lane. The presence of

[1]The content of this chapter is published in:"Ankita Gupta, Arvind Kumar Gupta. Exclusion process on roundabout traffic model with constraint resources. *Physical Review E,* 108(6):064116, 2023."

junctions in traffic flows enhances the efficient movement of all the traffic participants. In biological systems, microtubules form an intricate network within cells, serving as structural elements and providing pathways for intracellular transport. Motor proteins such as dynein and kinesin utilize these filaments as a transportation route, traversing along them bidirectionally and towing their cargo over substantial distances. These large networks of microtubules constitute of junctions leading to various diseases as a consequence of motor protein crowding [130,131].

Given the significance of junctions and bidirectional flow in various natural and man-made systems, we explore a modified version of the double chain section model where two distinct species of particles travel in opposite directions. Simultaneously, a global constraint on the total number of particles in the system is considered. Our aim is to explore the novel phase transitions and nontrivial impact of the limited particle resources on the phase plane. We exploit the idea of defining effective entrance-exit rates through each lane and the domain wall theory, to obtain explicit expressions for the density profiles and determine the parameter range for which we expect congestion and symmetry-breaking. We analyze how the choice of the boundary rates of the particles along with the number of resources available, controls the dynamics of the system. In addition, we present a comprehensive analysis by considering suitable limiting cases to gain insights into the steady-state behaviour of the system. Precisely, the dynamics of our system encourage us to answer the following questions. (i) How does the number of available particles regulate the overall dynamics of the system? (ii) Does the mean-field framework possess sufficient competence to analyze the stationary properties, such as phase diagrams and potential phase transitions? (iii) How does the presence of two bridges in the middle affect both the qualitative and quantitative changes in the complexity of the phase diagram?

3.2 Model

To understand the bidirectional movement observed in various driven diffusive systems passing through roundabouts, we present an open system that employs an exclusion process (TASEP) and incorporates two distinct types of particles in a constrained environment. Specifically, the setup comprises of two distinct lanes, denoted as P and Q, which facilitate the movement of particles in both directions. These lanes are connected by bridges, namely B_+ and B_-, as clearly illustrated in Fig. (3.1). The two species of particle moving in opposite directions are represented as $(+)$ and $(-)$. Lane P acts as an input/output lane for the $(+)/(-)$ species while lane Q acts as an output/input lane for the $(+)/(-)$ species. The bridge lane B_+ accommodates the $(+)$ species, whereas B_- caters to the $(-)$ species. Each lane is composed of fixed

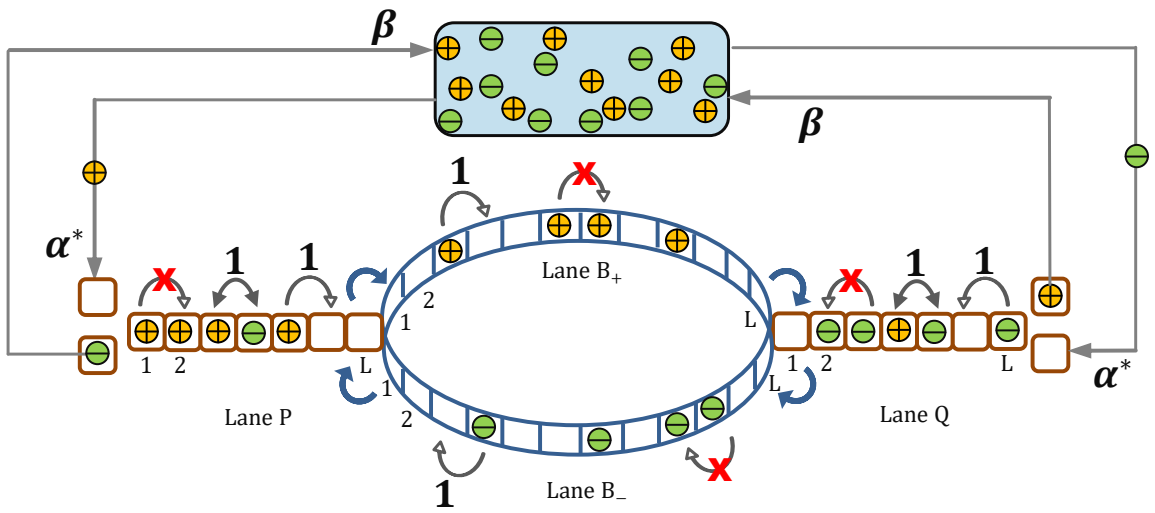

Figure 3.1: Model depiction in a diagrammatic form. Arrows indicate transitions that are permitted. Prohibited transitions are indicated by red crossed arrows. The two distinct species of particles progressing from left to right and right to left are represented by (+) and (−) symbols, respectively.

L sites identified as $i \in \{1, 2, \ldots, L\}$ (see Fig. (3.1)). The sites $i = 1$ and $i = L$ describe the left and right boundary whereas the rest $L - 2$ constitutes the bulk of each lane. The hard-core exclusion principle is enforced to prevent more than one particle from occupying a specific site at the same time, which mimics the physical constraints of various transport systems. The sites $i = 1$ of lane P and the site $i = L$ of lane Q are connected to a finite pool containing $N_r(t)$ identical particles. The total number of particles (N_t) in the system remains constant and does not vary at any given moment in time. Moreover, the pool is considered large enough to accommodate all the particles present in the system. The following transition rules govern the behaviour of the particles in each lane, which are also described in Fig. (3.1).

1. (+) **particle.** A positive particle is allowed to enter from the pool to the lane P through the left boundary ($i = 1$) with rate α^{eff}, provided this site is empty, i.e., neither occupied by (+) particle nor (−) particle. In the bulk, this particle can jump at a unit rate to the adjacent site if the target site is unoccupied. If a positive particle encounters a negative particle on the adjacent site, then they swap their positions with unit rate. As soon as this particle reaches the last site ($i = L$), it exits lane P to enter the first site of lane B_+ with the unit rate provided it is empty.

   Then, a (+) particle continues its movement along the bridge lane B_+ from left to right following the hard-core exclusion principle. On reaching the right boundary of lane B_+, it has a tendency to hop onto the first site of lane Q with unit rate, provided the latter site is free from particles of both kinds.

   In lane Q, this particle jumps along the bulk to the neighboring site if empty with

unit rate. If the next site contains a $(-)$ particle, then the two species exchange their positions with a unit rate. A $(+)$ particle finally escapes through the site $i = L$ of lane Q with the rate β to reenter the pool.

2. $(-)$ **particle.** A particle species of this kind follows similar dynamic rules as that of a positive species but in the opposite direction i.e., from right to left. However, here, the bridge B_- is utilized instead of B_+.

It is important to note that we have assumed that the rates for both the forward hopping and the exchange of positions are equal for the two different types of particles. Moreover, all the lanes in the system are considered to be of identical length.

The entrance rates for the particles of both kinds, denoted by α^{eff}, are controlled by the occupancy of the pool. For the sake of simplicity, we have assumed these arrival rates to be the same. To incorporate the effects of finite occupancy of the pool, we define the effective entrance rate α^{eff} as

$$\alpha^{eff} = \alpha N_r / N_t, \tag{3.1}$$

which has already been discussed in detail in previous chapters.

Now, the proposed model is characterized by α, β, L, and N_t which act as the controlling parameters for the steady-state properties. To reduce the number of parameters under consideration, we define a filling factor μ as $\mu = \frac{N_t}{4L}$ which keeps track of the total number of particles ($N_r(t)$ + count of particles on all the lanes) in the system with respect to the total number of sites in the system. Thus the controlling parameters for the system reduce to entrance-exit rates and the filling factor μ.

3.3 Master equations and mean-field analysis

We characterize the occupancy status of each site for every lane by the symbols $\tau_j^{+,i}$ and $\tau_j^{-,i}$ for the positive and the negative species, respectively. Here, $i \in \{1, 2, \ldots, L\}$ indicates the site number and $j \in \{\mathrm{P}, \mathrm{B}_{\pm}, \mathrm{Q}\}$ represents the corresponding lane. The governing densities of the bulk sites $(1 < i < L)$ for the bidirectional lanes $(j = P,\ Q)$ employing the master equations can be described as follows

$$\begin{aligned}
\frac{d\langle \tau_j^{+,i} \rangle}{dt} &= \langle \tau_j^{+,i-1}(1 - \tau_j^{+,i} - \tau_j^{-,i}) \rangle + \langle \tau_j^{+,i-1} \tau_j^{-,i} \rangle \\
&\quad - \langle \tau_j^{+,i}(1 - \tau_j^{+,i+1} - \tau_j^{-,i+1}) \rangle - \langle \tau_j^{+,i} \tau_j^{-,i+1} \rangle, \\
\frac{d\langle \tau_j^{-,i} \rangle}{dt} &= \langle \tau_j^{-,i+1}(1 - \tau_j^{-,i} - \tau_j^{+,i}) \rangle + \langle \tau_j^{-,i+1} \tau_j^{+,i} \rangle \\
&\quad - \langle \tau_j^{-,i}(1 - \tau_j^{-,i-1} - \tau_j^{+,i-1}) \rangle - \langle \tau_j^{-,i} \tau_j^{+,i-1} \rangle.
\end{aligned} \tag{3.2}$$

Here, the notation $\langle \dots \rangle$ denotes the statistical average. In the above equations, the positive and the negative terms on the right-hand sides correspond to the gain and loss of particles on the lane concerning the hopping and the swapping of the two species.

Similarly, for the bridge lanes, the particle evolution equations for the bulk can be written as

$$\begin{aligned}\frac{d\langle \tau_{B_+}^{+,i}\rangle}{dt} &= \langle \tau_{B_+}^{+,i-1}(1-\tau_{B_+}^{+,i})\rangle - \langle \tau_{B_+}^{+,i}(1-\tau_{B_+}^{+,i+1})\rangle,\\ \frac{d\langle \tau_{B_-}^{-,i}\rangle}{dt} &= \langle \tau_{B_-}^{-,i+1}(1-\tau_{B_-}^{-,i})\rangle - \langle \tau_{B_-}^{-,i}(1-\tau_{B_-}^{-,i-1})\rangle.\end{aligned}$$

After simplification, the particle evolution equations for all the lanes of the system gets modified to

$$\begin{aligned}\frac{d\langle \tau_{j}^{+,i}\rangle}{dt} &= \langle \tau_{j}^{+,i-1}(1-\tau_{j}^{+,i})\rangle - \langle \tau_{j}^{+,i}(1-\tau_{j}^{+,i+1})\rangle,\\ \frac{d\langle \tau_{j}^{-,i}\rangle}{dt} &= \langle \tau_{j}^{-,i+1}(1-\tau_{j}^{-,i})\rangle - \langle \tau_{j}^{-,i}(1-\tau_{j}^{-,i-1})\rangle.\end{aligned} \tag{3.3}$$

Now, all the equations governing the evolution of particles in each lane are decoupled, however, these equations are intractable in their present form due to the involvement of two-point correlators. So, we employ mean-field approximation which has worked as a vital tool to explore the behaviour of numerous many-body systems [34,53,132,133]. Mean-field in its simplest form neglects all the spatial correlations between neighboring particles and considers the occupancy of two adjacent sites to be independent of each other. To obtain the continuum limit of the model, we coarse-grain the discrete lane with constant $\epsilon = 1/L$ and re-scaled time as $t' = t/L$. In the continuum limit, the variables $\langle \tau_j^{+,i}\rangle$ and $\langle \tau_j^{-,i}\rangle$ are replaced with $\rho_j^{+,i}$ and $\rho_j^{-,i}$ and using the terms up to second-order in the Taylor series expression, we obtain

$$\frac{\partial \rho_j^{\pm}}{\partial t'} = \frac{\partial}{\partial x}\frac{\epsilon}{2}\frac{\partial \rho_j^{\pm}}{\partial x} \mp \rho_j^{+}(1-\rho_j^{+}). \tag{3.4}$$

The superscript i was dropped as the lanes are free from in-homogeneity of any type. At steady-state, the above equation reduces to

$$\frac{\epsilon}{2}\frac{\partial^2 \rho_j^{+}}{\partial x^2} + (2\rho_j^{+}-1)\frac{\partial \rho_j^{+}}{\partial x} = 0, \quad \frac{\epsilon}{2}\frac{\partial^2 \rho_j^{-}}{\partial x^2} - (2\rho_j^{-}-1)\frac{\partial \rho_j^{-}}{\partial x} = 0. \tag{3.5}$$

In the limit $\epsilon \to 0$, this equation yields $\frac{\partial J_j^{\pm}}{\partial x} = 0$, where $J_j^{\pm}$ gives us the bulk current of each species of particle as

$$J_j^{+} = \rho_j^{+}(1-\rho_j^{+}), \quad J_j^{-} = \rho_j^{-}(1-\rho_j^{-}). \tag{3.6}$$

In the following section, we intend to utilize mean-field approximation to examine the

stationary properties of the proposed model. To appropriately connect lanes P and Q with the bridge lanes, we must first define the effective entrance and exit rates for each lane. Further, we make use of notations $\rho_j^{+,i}$ and $\rho_j^{-,i}$ to represent the average particle density of the $(+)$ and $(-)$ particle, respectively, on site i in the jth lane. Moreover, the average densities in the bulk will be denoted by ρ_j^+ and ρ_j^-. The current induced by the $(+)$ and $(-)$ particles in each lane will be denoted by J_j^+ and J_j^-. Also, the symbol $J_j^{k,1}$ and $J_j^{k,L}$ is used to describe the current at the boundary sites on each lane. Considering that lane P(Q) operates as an input(output) lane for the positive (negative) species and lane Q(P) as an output(input) lane for positive(negative) particles, for analytical amenability we prefer to take that $j \in \{\text{in, B, out}\}$ for the rest of the article, where B stands for the respective bridge lane.

3.3.1 Dynamics of lanes P and Q

For the thorough theoretical investigation, we need to define effective entrance and exit rates for lanes P and Q. Taking into account that lane P(Q) acts as an input lane for positive(negative) particles and lane Q(P) behaves as an output lane for the negative(positive) species, we define the effective exit rate of $(+)$ and $(-)$ particles from the lane P and Q through the site $i = L$ and $i = 1$, as β_{in}^+ and β_{in}^-, respectively (see Fig. (3.2)). Similarly, the effective entrance rate of $(+)/(-)$ particles from bridge lane B_+/B_- to lane Q/P is denoted by $\alpha_{out}^+/\alpha_{out}^-$.

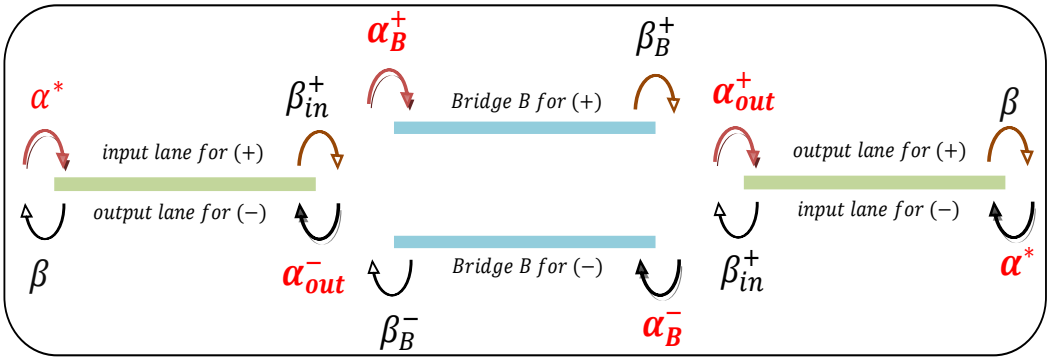

Figure 3.2: Representation of the proposed model with the fictitious defined entrance and exit rates through each lane required for analytical treatment.

Following mean-field approximation and the current continuity condition, the current flowing out of lane P(Q) is equal to the current passing from lane P(Q) to the bridge lane $B_+(B_-)$, which gives

$$\beta_{in}^+ \, \rho_{in}^{+,L} = \rho_{in}^{+,L} \, (1 - \rho_B^{+,1}), \quad \beta_{in}^- \, \rho_{in}^{-,1} = \rho_{in}^{-,1} \, (1 - \rho_B^{-,L}), \tag{3.7}$$

and can be simplified to obtain

$$\beta_{in}^{+} = 1 - \rho_{B}^{+,1}, \quad \beta_{in}^{-} = 1 - \rho_{B}^{-,L}. \tag{3.8}$$

Similarly, the current continuity argument suggests that the current passing through the bridge lane to lane Q/P must be equal to the inflow of current in lane Q/P, which can be written as

$$\begin{aligned} \alpha_{out}^{+}\ (1 - \rho_{out}^{+,1} - \rho_{in}^{-,1}) &= \rho_{B}^{+,L}\ (1 - \rho_{out}^{+,1} - \rho_{in}^{-,1}), \\ \alpha_{out}^{-}\ (1 - \rho_{in}^{+,L} - \rho_{out}^{-,L}) &= \rho_{B}^{-,1}\ (1 - \rho_{in}^{+,L} - \rho_{out}^{-,L}), \end{aligned} \tag{3.9}$$

and implies,

$$\alpha_{out}^{+} = \rho_{B}^{+,L}, \quad \alpha_{out}^{-} = \rho_{B}^{-,1}. \tag{3.10}$$

Next, we utilize the continuity of current within the bulk and at the boundaries of each lane to further analyze lane P. Subsequently, we extend a similar treatment to lane Q. According to the mean-field approximation, the bulk current of each species of particle on lane P can be expressed as

$$J_{in}^{+} = \rho_{in}^{+}(1 - \rho_{in}^{+}), \quad J_{out}^{-} = \rho_{out}^{-}(1 - \rho_{out}^{-}). \tag{3.11}$$

Similarly, the boundary currents are given by

$$\begin{aligned} J_{in}^{+,1} &= \alpha^{eff}(1 - \rho_{in}^{+,1} - \rho_{out}^{-,1}), \quad J_{in}^{+,L} = \beta_{in}^{+}\rho_{in}^{+,L}, \\ J_{out}^{-,L} &= \alpha_{out}^{-}(1 - \rho_{in}^{+,L} - \rho_{out}^{-,L}), \quad J_{out}^{-,1} = \beta\rho_{out}^{-,1}. \end{aligned} \tag{3.12}$$

Since, in the stationary state, the current is continuous throughout the lane, one can simply write that

$$J_{in}^{+,1} = J_{in}^{+,2} = \cdots = J_{in}^{+,L} = J_{in}^{+}, \quad J_{out}^{-,1} = J_{out}^{-,2} = \cdots = J_{out}^{-,L} = J_{out}^{-}. \tag{3.13}$$

It can be easily observed from Eqs. (3.11) and (3.12), the two bulk currents for the different species are decoupled and they interact effectively only at the boundaries. Therefore, lane P can be viewed as two independent single-species TASEP lanes with are connected through the boundaries only. Under this consideration, it is reasonable to define the modified entrance rates [34,53] for the two species to lane P by utilizing the current continuity condition described in Eq. (3.13), as

$$\alpha_{in_{eff}}^{+} = \frac{J_{in}^{+}}{\frac{J_{in}^{+}}{\alpha^{eff}} + \frac{J_{out}^{-}}{\beta}}, \quad \alpha_{out_{eff}}^{-} = \frac{J_{out}^{-}}{\frac{J_{out}^{-}}{\alpha_{out}^{-}} + \frac{J_{in}^{+}}{\beta_{in}^{+}}}. \tag{3.14}$$

As lane Q also portrays bidirectional flow, an analogous argument can be utilized

to define the modified entrance rates for the different particle species which results in,

$$\alpha^{+}_{out_{eff}} = \frac{J^{+}_{out}}{\frac{J^{+}_{out}}{\alpha^{+}_{out}} + \frac{J^{-}_{in}}{\beta^{-}_{in}}}, \quad \alpha^{-}_{in_{eff}} = \frac{J^{-}_{in}}{\frac{J^{-}_{in}}{\alpha^{eff}} + \frac{J^{+}_{out}}{\beta}}. \tag{3.15}$$

3.3.2 Dynamics of bridge lanes

We define that a positive particle can enter bridge lane B_+ from the lane P with an effective entrance rate α^{+}_{B} and can leave this lane with an effective exit rate β^{+}_{B} as depicted in Fig. (3.2). Similarly, a negative particle from lane Q can enter the bridge B_- with rate α^{-}_{B} and can exit to lane P with an effective exit rate of β^{-}_{B}.

The flow of each species of particle must remain continuous, which suggests that the current passing from the lane P/Q to B_+/B_- lane must be equal to the current entering the bridge lane, and can be written as

$$\alpha^{+}_{B}\ (1-\rho^{+,1}_{B}) = \rho^{+,L}_{in}\ (1-\rho^{+,1}_{B}), \quad \alpha^{-}_{B}\ (1-\rho^{-,L}_{B}) = \rho^{+,1}_{out}\ (1-\rho^{-,L}_{B}).$$

Similarly, the exit current from the bridge lane can be equated to the currents passing from the bridge lane to lane Q/P as

$$\beta^{+}_{B}\ \rho^{+,L}_{B} = \rho^{+,L}_{B}\ (1-\rho^{+,1}_{out}-\rho^{-,1}_{in}), \quad \beta^{-}_{B}\ \rho^{-,1}_{B} = \rho^{-,1}_{B}\ (1-\rho^{+,L}_{in}-\rho^{-,L}_{out}).$$

The above two equations can be simplified to obtain

$$\alpha^{+}_{B} = \rho^{+,L}_{in}, \quad \alpha^{-}_{B} = \rho^{-,1}_{out}, \quad \beta^{+}_{B} = 1-\rho^{+,1}_{out}-\rho^{-,1}_{in}, \quad \beta^{-}_{B} = 1-\rho^{+,L}_{in}-\rho^{-,L}_{out}. \tag{3.16}$$

3.3.3 Boundary dynamics

The first site ($i = 1$) of lane P and the last site ($i = L$) of lane Q is connected to a pool having a finite number of particles. As the total number of particles in the system remains conserved, one can write

$$N_t = N_r + N_P + N_Q + N_{B_+} + N_{B_-}, \tag{3.17}$$

where N_j, $j \in \{P, Q, B_+, B_-\}$ signifies the count of the number of positive and negative species on lane j. At steady-state, we can write these quantities as

$$\begin{aligned} N_P &= L\Big(\int_0^1 \rho^{+}_{in}dx + \int_0^1 \rho^{-}_{out}dx\Big), \quad N_{B_+} = L\int_0^1 \rho^{+}_{B}dx, \\ N_Q &= L\Big(\int_0^1 \rho^{+}_{out}dx + \int_0^1 \rho^{-}_{in}dx\Big), \quad N_{B_-} = L\int_0^1 \rho^{-}_{B}dx. \end{aligned} \tag{3.18}$$

Thus, Eq. (3.17) becomes

$$N_t = N_r + L\Big(\int_0^1 \sum_{j\ \in\{\text{in,B,out}\}} \big(\rho_j^+ + \rho_j^-\big)\, dx\Big). \tag{3.19}$$

To reduce the number of parameters to be investigated, the above equation can be rewritten as

$$\mu = r + \frac{1}{4}\Big(\int_0^1 \sum_{j\ \in\{\text{in,B,out}\}} \big(\rho_j^+ + \rho_j^-\big)\, dx\Big), \tag{3.20}$$

where $r = \frac{N_r}{4L}$ defines the pool quotient. Thus, the effective entrance rate is given by Eq. (3.1) is modified to $\alpha^{eff} = \alpha\frac{r}{\mu}$.

3.4 Analytic predictions

To begin, we first define the notion of labeling a possible phase in a phase diagram. Any given density profile can be expressed as $X_1-X_2-X_3/Y_1-Y_2-Y_3$. In this notation, X_1, X_2, and X_3 represent the phases exhibited by the positive particles in lane P, bridge B_+, and lane Q, respectively. Similarly, Y_1, Y_2, and Y_3 denote the phases displayed by the negative particles in lane Q, bridge B_-, and lane P, respectively. Additionally, by observing the phase exhibited by individual particle species in each lane, we identify whether the overall system's phase is symmetric or asymmetric. In the case of a symmetric phase, the bulk densities of both the particle species in their respective lanes are equal i.e., $\rho_{in}^+ = \rho_{in}^-,\ \rho_B^+ = \rho_B^-,\ \rho_{out}^+ = \rho_{out}^-$; meanwhile for asymmetric phases, the characteristics including currents and density profiles are generally different for the two-particle species.

The two-particle species can exhibit four possible phases in each lane, leading to a total of $4^6 = 4096$ phases displayed by the system. Clearly, listing all probable phases is not admissible. Since a phase of the form, $X_1 - X_2 - X_3/Y_1 - Y_2 - Y_3$ is equivalent to $Y_1 - Y_2 - Y_3/X_1 - X_2 - X_3$, that is the changing the role of the two species has no impact on the phase displayed, the number of phases gets reduced to 2080. The majority of these cases, however, cannot exist because of several constraints and are discussed in Appendix (3.8.1). Now, based on the observed stationary properties, including density profiles, effective entrance rates, and particle currents, we categorize the different phases as either symmetric or asymmetric.

3.4.1 Symmetric phases

During a symmetric phase, the system displays identical stationary properties for both the particle species, including particle densities and currents in each lane. This equivalence arises due to the consistency of the dynamical processes and the behaviour of the system which is indistinguishable between the two-particle types. Such a circumstance gives

$$J_{in}^{+} = J_{in}^{-}, \quad J_{in}^{-} = J_{out}^{+}, \quad J_{B}^{+} = J_{B}^{-}, \quad \rho_{in}^{+} = \rho_{out}^{-}, \quad \rho_{in}^{-} = \rho_{out}^{+}, \quad \rho_{B}^{+} = \rho_{B}^{-},$$

leading to $\beta_{in}^{+} = \beta_{in}^{-} = \beta_{in}, \quad \alpha_{B}^{+} = \alpha_{B}^{-} = \alpha_{B}, \quad \beta_{B}^{+} = \beta_{B}^{-} = \beta_{B}, \quad \alpha_{out}^{+} = \alpha_{out}^{-} = \alpha_{out}.$

This implies that modified entrance rates described by the Eqs. (3.14) and (3.15) alters to

$$\alpha_{in_{eff}}^{+} = \alpha_{in_{eff}}^{-} = \frac{J_{in}}{\frac{J_{in}}{\alpha^{eff}} + \frac{J_{out}}{\beta}} = \alpha_{in_{eff}}, \quad \alpha_{out_{eff}}^{+} = \alpha_{out_{eff}}^{-} = \frac{J_{out}}{\frac{J_{out}}{\alpha_{out}} + \frac{J_{in}}{\beta_{in}}} = \alpha_{out_{eff}},$$

where $J_{in}^{+} = J_{in}^{-} = J_{in}$ and $J_{out}^{+} = J_{out}^{-} = J_{out}$.

Therefore, utilizing the above conditions, one can calculate the effective entrance and exit rates of all the lanes and finally obtain the stationary density profile of a symmetric phase. We have used abbreviations (LD, HD, MC, and SP) to indicate lane phases in a symmetrical context: LD representing low density, HD for high density, MC for maximal current phase, and SP for the shock phase.

As a result, there are $4^3 = 64$ possible symmetric phases out of which there are only four achievable phases: LD-LD-LD/LD-LD-LD, LD-SP-LD/LD-SP-LD, SP-HD-LD/SP-HD-LD, and HD-HD-LD/HD-HD-LD. The rest of the phases are discarded based upon either physical or mathematical argument for which the complete explanations is detailed in Appendix (3.8.1). For the feasible phase, we provide the explicit expressions for the particle densities, currents, position of the shock, and the phase boundaries in Appendix (3.7).

3.4.2 Asymmetric phases

In our model, the two species of particles interact effectively at the boundaries of lane P as well as lane Q which is the sole factor affecting the symmetry between the distinct particle species. This leads to the emergence of the asymmetrical phases and subsequently, spontaneous symmetry-breaking phenomena. In an asymmetric phase, each species exhibits distinctive properties in terms of current and density, and this section examines the likelihood of the occurrence of such phases. To simplify the analysis, it is assumed that the positive particles outnumber the negative ones. To distinguish an asymmetrical phase from a symmetrical phase, we have used the notation

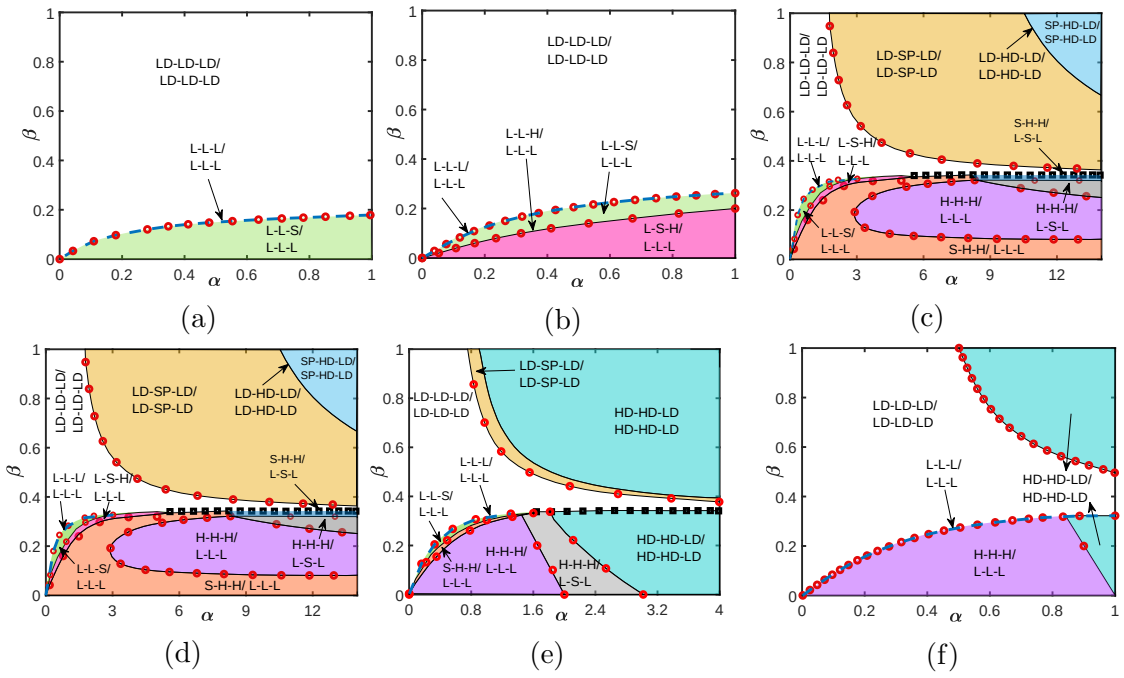

Figure 3.3: Stationary phase diagrams for different values of μ: (a) $\mu = 0.1$, (b) $\mu = 0.45$, (c) $\mu = 0.6$, (d) $\mu = 0.7$, (e) $\mu = 1.5$ and (f) $\mu \to \infty$. Solid lines represent theoretical findings while red circles denote Monte Carlo simulation results. The blue dashed curves indicate the L-L-L/L-L-L phase. The phases L-L-L/L-L-L, L-L-S/L-L-L, L-L-H/L-L-L, L-S-H/L-L-L, and L-H-H/L-L-L, all converge in a narrow region which is presented by black squares in panels (d) and (e).

of L for low density, H for high density, M for the maximal current phase, and S for the shock phase.

Theoretical investigation of such phases reveals that there are 11 attainable asymmetric phases for which the existence criteria, expressions of shock position, and effective entrance rates wherever possible are explained in Appendix (3.8). The remaining phases are eliminated based on theoretical reasoning, which is presented in Appendix (3.8.1).

3.5 Results: analysis and implications

To explore the dynamics of the system in the steady-state, we create phase diagrams in the parameter space (α, β) based on our theoretical investigations explained in the previous section as well as Appendices (3.7) and (3.8). The objective is to examine how the system's complex dynamics are affected by the global constrained on the resources available which is quantified by the variable μ. To verify our theoretical findings, we conduct Monte Carlo simulations (MCs) utilizing the Gillespie Algorithm (akin to kinetic Monte Carlo simulations) as discussed in Chapter (1). It has been observed that the consistency between simulation data and analytical predictions holds true across all

regimes. Alternatively, we can employ numerical techniques (refer to Appendix (2.9)) on the continuum version of the particle evolution equation, represented by Eq. (3.4), to obtain density profiles for any given phase. There are several advantages of adopting this approach. First, it is easier to implement compared to the analytical methods outlined in Appendices (3.7) and (3.8). Second, unlike the theoretical approach, this method can be readily adapted to more generalized models by incorporating changes in the master equation. Last, this approach allows for obtaining solutions in cases where the choice of functions in Eq. (3.1) leads to analytically intractable forms.

3.5.1 Role of filling factor

Using the analytical findings presented in Sections (3.4.1) and (3.4.2), we proceed to explicitly establish the mathematical expressions for the phase boundaries, whenever feasible, that distinguish the two phases. These phase boundaries are vital in discerning various phase configurations.

1. The boundary separating the LD-LD-LD/LD-LD-LD phase from LD-SP-LD/LD-SP-LD as obtained from Eq. (3.24) is

$$\beta = \frac{\alpha(2\mu - 1)}{3\alpha(\mu - 1) - 2\mu}. \tag{3.21}$$

2. For the LD-SP-LD/LD-SP-LD phase to LD-HD-LD/LD-HD-LD, the boundary is expressed as

$$\beta = \frac{\alpha(3\mu - 2)}{3\left(\alpha(3\mu - 2) - \mu\right)}, \tag{3.22}$$

   which is calculated from Eq. (3.25) by solving $x_w = 0$.

3. For the symmetric LD-LD-LD/LD-LD-LD to L-L-L/L-L-L, we have

$$\alpha^{-}_{out_{eff}} = \beta,$$

   where $\alpha^{-}_{out_{eff}}$ is given by Eq. (3.26).

4. The boundary between the L-L-S/L-L-L and L-S-H/L-L-L phases can be identified from Eq. (3.30) by setting $x_w = 0$ which can be realized as L-L-H/L-L-L phase.

5. Boundary separating the L-S-H/L-L-L and S-H-H/L-L-L phases, as determined by Eq. (3.31) with $x_w = 0$, corresponds to the L-H-H/L-L-L phase.

6. For the S-H-H/L-L-L and H-H-H/L-L-L phase the boundary is represented as

$$\alpha^{+}_{in_{eff}} = \beta, \tag{3.23}$$

for $\alpha^{+}_{in_{eff}}$ given in Eq. (3.27).

To perform a comprehensive analysis, we present phase diagrams for specific values of μ spanning from 0 to ∞. These diagrams exhibit significant topological changes in the parameter space (α, β) and are visually represented in Fig. (3.3). The figures are generated using carefully selected values of μ to highlight noteworthy modifications in the structure of the phase diagrams.

When the system contains only a small number of particles, approximately $\mu \approx 0.001$, a single symmetric phase, namely LD-LD-LD/LD-LD-LD, is observed. The scarcity of particles limits the effective particle influx into the lane, resulting in the manifestation of a low density phase in each lane. With the addition of more particles to the system, the number of phases increases to three. The phase diagram then consists of one symmetric phase (LD-LD-LD/LD-LD-LD) and two asymmetric phases (L-L-L/L-L-L and L-L-S/L-L-L), which disrupt the symmetry of the system as evident from Fig. (3.3a) for $\mu = 0.1$. This observation can be explained as follows: For lower values of β, there is a tendency for particles to accumulate primarily at the right end of the output lane. Consequently, the boundary layer at the right boundary infiltrates into the bulk region, resulting in the occurrence of a boundary-induced shock in the output lane.

Further increasing the particle count in the system reveals the emergence of two additional asymmetric phases: L-L-H/L-L-L and L-S-H/L-L-L, as depicted in Fig. (3.3b) for $\mu = 0.45$. The L-S-H/L-L-L phase appears adjacent to L-L-S/L-L-L, with L-L-H/L-L-L serving as a boundary curve that separates the L-L-S/L-L-L and L-S-H/L-L-L phase regions. When the value of μ exceeds 0.5, two new asymmetric phases, namely L-H-H/L-L-L and S-H-H/L-L-L, emerge alongside the L-S-H/L-L-L phase. Additionally, a symmetric phase (LD-SP-LD/LD-SP-LD) appears adjacent to the LD-LD-LD/LD-LD-LD phase, in addition to the already existing phases. Physically, the emergence of the high density (HD) phase in a lane is expected, as it cannot occur in the system for $\mu < 0.5$ due to an insufficient number of particles in the system to achieve the high density state. The critical value of μ at which the bulk-induced shock phase (LD-SP-LD/LD-SP-LD) emerges is 0.5 and is theoretically justified from Eq. (3.21). Furthermore, the L-H-H/L-L-L phase acts as a boundary curve that separates the S-H-H/L-L-L and L-S-H/L-L-L phase regions (see phase diagram given by Fig. (3.3c) for $\mu = 0.6$).

Beyond $\mu = 0.5$, the topology of the phase diagram undergoes substantial qualitative and quantitative changes. The phase plane becomes more intricate due

to the emergence of new symmetrical and asymmetrical phases as evident from Fig. (3.3d) for $\mu = 0.7$. Consequently, the phase diagram undergoes changes such as the translation of phase boundaries and contraction of existing phases. Notably, four new asymmetrical phases, specifically H-H-H/L-L-L, H-H-H/L-S-L, S-H-H/L-S-L, and L-H-H/L-S-L appear in the phase plane. Additionally, two symmetrical phases, LD-HD-LD/LD-HD-LD and SP-HD-LD/SP-HD-LD, emerge. The symmetric phase SP-HD-LD/SP-HD-LD appears adjacent to the symmetric LD-SP-LD/LD-SP-LD phase, and the boundary separating these two phases represents the LD-HD-LD/LD-HD-LD phase. The Eq. (3.22) provides the curve indicating the existence of the LD-HD-LD/LD-HD-LD phase. In the lower half region, when α takes on large values, a significant portion of the region is dominated by the H-H-H/L-L-L phase, which is adjacent to the S-H-H/L-L-L phase. Figure (3.3d) illustrates that for $\alpha \approx 5.5$, the boundary curves corresponding to L-L-L/L-L-L, L-L-H/L-L-L, and L-H-H/L-L-L all converge within a very narrow region of width approximately 0.02 with respect to β. Consequently, this narrow region is represented by 'black square' symbols in the phase diagram. The coordinates $(\overline{\alpha}, \overline{\beta})$ in the $\alpha - \beta$ plane, where the two curves represent the boundary of the H-H-H/L-L-L region given by Eq. (3.28) intersect, can be easily determined. This intersection occurs at the points where $\alpha^{-}_{in_{eff}} + \alpha^{-}_{out_{eff}} = \alpha^{+}_{in_{eff}}$. For a fixed value of $\alpha \geq \overline{\alpha}$, an increase in the value of β leads to a phase transition sequence: H-H-H/L-L-L $\rightarrow$ H-H-H/L-S-L $\rightarrow$ S-H-H/L-S-L $\rightarrow$ L-H-H/L-S-L $\rightarrow$ L-S-H/L-L-L $\rightarrow$ L-L-H/L-L-L $\rightarrow$ L-L-S/L-L-L $\rightarrow$ L-L-L/L-L-L $\rightarrow$ LD-LD-LD/LD-LD-LD.

Once μ exceeds the value 1, a new symmetric phase emerges in the phase diagram, referred to as HD-HD-LD/HD-HD-LD (see Fig. (3.3e)). In this phase, the HD (high density) region always maintains a maximal particle density of 1, while the low density region remains at 0. This phase can be interpreted as a congestion region, where there is no particle movement whatsoever. It is positioned adjacent to SP-HD-LD/SP-HD-LD in the upper half plane and is also neighbouring the H-H-H/L-S-L phase in the lower half plane. Finally, as $\mu \rightarrow \infty$, the phase diagram undergoes a substantial simplification. It displays only four distinct stationary phases: two symmetric phases, namely LD-LD-LD/LD-LD-LD and HD-HD-LD/HD-HD-LD, and two asymmetric phases, L-L-L/L-L-L and H-H-H/L-L-L as evident from Fig. (3.3f).

The aforementioned observations demonstrate that the presence of limited resources has a substantial impact on the phenomenon of symmetry-breaking. This effect occurs even with a relatively small number of particles in the system. In the forthcoming sections, we will elucidate the significant and abrupt phase transitions discussed earlier, as well as delve into the dynamics of shocks both boundary-induced and bulk-induced.

3.5.2 Shock dynamics

In this section, we will explore the characteristics of two distinct types of shocks that have been observed in the previous section. A shock that enters through either the left end of the input lane or the right end of an output lane is referred to as a boundary-induced shock. A bulk-induced shock refers to the occurrence of localized congestion within the interior of the system, away from the boundaries. It originates from the internal dynamics of the system rather than external influences at the boundaries. To delve into a detailed study of the phase transitions that lead to the formation of these types of shocks, we have selected a filling factor value and vary the boundary-controlling parameters α and β.

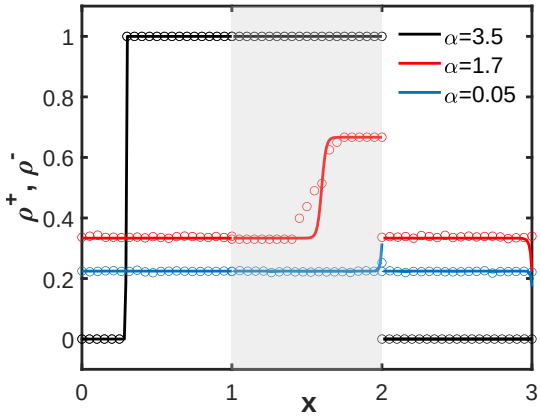

Figure 3.4: Phase transitions exhibited for $\mu = 0.8$ and $\beta = 1$ for varying values of α. The system evolves from LD-LD-LD/LD-LD-LD $\rightarrow$ LD-SP-LD/ LD-SP-LD $\rightarrow$ SP-HD-LD/SP-HD-LD. Since in the symmetric phase, the density profiles for the two species are identical, we plot the density profile only for the positive species. Solid lines give mean-field results while symbols correspond to Monte Carlo simulations. The shaded region for $x \in [1, 2]$ represents the bridge lane.

A bulk-induced shock in the symmetric LD-SP-LD/LD-SP-LD and SP-HD-LD/SP-HD-LD appears in the phase diagram, as evident from Fig. (3.3d). In the LD-SP-LD/LD-SP-LD, a discontinuity in the density profile is observed in the bridge lane for both particle species. While for the SP-HD-LD/SP-HD-LD, this discontinuity appears in the input lane, where the density profile connects a region of low density having constant particle density at 0 to a region of high density with density 1. The explicit expression for the location of the shock in LD-SP-LD/LD-SP-LD is computed in Eq. (3.25) which suggest that for fixed values of β and μ, an increase in α leads to an increase in the number of particles feed into the system which in turn sweeps the shock toward the left. This is affirmed by Fig. (3.4), which clearly shows that for $\beta = 1$ and $\mu = 0.8$, the high density region of the shock enhances and with an increase in α, the shock vanishes from the bridge lane. To validate it mathematically, we employ Eq. (3.25), which gives us the shock position in the LD-SP-LD/LD-SP-LD

phase as

$$x_w = \frac{6\beta\mu}{\alpha(3\beta - 1)} - 2(3\mu - 2).$$

The shock position clearly demonstrates that an increase in α causes the shock to shift toward the left, indicating the disappearance of the LD-SP-LD/LD-SP-LD phase. With further enhancement in α, this shock enters the input lane leading to an occurrence of the SP-HD-LD/SP-HD-LD phase. As already been examined theoretically, in this phase, a density profile connecting a region of density 0 to 1 is observed in the input lane, density 1 in the bridge lane, and the output lane has a constant density of 0 (see Appendix (3.7)).

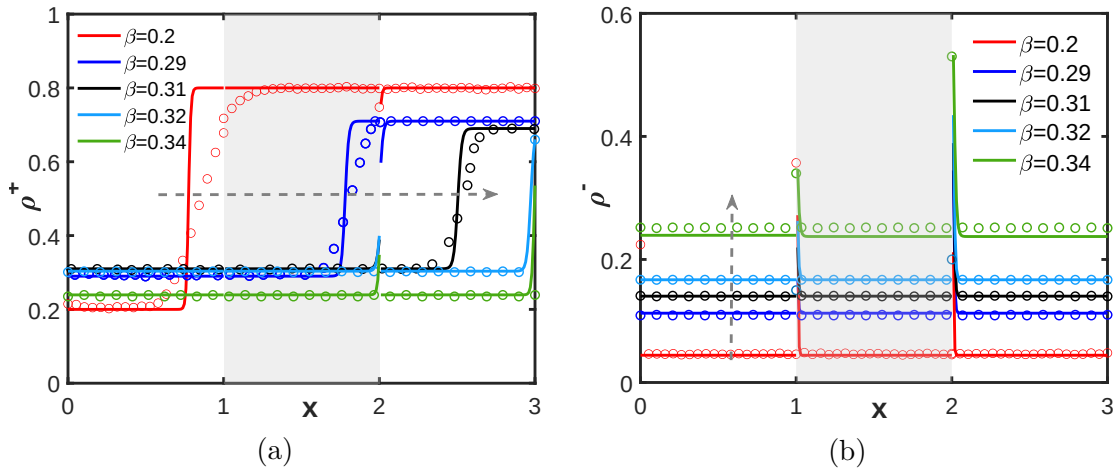

Figure 3.5: Phase transitions with respect to β for fixed values of the other parameters as $\alpha = 2$, and $\mu = 0.6$ representing evolution of the system from S-H-H/L-L-L $\rightarrow$ L-S-H/L-L-L $\rightarrow$ L-L-S/L-L-L $\rightarrow$ L-L-L/L-L-L $\rightarrow$ LD-LD-LD/LD-LD-LD. (a) and (b) shows the density profile for the (+) and the (-) species, respectively. Solid lines give mean-field results while symbols correspond to Monte Carlo simulations. The shaded region for $x \in [1, 2]$ represents the bridge lanes. The dotted arrow indicates the direction of increasing β.

Now, let us examine some key aspects of the localized shock induced by the boundary in the phase diagram for $\mu = 0.6$, as shown in Fig. (3.3c). When a particular lane undergoes a shock phase, we can determine the speed of the shock by calculating the difference between the exit rate and the entrance rate of that specific lane. For the system to exhibit a localized shock, the speed of the shock must be zero. To analyze the behaviour of the shock, we fix $\mu = 0.6$ and $\alpha = 2$, and examine the position of the shock relative to the exit rate parameter β. Figure (3.5a) illustrates the phase transitions of the positive species as β increases. We can observe the following sequence of transitions for the positive species: S-H-H $\rightarrow$ L-H-H $\rightarrow$ L-S-H $\rightarrow$ L-L-H $\rightarrow$ L-L-S $\rightarrow$ L-L-L. Throughout these transitions, the negative species consistently exhibit a low density phase in each lane. These transitions can be explained through the following

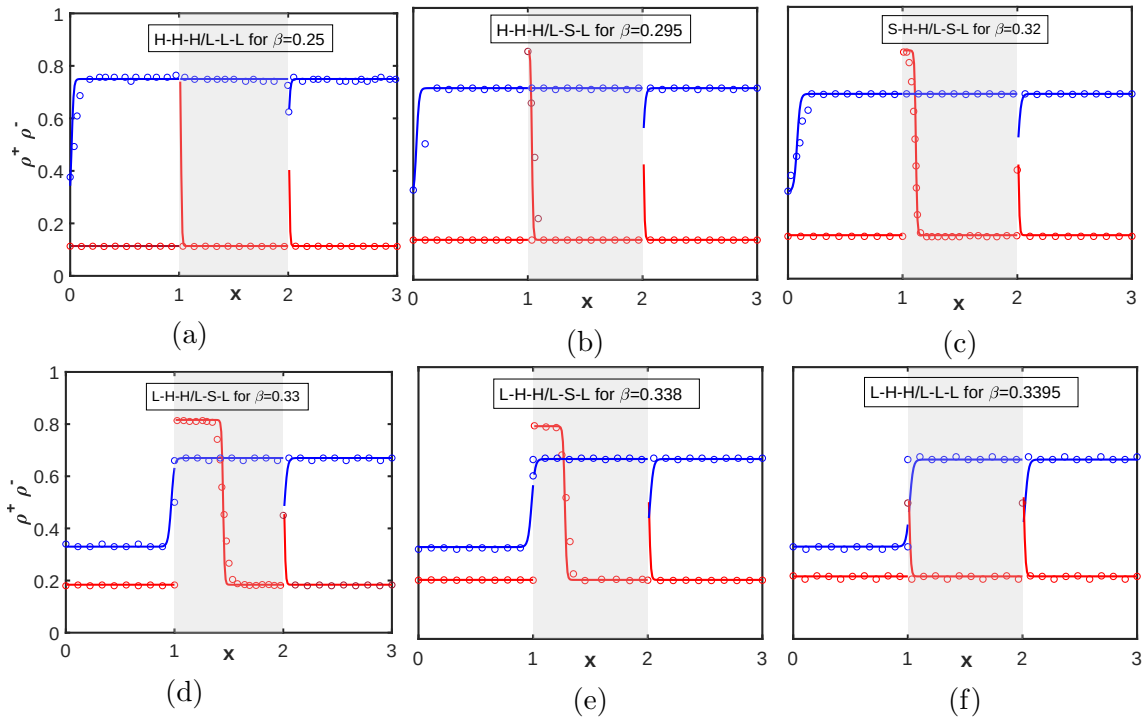

Figure 3.6: Dynamics of the phase involving shock for $\mu = 0.7$, $\alpha = 12$ and different values of β. (a) $\rightarrow$ (b) $\rightarrow$ (c) $\rightarrow$ (d) $\rightarrow$ (e) $\rightarrow$ (f) gives the order of the phase transition. Solid lines give mean-field results while symbols correspond to Monte Carlo simulations. The shaded region for $x \in [1, 2]$ represents the bridge lanes.

reasoning. For smaller values of β, a shock enters the input lane of the positive particles from the left end. The position of this shock can be determined using Eq. (3.31). As β increases, the effective entrance rate $\alpha^{+}_{in_{eff}}$ also increases, causing the shock to move towards the right. With further increments in β, the shock travels from lane P to the bridge lane and then to lane Q, ultimately leaving the system and resulting in the positive particles displaying a low density phase in each lane. Meanwhile the entrance rate of the negative species through lane Q which is $\alpha^{-}_{in_{eff}}$ also continues to increase with respect to β (see Fig. (3.5b)). Thus, if one considers the position of shock as the order parameter, then these transitions are of second-order.

Here, we will explore the changes occurring in the $\alpha - \beta$ plane for $\mu = 0.7$ by selecting a point within the H-H-H/L-L-L region, ensuring that α is large enough. Our focus will be on examining the density profile at various values of β (see Fig. (3.6)). To begin, we set $\beta = 0.25$ in this region and present Fig. (3.6a), where we observe an enhancement in the modified entrance rates of the two-particle species, given by $\alpha^{\pm}_{in_{eff}}$, as β increases. Initially, a bulk-induced shock phase, referred to as H-H-H/L-S-L, emerges in the system, characterized by a discontinuous density profile in the bridge lane for the negative species. As β further increases, a shock enters from the left end corresponding to the positive particles. This leads to a transition from the H-H-H/L-L-L phase to a bulk-induced shock phase H-H-H/L-S-L and finally to a boundary-induced

shock phase S-H-H/L-S-L. Importantly, as β increases, both shocks progressively shift from the left to the right. Around the critical value of $\beta \approx 0.332$, the shock in lane P reaches the right boundary, causing the shock in the bridge lane to reverse its direction. As β further increases, the latter shock moves back towards the left boundary, resulting in the system transitioning into the L-H-H/L-L-L phase. After attaining this phase the system evolves to L-S-H/L-L-L → L-L-H/L-L-L → L-L-S/L-L-L → L-L-L/L-L-L, whose details have already been discussed.

3.5.3 Back-and-forth transitions

We now examine a special characteristic in the phase diagram known as the back-and-forth transition, which emerges when observing the phase diagram for $\mu = 0.7$ (see Fig. (3.3d)) and in the limit as μ approaches infinity (see Fig. (3.3f)). The term 'back-and-forth transition' is defined as follows. When examining a particular phase diagram, if the system undergoes a transition from phase X to phase Y and then returns back to phase X, denoted as X→Y→X while adjusting a single parameter and keeping the remaining parameters constant, we refer to this phenomenon as the back-and-forth transition [58,107,134].

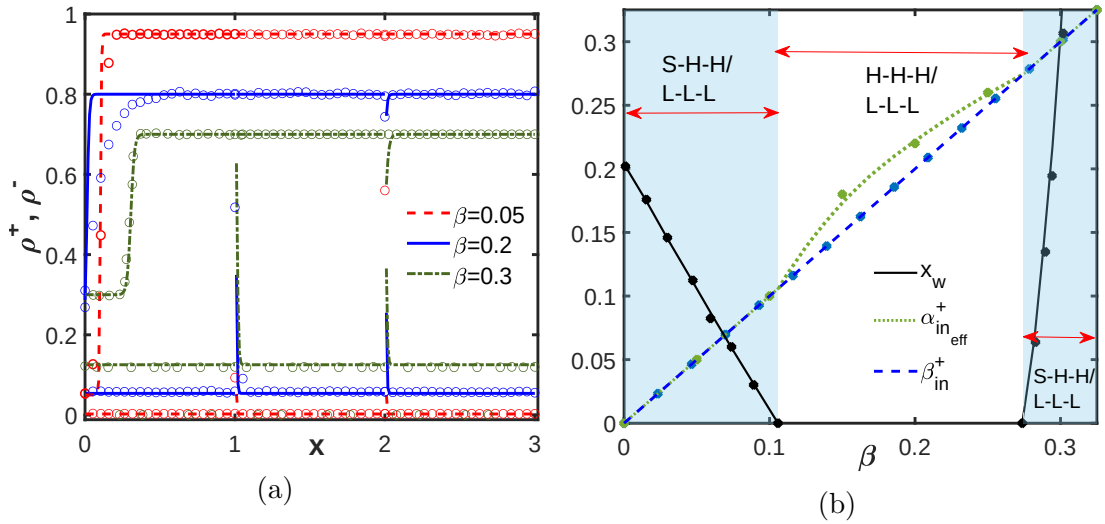

Figure 3.7: (a) Density profiles displaying back-and-forth transition for $\mu = 0.7$ and $\alpha = 4$ with $\beta = 0.05$ (S-H-H/L-L-L), 0.2 (H-H-H/L-L-L) and 0.3 (S-H-H/L-L-L). (b) Effective entry-exit rates and the position of shock x_w (given by Eq. (3.31)) of the positive particles for lane P for fixed $\mu = 0.7$ and $\alpha = 4$. Solid lines denote theoretical results and round symbols show Monte Carlo simulation results.

Upon closer examination of the phase diagram for $\mu = 0.7$, an interesting boundary emerges between the S-H-H/L-L-L and H-H-H/L-L-L regions. When we analyze the system's behaviour by fixing $\alpha = 4$, $\mu = 0.7$ and only varying the exit rate β, we observe a transition from the S-H-H/L-L-L phase to the H-H-H/L-L-L phase. Surprisingly, as β

continues to increase, the system transitions back to the S-H-H/L-L-L phase. Equation (3.23) provides us with the phase boundary between the S-H-H/L-L-L and H-H-H/L-L-L phases, clearly indicating that, when α and μ are held constant, the phase boundary follows a non-monotonic pattern with respect to β. This causes the phase boundary to take a turn around as can be seen in Fig. (3.3d). To illustrate these transitions in detail, we have plotted Fig. (3.7) to display various density profiles while keeping $\alpha = 4$, $\mu = 0.7$, and employing different values of β. The unusual behaviour of the system can be elucidated through the following intuitive explanation. When we fix $\alpha = 4$, initially increasing β results in a raised exit rate for both species of particles from their respective output lane. Consequently, a greater number of particles become available in the pool to be pushed onto the lanes. This leads to an enhancement in the modified entrance rates, i.e., $\alpha^{\pm}_{in_{eff}}$, for the two species of particles. As a result, the positive species starts accumulating on lane P, causing a hindrance to the exit of the negative species. This accumulation gives rise to a shock in lane P for the positive species, which moves towards the left as β continues to increase. During this stage, the system maintains equal entrance-exit rates in lane P for the positive species, but this equilibrium is disrupted as β further increases. Eventually, the shock reaches the left end, causing a phase transition from S-H-H/L-L-L to H-H-H/L-L-L at the critical value of $\beta = 0.1063$. Subsequently, the entrance rate of the positive species onto lane P remains higher than the exit rate from lane P, as confirmed by the theoretical Eq. (3.27). The modified entrance rate $\alpha^{+}_{in_{eff}}$ is a diminishing slope function of β, which eventually reaches the value β^{+}_{in}. At the critical value of $\beta = 0.2764$, the system once again exhibits the S-H-H/L-L-L configuration.

Similarly, the phase diagram depicted in Fig. (3.3e) also illustrates a recurring pattern of transitions. It begins with a movement from the symmetric HD-HD-LD/HD-HD-LD and the asymmetric L-L-L/L-L-L phases, followed by a shift to the symmetric LD-LD-LD/LD-LD-LD phase, and ultimately returning to the HD-HD-LD/HD-HD-LD phase. This progression can be explained as follows:

Consider the case where $\alpha = 1$ and μ tend towards infinity. In situations where resources are abundant, the entrance rate through the input lane remains fixed and is represented by the parameter α, which is smaller than β in this scenario. Consequently, a greater number of particles enter the system than exit, resulting in an accumulation of particles in the input and bridge lane, which leads to the HD-HD-LD/HD-HD-LD phase where the system shows a 1-1-0 density profile for each of the particle species.

However, as the value of β increases, more particles start leaving through the output lanes. This leads to a transition towards the L-L-L/L-L-L phase, and subsequently to the LD-LD-LD/LD-LD-LD phase. In the case of larger values of β, the increased particle exit rate from the output lane causes a low density phase to emerge in this lane. As a result, the other lanes experience a high density phase. If one considers the

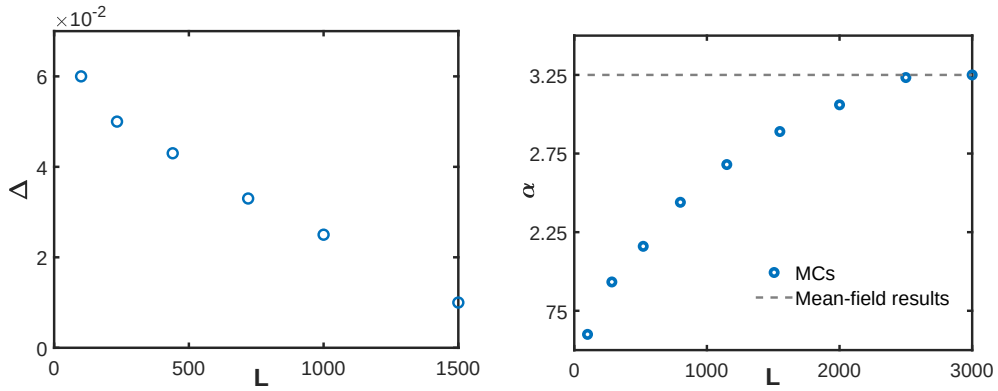

(a) (b)

Figure 3.8: (a) Variation of region width Δ of L-L-L/L-L-L phase with increasing β for fixed $\alpha = 0.4$ and $\mu = 0.45$ obtained through simulations. (b) Variation of phase boundary separating LD-SP-LD/LD-SP-LD region from SP-HD-LD/SP-HD-LD region for $\beta = 0.9$ and $\mu = 0.8$. The MCs results (symbols) approach the boundary obtained through a theoretical framework (dotted line) for larger values of L.

particle density as the order parameter, then these transitions are of first-order.

3.5.4 Finite-size effect

The exploration of the TASEP model incorporating bidirectional dynamics has provided insights into the impact of finite system size on the asymmetric low density phase. In our study, the asymmetric phase, L-L-L/L-L-L, emerges even at extremely small values of the filling factor μ and continues to persist as μ increases. Based on the theoretical investigation revealed by the mean-field framework, it has been observed that this phase remains confined to a curve in the phase plane as shown in Fig. (3.3). However, numerical simulations conducted using the Gillespie Algorithm for $L = 100$ demonstrate that this phase exists over a substantial region, rather than just a curve. Nevertheless, as the lattice length of each lane increases, the region encompassing this asymmetric phase shrinks, suggesting its disappearance in the thermodynamic limit and validating the theoretical findings. To examine this effect caused by finite lane size, we plot the region width Δ with respect to β of the L-L-L/L-L-L region displayed by the system while keeping $\alpha = 0.4$ and $\mu = 0.45$, as illustrated in Fig. (3.8a). As observed from the figure, the width of the L-L-L/L-L-L region decreases as the size of each lane, denoted by L, increases. Therefore, for sufficiently large systems, the observed region contracts, which aligns with our theoretical observations. It is important to mention that the size of the symbols depicted in Fig. (3.3) representing the simulation results have been appropriately chosen to reflect the impact of finite lane length.

The theoretical analysis of our model heavily relies on the assumption of a thermodynamic limit, where the number of sites in each lane (L) tends to infinity.

However, in Monte Carlo simulations, the length of each lane, denoted as L, is a finite value. This finite length effect is also noticeable in the boundary that separates the LD-SP-LD/LD-SP-LD phase from the SP-HD-LD/SP-HD-LD phase, which is identified as the LD-HD-LD/LD-HD-LD phase. It has been observed that as the value of L increases, the boundary predicted by the Monte Carlo simulations approaches the one obtained through theoretical analysis. In other words, we graph the position where this transition occurs for fixed values of $\mu = 0.8$ and $\beta = 0.9$ while increasing L. It is found that the deviation from the theoretically derived phase boundary decreases as L increases and for $L \approx 3000$, this deviation approaches the value obtained analytically (refer Fig. (3.8b)). Beyond this point, no further changes are observed in this position. A similar effect can be witnessed in the phase boundary between LD-SP-LD/LD-SP-LD and HD-HD-LD/HD-HD-LD phase. Thus we have refrained from plotting these phase boundaries through MCs in the phase diagram given by Fig. (3.3).

3.6 Conclusion

In this chapter, we study a particular variant of the exclusion model about roundabouts, consisting of two bridge lanes in the middle with particles travelling in opposite directions. These bridge lanes are intricately linked to a bidirectional TASEP lane on each side. A global constraint on the total number of particles in the system is considered and is characterized by a filling factor. The interactions of the bridge lanes with the side lane induce an inhomogeneity in the system which is dealt with by defining appropriate effective entrance and exit rates. Mean-field approximations are employed to calculate critical stationary characteristics, such as phase diagrams, significant density profiles, and phase transitions, to comprehend the impact of finite resources on the system dynamics. The theoretical findings are validated through dynamic Monte Carlo simulations performed by utilizing the Gillespie Algorithm.

The main goal of our theoretical analysis is to probe the effect of coupling the system to a finite pool on the spontaneous symmetry-breaking phenomenon. With an increase in the particle count, significant qualitative and quantitative changes are observed in the phase diagram. The exact location of the phases, the phase boundaries as well as the density profiles are governed by the entrance and exit rates from the extreme ends in addition to the filling factor. The complexity of the phase diagram is highly sensitive to the filling factor μ which controls the number of resources in the system. Though the phase diagram is comparatively simplified for smaller and larger values of μ, but for intermediate values the complexity is enhanced. This leads to a non-monotonic variation in the number of phases portrayed with increasing μ. Moreover, we found two congested phases where the particles are stuck in a jammed state and no further

movement is possible. The most striking property of the proposed study is the advent of a back-and-forth phase transition which exists even when there is no scarcity of particles available to the lanes. In addition to this, the system attains phases that display boundary-induced shock corresponding to one and bulk-induced shock with respect to the other particle species. To obtain insight into the nature of transitions across the phase boundaries, we have considered the position of shock as the order parameter. We present explicit calculations for phase boundaries and density profiles in both symmetric and asymmetric phases. Furthermore, we offer straightforward physical explanations to elucidate the theoretical observations.

3.7 Appendix: Symmetric phases

1. **LD-LD-LD/LD-LD-LD phase.** In this phase, both the particle species display a low density phase in all the lanes. Each lane is entry-dominated and the corresponding particle density is equal to the effective entrance rates of the respective lanes. So, the bulk and the boundary densities of each lane is given by

$$\begin{aligned} \rho_{in}^{1} &= \alpha_{in_{eff}}, & \rho_{in} &= \alpha_{in_{eff}}, & \rho_{in}^{+,L} &= J_{in}/\beta_{in}, \\ \rho_{B}^{+,1} &= \alpha_{B}, & \rho_{B} &= \alpha_{B}, & \rho_{B}^{+,L} &= J_{B}/\beta_{B}, \\ \rho_{out}^{+,1} &= \alpha_{out_{eff}}, & \rho_{out} &= \alpha_{out_{eff}}, & \rho_{out}^{L} &= J_{out}/\beta. \end{aligned}$$

The bulk currents in each lane is given by

$$J_{in} = \alpha_{in_{eff}}(1-\alpha_{in_{eff}}), \quad J_B = \alpha_B(1-\alpha_B), \quad J_{out} = \alpha_{out_{eff}}(1-\alpha_{out_{eff}}).$$

Necessary conditions for the existence of this phase are given by

$$\alpha_{in_{eff}} < \min\{\beta_{in}, 0.5\}, \quad \alpha_B < \min\{\beta_B, 0.5\}, \quad \alpha_{out_{eff}} < \min\{\beta, 0.5\}.$$

Inserting the boundary as well as bulk densities stated above in Eqs. (3.8), (3.10) and (3.16) to obtain

$$\begin{aligned} \alpha_{in_{eff}} = \alpha_{out_{eff}} = \frac{\alpha^{eff}\beta}{\alpha^{eff}+\beta}, \quad \beta_{in} = 1-\alpha_B, \\ \alpha_B = \alpha_{in_{eff}}, \qquad \beta_B = 1-\alpha_{out_{eff}}-\alpha_{in_{eff}}. \end{aligned}$$

All these above-attained expressions for the effective entrance and exit rates when plugged in Eq. (3.20) yields

$$\mu = r + \frac{6}{4}\alpha_{in_{eff}},$$

which provides us with the pool capacity as

$$r = \frac{1}{4\alpha}\left(2\mu(\alpha-\beta) - 3\alpha\beta + \sqrt{16\alpha\beta\mu^2 + \big(2\mu(\alpha-\beta) - 3\alpha\beta\big)^2}\right).$$

Under these circumstances, the existential condition for this phase is

$$\alpha_{in_{eff}} < \beta_B. \tag{3.24}$$

2. **HD-HD-LD/HD-HD-LD phase.** We assume that in this symmetric phase both the particle species manifest high density phase in their input as well as bridge lanes while the output lane displays LD phase. The specifications that support the extant of this asymmetric phase are

$$\rho_{in} = 1 - \beta_{in}, \quad \rho_B = 1 - \beta_B, \quad \rho_{out} = \alpha_{out_{eff}}.$$

One solves Eqs. (3.8) and (3.16) to get

$$\beta_B = \beta_{in} = 1 - \alpha_B, \quad \alpha_{out_{eff}} = 0.$$

Physically it implies that the density of positive species in lane Q given by $\alpha_{out_{eff}}$ is 0. This means that there is no particle movement from the bridge onto lane Q, suggesting that $\beta_{in} = \beta_B = 0$. Thus, we have that, the particle density in the input as well as the bridge is 1 while in the output lane, it is 0. As particle movement is not possible in this scenario, this phase can also be referred to as a congested phase.

Utilizing the particle number conservation given by Eq. (3.20), we have $r = \mu - 1$. So, it is evident that the HD-HD-LD/HD-HD-LD phase persists only when $\mu > 1$ and continues to exist as $\mu \to \infty$. As the particle density is independent of the boundary-controlling parameters, the phase boundaries for this region can only be calculated numerically.

3. **LD-SP-LD/LD-SP-LD phase.** The particle density, in this case, displays a constant density of $\alpha_{in_{eff}}$ in the input lanes, a shock in the bridge lanes where a constant density of α_B is connected to density $1 - \beta_B$ on the right and again low density phase in the output lanes with density $\alpha_{out_{eff}}$. In this case, one can compute the relation between the rates as

$$\alpha_B = \alpha_{in_{eff}}, \quad \alpha_{out} = 1 - \beta_B, \quad \beta_{in} = 1 - \alpha_B, \quad \beta_B = 1 - \alpha_{out_{eff}} - \alpha_B.$$

Utilizing the above equations to solve Eqs. (3.14) and (3.15) gives

$$\alpha_{in_{eff}} = \frac{\alpha^{eff}(4\beta-1)}{\alpha^{eff}+4\beta}, \quad \alpha_{out_{eff}} = \frac{\alpha^{eff}+2\beta(1-\alpha^{eff})}{\alpha^{eff}+4\beta}.$$

Since the existence of the shock phase in the bridge lane requires $\alpha_B = \beta_B$, we obtain the capacity of the pool as

$$r = \frac{\beta\mu}{\alpha(3\beta-1)}.$$

To calculate the position of the shock x_w, one needs to solve the Eq. (3.20), which gives

$$x_w = \frac{6\beta\mu - 2\alpha(3\beta-1)(3\mu-2)}{\alpha(3\beta-1)}. \tag{3.25}$$

Thus, one can write the existential condition for this phase as $0 < x_w < 1$.

4. **SP-HD-LD/SP-HD-LD phase.** In this case, Eqs. (3.10), (3.8) and (3.16) reduces to

$$\alpha_B = 1-\beta_{in}, \quad \beta_B = 1-\alpha_{out_{eff}}-\alpha_B, \quad \alpha_{out} = 1-\beta_B, \quad \beta_{in} = \frac{\beta_B(1-\beta_B)}{\alpha_B},$$

along with the modified entrance rates given by

$$\alpha_{in_{eff}} = \frac{\alpha_{in_{eff}}(1-\alpha_{in_{eff}})}{\frac{\alpha_{in_{eff}}(1-\alpha_{in_{eff}})}{\alpha^{eff}} + \frac{\alpha_{out_{eff}}(1-\alpha_{out_{eff}})}{\beta}}, \quad \alpha_{out_{eff}} = \frac{\alpha_{out_{eff}}(1-\alpha_{out_{eff}})}{\frac{\alpha_{out_{eff}}(1-\alpha_{out_{eff}})}{\alpha_{out}} + \frac{\beta_{in}(1-\beta_{in})}{\beta_{in}}}.$$

From the above equations, we can deduce that $\beta_{in} = \beta_B$ which further implies that $\alpha_{out_{eff}} = 0$. This indicates that the entrance of particles to the output lane is restrained, forcing the exit rate β_B from the bridge lane to take the value 0. As, $\beta_{in} = \beta_B = \alpha_{out_{eff}} = 0$, there are no positive particles in the output lane while the bridge lane is fully packed with particle density 1. Now, the input lanes display a shock phase where a density profile connects a region of low density to high density region with particle density changing from $\alpha_{in_{eff}}$ to $1-\beta_{in}$. The existence of this phase requires $\alpha_{in_{eff}}$ to remain equal to β_{in}, which implies that $\alpha_{in_{eff}} = 0$. Last, one can obtain the existential criteria for this phase numerically. As particle movement is not possible in this scenario, this phase is also referred to as a congested phase.

3.8 Appendix: Asymmetric phases

1. **L-L-L/L-L-L phase.** During the L-L-L/L-L-L phase, all lanes experience a low density phase, but the current and bulk density differ between the two types of particles. Upon calculating the effective rates for each lane, they are found to satisfy a simple relation expressed as

$$\alpha^{+}_{in_{eff}} = \alpha^{+}_{B} = \alpha^{+}_{out_{eff}} = 1 - \beta^{+}_{in} = 1 - \beta^{+}_{B} + \alpha^{-}_{in_{eff}},$$

along with $\alpha^{-}_{in_{eff}} = \alpha^{-}_{B} = \alpha^{-}_{out_{eff}} = 1 - \beta^{-}_{in} = 1 - \beta^{-}_{B} + \alpha^{+}_{in_{eff}}$. Here, α^{+}_{ineff} and $\alpha^{-}_{in_{eff}}$ are obtained by solving Eqs. (3.14) and (3.15) as

$$\begin{aligned}\alpha^{\pm}_{in_{eff}} =& \frac{1}{2(\alpha^{eff}-\beta)^2(\alpha^{eff}+\beta)}\Big(\beta^3 + \alpha^{eff}(\beta-1)\big(\beta^2 - (\alpha^{eff})^2\big) - (\alpha^{eff})^2\beta \\ & \mp \{(\alpha^{eff}-\beta)^2\big(\beta^4 + 2(\alpha^{eff})^3(1-\beta)\beta^2 - 2\alpha^{eff}\beta^4\big) \\ & + (\alpha^{eff})^4(1-2\beta-3\beta^2 + (\alpha^{eff})^2\beta^2(\beta^2+2\beta-2))\}\Big)\end{aligned} \tag{3.26}$$

The above expressions are used to determine the pool capacity as

$$r = \frac{1}{8\alpha}\Big(4\mu(\alpha+\beta) + 3\alpha(\beta-1) + \sqrt{16\alpha\beta(3-4\mu)\mu + \big(4\beta\mu + \alpha(4\mu+3\beta-3)\big)^2}\Big).$$

Thus, the constrained on the parameters to attain this phase is

$$\alpha^{-}_{out_{eff}} < \beta.$$

2. **H-H-H/L-L-L phase.** In this phase, the positive species portray the HD phase while the negative species display the entrance dominant phase in all the lanes. In such a scenario, the bulk currents are given by

$$\begin{aligned} &J^{+}_{in} = \beta^{+}_{in}(1-\beta^{+}_{in}), && J^{+}_{B} = \beta^{+}_{B}(1-\beta^{+}_{B}), && J^{+}_{out} = \beta(1-\beta), \\ &J^{-}_{in} = \alpha^{-}_{in_{eff}}(1-\alpha^{-}_{in_{eff}}), && J^{-}_{B} = \alpha^{-}_{B}(1-\alpha^{-}_{B}), && J^{-}_{out} = \alpha^{-}_{out_{eff}}(1-\alpha^{-}_{out_{eff}}) \end{aligned}$$

which assists us in writing the boundary densities for each lane. Again one can solve Eqs. (3.8), (3.10), and (3.16) along with Eqs. (3.14) and (3.15) to obtain the values of the effective entrance and exit rates for the positive species as

$$\begin{aligned} &\beta^{+}_{B} = 1 - \alpha^{+}_{out} = 1 - \alpha^{+}_{B} = \beta^{+}_{in} = \beta, \quad \alpha^{+}_{out_{eff}} = \frac{\beta(1-\beta)}{\beta + \alpha^{-}_{in_{eff}}}, \\ &\alpha^{+}_{in_{eff}} = \frac{\beta(1-\beta)}{\frac{\mu\beta(1-\beta)}{\alpha r} + \frac{\alpha^{-}_{out_{eff}}(1-\alpha^{-}_{out_{eff}})}{\beta}}, \end{aligned} \tag{3.27}$$

while for the negative species,

$$\begin{aligned} &\alpha^{-}_{B} = 1 - \beta^{-}_{in} = \alpha^{-}_{in_{eff}}, \quad \beta^{-}_{B} = \beta - \alpha^{-}_{out_{eff}}. \\ &\alpha^{-}_{in_{eff}} = \frac{1}{2}\left(\big(1+\alpha^{eff}\big) - \sqrt{\big(1+\alpha^{eff}\big)^2 - 4\alpha^{eff}\beta}\right), \end{aligned}$$

$$\alpha^{-}_{out} = \frac{\alpha^{-}_{in_{eff}}(1-\alpha^{-}_{in_{eff}})}{\beta - \alpha^{-}_{in_{eff}}},$$
$$\alpha^{-}_{out_{eff}} = \frac{1}{2}\left((1+\alpha^{-}_{out}) - \sqrt{(1+\alpha^{-}_{out})^2 - 4\alpha^{-}_{out}\beta}\right),$$

Here, the equation for the pool dynamics given by Eq. (3.20) gets converted to

$$\mu = r + \frac{\left(3(1-\beta) + 2\alpha^{-}_{in_{eff}} + \alpha^{-}_{out_{eff}}\right)}{4},$$

which gives the value of the pool capacity as

$$r = \frac{1}{8(3\alpha+4\mu)}\Big(3\alpha(4\mu-3) + 4\mu(6\beta+8\mu-9) + 3\sqrt{\alpha^2(3-4\mu)^2 + 16\mu^2 - 8\alpha\mu(3+6\beta^2-4\mu+4\beta(2\mu-3))}\Big).$$

Thus, one can identify the relevant region for this phase as

$$\alpha^{-}_{in_{eff}} + \alpha^{-}_{out_{eff}} \leq \beta \leq \alpha^{+}_{in_{eff}}. \tag{3.28}$$

3. **L-L-S/L-L-L phase.** During this phase, we make an assumption that the (+) particles are in a low density (LD) phase in lanes P and the bridge, while lane Q exhibits a discontinuity in the density profile, connecting a region of low density to high density. However, the (−) particles represent a low density phase in all the lanes. This phase persists when the boundary-controlling parameters satisfy the following conditions:

$$\begin{aligned} &\alpha^{+}_{in_{eff}} < \min\{\beta^{+}_{in}, 0.5\}, \quad && \alpha^{-}_{in_{eff}} < \min\{\beta^{-}_{in}, 0.5\}, \\ &\alpha^{+}_{B} < \min\{\beta^{+}_{B}, 0.5\}, && \alpha^{-}_{B} < \min\{\beta^{-}_{B}, 0.5\}, \\ &\alpha^{+}_{out_{eff}} = \beta < 0.5, && \alpha^{-}_{out_{eff}} < \min\{\beta, 0.5\}. \end{aligned} \tag{3.29}$$

The effective boundary rates as retrieved from Eqs. (3.8), (3.10) and (3.16) is $\alpha^{+}_{in_{eff}} = \alpha^{+}_{B}$, $\alpha^{-}_{in_{eff}} = \alpha^{-}_{B}$, and

$$\alpha^{+}_{out} = \frac{\alpha^{+}_{in_{eff}}(1-\alpha^{+}_{in_{eff}})}{\beta^{+}_{B}}, \quad \alpha^{-}_{out} = \frac{\alpha^{-}_{in_{eff}}(1-\alpha^{-}_{in_{eff}})}{\beta^{-}_{B}},$$

along with $\beta^{+}_{B} = 1 - \alpha^{-}_{in_{eff}} - \alpha^{+}_{out_{eff}}$, $\beta^{-}_{B} = 1 - \alpha^{+}_{in_{eff}} - \alpha^{-}_{out_{eff}}$.

These values can now be substituted in Eqs. (3.14) and (3.15) to get

$$\alpha^{-}_{in_{eff}} = \frac{(1+\alpha^{eff}) - \sqrt{(1+\alpha^{eff})^2 - 4\alpha^{eff}\beta}}{2},$$

$$\alpha^{+}_{in_{eff}} = \frac{1}{2\beta}\left(\beta(1+\alpha^{eff}) - \sqrt{\beta^2(1-\alpha^{eff})^2 + 4\alpha^{-}_{in_{eff}}\alpha^{eff}\beta(1-\alpha^{-}_{in_{eff}})}\right).$$

Since the flow of particles is continuous throughout the system, we have $\alpha^{+}_{in_{eff}} = \alpha^{+}_{B} = \alpha^{+}_{out_{eff}}$ and $\alpha^{-}_{in_{eff}} = \alpha^{-}_{B} = \alpha^{-}_{out_{eff}}$. To acquire the value of pool capacity, one can solve the condition that $\alpha^{+}_{out_{eff}} = \beta$ which is the requirement for lane Q to remain in the S phase for the positive species.

Now, the only variable that is left to be calculated is x_w, the position of shock. Note that

$$\int_0^1 \rho^{+}_{out}dx = \int_0^{x_w} \alpha^{+}_{out_{eff}}dx + \int_{x_w}^1 (1-\beta)dx,$$

and finally one can revisit Eq. (3.20) to obtain the value of the shock position as

$$x_w = \frac{4(\mu - r) - 3\alpha^{-}_{in_{eff}} - 2\alpha^{+}_{in_{eff}} - 1 + \beta}{2\beta - 1}. \tag{3.30}$$

Thus, one needs to identify the region where Eq. (3.29) as well as the condition $0 < x_w < 1$ is obeyed. As $x_w \to 1$, we reach the L-L-L/L-L-L phase whereas when x_w takes the value 0, the shock position shifts towards the left end of lane Q and the system exhibits the L-L-H/L-L-L phase. In the limiting case of $\mu \to \infty$, this phase does not exist.

4. **L-L-H/L-L-L phase.** The sole distinction between this phase and the L-L-S/L-L-L phase lies in the location of the shock within lane Q for the positive species. In the previous scenario, the shock had to be positioned away from the boundaries, whereas in this case, the value of x_w needs to be precisely 0 to achieve the L-L-H/L-L-L phase. It is important to note that the L-L-H/L-L-L phase does not exist in the limit where μ approaches infinity. Furthermore, this phase serves as a boundary that separates the region of L-L-S/L-L-L from the region of L-S-H/L-L-L.

5. **L-S-H/L-L-L phase.** Once again, we follow a similar procedure as we did for the previous phases. The continuous flow of particles within the system implies that $\alpha^{+}_{in_{eff}} = \alpha^{+}_{B}$, $\beta^{+}_{B} = \beta$, and $\alpha^{-}_{in_{eff}} = \alpha^{-}_{B} = \alpha^{-}_{out_{eff}}$. To determine the values of these modified entrance rates, we utilize Eqs. (3.14) and (3.15), resulting in:

$$\alpha^{-}_{in_{eff}} = \frac{1}{2}\left((1+\alpha^{eff}) - \sqrt{(1+\alpha^{eff})^2 - 4\alpha^{eff}\beta}\right),$$
$$\alpha^{+}_{in_{eff}} = \frac{1}{2\beta}\left(\beta(1+\alpha^{eff}) - \sqrt{\beta^2(1-\alpha^{eff})^2 + 4\alpha^{-}_{in_{eff}}\alpha^{eff}\beta(1-\alpha^{-}_{in_{eff}})}\right).$$

By solving $\alpha^{+}_{B} = \beta_B$, the necessary condition for the existence of S phase in the bridge lane, we can determine the pool capacity. Furthermore, the position of the

shock can be obtained using Eq. (3.20) as

$$x_w = \frac{4(\mu - r) - 2(1 - \beta) - 3\alpha^-_{in_{eff}} - \alpha^+_{in_{eff}}}{\alpha^+_{in_{eff}} + \beta - 1}.$$

When the value of x_w approaches 1, the system manifests the L-L-H/L-L-L phase. Conversely, as x_w tends to 0, L-H-H/L-L-L is attained. Additionally, this phase disappears as μ approaches infinity.

6. **S-H-H/L-L-L phase.**The continuous flow of particles leads to significant implications, particularly regarding the bulk densities of lane P, bridge, and Q. Specifically, the bulk density corresponding to the negative species is given by $\alpha^-_{in_{eff}}$, which remains consistent across all the three lanes. Similarly, for the positive species, we can establish the requirement that $\beta^+_{in} = \beta^+_B = \beta$ to maintain a continuous flow. By utilizing these conditions in Eqs. (3.14) and (3.15) we obtain the following expressions

$$\alpha^-_{in_{eff}} = \frac{1}{2}\left(\left(1 + \alpha^{eff}\right) - \sqrt{\left(1 + \alpha^{eff}\right)^2 - 4\alpha^{eff}\beta}\right),$$
$$\alpha^+_{in_{eff}} = \frac{1}{2\beta}\left(\beta(1 + \alpha^{eff}) - \sqrt{\beta^2(1 - \alpha^{eff})^2 + 4\alpha^-_{in_{eff}}\alpha^{eff}\beta(1 - \alpha^-_{in_{eff}})}\right).$$

To acquire the capacity of the pool, one can solve $\alpha^+_{in_{eff}} = \beta$. Additionally, the position of the shock can be calculated from Eq. (3.20) as

$$x_w = \frac{4(\mu - r) - 3(\alpha^-_{in_{eff}} + 1 - \beta)}{2\beta - 1}. \tag{3.31}$$

The region of existence for this phase can be expressed in a similar manner as demonstrated for other cases.

7. **L-H-H/L-L-L phase.** Here, the positive species display the LD phase in lane P while the other two lanes are in high density phase whereas the negative species of all the lanes are in entrance dominated phase. Similar to the previous scenario, we can derive the following expressions

$$\alpha^-_{in_{eff}} = \frac{1}{2}\left(1 + \alpha^{eff} + \sqrt{(1 + \alpha^{eff})^2 - 4\alpha^{eff}\beta}\right),$$
$$\alpha^-_{out_{eff}} = \alpha^-_{in_{eff}} = \alpha^-_B,$$
$$\alpha^+_{in_{eff}} = \frac{1}{2\beta}\left(\beta(1 + \alpha^{eff}) - \sqrt{\beta^2(1 - \alpha^{eff})^2 + 4\alpha^-_{in_{eff}}\alpha^{eff}\beta(1 - \alpha^-_{in_{eff}})}\right).$$

The existence of this phase is determined by the position of x_w in S-H-H/L-L-L reaching the right boundary of lane P, specifically when $x_w = 1$. This condition

defines the curve that represents the existence of this phase.

8. **H-H-H/L-S-L phase.** During this phase, the positive species display exit dominated phase in the input, bridge, and output lane, whereas the other species of particles are in entrance dominated phase in the input and output lane, with the bridge lane exhibiting a shock phase. The modified and effective entry-exit rates for the different lanes can be derived similarly to the previous phase which provides us with

$$\alpha^{-}_{in_{eff}} = \frac{1}{2}\left(1+\alpha^{eff}+\sqrt{(1+\alpha^{eff})^2-4\alpha^{eff}\beta}\right), \quad \alpha^{-}_{out_{eff}} = \frac{\beta}{2},$$
$$\alpha^{+}_{out_{eff}} = \frac{\beta(1-\beta)}{\beta+\alpha^{-}_{in_{eff}}}, \quad \alpha^{+}_{in_{eff}} = \frac{8\alpha^2(1-\beta)}{(4(1-\beta)-\alpha^2)(2-\beta)}, \quad \beta^{-}_{B} = \beta-\alpha^{-}_{out_{eff}},$$

along with the conditions $\beta^{+}_{in} = \beta^{+}_{B} = \beta$ and $\alpha^{-}_{in_{eff}} = \alpha^{-}_{B}$. The condition for the existence of the shock phase in the bridge lane corresponding to the negative species, $\alpha^{-}_{B} = \beta^{-}_{B}$, is utilized to determine the pool capacity and is given by

$$r = \frac{\mu(2-\beta)}{2\alpha}. \tag{3.32}$$

The position of the shock can be determined from Eq. (3.20) as

$$x_w = \frac{8(\mu-r-1)+5\beta}{2(\beta-1)}. \tag{3.33}$$

Thus, the necessary condition for the existence of this phase can be written as

$$0 < x_w < 1, \quad \beta < \min\{\alpha^{+}_{out_{eff}}, \alpha^{-}_{in_{eff}}\}.$$

This phase no longer exists in the limiting case of μ tends to infinity.

9. **H-H-H/L-H-L phase.** The main distinction between this phase and the H-H-H/L-S-L phase is the specific location of the shock within the bridge lane for the negative species. Unlike the previous scenario where the shock needed to be positioned away from the boundaries; the value of x_w in the H-H-H/L-S-L must be precisely 0 for the system to achieve the H-H-H/L-H-L phase. As μ tends towards infinity, the H-H-H/L-H-L phase becomes nonexistent.

10. **S-H-H/L-S-L phase.** The same analytical approach can be employed for this phase as in the other cases. However, due to the limited number of equations available, it is not possible to calculate the exact location of the shock or derive an explicit formulation for the phase boundaries.

11. **S-H-H/L-H-L phase.** In this phase, the effective entrance and exit rates can be

obtained analogously as done for the S-H-H/L-L-L phase. These expressions can further be utilized to calculate the position of the shock as well as the pool capacity.

3.8.1 Discarded phases

- The total particle density of the bidirectional lanes cannot be greater than one i.e., $\rho_{in}^{+}+\rho_{out}^{-} \not> 1$ and $\rho_{out}^{+}+\rho_{in}^{-} \not> 1$. So, all the phases of the form $X_1-X_2-X_3/Y_1-Y_2-Y_3$ where $X_1, Y_3 \in$ {H/HD, S/SP, M/MC} cannot persists.
- If $X_1 \in$ {LD/L, HD/H}, then $X_2 \neq$ MC/M.
- If $X_1 =$ MC/M, then $X_2 \notin$ {LD/L, HD/H, MC/M}.
- The remaining phases pose a challenge when attempting to evaluate Eqs. (3.8), (3.10), (3.16), as well as Eqs. (3.14) and (3.15), as their simultaneous resolution leads to a state of self-inconsistency.

Chapter 4

Reservoir crowding in a dynamic disordered bidirectional system with narrow entrances

In the previous chapters, we have examined a version of the exclusion process involving two-particle species moving on a one-dimensional lane. In the current chapter[1], we will discuss a bidirectional model where particles travel in opposite directions on different lanes and their movement is influenced by impurities, both of which are limited in the system. Specifically, the particle reservoir features reservoir crowding, which affects the entry-exit rates of particles. The movement of the particles is obstructed by the presence of defects that stochastically bind/unbind from each site.

4.1 Motivation and background

We have already examined the narrow entrances feature observed in diverse transportation phenomena in Section (1.5.3). Aside from extending the classic exclusion model to multi-channel transport, the dynamics of lanes in certain scenarios depend on competing for a pool of limited resources. These models have demonstrated broad relevance in a variety of physical and biological systems, including protein synthesis, motor protein movement, parking garage difficulties, and traffic [64–67]. Such dynamics observed in diverse real-world phenomena have been incorporated in various single as well as multi-lane systems [64,66,102,105,132,135,136]. In these variants, the entrance rate of particles is regulated by the occupancy of the reservoir, resulting in the addition of localized shock region in the phase plane, which is in contrast to the situation when infinite resources are available. However, it is reasonable to expect that a crowded reservoir not only increases the entrance rate of particles but may also hinder their escape rate from the lanes. For instance, in the 'parking garage problem', a crowded garage can slow down the exit rate of vehicles from the road into the garage. Few recent studies have examined a variant of TASEP known as 'reservoir crowding', which

[1]The content of this chapter is published in "Ankita Gupta, Arvind Kumar Gupta. Reservoir crowding in a dynamically disordered bidirectional system with narrow entrances. *Chaos, Solitons & Fractals,* 178:114318, 2024."

incorporates the impact of reservoir occupancy on exit as well as the entry rates [58,69,70]. This variant effectively replicates situations similar to those observed in real-world scenarios.

Considering the characteristics of the disorder discussed in Section (1.5.5), several studies have focused on incorporating different type of defects such as slower hopping rate [6,72,98,106,137–144], binding/unbinding of defect from single site [70,103,145–147] and extended objects [148] along with features such as Langmuir kinetics [149–152]. Recent investigation has been conducted on a scenario in which defects can adhere to and detach from each site [153,154]. In this direction, many studies have sought to incorporate diverse features such as finite resources [155], coupling between two-lanes [156,157] and Langmuir kinetics [149] to mimic different real-life situations. However, in our opinion, the role of dynamic disorder which stochastically binds and unbinds has not been explored much in a multi-channel framework.

In the majority of the literature, these impurities are considered to be abundant in nature, which is a bit far from reality. Inspired by the diverse applications of the dynamics described above in various physical and biological systems, we investigate a two-lane TASEP system with narrow entrances that incorporate the binding and unbinding of a defect on each site. Our purpose is to investigate the impact of global constraints on the resource availability of both the particles and the defects. The entry exit of the particle to the lanes features the reservoir crowding phenomenon, while for the defect only the entry rate is affected. Our aim is to explore the impact and interplay between two different dynamics involved in the system. We would like to inspect, how the addition of dynamic defects alters the overall dynamics of the system, in particular the stationary particle currents. The primary goal is to scrutinize whether the basic mean-field theory is capable of capturing the steady-state properties of a system with reservoir crowding. Subsequently, we intend to scrutinize the impact of constrained resource availability on intricate dynamic processes, assessing both qualitative and quantitative aspects, with a specific focus on the emergence of spontaneous symmetry-breaking (SSB) phenomena.

4.2 Stochastic model with dynamic defects

To study the impact of defects and bidirectional mobility aided by motors in a limited environment, this section intends to extend the two-lane transport system with narrow entrances described in Refs. [60,102]. These models have been previously utilized to describe the motion of single as well as multiple motor systems in various realistic physical and biological systems. The present model mimics the movement of particles travelling in opposite directions along two one-dimensional lanes with dynamic

defects. In particular, we consider two parallel open lanes, denoted as lane A and lane B, each comprising exactly L sites labelled as $i = 1, 2, \ldots, L$. The sites 1, L of each lane are known as the boundary sites while the rest are referred to as the bulk. In the illustrated system shown in Fig. (4.1), particles (depicted by circles) exhibit unidirectional horizontal movement, travelling from left to right in lane A and from right to left in lane B. The system adheres to the general TASEP paradigm, wherein each site within the lanes can accommodate only one particle at most due to the exclusion principle.

To introduce dynamic disorder into the system, we introduce another species known as defects, visually represented by squares in Fig. (4.1). These defects are constrained to move only vertically on each site. As a result, they can hinder the movement of particles along the horizontal direction, causing disruptions and reducing the overall flow of particles through the lanes. To restrict the presence of particles and defects within the system, we implement a global constraint on their quantities. This constraint is implemented through the introduction of reservoirs labelled as R_p and R_d, designated to contain particles and defects, respectively. We assume the reservoir R_p/R_d has sufficient capacity to accommodate all the particles/defects in the system. In Fig. (4.1), we present a schematic representation of a bidirectional system with dynamic disorder in a constraint environment. The diagram showcases two-lanes with narrow entrances and includes the transition rates for all possible scenarios within the system.

To characterize the micro-state of the system, we defined two sets of Bernoulli numbers: one for the particle denoted by $\tau = \tau_j^i$ and another for the defects denoted by $\nu = \nu_j^i$ at the ith site on the jth lane where $i \in \{1, 2, \ldots, L\}$ and $j \in \{\text{A, B}\}$. Each of these variables can take on values of either '0' or '1', with 1 indicating the presence of a particle or defect and 0 indicating the absence of a particle or defect. At each time step, a lane site is chosen stochastically and updated according to its dynamical rules. The sub-processes that govern the movement of particles and defects on each site are as follows:

- **Bulk Dynamics**.

1. *Particle dynamics.* At sites $i = 2, \ldots, L-1$, the movement of particles in lane A is governed by the conditions $\tau_A^i = 1$ and $\tau_A^{i+1} = 0$. In other words, a particle situated at the ith site in lane A can move to the adjacent site $(i+1)$ with a rate of p_i if the latter site is unoccupied. The value of p_i depends on the presence or absence of a defect at the latter site and is defined as follows

$$p_i = \begin{cases} 1, & \text{if } \nu_A^{i+1} = 0, \\ p_d, & \text{if } \nu_A^{i+1} = 1. \end{cases} \tag{4.1}$$

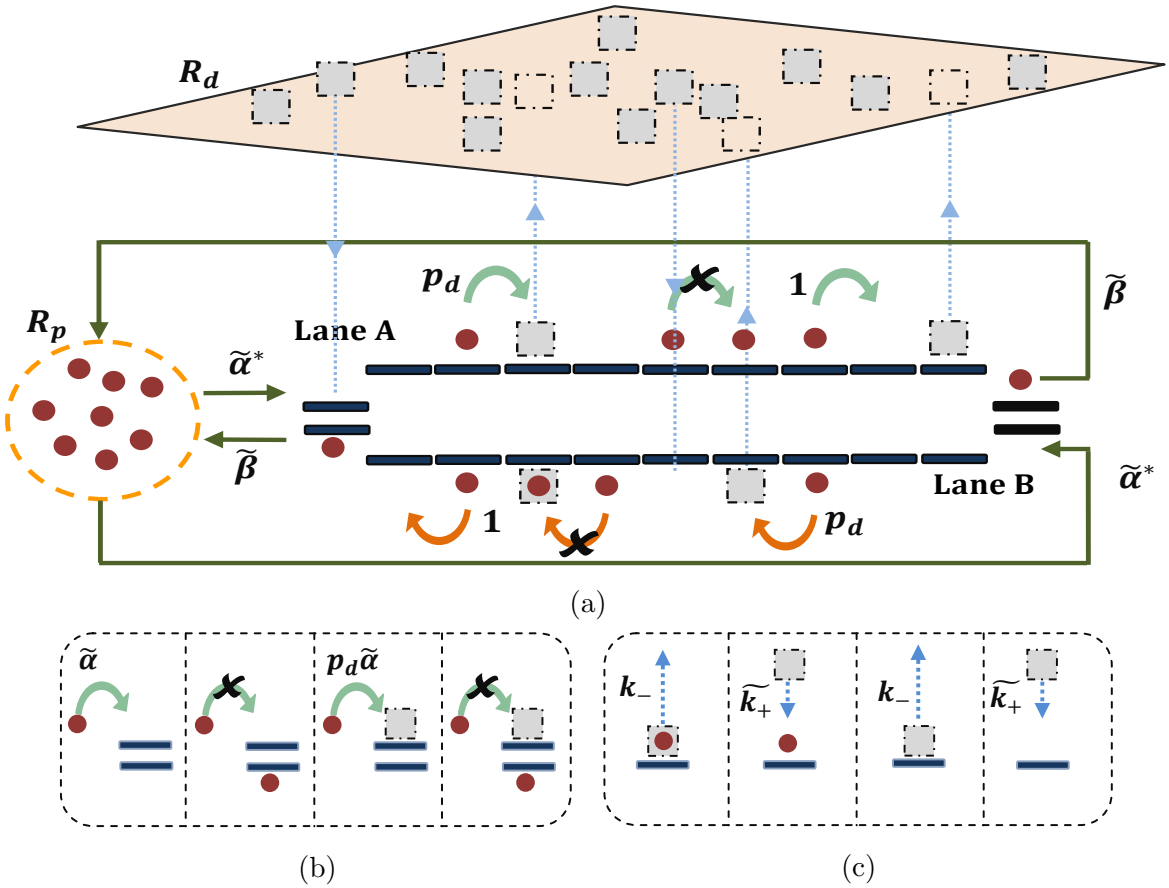

Figure 4.1: (a) A schematic of the two-lane TASEP with narrow entrances and dynamic defects competing for finite resources is shown. Particles (Defects) are depicted by circles (squares). Arrows represent allowed transitions, while crosses indicate prohibited ones. The effective injection and removal rates of the particles are denoted as $\widetilde{\alpha}^*$, and $\widetilde{\beta}$ respectively. (b) Narrow entrance implementation: For a particle to enter a lane, both the target site and the exit site of the other lane must be empty, and particle interactions are limited to the boundaries. (c) Dynamic behaviour of defects: Binding occurs with rate $\widetilde{k_+}$, while unbinding happens with the constant rate k_-.

Here, p_d, $(0 \leq p_d \leq 1)$, represents the slow forward moving rate of a particle when a defect is present at the target site. Lane B exhibits similar dynamics, albeit in the opposite direction.

2. *Defect dynamics.* The lanes facilitate the binding and unbinding of a defect on each site following the defect-defect exclusion principle, with rates $\widetilde{k_+}$ and k_-, respectively. The presence of a particle at the target site does not affect the binding process. Additionally, it is important to note that defects do not undergo horizontal movement along the lanes. Thus, their motion is solely restricted to vertical transitions between sites and the reservoir R_d. The conservation of the number of defects in the closed environment impacts the effective binding rate $\widetilde{k_+}$, which is dynamically influenced by the occupancy of the reservoir R_d. By denoting

the total number of defects in the system as N_d and the instantaneous number of particles in the reservoir by $N_{r_d}(t)$, we can express this binding rate as follows:

$$\widetilde{k_+} = k_+ f(N_{r_d}(t)). \tag{4.2}$$

Here, k_+ is the intrinsic binding rate in the presence of an infinite number of defects. This function f must be an increasing function of N_{r_d} whose details will be discussed at the end of this section. Moreover, in this study, we have set $k_+, k_- \gtrsim 1$, as simple mean-field approximation has been reported to work effectively, in this case [153].

- **Boundary Dynamics**: Here, we explore the impact of constrained entrances and limited availability of resources on the transition rates of particles at the sites $i = 1$ and $i = L$. The defects adhere to the same dynamical rules on the boundary sites as they do in the bulk.

  1. *Constraint entrances.* Particles can enter lane A through site $i = 1$ with an effective rate $\widetilde{\alpha}^*$ if both the target site and the exit site $i = L$ on lane B are unoccupied. This effective entrance rate depends on the status of the defect at the first site and is defined as follows:

$$\widetilde{\alpha}^* = \begin{cases} \widetilde{\alpha}, & \text{if } \nu_A^1 = 0, \\ \widetilde{\alpha} p_d, & \text{if } \nu_A^1 = 1. \end{cases} \tag{4.3}$$

  Similarly, the effective entrance rate $\widetilde{\alpha}^*$ for a particle to enter lane B from the site $i = L$ relies on the vacancy of the exit site in lane A and is influenced by the presence or absence of defects at the target site. The hopping criteria for a particle from the entrance site to the neighbouring site is the same as that in the bulk.

  2. *Reservoir Crowding.* The entry and exit rates of the particles through the sites $i = 1$ and $i = L$ of each lane are parameterized by $\widetilde{\alpha}$ and $\widetilde{\beta}$, each of which can take any positive values. These rates are dynamically controlled by the reservoir R_p and can be written as

$$\widetilde{\alpha} = \alpha g(N_{r_p}(t)), \quad \widetilde{\beta} = \beta h(N_{r_p}(t)), \tag{4.4}$$

  where $N_{r_p}(t)$ is the occupation of the reservoir R_p at any instance of time t.

The rate functions $g(N_{r_p}(t))$ and $h(N_{r_p}(t))$ regulate the inflow and outflow of particles onto the lanes, respectively. In a general setting, when there are more particles in the reservoir, not only does it increase the influx of particles into the lanes, but it

also hinders the out-flux of particles from the lanes back to the reservoir. Conversely, when the reservoir holds fewer particles, the opposite effect occurs, allowing for easier outflow of particles from the lanes to the reservoir. Thus, the function g and h must be assumed to be monotonically increasing and decreasing functions of the N_{r_p}. Due to the monotonic nature and positive definiteness of their dependencies on N_{r_p}, the coupling between g and h should be designed in such a way that an increase in one leads to a decrease in the other. So, we defined these as $g(N_{r_p}(t)) = N_{r_p}(t)/N_p$ and $h(N_{r_p}(t)) = 1 - N_{r_p}(t)/N_p$ [69] where N_p refers to the total number of particles in the system. Similarly, the rate function $f(N_{r_d}(t))$ can be taken as $f(N_{r_d}(t)) = N_{r_d}(t)/N_d$ which regulates the binding of the defect onto the lanes. While there are infinite possible ways to choose these functions, the selection is made based on analytical amenability. In other scenarios, although the quantitative behaviour may vary, the qualitative nature of the system remains consistent.

We have now completely defined the model and our objective is to investigate the impact of a global constraint on both the number of particles and defects in the system. To delve deeper into the dynamics of this constrained system, we introduce parameters known as filling factors, defined as $\mu_k = \frac{N_k}{2L}$, $k = p, d$. These ratios define the population of particles and defects of the whole model (lane and reservoirs combined) relative to the total number of sites $2L$, thus $0 \leq \mu_k < \infty$, $k = p, d$. In the limiting case of $\mu_p \to \infty$ which signifies an abundance of particles, the effective entry-exit rates, $\widetilde{\alpha}$ and $\widetilde{\beta}$ converges to the intrinsic entry rate α and 0. If we set $p_d = 1$, indicating that the presence of a defect does not affect particle dynamics, our model deviates from the two-lane constrained entrances TASEPs with infinite resources [60]. Instead, this model converges to a specific scenario of the system considered in Ref. [60], with the exit rate approaching 0.

4.3 Theoretical analysis: Master equations

In this section, we will provide a detailed theoretical framework to analyze the system's behaviour by deriving time evolution equations for particles and defects.

4.3.1 Particle density evolution

The evolution of particle density is governed by the following master equations, which describe the mean-site occupation density for lanes A and B at each bulk site $(2, 3, \ldots, L-1)$ given by

$$\frac{d\langle \tau_A^i \rangle}{dt} = J_A^{i-1,i} - J_A^{i,i+1}, \qquad \frac{d\langle \tau_B^i \rangle}{dt} = J_B^{i+1,i} - J_B^{i,i-1}, \tag{4.5}$$

where the notation $\langle \dots \rangle$ represents the statistical average. Here, $J_A^{i,i+1}/(J_B^{i,i-1})$ corresponding to the bulk current passing from the ith site to $(i+1)/(i-1)$th site in lane A/B defined as

$$J_A^{i-1,i} = \langle (1-\nu_A^i)\tau_A^{i-1}(1-\tau_A^i)\rangle + p_d\langle \nu_A^i\tau_A^{i-1}(1-\tau_A^i)\rangle,$$
$$J_B^{i,i-1} = \langle (1-\nu_B^{i-1})\tau_B^i(1-\tau_B^{i-1})\rangle + p_d\langle \nu_B^{i-1}\tau_B^i(1-\tau_B^{i-1})\rangle.$$

In the above equations, the first term of the right-hand side represents the hopping of a particle to a neighbouring empty site in the absence of a defect at the target site, while the second term accounts for the presence of a defect at the target site. It is important to note that the particles as well as the defects adhere to the hard-core exclusion principle, meaning that each site can accommodate a maximum of one particle and a maximum of one defect or both. At the boundaries of each lane, one can express the bulk currents as

$$\begin{aligned} J_A^{entry} &= \widetilde{\alpha}\langle (1-\nu_A^1)(1-\tau_A^1)(1-\tau_B^1)\rangle + \langle p_d\nu_A^1(1-\tau_A^1)(1-\tau_B^1)\rangle, \\ J_B^{entry} &= \widetilde{\alpha}\langle (1-\nu_B^L)(1-\tau_B^L)(1-\tau_A^L)\rangle + \langle p_d\nu_B^L(1-\tau_B^L)(1-\tau_A^L)\rangle, \\ J_A^{exit} &= \widetilde{\beta}\langle \tau_A^L\rangle, \\ J_B^{exit} &= \widetilde{\beta}\langle \tau_B^1\rangle. \end{aligned} \tag{4.6}$$

It should be noted that the Eqs. (4.3.1) and (4.6) involve one-point and three-point correlations which may be intractable in the present form.

4.3.2 Defect density evolution

The master equation governing the evolution of the average occupation number of defects on each site in the system is expressed as follows:

$$\frac{d\langle \nu_j^i\rangle}{dt} = \widetilde{k_+}\langle (1-\nu_j^i)\rangle - k_-\langle \nu_j^i\rangle. \tag{4.7}$$

This equation is valid for all sites i $(i = 1, 2, \dots, L)$ and $j = A, B$. Notably, we have taken into account the binding and unbinding of defects at the boundary sites as well.

4.3.3 Discrete to continuum mean-field equations

The master equation for defects described in Eq. (4.7) is amenable to analysis due to its dependence solely on one-point correlators. Additionally, this equation satisfies the principle of detailed balance, which implies that the defect density will ultimately reach a stable equilibrium state.

However, the particle dynamics given by Eqs. (4.5), (4.3.1), and (4.6) involves terms

with one-point and three-point correlators, making the system difficult to solve directly in its present form. To tackle these challenges, we adopt the mean-field theory (MFT), a widely used technique in bidirectional models [60,102], to simplify the mathematical treatment. Factorizing the correlation functions as the product of their averages using mean-field approximation, we get $\langle \nu_q^a \tau_r^b \tau_s^c \rangle = \langle \nu_q^a \rangle \langle \tau_r^b \rangle \langle \tau_s^c \rangle$, for $q, r, s \in \{A, B\}$ and $a, b, c \in \{1, 2, \ldots, L\}$.

Further, we define the mean-field densities at each site of either lane as $\rho_j^i = \langle \tau_j^i \rangle$ and $\sigma_j^i = \langle \nu_j^i \rangle$. In order to obtain a continuum description of the model in the thermodynamic limit $L \to \infty$, we coarse-grain the discrete lanes with constant $\epsilon = 1/L$ and rescale the time as $t' = t/L$. Applying Taylor series expansion and retaining terms up to second-order, we get

$$\rho_j^{i\pm1} = \rho_j^i \pm \epsilon \frac{\partial \rho_j^i}{\partial x} + \frac{\epsilon^2}{2} \frac{\partial^2 \rho_j^i}{\partial x^2} + \mathcal{O}(\epsilon^3). \tag{4.8}$$

Since the system's transition rules are site-independent, each site in the bulk follows the same dynamics. As a result, we can drop the subscript 'i' to represent the bulk sites collectively. Thus, the continuum mean-field densities of the bulk sites of each lane evolve as follows

$$\frac{\partial}{\partial t'} \begin{bmatrix} \rho_A \\ \rho_B \end{bmatrix} + \frac{\partial}{\partial x} \begin{bmatrix} J_A \\ -J_B \end{bmatrix} = \frac{\epsilon}{2} \begin{bmatrix} (1 - \sigma_A(1 - p_d)) \frac{\partial^2 \rho_A}{\partial x^2} \\ (1 - \sigma_B(1 - p_d)) \frac{\partial^2 \rho_B}{\partial x^2} \end{bmatrix}. \tag{4.9}$$

Here,

$$J_A = (1 - \sigma_A(1 - p_d))\, \rho_A(1 - \rho_A), \quad J_B = (1 - \sigma_B(1 - p_d))\, \rho_B(1 - \rho_B), \tag{4.10}$$

gives the bulk currents of particles in each lane. In the steady-state, the above equation is translated to

$$(1 - \sigma_j(1 - p_d)) \left(\frac{\epsilon}{2} \frac{\partial^2 \rho_j}{\partial x^2} \pm (2\rho_j - 1) \frac{\partial \rho_j}{\partial x} \right) = 0, \tag{4.11}$$

where $+(-)$ in the above equation corresponds to the particles on lane A(B). In the limit $\epsilon \to 0$, this equation yields $\frac{\partial J_j}{\partial x} = 0$. Similarly, the boundary currents at a steady-state translate to

$$\begin{aligned} J_A^{entry} &= \widetilde{\alpha} \left(1 - p_d(1 - \sigma_A^1)\right) (1 - \rho_A^1)(1 - \rho_B^1), \\ J_B^{entry} &= \widetilde{\alpha} \left(1 - p_d(1 - \sigma_B^L)\right) (1 - \rho_B^L)(1 - \rho_A^L), \\ J_A^{exit} &= \widetilde{\beta} \rho_A^L, \\ J_B^{exit} &= \widetilde{\beta} \rho_B^1. \end{aligned} \tag{4.12}$$

Furthermore, by performing a similar coarse-graining for the defect density $\langle \nu_j^i \rangle$ by σ_j^i,

the defect evolution equation expressed in Eq. (4.7) simplifies to

$$\frac{d\sigma_j}{dt} = \widetilde{k_+}(1-\sigma_j) - k_-\sigma_j, \quad j = A, B. \tag{4.13}$$

Note that the subscript 'i' is dropped as the defect dynamics do not involve inhomogeneity of any kind throughout the lanes. The steady-state defect density σ_j is solely determined by the binding and unbinding rates of the defects and reaches a constant value σ for both the lanes expressed as

$$\sigma = \frac{\widetilde{k_+}}{\widetilde{k_+} + k_-}. \tag{4.14}$$

For the special case of $k_+ = 0$, no defect can bind onto the lanes, hence, the defect density $\sigma \to 0$. Consequently, particle movement becomes unhindered, simplifying the governing equations of the system (given by Eqs. (4.3.1) and (4.6)) for a two-lane bidirectional narrow entrances model with reservoir crowding, which has not been investigated in the existing literature.

Now, the aspect that remains to be addressed in the defect dynamics is the inclusion of finite resources. A global constraint on the number of defects in the system affects their binding rate while the unbinding rate remains unaffected. To determine the effective binding rates given by Eq. (4.2), we utilize the Principle of Number Conservation for defects in the system which states that $N_{r_d} + 2L\int_0^1 \sigma\, dx = N_d$. We define the density of the reservoir R_d by $r_d = N_{r_d}/(2L)$. Thus, one can establish a relationship between the reservoir density and the filling factor for defects as follows

$$\mu_d = r_d + \sigma. \tag{4.15}$$

By substituting the defect density provided by Eq. (4.14) into the above expression, we obtain

$$r_d = \frac{1}{2k_+}\Big(\mu_d(k_+ - k_-) - k_+\sqrt{\big(\mu_d(k_+ - k_-) - k_+\big)^2 + 4k_-k_+\mu_d^2}\Big), \tag{4.16}$$

which can be further used to retrieve the density of the defects. Note that the binding and unbinding of defects onto the lanes do not have a direct impact on the particle densities; however, they are implicitly related through the defect density. Henceforth, our attention is directed towards analyzing the defect dynamics as a whole, rather than considering the binding and unbinding rates separately. This approach reduces the number of parameters in our system while maintaining a comprehensive analysis of its behaviour.

Let us now shift our focus back to the particle dynamics. The expression for the

steady-state bulk current, as described by Eq. (4.10), the parameters σ and p_d represent the impediment caused to the particles due to the presence of defects in the system. Moreover, it is evident from Eq. (4.10) that the factor $(1-\sigma(1-p_d))$ scales the overall particle current of the lanes. Thus, we refer to this term as the scaling factor which quantifies the impact of defects on the system and is denoted by 'c'. From here onward, we will employ this parameter for two advantageous purposes. Firstly, it helps in reducing the complexity of the parameter space. Secondly, it simplifies subsequent expressions encountered during our analysis. Also, for $p_d \to 1$, the defects do not impede the movement of particles on the lanes and the hindrance caused by defects becomes negligible. Consequently, the steady-state current on the lattice is reduced to that of a conventional two-lane TASEP system with narrow entrances. However, in case $\sigma \to 1$ and $p_d \to 0$, the maximum hindrance is observed in the particle movement, leading to a complete absence of steady-state current throughout the lanes.

To account for the influence of coupling the system to a finite pool of particles, we apply the Principle of Number Conservation (PNC), similar to how it was utilized for defects. This allows us to establish a relationship between the filling factor μ_p and the reservoir density r_p given by

$$\mu_p = r_p + \frac{1}{2}\int_0^1 (\rho_A + \rho_B)dx. \tag{4.17}$$

From Eqs. (4.10) and (4.12), it is evident that the interaction between particles from both lanes takes place solely at the boundaries. Therefore, the proposed system can be viewed as two-independent single-lane TASEPs associated with a common finite reservoir, having the same exit rate $\widetilde{\beta}$. The effective entry rates of particles in both lanes can be obtained by applying the current continuity principle in the bulk and at the boundaries of the lanes [60]. This approach yields the following expressions for the effective entry rates

$$\alpha_A^{eff} = \widetilde{\alpha}(1-\rho_B^1), \quad \alpha_B^{eff} = \widetilde{\alpha}(1-\rho_A^L), \tag{4.18}$$

along with $\widetilde{\beta} = \beta\left(1-\frac{r_p}{\mu_p}\right)$ and $\widetilde{\alpha} = \alpha\frac{r_p}{\mu_p}$.

Now, our aim is to calculate the effective rates α_A^{eff}, α_B^{eff}, and $\widetilde{\beta}$, as well as the particle densities, by utilizing Eqs. (4.14), (4.15), and (4.17) along with Eq. (4.18). These explicitly derived expressions for the effective rates will enable us to quantify the stationary properties of the system, such as phase diagrams, density profiles, particle currents, and potential phase transitions.

4.4 Mean-field theory

The particle input and output at the boundaries play a crucial role in governing the transport state within both lanes. So, it becomes highly important to examine all conceivable phase transitions and significant steady-state properties, such as density profiles and particle currents, with respect to their intrinsic entry and exit rates in the system. Even though the dynamics of the particles in both lanes are identical, the stationary properties of the system may not necessarily be the same for particles moving in different directions. Hence, the system's ability to exhibit both symmetric and asymmetric phases forms the basis for our further discussion [60,102]. In the absence of reservoir crowding, dynamic defects, and any constraints on available resources, our model simplifies to a well-studied two-lane system with narrow entrances [60], which exhibits spontaneous symmetry-breaking in the form of H/L and L/L phases. By limiting the number of resources in the system while maintaining a constant exit rate, a different asymmetric phase known as S/L emerges [102].

In the proposed model, effective interactions between the lanes occur exclusively at the boundary sites, allowing us to consider each lane as a one-dimensional TASEP lane with dynamic defects and reservoir crowding. This one-lane model has not yet been studied to the best of our knowledge. As seen earlier, the introduction of a defect into the system resulted in a scaling of the bulk current with the parameter 'c'. As a result, this parameter exerts an influence on the particle density of the system in different phases when it reaches a stationary state. In this case, the particle currents at each site can be written as $J^{enter} = c\widetilde{\alpha}\,(1-\rho(0))\,,\ J^{bulk} = c\rho(1-\rho)$, and $J^{exit} = \widetilde{\beta}\rho(1)$. By equating the entry and exit currents with the bulk current for the LD and HD phases, respectively, we can determine the steady-state particle densities. This yields the following expressions:

$$\rho(0) = \widetilde{\alpha}, \qquad \rho(1) = 1 - \widetilde{\beta}/c. \tag{4.19}$$

In the entrance-dominated LD phase, the particle density is equal to $\rho(0)$, while in the exit-dominated HD phase, it is given by $\rho(1)$. The bulk-dominated maximal current (MC) phase is specified by the condition $\frac{\partial J^{bulk}}{\partial \rho} = 0$ which yields $\rho = 1/2$. The shock phase is characterized by a region of density $\rho(0)$ on the left and $\rho(1)$ on the right. Finally, to calculate the effective entry-exit rates, the particle number conservation criteria is utilized. Table (4.1) provides a summary of the results obtained from studying a one-dimensional system with dynamic defects under the influence of reservoir crowding.

Provoked by these notable dynamics we investigate a two-lane TASEP with constrained entrances and dynamic defects under the effect of reservoir crowding. In

Phase	ρ^1	ρ^{bulk}	ρ^L	Phase Region	r
LD	$\widetilde{\alpha}$	$\widetilde{\alpha}$	$\frac{c\widetilde{\alpha}(1-\widetilde{\alpha})}{\widetilde{\beta}}$	$\widetilde{\alpha} < \min\{0.5, \widetilde{\beta}/c\}$	$\frac{\mu^2}{\mu+\alpha}$
HD	$1-\frac{\widetilde{\beta}}{c\widetilde{\alpha}}\left(1-\frac{\widetilde{\beta}}{c}\right)$	$1-\frac{\widetilde{\beta}}{c}$	$1-\frac{\widetilde{\beta}}{c}$	$\widetilde{\beta}/c < \min\{0.5, \widetilde{\alpha}\}$	$\frac{\mu(\beta-c(1-\mu))}{\beta+c\mu}$
MC	$1-\frac{1}{4\widetilde{\alpha}}$	$\frac{1}{2}$	$\frac{c}{4\widetilde{\beta}}$	$0.5 < \min\{\widetilde{\alpha}, \widetilde{\beta}/c\}$	$\mu-\frac{1}{2}$
S	$\widetilde{\alpha}$	$\widetilde{\alpha}(u(t)-u(t-x_w))$ $1-\left(\frac{\widetilde{\beta}}{c}\right)u(t-x_w)$	$1-\frac{\widetilde{\beta}}{c}$	$0 < x_w < 1$	$\frac{\beta\mu}{\beta+c\alpha}$

Table 4.1: Summary of the results for the particle densities, existence conditions and reservoir density of a reservoir crowding featured dynamically disordered one-dimensional lane with L sites. Here, ρ^1, ρ^{bulk}, and ρ^L give the particle density at entry site, bulk, and exit site, respectively. The position of the shock is denoted by x_w, the filling factor by μ and the scaling factor by 'c'. Also, u is the unit step function.

the proposed model, each lane can exhibit one of the four possible stationary states: LD, HD, MC, or SP. Considering the nature of the phases, there are a total of eleven possible phases, but not all of them exist due to various restrictions. For example, the possibility of having the M phase in one-lane and the L, H or S phase in the other lane can be easily discarded because their existence conditions are inconsistent with each other. The S/H phase can be easily discarded through mathematical arguments. The remaining phases require further theoretical analysis to determine their existence conditions.

4.5 Feasible phases

This section outlines the process for obtaining the effective rates and the position of shock, wherever applicable for all the probable phases. As already discussed, in symmetrical phases, both lanes exhibit similar characteristics, as indicated by the following conditions: $\alpha_A^{eff} = \alpha_B^{eff}, \quad \rho_A = \rho_B, \quad J_A = J_B$. Since, the effective entrance rates, bulk densities and currents are equal for the two-lanes, we use the common notation α_{eff}, ρ, and J to represent these quantities, respectively.

On the other hand, in asymmetrical phases, usually, $\alpha_A^{eff} \neq \alpha_B^{eff}, \quad \rho_A \neq \rho_B, \quad J_A \neq J_B$. Here, α_j^{eff} gives the effective entrance rate, while, ρ_j and J_j are the bulk particle densities and currents in the jth lane.

4.5.1 Symmetrical phases

- **Low density phase (LD/LD).** We assume that both the lanes are in an entry-dominated phase with bulk current written as $J = c\alpha^{eff}(1-\alpha^{eff})$. Equating

this to the boundary current at the exit site of lane B gives

$$\rho_B^1 = \frac{c\alpha^{eff}(1-\alpha^{eff})}{\widetilde{\beta}}. \tag{4.20}$$

Substituting this expression into Eq. (4.18), we can determine the effective entry rate of particles as

$$\alpha^{eff} = \frac{\widetilde{\beta} + c\widetilde{\alpha} - \sqrt{(\widetilde{\beta}+c\widetilde{\alpha})^2 - 4c\widetilde{\alpha}^2\widetilde{\beta}}}{2c\widetilde{\alpha}}. \tag{4.21}$$

We can then plug this value into Eq. (4.17) to calculate the density of the particle reservoir, expressed by

$$r_p = \frac{1}{2}\left(\mu_p - 1 + \frac{\beta(\alpha+\mu_p)}{c\alpha\mu_p} - \sqrt{\left(\frac{\beta(\alpha+\mu_p)}{c\alpha\mu_p} - 1 + \mu_p\right)^2 - 4\frac{\beta\mu_p}{c\alpha}}\right). \tag{4.22}$$

Since the expressions in terms of intrinsic rates are quite complex, we present the conditions for the existence of this phase using effective rates as follows

$$\alpha^{eff} < \left\{0.5, \widetilde{\beta}/c\right\}. \tag{4.23}$$

- **Maximal current phase (MC/MC).** In this phase, each lane exhibits the maximum particle flow, given by $J = c/4$, with a density of $\rho = 1/2$. Using Eq. (4.12), the exit current through Lane B can be expressed as $J_B^1 = \widetilde{\beta}\rho_B^1$. Applying the principle of current continuity, the bulk current must be equal to the exit current, leading to the relation $\rho_B^1 = c/4\widetilde{\beta}$. Substituting this expression into Eq. (4.18), we obtain the effective entry rate of the particles as

$$\alpha^{\text{eff}} = \widetilde{\alpha}\left(1 - \frac{c}{4\widetilde{\beta}}\right). \tag{4.24}$$

To determine the reservoir density of the pool, we utilize the Principle of Number Conservation (PNC) given by Eq. (4.17), which gives us $r_p = \mu_p - 1/2$. The conditions for the existence of this phase ($\alpha_{\text{eff}} > 1/2$ and $\widetilde{\beta}/c > 1/2$) can be rewritten as

$$\beta > c\mu_p, \quad \alpha > \frac{2\beta\mu_p}{(2\mu_p - 1)(2\beta - c\mu_p)}. \tag{4.25}$$

- **High density phase (HD/HD).** This phase occurs when both lanes are in an exit-dominated phase with the bulk particle density equal to the density at the exit site of Lane A. Consequently, in this phase, the effective entry rate can be expressed as

$$\alpha^{eff} = \frac{\widetilde{\alpha}\beta}{c}\left(1 - \frac{r_p}{\mu_p}\right). \tag{4.26}$$

The reservoir density can be calculated by using Eq. (4.17) as

$$r_p = \frac{\mu_p\left(\beta - c(1-\mu_p)\right)}{\beta + c\mu_p}. \tag{4.27}$$

The feasible region corresponding to this phase satisfies

$$\beta < \min\left\{c\mu_p, \frac{c\left(\alpha(\mu_p - 1) - \mu_p\right)}{1-\alpha}\right\}. \tag{4.28}$$

- **Shock phase (SP/SP).** In the symmetric shock phase (SP/SP), both lanes exhibit a discontinuity in the bulk, characterized by a transition from a low density region to a high density region. The currents at the boundary sites are described by the equations:

$$J_A^1 = J_B^L = c\alpha^{eff}(1-\alpha^{eff}), \quad J_A^L = J_B^1 = \widetilde{\beta}(1 - \frac{\widetilde{\beta}}{c}).$$

By utilizing the exit current of lane A in Eq. (4.18), we obtain the expression for α^{eff} as

$$\alpha^{eff} = \frac{\alpha\beta r_p}{c\mu_p}\left(1 - \frac{r_p}{\mu_p}\right). \tag{4.29}$$

The existence of a shock phase in a lane requires $\alpha^{eff} = \widetilde{\beta}/c$, which implies that the reservoir density is equal to μ_p/α. Let x_w denote the location of the shock within this phase. We can express the integral of ρ over the range from 0 to 1 as

$$\int_0^1 \rho dx = \int_0^{x_w} \alpha^{eff} dx + \int_{x_w}^1 \left(1 - \frac{\widetilde{\beta}}{c}\right) dx. \tag{4.30}$$

This can be further substituted in Eq. (4.17) to retrieve the position of shock as

$$x_w = \frac{\beta(1-\alpha) + c\left(\alpha + \mu_p(1-\alpha)\right)}{c\alpha + 2\beta(1-\alpha)}. \tag{4.31}$$

Finally, the boundary parameters must satisfy the following conditions for the SP/SP phase to exist:

$$\widetilde{\beta} < 0.5c, \quad 0 < x_w < 1. \tag{4.32}$$

4.5.2 Asymmetrical phases

- **High-low density phase (H/L).** Without loss of generality, we assume that the particles of lane A are in a high density phase while those of lane B display a low density phase. Since the particle flow is continuous in each lane, we have the following boundary currents $J_A^L = \widetilde{\beta}\rho_A^L$, $J_B^1 = \widetilde{\beta}\rho_B^1 = c\alpha_B^{eff}(1-\alpha_B^{eff})$. By substituting these

expressions into Eq. (4.18), we obtain

$$\alpha_B^{eff} = \widetilde{\alpha}\frac{\widetilde{\beta}}{c}, \quad \alpha_A^{eff} = \widetilde{\alpha}\left(1 - \frac{J_B^1}{\widetilde{\beta}}\right). \tag{4.33}$$

The particle number conservation, Eq. (4.17), can be rewritten as:

$$\mu_p = r_p + \frac{\left(\alpha_B^{eff} + 1 - \widetilde{\beta}/c\right)}{2}, \tag{4.34}$$

which allows us to calculate the reservoir density as

$$\frac{\mu_p}{2\alpha\beta}\Big(\beta(1+\alpha) + 2c\mu_p - \sqrt{\beta^2(\alpha-1)^2 + 4c\beta(\alpha + \mu_p - \alpha\mu_p) + 4c^2\mu_p^2}\Big).$$

By using the expressions for the boundary parameters and the reservoir density obtained above, the existence conditions for this phase can be formulated as:

$$\alpha_B^{eff} < \widetilde{\beta}/c < \alpha_A^{eff}. \tag{4.35}$$

- **Shock-low density phase (S/L).** When this scenario occurs, the particles of lane A portray a shock phase while those of lane B are in low density phase. This phase persists when the boundary-controlling parameters ensure the following constraints:

$$J_A = \widetilde{\beta}(1 - \widetilde{\beta}/c) = c\alpha_A^{eff}(1 - \alpha_A^{eff}), \quad J_B = \alpha_B^{eff}(1 - \alpha_B^{eff}).$$

Let x_w is the position of shock in the density profile on lane A. Then, we have $\int_0^1 \rho_A \; dx = \int_0^{x_w} \alpha_A^{eff} \; dx + \int_{x_w}^1 (1 - \widetilde{\beta}/c) \; dx$. The effective entrance rates for the particles can be retrieved from Eq. (4.18) as

$$\alpha_B^{eff} = \widetilde{\alpha}\frac{\widetilde{\beta}}{c}, \quad \alpha_A^{eff} = \widetilde{\alpha}\Big(1 - \frac{c\alpha_B^{eff}(1 - \alpha_B^{eff})}{\widetilde{\beta}}\Big).$$

To calculate the reservoir density, we utilize the criteria for a lane to display shock phase which states that the α_A^{eff} must be equal to $\widetilde{\beta}/c$. To procure the position of the shock, we utilize PNC given by Eq.(4.17) which in this case reduces to

$$\mu_p = r_p + \frac{1}{2}\left(x_w\frac{\widetilde{\beta}}{c} + (1 - x_w)\big(1 - \frac{\widetilde{\beta}}{c}\big) + \alpha_B^{eff}\right), \tag{4.36}$$

and the position of shock is given by

$$x_w = \frac{\widetilde{\beta} - c(1 + \alpha_B^{eff} - 2\mu_p + 2r_p)}{2\widetilde{\beta} - c}. \tag{4.37}$$

Thus, for this phase to persist, the boundary-controlling parameters must satisfy the following conditions

$$0 < x_w < 1, \quad \alpha_B^{eff} < \min\{0.5, \widetilde{\beta}/c\}. \tag{4.38}$$

- **Low-low density phase (L/L).** In this phase, although both the lanes are in entry-dominated phase, their particle densities differ. By using the bulk and boundary currents of each lane, we can determine the densities at the exit sites of both lanes:

$$\rho_A^L = \widetilde{\alpha}\left(1 - \frac{c\alpha_A^{eff}(1-\alpha_A^{eff})}{\widetilde{\beta}}\right), \quad \rho_B^1 = \widetilde{\alpha}\left(1 - \frac{c\alpha_B^{eff}(1-\alpha_B^{eff})}{\widetilde{\beta}}\right). \tag{4.39}$$

These expressions can be substituted into Eq. (4.18) and solved to obtain the explicit values of α_A^{eff} and α_B^{eff} as

$$\alpha_j^{eff} = \frac{1}{2}\left[1 - \frac{\widetilde{\beta}}{c\widetilde{\alpha}} \pm \sqrt{1 - \frac{\widetilde{\beta}}{c}\left(4 + 2\frac{1}{\widetilde{\alpha}} - 3\frac{\widetilde{\beta}}{c\widetilde{\alpha}^2}\right)}\right],$$

where $+$ corresponds to lane A and $-$ for lane B. Upon utilizing these values in Eq. (4.17), the reservoir density r_p can be obtained as

$$r_p = \frac{1}{4c\alpha}\Big(2c\mu_p\alpha - \beta - c\alpha + \sqrt{(\beta + c\alpha - 2c\mu_p\alpha)^2 + 8c\alpha\beta\mu_p}\Big). \tag{4.40}$$

The feasible region corresponding to this phase must satisfy

$$\max\{\alpha_A^{eff}, \alpha_B^{eff}\} < \min\{0.5, \widetilde{\beta}/c\}. \tag{4.41}$$

4.6 Results and discussions

Our objective is to investigate how the constraints placed on the number of particles and defects, represented by the filling factors μ_k, as well as the dynamics of defects quantified by the scaling factor, affect the stationary properties of the system. To achieve this goal, we utilize the analytical techniques discussed in Section (4.4) to analyze the behaviour of the system across the $\alpha - \beta$ plane. Within our theoretical framework, we make the simplifying assumption of neglecting particle correlations and the outcomes are obtained in the thermodynamic limit ($L \to \infty$) which necessitates the validation of our theoretical predictions through computer simulations. To validate the accuracy of our theoretical outcomes, we utilize Monte Carlo simulations by considering the size of the lanes as $L = 1000$.

Now, we specifically study the role of various parameters and their qualitative as well as quantitative effects on the system properties of the proposed model. Firstly, we analyze the impact of reservoir crowding, followed by the investigation of defect dynamics.

4.6.1 Effect of reservoir crowding

To conduct a thorough analysis, we present phase diagrams that illustrate significant topological changes in the parameter space (α, β) for specific values of $\mu_p \in (0, \infty)$ and $c = 1$ (refer to Fig. (4.2)). These phase diagrams offer a comprehensive understanding of the system's behaviour across different values of the controlling parameters.

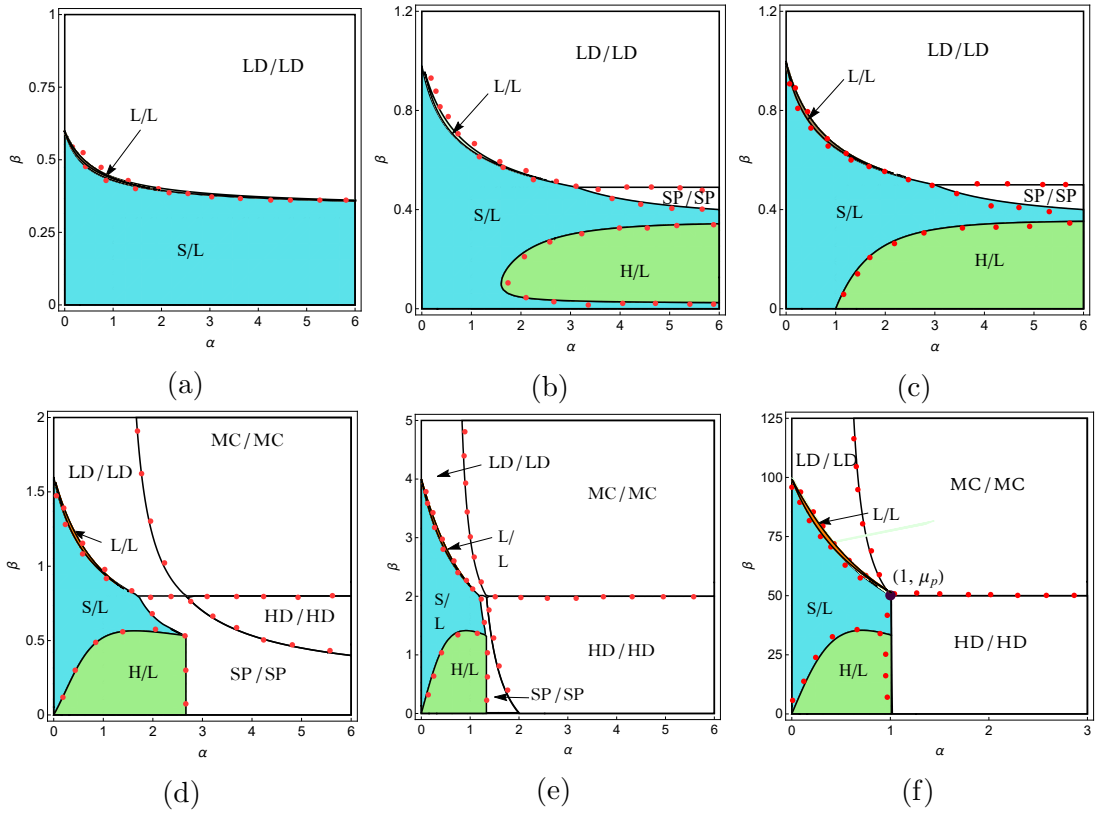

Figure 4.2: Stationary phase diagram for: (a) $\mu_p = 0.3$, (b) $\mu_p = 0.49$, (c) $\mu_p = 0.5$, (d) $\mu_p = 0.8$, (e) $\mu_p = 2$, and (f) $\mu_p = 50$ with $c = 1$. White regions represent symmetric phases, while coloured regions indicate asymmetric phases. The red symbols correspond to results from Monte Carlo simulations and solid lines are theoretical findings.

Initially, when the system has significantly less number of particles in the system, the phase diagram consists of three distinct phases namely one symmetric phase (LD/LD) and two asymmetric phases (L/L and S/L), as depicted in Fig. (4.2a) for $\mu_p = 0.3$. It is important to highlight that these three phases persist even for extremely small values of μ_p ($\mu_p \to 0^+$), underscoring their significance in influencing the system's behaviour. Consequently, the system exhibits a symmetry-breaking phenomenon even for very

small values of the filling factor μ_p. This argument can be further supported by Eqs. (4.38) and (4.23), which delineate the phase boundaries from S/L to L/L and L/L to LD/LD regions, respectively. These boundaries intersect at the point $(\alpha, \beta) = (0, 2\mu_p)$ which exists for any value of μ_p.

We encounter only these three phases in the phase diagram until the critical value $\mu_p^{C_1} \approx 0.31$ as theoretically computed from Eq. (4.32). Beyond this critical threshold of μ_p, a new symmetric phase, referred to as SP/SP, emerges in the phase diagram alongside the S/L phase. The boundary separating the S/L and SP/SP phases can be determined using Eq. (4.38). There are no significant qualitative alterations in the phase diagram until we reach another critical point at $\mu_p^{C_2} \approx 0.43$, except for the expansion of the SP/SP and S/L phases and the contraction of the L/L phase. This critical value $\mu_p^{C_2}$ is determined from Eq. (4.35).

After $\mu_p^{C_2}$, the system exhibits the emergence of the H/L phase in the phase diagram (see Fig. (4.2b)). At this stage, the system displays a total of five phases: two symmetric and three asymmetric phases. One observation that can be made based on Fig. (4.2b) is that the phase boundary between the H/L phase and the S/L phase does not cross the α-axis. However, precisely at $\mu_p^{C_3} = 0.5$ (calculated from Eq. (4.28)), this phase boundary intersects the α-axis as evident from Fig. (4.2c). Moreover, beyond $\mu_p^{C_3}$, the phase diagram exhibits the emergence of two symmetric phases namely MC/MC and HD/HD, as shown in Fig. (4.2d) for $\mu_p = 0.8$. The critical value after which HD/HD and MC/MC phases emerge in the phase diagram is $\mu_p^{C_3}$ and can be affirmed from Eq. (4.25) as well as Eq. (4.28). Here, the boundary that separates the MC/MC phase from the HD/HD phase can be derived by utilizing Eq. (4.28), which yields $\beta = \mu_p$. Moreover, the phase boundary that distinguishes the H/L phase from the SP/SP phase can be computed from Eq. (4.35) by solving $\alpha_B^{eff} - \widetilde{\beta} = 0$ which yields $\alpha = 2\mu_p/(2\mu_p - 1)$.

Now a further increment in μ_p results in the expansion of MC/MC, HD/HD and S/L phase regions, while the region corresponding to H/L, SP/SP and S/L phases shrinks (see Fig. (4.2e)). Finally, at the critical value of $\mu_p^{C_4} \approx 50$, the SP/SP phase disappears from the phase diagram. It is significant to mention here that for $\mu_p \in (\mu_p^{C_3}, \mu_p^{C_4})$ the system manifest all the probable feasible phases. After $\mu_p^{C_4} < \mu_p$, no topological changes are realized in the phase diagram except for repositioning the phase boundaries. Finally, the system exhibits three asymmetric and three symmetric phases, which persist for larger values of μ_p. In the limiting case of $\mu_p \to \infty$, the invariant structure of the phase diagram can be retrieved as the exit parameter β tends to infinity.

To summarize, Fig. (4.3) provides an overview of the potential phase transitions within the phase diagram as a function of the system's particle count. It is evident that the system can exhibit a maximum of four symmetric phases (LD/LD, SP/SP, HD/HD, and MC/MC) and three asymmetric phases (L/L, S/L, and H/L), which are attainable

for different values of μ_p. The number of phases observed in the system follows a non-monotonic pattern concerning μ_p. As illustrated in Fig. (4.3), the number of achievable phases initially increases from 3 to 4, then to 5, reaches 7, and subsequently decreases to 6 once $\mu_p > \mu_p^{C_4}$. Within the range of $\mu_p \in (C_3,\ C_4)$, the topology of the phase diagram becomes complex and the system manifests all seven potential phases. A significant outcome arising from the incorporation of the reservoir crowding effect

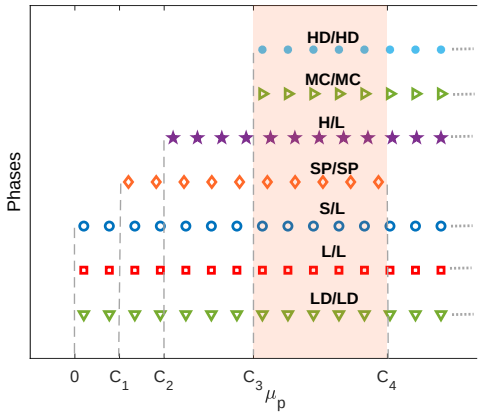

Figure 4.3: Possible phase transitions observed in the system with increasing values of μ_p. The values C_i indicate critical values of μ_p at which difference phases appear and disappear. In particular, $C_1 \approx 0.31$, $C_2 \approx 0.43$, $C_3 \approx 0.5$, and $C_4 \approx 50$. In the shaded region $\mu_p \in (C_3, C_4)$, all the seven phases persists in the system.

into particle dynamics is the manifestation of a localized shock in the density profile, a feature that does not occur in the presence of an infinite number of particles [60,102]. Similar consequences have been reported in various models, attributed to the influence of reservoir crowding [58,69]. This insight is supported by examining the coordinates of the quintic point given by $(1, \mu_p)$, where the phase boundaries of five phases - S/L, L/L, LD/LD, MC/MC, and HD/HD intersect. It signifies that as μ_p increases, this point consistently shifts upward, indicating the persistence of the S/L phase in the phase diagram.

In the forthcoming sections, we intend to provide a brief discussion of the important features that can be derived from the analysis of Fig. (4.2).

4.6.2 Back and forth transition

Let us now delve into one of the prominent characteristics of the proposed model, which arises from the intricate relationship between limited resources and narrow entrances, specifically for $\mu_p < 0.5$ i.e., for a smaller number of particles. The topology of the phase diagram, in this case, is peculiar (see Fig. (4.2b)), resulting in a unique type of phase transition known as the back-and-forth, which is solely obtained by manipulating the intrinsic removal rate β and keeping all the other parameters constant. Notably, there is a transition from the shock phase (S) to the high density (H) phase and then

returns to the shock (S) phase in lane A, while the particle of lane B remains in the L phase. This forms a back-and-forth phase transition in the system from S/L → H/L → S/L as affirmed from Fig. (4.4a). To support this argument, we study the density profiles and the position of shock for a fixed value of $\mu = 0.45$, $\alpha = 7$, $c = 1$ and vary β (see Fig. (4.4)). This can be explained intuitively by the following argument. The

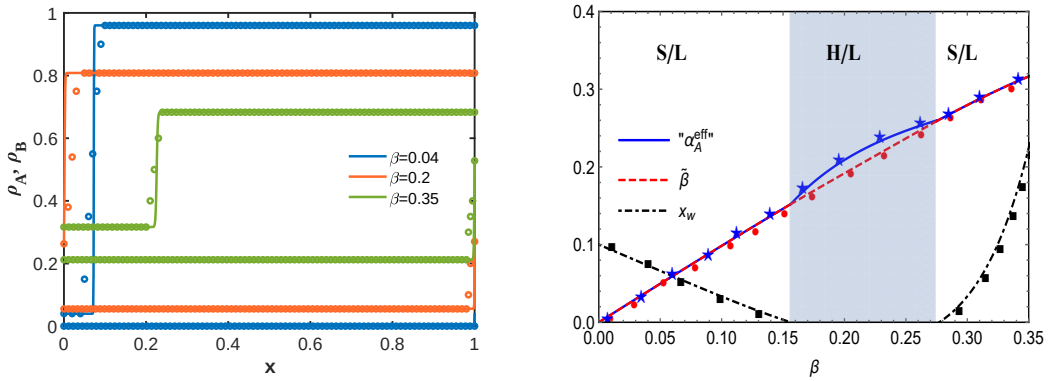

(a) (b)

Figure 4.4: (a) Density profile for $(\alpha, c, \mu_p) = (7, 1, 0.45)$ and different values of β. (b) Effective entrance rate (α_A^{eff}) , effective exit rate $(\widetilde{\beta})$ and the position of the shock (x_w) with respect to β for $(\alpha, c, \mu_p) = (7, 1, 0.45)$. Lines denote theoretical findings while symbols correspond to simulation results.

system initially displays S/L for smaller values of β and fixed α. It is observed that the position of shock described by the variable x_w in lane A initially decreases with respect to β and tends towards 0 (as evident from Fig. (4.4b)). Physically it means that with an increment in β, the effective exit rates of particles are enhanced which in turn results in an increased effective entry rate of the species leading to accumulation of the particles on lane A. Accordingly the shock moves towards the left, resulting in the manifestation of H/L phase by the system.

Furthermore, the effective entrance rate α_A^{eff} and the exit rate $\widetilde{\beta}$ remain unequal, implying that the system does not support the criteria for the persistence of the shock phase in lane A. Specifically, it can be confirmed from Fig. (4.4b) that α_A^{eff} remains greater than $\widetilde{\beta}$ in the H/L phase. Now, the phase boundary of this phase for $\mu = 0.45$, as theoretically calculated by Eq. (4.35) is given as $\widetilde{\beta} = \alpha_A^{eff}$. Analyzing the behaviour of this boundary in the $\alpha - \beta$ plane reveals that α is a non-monotonic, multivalued function of β. Initially, α decreases, then exhibits a u-turn at approximately $\alpha \approx 1.607$, and subsequently increases.

Moreover, when the system is in the H/L phase and β continues to increase, the peculiar behaviour of the phase boundary drives the system back to the S/L phase. The shock once again begins to enter from the left end at $\beta \approx 0.332$ resulting in $x_w \in (0, 1)$. This finding is confirmed by Fig. (4.4), which displays the density profiles for various β values and illustrates the position of the shock.

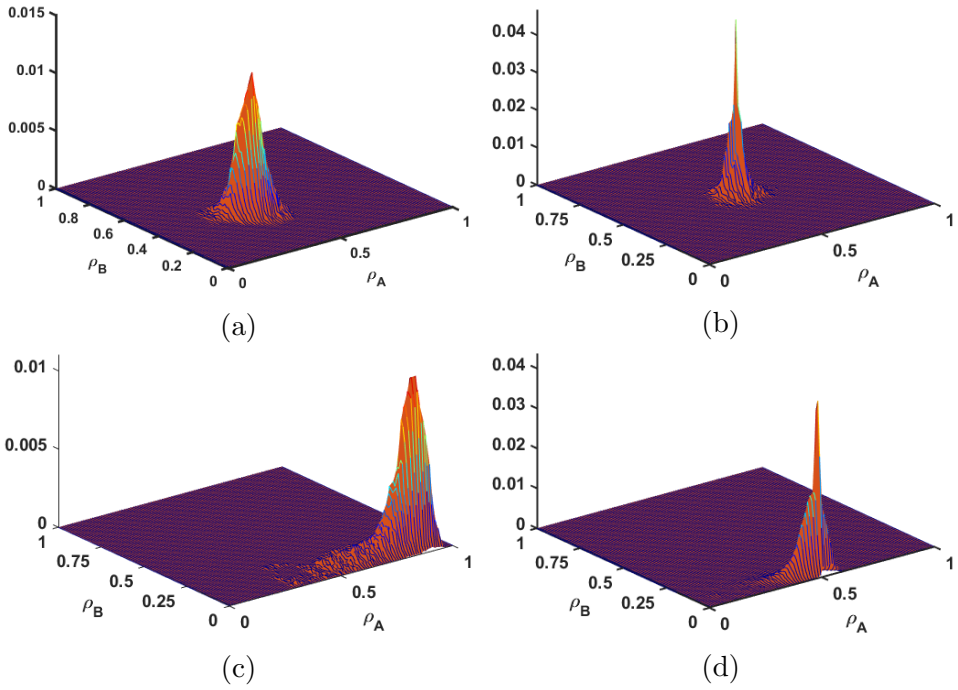

Figure 4.5: Particle density histogram plotted through Monte Carlo simulations for (a) LD/LD, (b) MC/MC, (c) H/L, and (d) S/L phases. The parameters are $(\alpha, \beta, \mu_p) = (3, 1, 0.49)$, $(3, 4, 2), (1, 0.5, 2)$, and $(2, 0.2, 0.3)$ in (a–d) with $c = 1$.

4.6.3 Spontaneous symmetry-breaking

A noteworthy characteristic of a bidirectional system is the occurrence of spontaneous symmetry-breaking. Our previous analysis reveals the presence of three asymmetric phases: S/L, H/L, and L/L analogous to the findings of Refs. [60,102]. This symmetry-breaking arises due to the stochastic nature of particle movements and interactions between them at the boundaries. To conduct a comprehensive exploration of this phenomenon using Monte Carlo simulations, we create particle density histograms by continuously monitoring the instantaneous densities of the species of the two-lanes, ρ_A and ρ_B. In our simulations, we use a system size of $L = 1000$, excluding the initial 10^9 time steps and collecting data over the subsequent 9×10^9 time steps. While examining the density histogram distribution, if the peak corresponds to $\rho_A = \rho_B$, we categorize the phase as symmetric; otherwise, it is labelled as asymmetric. Typical density histograms for LD/LD, MC/MC, H/L, and S/L phases are displayed in Fig. (4.5). One can clearly observe from Figs. (4.5a) and (4.5b) that the peak is attained for $\rho_A = \rho_B$. For LD/LD phase $\rho_A = \rho_B < 1/2$ whereas for MC/MC phase this value is exactly equal to 0.5. In Fig. (4.5c) - (4.5d), an off-diagonal peak appears which validates the existence of asymmetric phases in the system. Specifically, in Fig. (4.5c), the peak in distribution is achieved at $\rho_A > 1/2$, $\rho_B < 1/2$ for H/L phase and in case of S/L phase, the peak occurs at $0 < \rho_A < 1$, $\rho_B < 1/2$ as shown in Fig. (4.5d).

4.6.4 Size-scaling dependencies of phases

To corroborate the finite-size effect, we investigate into how varying the system size, denoted by L, influences the density profiles while keeping the parameter μ_p fixed at 0.8. The results, as depicted in Fig. (4.6a), clearly demonstrate that as L increases, it primarily leads to the sharpening of shock profiles within the S/L phases. Importantly, the underlying phase remains unaffected despite these changes. Similar findings can be extended to the case of the MC/MC phase where only the boundary is affected (see Fig. (4.6b)).

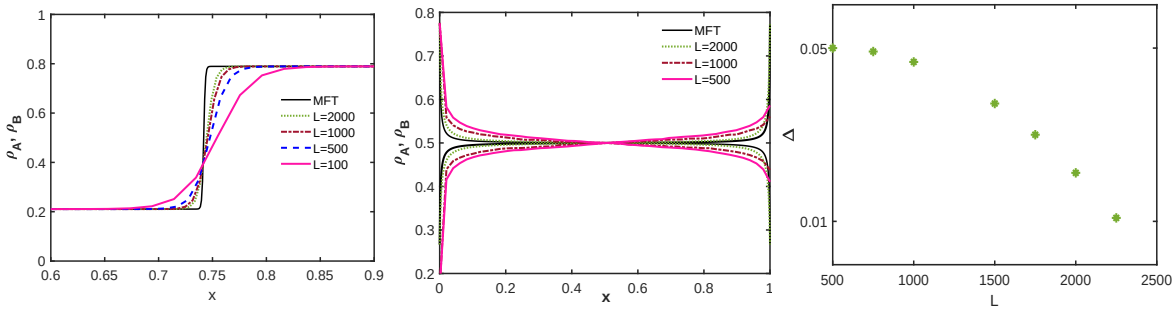

(a) (b) (c)

Figure 4.6: Finite-size effect on density profile of (a) shock in S/L phase for $(\alpha, \beta, \mu_p) = (0.5, 0.5, 0.5)$ and (b) MC/MC phase for $(\alpha, \beta, \mu_p) = (4, 1.5, 0.8)$. (c) Variation of region width Δ of L/L phase with increasing lane length L for fixed $\alpha = 1$ and $\mu_p = 0.5$.

Another effect of the finite-size of the lanes is seen in the L/L phase. It has been noted that as the system size increases, the region exhibiting asymmetric LD phase diminishes, indicating that this region either becomes confined to a line or completely vanishes in the thermodynamic limit. To illustrate this, we have graphed the width of the L/L phase (Δ) while keeping $\alpha = 1$ and $\mu_p = 0.5$ fixed and varying β in Fig. (4.6c). As depicted in the figure, the width of the L/L region decreases as the system size L increases. Thus, for sufficiently large systems, the L/L region contracts, aligning with findings from earlier research where similar observations were documented [58,102].

4.6.5 Influence of defects

As elucidated in previous sections, the introduction of dynamic defects at every site within the two-lanes (bulk and boundary) leads to a translation of the particle current, characterized by the scaling factor 'c'. The expression for this parameter and the defect density can be explicitly derived by employing Eqs. (4.14) and (4.16), yielding

$$\sigma = \frac{P + \sqrt{Q^2 + 4k_- k_+ \mu_d^2}}{Q + \sqrt{Q^2 + 4k_- k_+ \mu_d^2}}, \quad c = 1 - (1 - p_d)\sigma, \tag{4.42}$$

where the value of $P = (k_+(\mu_d - 1) - k_-\mu_d)$ and $Q = (k_+(\mu_d - 1) + k_-\mu_d)$. Note that the scaling factor is a non-linear complex function of four parameters: the defect binding and unbinding rates (k_+, k_-), the strength of the defect (p_d), and the filling factor (μ_d). Moreover, this factor has an impact on the stationary particle current (denoted by J_A and J_B), subsequently affecting the particle densities, ρ_A and ρ_B. Hence, it becomes essential to analyze the impact of each parameter separately.

- **Limited availability of defects.**

  Here, we explore the effects of implementing a global constraint on the overall quantity of available defects within the system. For fixed values for k_+, k_-, and p_d, it becomes evident from Fig. (4.7), the defect density σ consistently rises, while the scaling factor 'c' decreases monotonically as a function of μ_d. Physically, this trend indicates that with an increasing number of defects, there is a higher accumulation of sites bound to defects within the lanes. Consequently, it results in an enhanced defect density and a subsequent decrease in the overall particle flow. In the absence of any constraint on

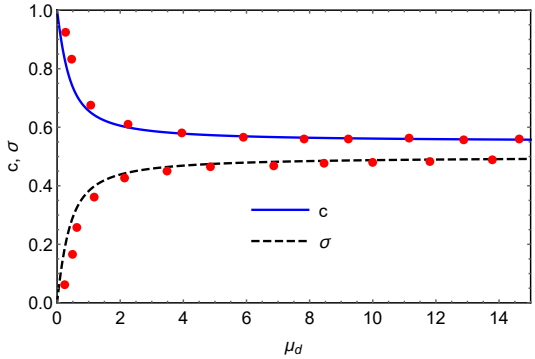

Figure 4.7: Plot for the defect density and the scaling factor 'c' vs the filling factor μ_d with $k_+ = k_- = 1, p_d = 0.1$, and $\mu_p = 0.8$. Solid lines depict theoretical findings whereas symbols denote Monte Carlo simulation results.

  the number of available defects (i.e., when $\mu_d \to \infty$), both the defect density and the scaling factor 'c' converge towards fixed values, which can be expressed as follows:

$$\sigma = \frac{k_+}{k_+ + k_-}, \quad c = 1 - \frac{k_+(1 - p_d)}{k_+ + k_-}. \tag{4.43}$$

  The defect density is solely dictated by the defect binding rate k_+ and the unbinding rate k_-. Specifically, for the specified parameter values of $(k_+, k_-, p_d) = (1, 1, 0.1)$, σ approaches 0.5, and c tends towards 0.55 as also evident from Fig. (4.7).

  To investigate the influence of alterations in μ_d on the phase diagram, we assess the changes occurring in the phase boundaries while maintaining the parameters $(k_+, k_-, p_d) = (1, 1, 0.1)$ and considering different values of α (see Fig. (4.8)). The particle filling factor μ_p is set at 0.8, taking into consideration Fig. (4.2d), which

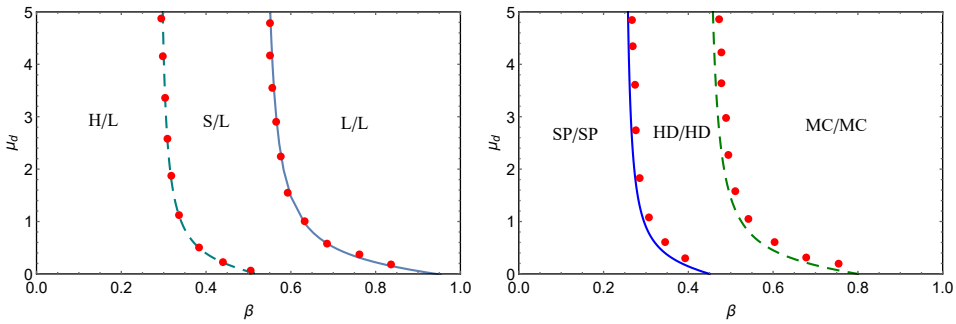

Figure 4.8: Variation in the phase boundaries between different values with increasing values of μ_d and $k_+ = k_- = 1, p_d = 0.1, \mu_p = 0.8$ for: (a) $\alpha = 1$ and (b) $\alpha = 5$. Solid lines depict theoretical findings whereas symbols denote Monte Carlo simulation results.

illustrates the maximum number of attainable phases in a single phase diagram. It can be observed that for $\mu_d = 0$, the scaling factor attains its maximum value 1 while the scarcity of defects leads to 0 defect density. Consequently, the defects do not impede the particle movement at all, leading to the maximum particle flow. This allows us to achieve the results for a two-lane system with constrained entrances, along with the inclusion of reservoir crowding which has not been investigated yet. With an increase in μ_d, we observe a reduction in the regions corresponding to H/L, S/L, SP/SP, and HD/HD phases, while the LD/LD and MC/MC regimes expand. Moreover, as anticipated for $\mu_d \to \infty$, the boundaries separating S/L from H/L and LD/LD region and HD/HD from SP/SP and MC/MC region approaches constant values.

- **Strength of the defect.**

  This section explains the influence of the hopping rate of particles in the presence of a defect, denoted by p_d, (which signifies the strength of the defect) on the system's stationary properties. The motion of particles relies on whether the adjacent site contains a defect or not. When there is no defect present, particles move unhindered with a probability of 1. However, if the next site is occupied by a defect, the hopping rate is altered to p_d and falls within the range of $[0, 1]$. Consequently, a reduction in the magnitude of p_d leads to an elevated obstruction in the movement of particles.

  As expressed in Eq. (4.42), it is important to note that the hopping rate p_d does not influence the defect density σ. However, when holding the other parameters constant, the scaling factor 'c' demonstrates a linear relationship with p_d, leading to only the translation of the phase boundaries.

- **Effect of binding/unbinding of defect.**

  Another set of parameters influencing the system properties are the binding and the unbinding rates characterized by the variables k_+ and k_-. In the limiting case

of $k_+ \to \infty$, one can determine from Eq. (4.42) that the defect density converges to a constant value when the other parameters such as k_- and μ_p are fixed. This convergence can be theoretically expressed as

$$\sigma \to \begin{cases} \mu_d, & \text{if } 0 \leq \mu_d < 1, \\ 1, & \text{if } 1 < \mu_d. \end{cases}$$

This can be physically understood by the following argument. When $0 \leq \mu_d < 1$, it signifies that there are fewer defects in the system than the total number of available sites, i.e., $N_d < 2L$. As k_+ takes significantly large values, all defects tend to stay associated with the lanes, resulting in the defect density equating to μ_d. Conversely, when $\mu_d > 1$, the number of defects surpasses the total site count, which is $2L$. In this scenario, the defect density reaches its maximum value of 1, since each site can only accommodate one defect, adhering to the exclusion principle.

If all the parameters except the binding constant remain constant and k_- approaches infinity, defects cease to attach to any site within the system. Consequently, defects no longer slow down the particle's movement on any lane, enabling particles to flow freely along the lanes without any hindrance.

4.7 Conclusion

In this work, we have attempted to study the non-equilibrium dynamics of a two-lane TASEP model with dynamic disorder under constrained entrances where particles travelling in opposite directions interact only at the boundaries. This disorder is incorporated in the form of defects that can appear and disappear stochastically from each site irrespective of the presence or absence of a particle on the respective sites. These defects when attached to a site, they act as an inhomogeneity by slowing down the movement of particles. The total number of particles and defects remains constant in the system and is characterized by the corresponding filling factors. The feature of reservoir crowding for the particles is incorporated which regulates the entry and exit of particles onto the lanes, while for the defects only the entry rate is affected.

The system has been analyzed by utilizing the continuum mean-field framework which neglects all kinds of correlations such as particle-particle, defect-defect and particle-defect. An important element of our theoretical approach is the reduction of the parameters associated with defect dynamics from four to one. The parameters that previously described binding, unbinding, defect quantity, and slowdown rate, all of which collectively governed the defect kinetics in the model, have been combined into a single parameter referred to as the scaling factor. This scaling factor effectively influences the overall particle flow within the system. Interestingly, it does not affect

the dynamics of the defect, which greatly reduces the complexity of the mathematical treatment.

Further, the incorporation of the narrow entrances at the entry-exit sites is dealt with by defining the effective entrance of particles to the lanes. This assists us in obtaining the explicit expressions for the particle densities, particle current and the corresponding phase boundaries for both symmetric as well as asymmetric phases. Our theoretical analysis uncovers the presence of up to seven attainable phases, including four symmetric and three asymmetric phases. Moreover, the impact of the global constraint on the number of particles is discussed, particularly on the qualitative topology of the stationary phase diagram. It has also been observed that the number of phases displayed shows a non-monotonic trend with increasing the number of particles in the system. The critical values at which the phases appear and disappear have also been calculated theoretically. Despite the symmetry in the dynamics of the two-lanes, the system manifests a spontaneous symmetry-breaking phenomenon that exhibits for all values of the filling factor. To thoroughly understand this phenomenon, a detailed analysis of the particle density histogram is conducted. An important consequence of including reservoir crowding in the model is the existence of a back-and-forth transition which is obtained by varying the intrinsic exit rate and keeping all other parameters fixed. Another remarkable feature is the sustained presence of a localized domain wall in the density profile since it persists for a very small number of particles in the system and continues to endure even for abundant particle resources.

Finally, incorporating defect dynamics into the system impacts not only the behaviour of defects themselves but also influences particle densities. As a consequence, the scaling factor translates the particle current, with no substantial impact on the system's stationary properties. Nevertheless, the system's characteristics are affected primarily in quantitative terms, leading to a shift in the phase boundaries. A brief discussion is provided on the effect of each parameter related to defect dynamics on the stationary system properties. Lastly, a random-sequential update method is employed for conducting Monte Carlo simulations of the system. The computational outcomes are in good agreement with the numerical results.

The main objective of this study was to elucidate the dynamic characteristics of the two-lane system under investigation, and the findings we presented successfully describe the impact of dynamic defects. We utilized a generic model that can be applied to gain insights into the behaviour of some non-equilibrium transportation processes, including both natural phenomena and human-made systems under the influence of reservoir crowding, constraint entrances and dynamic defects. This study can be further extended to incorporate a more realistic scenario involving a diffusive reservoir, where the entry and exit site serve as a sink and source for the particle concentration.

Chapter 5

Competition for resources in an exclusion model with biased lane-changing mechanism

In this chapter[1], inspired by the inclination of particles to adhere and separate from filaments and pathways, we introduce a two-lane TASEP model. One lane functions as a feeder, while the other operates as a receiver. We analyze this model within a constrained setting, where the influx of particles is controlled by the reservoir's density. We establish a theoretical framework by using vertical mean-field theory with singular perturbation technique. The analytical findings are supported by numerical and stochastic validation using a finite-difference scheme and the Gillespie algorithm.

5.1 Introduction

Despite the considerable research devoted to biased lane-changing mechanisms in the multi-lane exclusion model, there remains a notable gap in the literature regarding studies focused on limited particle resources. Our objective is to establish a theoretical framework for the system and explore the influence of restricted particle resources on stationary properties, while also characterizing its fundamental features. We employ the concept of boundary layer analysis to derive a comprehensive solution for the density profiles as well as the phase boundaries. These findings are then employed to construct a phase diagram that elucidates both bulk and surface transitions. The present research distinguishes itself from previous investigations in several ways. (i) A global constraint on particle resources is introduced. (ii) Lane-changing takes precedence over forward movement, with the former being a certain event. This means that the lane-changing mechanism is biased towards a specific lane. (iii) We provide explicit theoretical expressions for the stationary properties of the system. (iv) Validation of the results is carried out through numerical and stochastic approaches, utilizing finite difference methods and simulations. (v) Finally, boundary layer analysis is also performed.

[1]The content of this chapter is published in: "Ankita Gupta, Arvind Kumar Gupta. Competition for resources in an exclusion model with biased lane-changing mechanism. *Physical Review E,* 109(3):034132, 2024."

5.2 Description of the model

To mimic the transportation of entities along different pathways, we formulate a model that consists of two parallel one-dimensional lattices, identified as lane A and lane B, with each lane comprising of L sites. The sites are enumerated as $i = 1, 2, \ldots, L$, where the boundaries of each lane are represented by $i = 1$ and $i = L$, while the remaining sites constitute the bulk. In strict accordance with the hard-core exclusion principle, each lattice site is constrained to accommodate no more than a single particle.

Particles experience horizontal drifting as they engage in unidirectional motion from the left to the right along the lanes. Moreover, these lanes allow vertical mobility of particles; specifically, lane A facilitates desorption, while lane B functions as an absorption pathway as shown in Fig. (5.1). The extreme boundaries of the lanes (at site $i = 1$ and $i = L$) are connected to a reservoir with a finite capacity. This naturally imposes a restriction on the overall number of particles in the system. Let us use the notation N_t to signify the total number of particles in the system and $N_r(t)$ to represent the number of particles in the reservoir at any instant of time. Note that the reservoir has abundant capacity to contain all the particles present in the system. Moreover, this restriction influences the rates at which particles flow from the reservoir into the lanes, which will be elucidated later on. This arrangement creates a regulated environment in which the total number of particles on the lanes is determined by the interaction between the dynamics of interconnected lanes and the particle reservoir. At each time step, a site is chosen randomly and updated in accordance with the system's dynamic rules, which are delineated as follows:

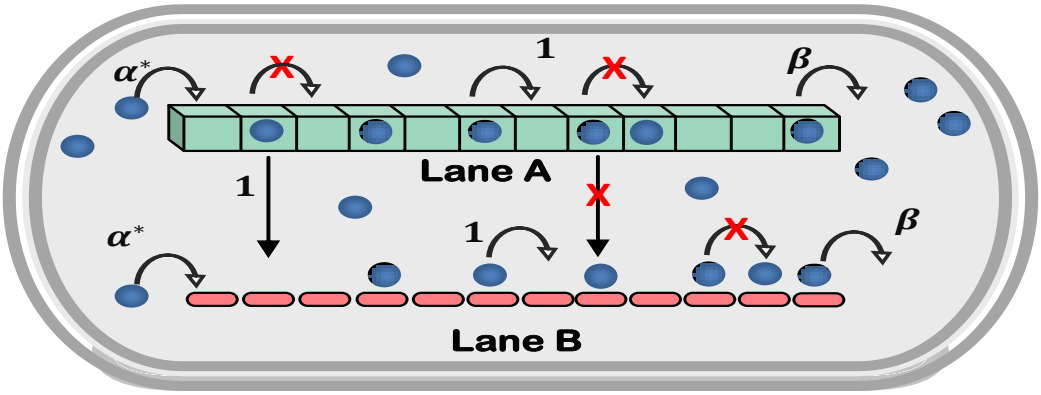

Figure 5.1: Illustration of the two-lane exclusion model with open boundaries. Lane A functions as a feeder lane, while lane B serves as an absorber lane. Arrows represent permissible transitions, while crosses indicate restricted transitions. The variables α^* and β represent the entry and exit rates, respectively.

- **Bulk sites:** For lane A, the displacement of a particle from the ith site relies on the status of the ith site on lane B. In case, site i on lane B is vacant, a particle from

the ith site of lane A is compelled to depart and then reconnects to the ith site on lane B at a unit rate. If the intended site on lane B is not vacant, the particle is then required to continue its horizontal movement along the lane with a unit rate, given that the neighbouring site is unoccupied. This indicates that a particle on lane A tends to prefer detachment over unidirectional movement.

- **Entrance site:** A particle from the reservoir has the potential to enter through the first site $i = 1$ of lane A at a rate of α^*, given that the respective site is unoccupied. In the presence of a particle at this site, it initially attempts to attach to the first site of lane B. If this attachment is not achievable, the particle then proceeds with its unidirectional movement along lane A.

- **Exit site:** A particle positioned at the Lth site on lane A, first tries to detach from its lane and attach to the last site of lane B, given that the target site is unoccupied. If no successful attachment occurs, the particle exits lane A at a rate of β to rejoin back the reservoir.

In lane B, particles enter from the initial site with a rate of α^* and move along the lane from left to right at a unit rate, following the exclusion principle. Upon reaching the final site, they return to the reservoir with a rate of β. Additionally, each unoccupied site in lane B can absorb incoming particles from the corresponding vertical site in lane A at a unit rate.

The extreme ends of the lanes are connected to a limited particle reservoir, indicating that the total particle count remains conserved in the system. This conservation is expressed by

$$N_t = N_r(t) + N_A(t) + N_B(t), \tag{5.1}$$

where $N_A(t)$ and $N_B(t)$ denote the number of particles on lanes A and B, respectively. Now, implementing a global constraint on the total particle count results in the regulation of the inflow rate of particles into the lanes based on the number of particles present in the reservoir. Generally, a diminished particle count in the reservoir suggests lower entry rates, while an increased reservoir content corresponds to elevated entrance rates. Therefore, it is rational to consider the entrance rate [110] as

$$\alpha^* = \alpha \frac{N_r(t)}{N_t}. \tag{5.2}$$

Here, α represents the inherent entrance rate of particles in the absence of any restrictions on the particle number. It is evident that $N_r(t) \leq N_t$, indicates that entry rates are bounded between 0 and α. As N_t tends towards infinity, the ratio N_r/N_t approaches 1, resulting in the convergence of α^* to α. In this scenario, our model

reduces to a well-examined two-lane coupled model with infinite resources [81,85]. If one eliminates the horizontal mobility of particles in lane B within the present model, it transforms into the model discussed in Ref. [158] under specific conditions. Moreover, the current model can be conceptualized as two parallel exclusion lanes where lane A exhibits diffusive dynamics and serves as a feeder for lane B, meanwhile, lane B exclusively involves the one-dimensional transport of particles.

5.3 Theoretical approach

The occupancy status of any site in the system can be expressed through a set of binary numbers denoted by τ_A^i and τ_B^i for lanes A and B, respectively, where i signifies the site number. This variable $\tau_A^i(\tau_B^i)$ is assigned a '0' if the ith site on lane A(B) is unoccupied and a '1' if it contains a particle.

The temporal variations in particle occupancy in the bulk sites ($1 < i < L$) of both the lanes, as outlined by the master equations, can be stated as follows:

$$\langle \dot{\tau_A^i} \rangle = J_A^{i-1} - J_A^{i-1} - \mathcal{V}^i, \qquad \langle \dot{\tau_B^i} \rangle = J_B^{i-1} - J_B^i + \mathcal{V}^i.$$

Here, J_j^i is the current passing from the site i to $i+1$ in lane j, ($j \in \{A,\ B\}$) and $\mathcal{V}^i$ is the vertical transverse current from lane A to B. Also, the symbol $\langle \dots \rangle$ represents the statistical average. The values of these particle currents involving one or two-point correlators can be expressed as

$$J_A^{i-1} = \langle \tau_A^i (1 - \tau_A^{i+1}) \tau_B^i \rangle, \quad J_B^i = \langle \tau_B^i (1 - \tau_B^{i+1}) \rangle, \quad \mathcal{V}^i = \langle \omega \tau_A^i (1 - \tau_B^i) \rangle, \tag{5.3}$$

where $\omega = 1$ is the detachment/attachment rate from/to lane A/B. At the boundary sites ($i = 1,\ L$), we have

$$\begin{aligned} \langle \dot{\tau_A^1} \rangle &= \alpha^* \langle (1 - \tau_A^1) \rangle - J_A^1 - \mathcal{V}^1, & \langle \dot{\tau_A^L} \rangle &= J_A^{L-1} - \beta \langle \tau_B^L \rangle - \mathcal{V}^L, \\ \langle \dot{\tau_B^1} \rangle &= \alpha^* \langle (1 - \tau_B^1) \rangle - J_B^1 + \mathcal{V}^1, & \langle \dot{\tau_B^L} \rangle &= J_B^{L-1} - \beta \langle \tau_B^L \rangle + \mathcal{V}^L. \end{aligned} \tag{5.4}$$

To analyze this system further, it is often satisfactory to apply simple mean-field theory [159] in which, the n-point correlation function is substituted with the product of n individual 1-point correlator functions neglecting all possible correlations.

5.3.1 Continuum limit

We derive the continuum version of the proposed model by coarse-graining the discrete lattice with a lattice constant $\epsilon = 1/L$ and transforming both space and time as $x = i/L \in [0, 1]$ and $t' = t/L$, respectively. Replacing the discrete variables τ_A^i and

τ_B^i with continuous variables $\rho_A^i(x)$ and $\rho_B^i(x)$, respectively, and retaining terms up to second-order in the Taylor series expansion, we obtain

$$\frac{\partial \rho_A}{\partial t'} = \frac{\epsilon \rho_B}{2}\frac{\partial^2 \rho_A}{\partial x^2} + J_A\frac{\epsilon}{2}\frac{\partial^2 \rho_B}{\partial x^2} + \epsilon(1-\rho_A)\frac{\partial \rho_A}{\partial x}\frac{\partial \rho_B}{\partial x} - \rho_B(1-2\rho_A)\frac{\partial \rho_A}{\partial x} - J_A\frac{\partial \rho_B}{\partial x} - L\rho_A(1-\rho_B), \tag{5.5}$$

$$\frac{\partial \rho_B}{\partial t'} = \frac{\epsilon}{2}\frac{\partial^2 \rho_B}{\partial x^2} + \frac{\partial J_B}{\partial x} + L\rho_A(1-\rho_B). \tag{5.6}$$

Note that the subscript i is dropped as each lane is free from inhomogeneity of any kind. The symbols J_A and J_B describe the bulk mean-field particle currents in lanes A and B given by $J_A = \rho_A(1-\rho_A)$ and $J_B = \rho_B(1-\rho_B)$, respectively. The last term in both the Eqs. (5.5) and (5.6) is a result of vertical coupling between the lanes. It is important to note that this term involves multiplication by the lattice length L, indicating the need to re-scale the coupling rates for observing competition between vertical and horizontal movements.

As the boundaries of each lane exhibit distinct behaviour compared to the bulk, it is necessary to examine their evolution discretely, as outlined in Eq. (5.4). At the steady state and in the continuum limit ($L \to \infty$), the density evolution equations at the boundaries simplify to $\rho_A(0) = \rho_B(0) = \alpha^*$ and $\rho_A(1) = \rho_B(1) = 1-\beta$.

The quantity of our interest is the solution of the system at steady-state which can be achieved by setting the time derivative equal to zero. Doing so leads to a set of singularly perturbed differential equations given by

$$\begin{aligned}\frac{\epsilon \rho_B}{2}\frac{\partial^2 \rho_A}{\partial x^2} + J_A\frac{\epsilon}{2}\frac{\partial^2 \rho_B}{\partial x^2} + \epsilon(1-\rho_A)\frac{\partial \rho_A}{\partial x}\frac{\partial \rho_B}{\partial x} - \rho_B(1-2\rho_A)\frac{\partial \rho_A}{\partial x} \\ - J_A\frac{\partial \rho_B}{\partial x} - L\rho_A(1-\rho_B) = 0, \\ \frac{\epsilon}{2}\frac{\partial^2 \rho_B}{\partial x^2} + \frac{\partial J_B}{\partial x} + L\rho_A(1-\rho_B) = 0.\end{aligned} \tag{5.7}$$

Roughly speaking in a singular perturbation problem [160], the transition as the limit $\epsilon \to 0$ is not gradual but rather abrupt. As the perturbation parameter ϵ diminishes, there is a sudden change in the nature of the problem. Typically, a singular perturbation problem arises when the perturbation parameter ϵ is introduced into a differential equation to scale the highest derivative in the equation. Consequently, as ϵ approaches 0, the order of the differential equation decreases, and the solution to the lower-order differential equation fails to satisfy all the boundary conditions or initial conditions at the same time. Thus, the solution experiences an abrupt cessation as ϵ tends to 0 indicating the formation of boundary layers. To find a global solution to the system, valid on the whole domain, we need to find two solutions: the inner-solution and the outer-solution. The outer-solution captures the behaviour away from the boundary

layer, while the inner-solution provides a detailed description of the boundary layer. Finally, it is essential to match these solutions effectively to derive the particle density at each site. We begin by exploring analytical and numerical methods to derive the outer-solutions.

5.4 Bulk solution

Here, we present two approaches for obtaining the outer-solution or the bulk particle density for each lane.

5.4.1 Numerical technique

In this context, we outline an approach to deduce the density profile of the system by numerically solving the continuum formulations of the partial differential equations as presented in Eqs. (5.5) and (5.6). This technique offers two primary benefits. Firstly, it is straightforward to implement and can be readily adapted for generalizations of the current model. Secondly, it proves valuable in situations where analytical treatment of the problem is unfeasible, providing an alternative means to derive solutions. The initial step involves discretizing the partial differential equation using a finite difference operator, following a similar approach as demonstrated in previous chapters (refer to Appendix (2.9)).

In the following section, we derive explicit expressions for the particle densities and currents at each site within both lanes. These expressions will simplify our task and facilitate a more comprehensive analysis of the stationary properties.

5.4.2 Cluster mean-field theory

To obtain explicit expressions for essential stationary properties in the current model, it is crucial to employ a theoretical framework that adequately accounts for correlations. An example of such a theory is the vertical cluster mean-field, which specifically addresses the behaviour of particles along the vertical direction. This methodology has proven to be valuable in accurately capturing the properties of various two-lane transport systems [81–85].

The current system allows for three types of vertical clusters: fully occupied, half-filled, and fully empty as shown in Fig. (5.2a). In the case of a fully filled vertical cluster, denoted as (11), both sites are occupied. On the other hand, scenarios (01) and (10) represent half-filled situations, with particles located in either lane A or lane B, respectively. Finally, an empty cluster is designated by (00). Let us define the probabilities for these potential configurations of a vertical cluster by P_{11}, P_{01}, P_{10},

and P_{00}. For the conservation of probabilities, it is necessary that

$$P_{00} + P_{10} + P_{01} + P_{11} = 1, \tag{5.8}$$

which is also called as the normalization condition. Thus, the bulk particle densities on each lane can be expressed by utilizing these vertical cluster probabilities as

$$\rho_A = P_{11} + P_{10}, \quad \rho_B = P_{11} + P_{01}. \tag{5.9}$$

The absence of any form of inhomogeneity in the bulk indicates a reasonable assumption that the cluster probabilities remain unaffected by the spatial position of the vertical cluster. Thus, the master equation governing the evolution of these vertical clusters can be expressed as

$$\frac{dP_{11}}{dt} = P_{01}P_{10} + P_{11}P_{01} + P_{11}P_{10} - 2P_{11}P_{00} - P_{11}P_{01} - P_{11}P_{10}, \tag{5.10}$$

$$\frac{dP_{10}}{dt} = 2P_{11}P_{00} + P_{11}P_{10} - P_{10}. \tag{5.11}$$

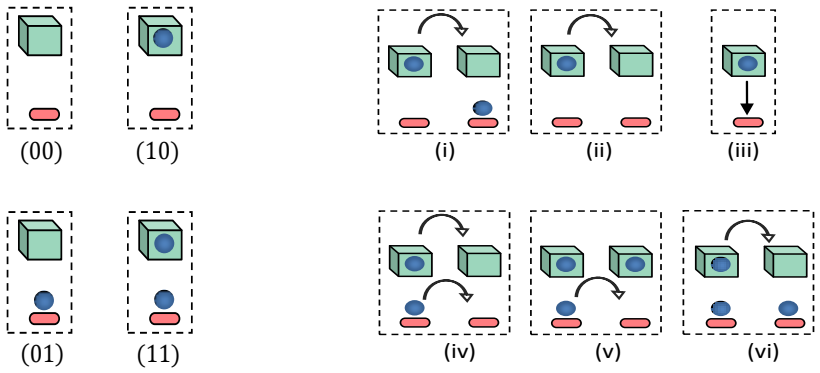

(a) (b)

Figure 5.2: (a) Possible states of a vertical cluster in the two-lane system. (b)Feasible transitions in a vertical cluster. (i) $P_{10}P_{01}$, (ii) $P_{10}P_{00}$, (iii) P_{10}, (iv) $P_{11}P_{00}$, (v) $P_{11}P_{10}$, and (vi) $P_{11}P_{01}$.

Each expression on the right-hand side can be easily comprehended through the visual representations depicted in Fig. (5.2b). The master equation corresponding to P_{01} can be formulated using a similar approach and deriving the equation for P_{00} becomes straightforward by applying the normalization condition outlined in Eq. (5.8).

Our primary objective is to discern the solutions corresponding to the long-term behaviour of the system. Consequently, we establish the following conditions:

$$\frac{dP_{00}}{dt} = \frac{dP_{10}}{dt} = \frac{dP_{01}}{dt} = \frac{dP_{11}}{dt} = 0. \tag{5.12}$$

By utilizing Eq. (5.8) as well as Eqs. (5.10) - (5.11) in Eq. (5.12), we derive the following set of equations written as

$$2P_{11}P_{00} = P_{01}P_{10}, \quad 2P_{11}P_{00} + P_{11}P_{10} = P_{10}. \tag{5.13}$$

These equations can be solved concurrently, leading to two distinct scenarios:

$$(i)\ P_{10} = P_{11} = 0, \qquad (ii)\ P_{10} = P_{00} = 0. \tag{5.14}$$

By applying the particle density expression for each lane as outlined in Eq. (5.9) to the above equations, we can draw two conclusions: In scenario (i) lane A displays zero particle density, whereas in (ii) lane B is entirely occupied with a particle density of 1.

Before proceeding with further analysis, it is essential to highlight that the system is subject to open boundary conditions. To conduct a comprehensive examination of the system, one must account for both the entry and exit currents from the system, represented by the following equations

$$\begin{aligned} J_A(0) &= \alpha^*(1 - P_{11} - P_{10}), \quad J_A(1) = \beta P_{11}, \\ J_B(0) &= \alpha^*(1 - P_{11} - P_{01}), \quad J_B(1) = \beta(P_{11} + P_{01}). \end{aligned} \tag{5.15}$$

Similarly, the bulk current for each lane can be stated by

$$J_A = P_{11}(1 - P_{11} - P_{10}), \quad J_B = P_{11} + P_{01}(1 - P_{11} - P_{01}). \tag{5.16}$$

As the particle current remains consistently continuous across the system, it allows us to establish a relationship between the bulk and boundary currents:

$$J_A(0) + J_B(0) = J_A + J_B = J_A(1) + J_B(1). \tag{5.17}$$

Now, we can leverage the fact that the system is connected to a finite particle reservoir with a reservoir occupancy of N_r. Returning to the particle number conservation (PNC) equation, as expressed in Eq. (5.1), we can restate it as

$$\mu = r + \frac{1}{2}\left(\int_0^1 \rho_A(x)dx + \int_0^1 \rho_B(x)dx\right). \tag{5.18}$$

In this context, $\mu = N_t/(2L)$ signifies the filling factor, which is a measure of the ratio of the total number of particles to the total number of sites in a system. Furthermore, we employ the variable r to denote the reservoir density.

Now, with all the essential components in hand, our attention shifts to a comprehensive analysis of the important stationary properties of the system. The

objective is to derive explicit expressions for both particle densities and reservoir density. This will be achieved by leveraging the solutions obtained from the vertical master equation, as indicated by Eq. (5.14), and by incorporating the principles of current continuity, as expressed in Eq. (5.17) and particle number conservation, as given in Eq. (5.18). These explicit expressions will subsequently be employed to quantify the stationary characteristics of the system, encompassing phase diagrams, density profiles, particle currents, and potential phase transitions.

Now, let us explore the possible stationary phases that could endure in the two-lane strongly coupled system with constrained resources. To begin, we employ the notation P/Q to represent a phase of the system, where P and Q signify a phase manifested by lanes A and B, respectively. Derived from the two solutions to vertical probabilities outlined in Eq. (5.14), two distinct scenarios emerge. (*i*) lane A exhibits zero particle density, whereas in case (*ii*) lane B is completely filled with a maximum particle density of 1. Both of these cases depict a condition of zero particle current, leading us to label the corresponding phases in the respective lanes as ZC_0 and ZC_1, where the subscript indicates the particle density. In each of these situations, the opposing lane can manifest any of the four phases: LD, HD, MC, and S. Now, we examine each of these situations individually.

5.4.2.1 Zero particle current in lane A: ($\mathbf{ZC_0/Q}$)

Let us start by considering the scenario where $P_{10} = P_{11} = 0$. According to Eq. (5.9), we get $\rho_A = 0$, signifying the case of zero particle density in lane A. Consequently, the particle currents given by Eqs. (5.15) and (5.16) are simplified to

$$\begin{aligned} &J_A(0) = \alpha^*, && J_A = 0, && J_A(1) = 0, \\ &J_B(0) = \alpha^*(1 - P_{01}), && J_B = P_{01}(1 - P_{01}), && J_B(1) = \beta P_{01}. \end{aligned} \tag{5.19}$$

With $P_{10} = 0$ and $P_{11} = 0$ in this system, the vertical cluster (01) can be interpreted as particles, and the corresponding holes are denoted by (00). Thus, the two-lane system can be viewed as one-lane system with some entrance rate α^{eff} and exit rate β. Here, lane A is in the ZC_0 phase and the other lane can assume one of the following phases: LD, HD, MC, or S. Now, we scrutinize each of these phases individually.

1. **$\mathbf{ZC_0}$/LD phase.** In this entrance dominated phase, the particle current is governed by the entry parameter implying that $P_{01} = \alpha^{eff}$. By utilizing the continuity of current across the lanes, we can write

$$\alpha^{eff}(1 - P_{01}) = \alpha^* + \alpha^*(1 - P_{01}).$$

The above can be solved to calculate the expression for the effective entrance rate

as

$$\alpha^{eff} = \frac{1}{2}\left(1 + \alpha^* - \sqrt{(1+\alpha^*)^2 - 8\alpha^*}\right), \tag{5.20}$$

which is valid for $\alpha^* < \frac{1}{6}$ We must recall that the parameter α^* is regulated by the reservoir density r and the filling factor μ. Thus, we exploit the particle conservation criteria given by Eq. (5.18), which can be restated as $\mu = r + \alpha^{eff}/2$ and then solved to determine the value of reservoir density as

$$r = \frac{1}{2(\alpha + 2\mu)}\left(\alpha(\mu-1) + \mu(4\mu-1) + \sqrt{\alpha^2(\mu-1)^2 + 2\alpha(1-3\mu)\mu + \mu^2}\right).$$

The existential criteria for this phase can be written as follows

$$\alpha^{eff} < \beta, \quad \alpha^* < \frac{1}{6}. \tag{5.21}$$

In the limit, $\mu \to \infty$, α^* tends to converge to α. This results in the effective rate α^{eff} matching the calculated effective rate for this phase when resources are infinite, as detailed in Ref. [81].

2. **ZC_0/HD phase.** Here, lane A remains in the zero current phase while lane B displays high density phase. The current continuity equation in this case takes a simplified form

$$P_{01}(1 - P_{01}) = \beta P_{01} \implies P_{01} = 1 - \beta. \tag{5.22}$$

Utilizing PNC, we retrieve the reservoir density $r = \frac{2\mu - 1 + \beta}{2}$. The feasible region corresponding to phase requires β to remain less than 0.5 and the effective entrance rate which leads to

$$\frac{2\mu\beta(1-\beta)}{(2-\beta)(2\mu - 1 + \beta)} < \alpha < \frac{2\beta\mu}{(2\mu - 1 + \beta)}. \tag{5.23}$$

Clearly, when $\mu \to \infty$, the condition for the existence of a (0/HD) phase in a system with no constraint on particle resources is recovered [81].

3. **ZC_0/MC phase.** Let us assume that lane B exhibits maximal current phase with particle density given by 0.5 and current equal to 0.25. In such a scenario, we get $P_{00} = P_{01} = 0.5$. By particle number conservation, the value of reservoir density can be procured as

$$r = \mu - 0.25. \tag{5.24}$$

Moreover, the other parameters are $\alpha^{eff} = 3\alpha^*$ and $\alpha^* = \frac{\alpha(4\mu-1)}{4\mu}$. Using all these expressions, the condition for the existence of this phase can be framed by

$$\max\left\{\alpha^*, \frac{1}{2}\right\} < \beta, \quad \frac{1}{6} < \alpha^* < \frac{1}{2}. \tag{5.25}$$

As μ approaches infinity, the expression for the effective entry rate coincides with the scenario involving infinite resources, as documented in Ref. [81].

4. **ZC_0/S phase.** Presume that lane A displays particle density 0, while lane B exhibit a discontinuity in the density profile connecting a section of low density on the left to a section of high density on the right. We prefer to denote the position of this sudden transition in lane B by x_B.

   As lane B is in the low density phase on the left, we observe that $P_{01} = \alpha^{eff}$ near the left boundary, and the effective entrance rate remains the same, as indicated by Eq. (5.20). The criteria for the persistence of the shock phase require that the entry rate must be equal to the exit rate, thus leading to

$$r = \frac{\beta\mu(1-\beta)}{\alpha(2-\beta)}. \tag{5.26}$$

   The only variable remaining to be determined is the position of the shock, which can be derived from the conservation of particles and expressed in a simplified form as

$$x_B = \frac{1-\beta-2(\mu-r)}{\alpha(2-\beta)}. \tag{5.27}$$

   Finally, the boundary parameters must satisfy the following to display this phase:

$$0 < x_B < 1, \quad \beta < 0.5. \tag{5.28}$$

   This phase ceases to exist in case $\mu \to \infty$.

5.4.2.2 Zero particle current in lane B: (P/ZC_1)

Now, let's consider the alternate scenario where $P_{00} = P_{10} = 0$. As a consequence, the particle density in lane B reaches its maximum value of 1, resulting in zero particle current. The revised value of the particle currents are detailed as follows:

$$\begin{aligned} &J_A(0) = \alpha^*(1-P_{11}), \quad J_A = P_{11}(1-P_{11}), \quad J_A(1) = \beta P_{11}, \\ &J_B(0) = 0, \qquad\qquad J_B = 0, \qquad\qquad J_B(1) = \beta. \end{aligned} \tag{5.29}$$

In this situation, particles in lane B are represented by the fully filled vertical cluster (11), while a vacancy corresponds to (10). Consequently, in this case, the two-lane system can be conceptualized as a one-dimensional TASEP system with an entry rate of α^* and an effective exit rate denoted by β^{eff}. Also, lane B remains in the ZC_1 phase, while lane A can exhibit any of the four phases: LD, HD, MC, and S.

1. **HD/ZC_1 phase.** The stationary particle density of lane A is given by $1 - \beta^{eff}$,

while that of lane B is 0. This relationship implies that $P_{11} = 1 - \beta^{eff}$. Applying the current continuity principle, we have

$$P_{11}(1 - P_{11}) = \beta P_{11} + \beta = \beta^{eff} P_{11}. \tag{5.30}$$

Solving this equation yields the value of the effective exit rate as

$$\beta^{eff} = \frac{1}{2}\left(1 + \beta - \sqrt{(1+\beta)^2 - 8\beta}\right). \tag{5.31}$$

Now we make use of Eq. (5.18) to calculate reservoir density expressed as

$$r = \frac{1}{4}\left(\beta - 3 + 4\mu - \sqrt{1 - 6\beta + \beta^2}\right). \tag{5.32}$$

Finally, the conditions fulfilled by this phase are delineated as

$$\beta^{eff} < \alpha^*, \quad \beta < \frac{1}{6}. \tag{5.33}$$

2. **LD/ZC$_1$ phase.** During this phase, we assume that lane A portray the LD phase. In such scenarios, $P_{11} = \alpha^*$ and the reservoir density is given by

$$r = \frac{\mu(2\mu - 1)}{\alpha + 2\mu}. \tag{5.34}$$

Under these circumstances, the existential condition for this phase is

$$\frac{\alpha^*(1 - \alpha^*)}{2 - \alpha^*} < \beta < \alpha^* < \frac{1}{2}. \tag{5.35}$$

3. **MC/ZC$_1$ phase.** During this phase, lane A experiences a maximal current phase with particle density given by 0.5. So, we have $P_{11} = P_{01} = 0.5$. The resulting reservoir density is given by $r = \mu - 0.75$. The effective exit rate can be obtained straightforwardly as $\beta^{eff} = 1 - \beta$. Therefore, this phase persists only when

$$\frac{1}{6} < \beta < \frac{1}{2} < \alpha^*. \tag{5.36}$$

4. **S/ZC$_1$ phase.** In this scenario, a shock persists in lane A, linking a segment with particle density α^* on the left to a region with particle density $1 - \beta^{eff}$ on the right, separated at the point denoted by x_A. The effective exit rate retains the same value as expressed in Eq. (5.31). For lane A to display the shock phase, it must adhere to

the condition $\alpha^* = \beta^{eff}$, providing us with the reservoir density expressed as

$$r = \frac{\mu\left(1+\beta-\sqrt{1-6\beta+\beta^2}\right)}{2\alpha}. \tag{5.37}$$

Revisiting Eq. (5.18) allows us to calculate the shock position in this case, given by

$$x_A = \frac{2-\alpha^*-2(\mu-r)}{1-2\alpha^*}. \tag{5.38}$$

Hence, the determined region for this phase must meet the criteria of $0 < x_A < 1$ in conjunction with $\alpha^* < 0.5$. This phase vanishes when μ tends to 0.

In addition to the aforementioned phases, several other phases are observed, arising from the combination of the two scenarios. During these phases, certain region of the system exhibit $\mathrm{P/ZC_1}$, while the remaining part displays $\mathrm{ZC_0/Q}$. Considering that particle current must remain continuous across each lane, these two scenarios can be appropriately aligned.

5.4.2.3 Other phases

We choose to represent these phases as R-S/M-N, where R(S) indicates the type of stationary phase on the left(right) of lane A, while M(N) denotes the stationary phase on the left(right) of lane B. The stationary properties for such phases are discussed below.

1. **LD-$\mathrm{ZC_0}$/$\mathrm{ZC_1}$-HD phase.** In this phase, we observe a $\mathrm{LD/ZC_1}$ phase on the left connected to a $\mathrm{ZC_0/HD}$ region on the right, and the position of the domain wall in each lane is represented by x_A and x_B. As mentioned previously, this phase can be visualized as two single-lane TASEP models. The first has an entry rate of α^* and an exit rate of β^{eff}, while the other subsystem has α^{eff}-β as the boundary parameters.

   To ensure current continuity in the system, the shock position must be synchronized between both lanes. Therefore, we employ the notation x_s to represent the common shock position. Additionally, for the system to maintain the shock phase, we must have $\alpha^{eff} = \beta^{eff}$, which leads to the condition $\alpha^* = \beta$, enabling us to derive the reservoir density as $r = \beta\mu/\alpha$. To determine the position of the shock in this phase, we use the conservation of particles, transforming Eq. (5.18) into:

$$\mu = r + \frac{1}{2}\left[\int_0^{x_s}(\alpha^*+1)dx + \int_{x_s}^{1}(0+1-\beta)dx\right] \tag{5.39}$$

   which yields

$$x_s = \frac{2(\mu-r)-(1-\beta)}{2\beta}. \tag{5.40}$$

Thus, the identified region in the phase diagram corresponding to this phase is

$$0 < x_s < 1, \quad \beta < 0.5. \tag{5.41}$$

In the presence of an infinite supply of particles, this phase does not persist.

2. **MC-ZC_0/ZC_1-MC phase.** Here, the left bulk of the system remains in MC/ZC_1 phase while the right bulk displays ZC_0/MC phase. As elaborated in the preceding case, the synchronization of the shock position between two lanes is evident. Specifically, the particle density in each lane can be written as

$$\rho_A = \begin{cases} 0.5, & \text{if } 0 < x < x_s, \\ 0, & \text{if } x_s < x < 1, \end{cases} \quad \rho_B = \begin{cases} 1, & \text{if } 0 < x < x_s, \\ 0.5, & \text{if } x_s < x < 1, \end{cases} \tag{5.42}$$

where x_s gives the common shock position. Therefore, this phase is entirely dominated by the bulk. The position of the shock can be determined by applying particle-hole symmetry.

In the limit as μ approaches infinity, the shock position stabilizes at 0.5 [81], leading us to characterize this phase as a Meissner phase.

The analysis presented thus far yields the outer-solution, representing the bulk particle density for both lanes. Now, we will explore the methodology for calculating the inner-solutions associated with each phase.

5.5 Inner-solution: Boundary layer analysis

To elucidate the characteristics of the boundary layer, we first analyze the behaviour of the system in the thermodynamic limit. Under this condition, Eq. (5.7) transforms into a set of first-order differential equations, each accompanied by two boundary conditions, resulting in an over-determined system. In such cases, a boundary layer is observed either within the bulk or at the boundaries. The solution of the first-order differential equations is called the outer or bulk solution and delineates the major portion of the density profile, whose thorough analysis has been conducted in the preceding section. Such a solution will be denoted by ρ_A^b and ρ_B^b for the two lanes.

Here, we provide a summary of the methodology associated with obtaining the boundary layer solution. For a comprehensive understanding, readers can refer to Ref. [161]. The outer-solution satisfies a first-order differential equation, accommodating at most a single boundary condition. To address the other condition, a boundary layer emerges within the density profile. This layer must adhere to two essential criteria: (i) It must fulfill the other boundary condition, and (ii) it must asymptotically approach the

outer-solution. Generally, the boundary layer satisfies one boundary condition, while the outer-solution addresses the other. Nevertheless, in certain scenarios, a boundary layer within the system's bulk can separate two outer-solutions, each of them meeting one of the boundary conditions. Therefore, it can be concluded that the presence of this layer is not confined solely to the peripheries or boundaries of the system. This boundary layer solution is referred to as the inner-solution and is denoted by ρ_A^{in}/ρ_B^{in}.

In the preceding section, we have successfully determined the outer-solution by examining two distinct situations: the first involving zero particle current along with density zero in lane A, and the second featuring zero particle current in lane B but with a maximum particle density set at 1. Since the boundary layer solution must asymptotically align with the outer-solution, it is crucial to compute the inner-solution while taking into account the characteristics of the outer-solution.

1. **Zero particle current in lane A.** As elucidated earlier, the stationary characteristics in this scenario are dictated by Eq. (5.19), where both the particle current and density in the bulk as well as at the exit sites of lane A are precisely zero, but a non-zero particle current is present at the entrance site. Consequently, we expect the existence of a boundary layer merely at the left boundary in lane A.

   Our primary objective now is to compute the boundary layer or the inner-solution pertaining to lane B. We have the following continuum system at the steady state

   $$\frac{\epsilon}{2}\frac{\partial^2 \rho_B}{\partial x^2} + (1 - 2\rho_B)\frac{\partial \rho_B}{\partial x} = 0. \tag{5.43}$$

   To derive a boundary layer solution, it is convenient to introduce a re-scaled variable, denoted as $a = (x - x_0)/\epsilon$, where x_0 signifies the location of the boundary layer. If there is a boundary layer at the left end, x_0 is set at 0, and with ϵ approaching 0, the variable a tends towards ∞. Similarly, in case $x_0 = 1$, then $a \to -\infty$ as $\epsilon \to 0$.

   Now, in terms of the re-scaled position, the differential equation given by Eq. (5.43) gets modified to

   $$\frac{1}{2}\frac{d^2 \rho_B^{in}}{da^2} + (2\rho_B^{in} - 1)\frac{d\rho_B^{in}}{da} = 0, \tag{5.44}$$

   which on integrating once yields

   $$\frac{1}{2}\frac{d\rho_B^{in}}{da} - \rho_B^{in}(1 - \rho_B^{in}) = k_0, \tag{5.45}$$

   where k_0 is the constant of integration. Calculating the value of this constant using the criteria that the inner-solution must saturate to the outer-solution gives $k_0 =$

$\rho_B^b(\rho_B^b - 1)$. Further integration yields:

$$\begin{aligned} \rho_B^{in}(a) &= \frac{1}{2} + \frac{|2\rho_B^b - 1|}{2}\coth\left(a|2\rho_B^b - 1| + k_2\right), \\ \rho_B^{in}(a) &= \frac{1}{2} + \frac{|2\rho_B^b - 1|}{2}\tanh\left(a|2\rho_B^b - 1| + k_2\right). \end{aligned} \tag{5.46}$$

Here, $\frac{1}{|2\rho_B^b - 1|}$ is the width of the boundary layer with respect to a and the constant k_2 gives the centre of the boundary layer. Moreover, these constants depend on the boundary condition that the inner-solution satisfy.

We adopt the notation T_k/C_k to describe a boundary layer of tanh / coth type as given by Eq. (5.46) for the different phases of the system. Here, k can take the values l, b, or r indicating the presence of a boundary layer at the left end, in the bulk, or at the right end, respectively. In the following discussion, we scrutinize each of the previously mentioned scenarios regarding the outer-solution for their corresponding boundary layer solutions.

- **ZC$_0$/LD phase.** In this particular case, the outer-solution for lane B satisfies the left boundary condition at $x = 0$, clearly indicating the manifestation of a boundary layer at the right end. Here, the corresponding bulk densities are $\rho_A^b = 0$ and $\rho_B^b = \alpha^{eff}$, where α^{eff} is determined by Eq. (5.20).

  In lane A, only the entry current is non-zero, giving rise to a boundary layer of C_l type characterized by a positive slope. On the other lane, two distinct types of boundary-layer solutions appear in the vicinity of the boundary at $x = 1$ depending upon the entry-exit parameters. When $\alpha^{eff} < 1 - \beta$, the boundary layer exhibits a positive slope, and the corresponding inner-solution follows a tanh-type profile. Conversely, when $\alpha^{eff} > 1 - \beta$, the boundary layer displays a negative slope, and the inner-solution takes on a coth-type profile. Thus the two types of boundary layers in this case are denoted by C_l/T_r and C_l/C_r which are separated by the boundary $\alpha^{eff} = 1 - \beta$. We prefer to use the term 'surface transitions' to describe such changes occurring within a specific phase.

- **ZC$_0$/HD phase.** Similar to the previous case, a boundary layer of C_l type emerges in lane A. The outer-solution in lane B is an exit-dominated phase and adheres to the right boundary condition, while the inner-solution satisfies the condition at $x = 0$. When $1 - \beta < \alpha^{eff}$, the boundary layer must have a positive slope, making it necessary to employ a coth-type inner-solution. Conversely, when $1 - \beta > \alpha^{eff}$, the boundary layer, featuring a negative slope, is associated with a tanh-type solution. Therefore, the boundary layer solution C_l/T_l is distinguished from C_l/C_l by the line $\alpha^{eff} = 1 - \beta$.

- **ZC$_0$/S phase.** In this context, a stationary shock emerges in the density profile

of lane B, connecting a region of LD phase with a particle density of $\alpha^{eff} = \alpha^*$ to an HD phase with density $1 - \beta$. The position of this shock is denoted as x_B and is determined by Eq. (5.27). Consequently, the outer-solution comprises of two segments: one with a density less than 0.5 (on the left) and the other greater than 0.5. This gives rise to a boundary layer of the tanh-type, thus labelled as C_l/T_b.

- **ZC_0/MC phase.** Here, lane B exhibits a maximal current phase where the bulk density is precisely equals 0.5. To satisfy the two boundary conditions, specifically $\rho_B(0) = \alpha^*$ and $\rho_B(1) = 1 - \beta$, a boundary layer must be present at each end. The conditions for the existence of this phase are $\alpha^* > 0.5$ and $\beta > 0.5$, implying that $\rho_B(1) < 0.5 < \rho_B(0)$. Consequently, a boundary layer of coth-type appears at both ends and can be denoted as $C_l/C_{l,r}$.

2. **Zero particle current in lane B.** The stationary particle currents in this instance are determined by Eq. (5.29), indicating the emergence of a boundary layer on the right boundary of lane B. Following a similar procedure as in the previous case, two types of boundary layers are identified, labelled as tanh-type and coth-type.

   - **HD/ZC_1 phase.** In this case, two distinct types of boundary conditions are observed: T_l/C_r and C_l/C_r which are distinguished by the line $\alpha^* = 1 - \beta^{eff}$.
   - **LD/ZC_1 phase.** A tanh-type boundary layer is observed in lane A when $\alpha^* < 1 - \beta^{eff}$, whereas it is of coth-type when $\alpha^* > 1 - \beta^{eff}$.
   - **S/ZC_1 phase.** A stationary shock phase manifests in the density profile with the shock position denoted as x_A. The corresponding boundary layer is characterized by T_b/C_r.
   - **MC/ZC_1 phase.** In this case, a boundary layer of the type $C_{l,r}/C_r$ emerges in the density profile.

3. **Other phases.** As previously explained, in such phase, lane A exhibits the P-ZC_0 phases, while the other displays the ZC_1-Q phase.

   - **LD-ZC_0/ZC_1-HD phase.** In this phase, the boundary layer is not limited to the boundaries; rather, it manifests in the bulk in the form of a shock at the position x_s, thus taking on the form of C_b/C_b.
   - **MC-ZC_0/ZC_1-MC phase.** Applying a similar approach, in this case, a boundary layer of the type $C_{l,b}/C_{b,r}$ emerges.

5.6 Results and discussion

In this section, we conduct a thorough exploration of the steady-state characteristics within the proposed model, with a particular emphasis on the stationary phase

diagrams. To validate the theoretical findings, we perform Kinetic Monte Carlo simulations (akin to Gillespie Algorithm) with the lattice size of each lane $L = 1000$. These simulation points are graphed with an accuracy of less than 2% in each figure, a precision reflected by the size of the symbols employed in the plots.

5.6.1 Stationary phase diagrams

We examine the stationary behaviour of the system under different filling factors in the $\alpha - \beta$ phase plane. The values of μ are selected such that they explain all the possible and crucial structural changes in the phase diagrams.

Figure (5.3) presents stationary phase diagrams for various filling factor values, capturing topological changes and providing a comprehensive characterization of phases through their boundary layers. Solid lines denote bulk transitions, while dashed lines indicate surface transitions. Theoretical critical values for μ that correspond to qualitative changes can be obtained from Eqs. (5.24), (5.35), and (5.33) and are given by

$$\mu_{c_1} = 0.25, \quad \mu_{c_2} = 0.5, \text{ and } \mu_{c_3} = 0.75. \tag{5.47}$$

For $\mu \leq \mu_{c_1}$, the phase diagram is characterized by only two stationary phases: ZC_0/LD and ZC_0/S (refer to Fig. (5.3a)). As μ increases within the range $\mu_{c_1} \leq \mu \leq \mu_{c_2}$, four distinct phases emerge, namely ZC_0/HD, ZC_0/MC, LD-ZC_0/ZC_1-HD, and MC-ZC_0/ZC_1-MC, as evident from Fig. (5.3b). Beyond the critical value μ_{c_2}, the system undergoes substantial topological changes both qualitatively and quantitatively, with the addition of LD/ZC_1 and S/ZC_1 phases. So, the phase schema now exhibits a total of 8 phases, as depicted in Fig. (5.3d). The domain occupied by the MC-ZC_0/ZC_1-MC phase can be classified into two types. In one, the position of the shock is contingent upon the boundary parameters $\alpha-\beta$, while in the other, the position is consistently fixed at 0.5, no longer influenced by the rates α and β. Thus, the latter case can be categorized as a Meissner phase. After the critical value μ_{c_3}, two new phases emerge in the phase diagram namely, MC/ZC_1 and HD/ZC_1 as shown in Fig. (5.3e). At this point, the phase diagram displays the maximum number of phases and includes all possible phases for the system. A further increase in the value of μ results in the shrinkage and expansion of the phase regions (see Fig. (5.3f) - Fig. (5.3h)). Finally, in the limit $\mu \to \infty$, the phase diagram becomes much simpler, consisting of only seven phases as shown in Fig. (5.3i) and the results of Ref. [81] are recovered.

Now, we would like to emphasize a few observations that can be derived from these phase diagrams. In all the phases of the form ZC_0/Q where Q $\in$ {LD, HD, MC, S}, as confirmed by Eq. (5.19), particles enter both lanes, but exit exclusively from lane B. The detachment(attachment) of particles from(to) lane A(B) compels the particles to swiftly shift to lane B upon entry through lane A. Consequently, particle progression

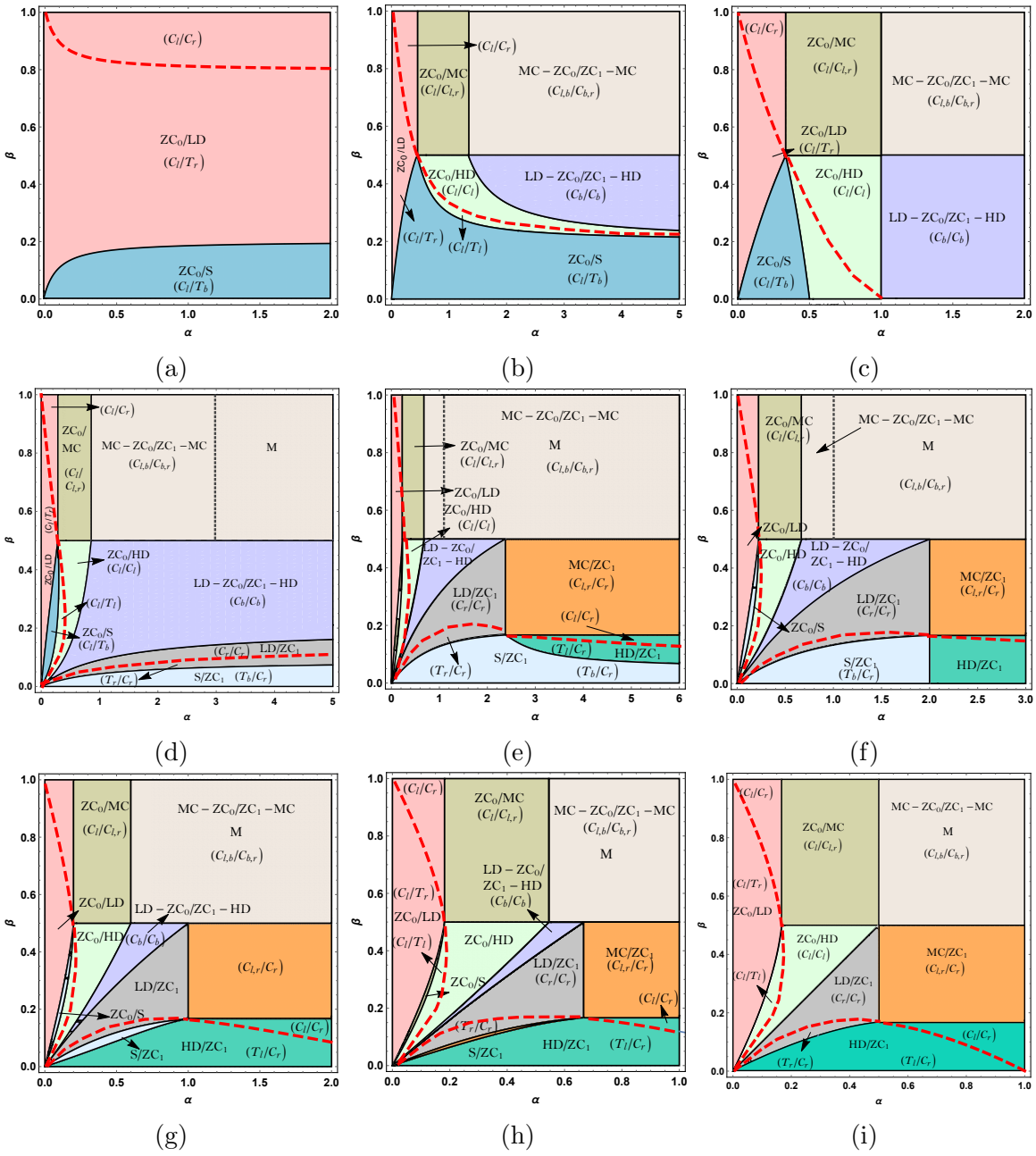

Figure 5.3: Phase diagrams for stationary states for different values of μ: (a) $\mu = 0.1$, (b) $\mu = 0.4$, (c) $\mu = 0.5$, (d) $\mu = 0.6$, (e) $\mu = 0.9$, (f) $\mu = 1$, (g) $\mu = 1.5$, (h) $\mu = 3$, and (i) $\mu \to \infty$. Each diagram delineates both bulk and surface transitions, categorized through boundary layer analysis. Solid lines denote bulk transitions, while dashed (thick red) lines describe surface transitions. M designates the Meissner phase phase corresponding to MC-ZC_0/ZC_1-MC phase which is independent of the boundary parameters.

occurs solely along lane B. In phases exhibiting zero particle current in lane B and density equal to 1 (P/ZC_1 form), particles enter exclusively through lane A, yet they exit through both lanes. It is evident from Fig. (5.3) that these phases exist primarily for smaller values of β, indicating that a slow exit rate results in the accumulation of particles in lane B until a point is reached where no particle movement becomes

possible. Thus, the mobility of the particles is only possible in lane A.

A noteworthy observation in the current system is the identification of two phases characterized by downward shocks. Typically a downward shock refers to a sudden and significant decrease in the particle density. Such types of shocks are observed in LD-ZC_0/ZC_1-HD phase and MC-ZC_0/ZC_1-MC phase. In LD-ZC_0/ZC_1-HD phase, the position of the downward shock is given by Eq. (5.40) which depends upon two parameters μ and β. This shock links a segment in the low density phase on the left to the zero density phase on the right in lane A. Simultaneously, in lane B, it connects a region with particle density 1 on the left to the high density phase on the right. Furthermore, the location of this downward shock is coordinated in both lanes. A similar observation applies to the MC-ZC_0/ZC_1-MC phase, but the downward shock remains within the interval $[0, 0.5]$. When this position is precisely equals 0.5, we prefer to characterize the phase as the Meissner phase, as in this case, the density profiles are independent of the boundary parameters $\alpha - \beta$. In these phases, the entry of the particles is limited solely through lane A. However, owing to the attachment-detachment mechanism, their exit is exclusively facilitated through lane B. Now, we will discuss each of these shock phases in detail in the upcoming section.

5.6.2 Shock dynamics and phase transitions

In this section, we commence our discussion by scrutinizing the characteristics of the diverse types of shocks present in the system. There are four phases involving a discontinuity in the density profiles, namely ZC_0/S, S/ZC_1, LD-ZC_0/ZC_1-HD, and MC-ZC_0/ZC_1-MC. In the former two phases, there is an upward shock confined to only one lane. Conversely, the latter two phases display a synchronized downward shock in both lanes.

5.6.2.1 Upward unsynchronized shock

Initially, our attention is directed towards examining how the shock propagates in ZC_0/S and S/ZC_1 phase concerning variations in both the entry and exit rates. This analysis relies on the analytical expression derived in Sections (5.4.2.1) and (5.4.2.2). The shock's velocity in ZC_0/S and S/ZC_1 phases is given by

$$V = \begin{cases} \beta - \alpha^{eff}, & \text{for } ZC_0/S \text{ phase}, \\ \beta^{eff} - \alpha^{*}, & \text{for } S/ZC_1 \text{ phase}, \end{cases}$$

where α^{eff} and β^{eff} is given by Eq. (5.20) and (5.31), respectively. To achieve a stationary shock, the velocity must be zero, indicating that $\beta = \alpha^{eff}$ and $\beta^{eff} = \alpha^{*}$.

The position of the shock can be represented as

$$x_B = \frac{1-\beta-2(\mu-r)}{\alpha(2-\beta)}, \quad x_A = \frac{2-\alpha^*-2(\mu-r)}{1-2\alpha^*},$$

corresponding to ZC_0/S and S/ZC_1 phase, respectively. To analyze the behaviour of

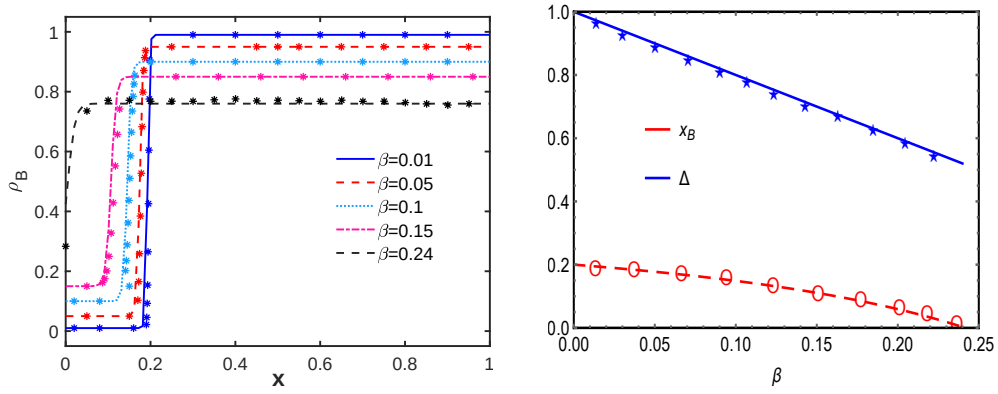

(a) (b)

Figure 5.4: (a) Density profiles of particles in lane A with $\alpha = 2$, $\mu = 0.4$, and $\beta = 0.01,\ 0.05,\ 0.1,\ 0.15$, and $\beta = 0.24$. (b) Position and height of the shock in ZC_0/S phase with respect to β for fixed $\alpha = 2$ and $\mu = 0.4$. The variable $\Delta = 1-\beta-\alpha^{eff}$ gives the height of the shock. Symbols describe Monte Carlo results, while solid/dashed/dotted lines correspond to theoretical findings.

the shock in the ZC_0/S phase, we fix $\mu = 0.4$ and $\alpha = 2$ and systematically vary the exit rate β. In Fig. (5.4), we present density profiles, shock position, and shock height for different values of β, providing a visual representation of the shock's dynamics. The observation reveals that with increasing β, the shock moves from the left towards the right and eventually reaches the left boundary of lane B, as depicted in Fig. (5.4). Furthermore, the shock height decreases linearly with respect to β. The corresponding value of height of the shock is $\Delta = 1-\beta-\alpha^{eff} = 1-2\beta$ and maintains a positive value as x_B approaches 0. This phenomenon suggests the existence of a tanh-type boundary layer at the left end, signifying a transition from the ZC_0/S phase to the ZC_0/HD phase. Physically, this can be understood as follows. When $\beta = 0$, signifying a zero exit rate, particles tend to accumulate near the right end of lane B. As a result, the particle number in the reservoir increases, ultimately enhancing the effective entry rate. Consequently, the particle density at the left end rises while at the right end, it decreases, resulting in a reduction in the height of the shock. Conversely, in investigating the propagation of the shock with fixed $\mu = 0.4$ and $\beta = 0.2$, while varying α, it is noted that the rapid movement of x_A inversely correlates with α, causing the shock height to shift swiftly from 1 to 0 (see Fig. (5.5)). Meanwhile, the shock height maintains a steady value of $1-2\beta$.

Comparable analyses can be employed to investigate the S/ZC_1 phase. When

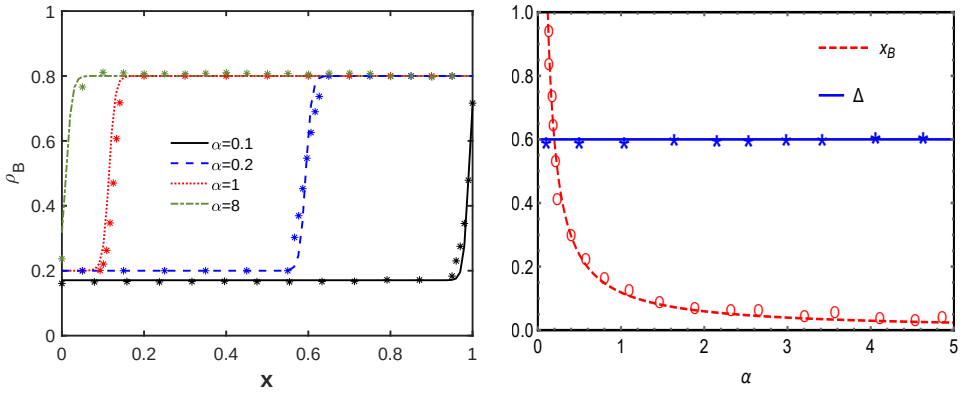

(a) (b)

Figure 5.5: (a) Density profiles of particles in lane A with $\beta = 0.2$, $\mu = 0.4$, and $\alpha = 0.1,\ 0.2,\ 1$, and $\beta = 8$. (b) Position and height of the shock in ZC_0/S phase with respect to α for fixed $\beta = 0.2$ and $\mu = 0.4$. The variable $\Delta = 1 - \beta - \alpha^{eff}$ gives the height of the shock. Symbols describe Monte Carlo results, while solid/dashed/dotted lines correspond to theoretical findings.

(μ, β) is fixed at $(0.9, 0.1)$, the shock consistently moves towards the left and its height stabilizes at a constant value of $-\beta + \sqrt{1 - 6\beta + \beta^2}$ which can be computed by utilizing Eq. (5.38).

5.6.2.2 Downward synchronized shock

Now, we explore the shock dynamics for the phases involving synchronized shocks in both lanes. Employing $\mu = 1$ and $\beta = 0.4$, we continuously increase the entry rate of the particles (refer to Fig. (5.6)). The position and the height of the shock in this category is given by

$$x_s = \frac{2(\mu - r) - (1 - \beta)}{2\beta}, \quad \Delta = \beta. \tag{5.48}$$

The system enters this phase at $\alpha \approx 0.58$ just before which the system manifests the ZC_0/HD phase. As the value of α increases, the position of the boundary layer starts shifting from the left end of the lanes to enter the bulk of both the lanes and thus the system exhibits the LD-ZC_0/ZC_1-HD phase constituting a downward shock in each lane. At the critical value of $\alpha \approx 1.34$, this downward shock reaches the right end of the lanes and the system transitions into LD/ZC_1 phase. However, no change in the height of the shock occurs, finally, a boundary layer of coth-type is detected in LD/ZC_1 for both lanes. From the above analysis, one can conclude that a second-order transition occurs from ZC_0/HD to LD-ZC_0/ZC_1-HD to LD/ZC_1 phase if one considers particle density as the order parameter.

Upon investigation of the other scenario, i.e., fixing $\alpha = 0.8$, and changing β, we observe a continuous phase transition from LD-ZC_0/ZC_1-HD phase to MC-ZC_0/ZC_1-MC phase as shown in Fig. (5.7). At $(\alpha, \beta) = (0.8, 0.28)$, the system is in

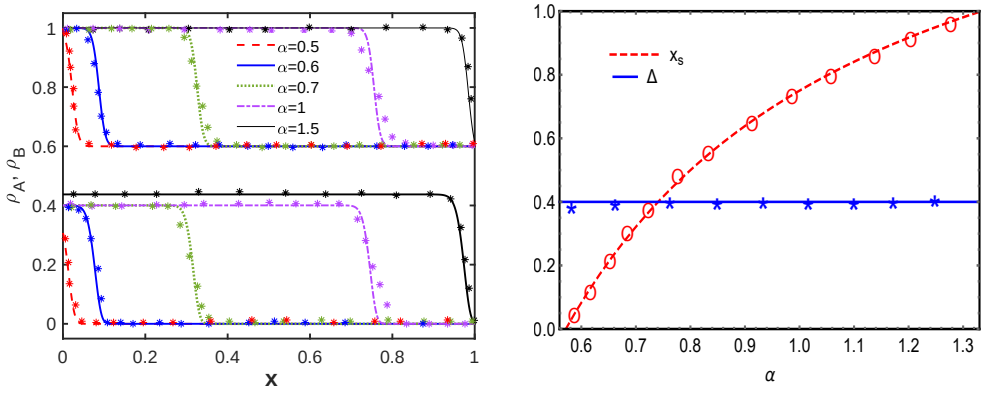

(a) (b)

Figure 5.6: (a) Density Profile and (b) position as well as the height of the shock in LD-ZC_0/ZC_1-HD phase for fixed $(\mu, \beta) = (1, 0.4)$. The variable $\Delta = \beta$ gives the height of the shock. Symbols describe Monte Carlo results, while solid/dashed lines correspond to theoretical findings.

LD/ZC_1. If one monitors the position and the height of the shock, they monotonically decrease and increase, respectively with an increasing exit rate up till $\beta = 0.5$. Both of these values saturate at the point $\Delta = 0.5$, thus violating the condition of existence of LD-ZC_0/ZC_1-HD phase. So, the system transitions into MC-ZC_0/ZC_1-MC phase indicating a second-order continuous transition.

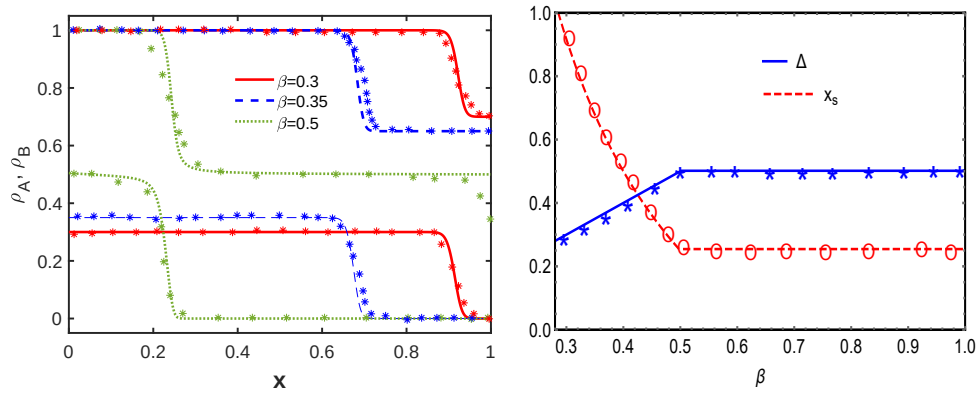

(a) (b)

Figure 5.7: (a) Density Profile and (b) position as well as the height of the shock in LD-ZC_0/ZC_1-HD phase for fixed $(\mu, \alpha) = (1, 0.8)$ and different values of β. The variable Δ gives the height of the shock. Symbols describe Monte Carlo results, while solid/dashed lines correspond to theoretical findings.

5.7 Summary and conclusion

To summarize, we offer a thorough overview of two totally asymmetric simple exclusion lanes: one characterized by particle detachment and the other by particle

attachment. In particular, the particles of a specific lane are compelled to move vertically once the corresponding vertical site becomes vacant. If this vertical movement is not feasible, they simply pursue horizontal motion along their designated lane. Investigation of this interconnected system occurs within a constrained resource setting, where the filling factor defines the number of particles in the system. This restriction influences the entry rate of particles into the lanes.

The particle movement relies significantly on the vertical site in the adjacent lane, so we employ the vertical cluster mean-field technique to establish a theoretical framework. This approach aids in deriving explicit expressions for the bulk stationary properties of each lane. However, to thoroughly analyze the system, we utilize singular perturbation theory to explore the stationary properties of the system in detail. To corroborate our analytical findings, we conduct kinetic Monte Carlo simulations (equivalent to the Gillespie algorithm) for validation, complemented by a numerical approach involving a finite difference scheme applied to the continuum version of the system.

By employing a combination of analytical and numerical methods, we investigate the influence of limited particle resources on critical stationary properties of the system, including phase diagrams, particle densities, and phase transitions. Our analysis reveals two types of stationary phases: (i) one lane displays zero particle density, while (ii) the other lane exhibits maximum particle density, each implying no particle flow. The phase diagram undergoes notable qualitative and quantitative changes as the particle count in the system varies. Initially less complex, the phase diagram becomes more intricate with an intermediate particle count, eventually settling again into a simpler form. Specifically, the number of phases transitions from 2 to 6 to 8 to 10, where it reaches its maximum before decreasing to 7 in the case of infinite particle resources. This implies that the number of phases that can persists follows a non-monotonic trend with increasing particles in the system. Each phase diagram exhibits both bulk and surface transitions, the latter arising from the presence of a boundary layer in the system. Precisely, two types of surface transitions, tanh and coth, are observed in the system.

A salient feature of our study is the manifestation of both upward and downward shock in the system. The bulk solution to the left of an upward shock exhibits a smaller magnitude compared to the bulk solution on the right side. Conversely, in the scenario of a downward shock, this trend is reversed. The system manifests two phases marked by an upward shock and two phases defined by a downward shock. Under a specific set of parameters, the upward shock is localized to one lane within the system. Conversely, in the case of a downward shock, both lanes experience this phenomenon, and the shocks in both lanes are synchronized. We analyze the propagation of shocks concerning changes in both entrance and exit rates, aiming for a comprehensive understanding of the phase transitions occurring in the system.

Chapter 6

Particle creation and annihilation in an exclusion process on networks

So far, we've addressed the implications of finite resources on both single and multiple-lane structures. However, various scenarios involve complex network topologies where the entities perform attachment and detachment, a phenomenon known as Langmuir Kinetics. This chapter[1] is dedicated to exploring a junction-type structure wherein certain segments converge at the junction and subsequently diverge, forming multiple segments, each integrated with Langmuir Kinetics.

6.1 Motivation and background

The key to rationalizing the stochastic dynamics on a network is to understand the processes at the junction. Junctions can be thought of as locations where traffic changes its route or directions. Several generalizations of the TASEP network with junctions have been employed. For example, the quantitative characterization of a single-lane road that bifurcates into two equivalent branches and subsequently merges again into a single lane has been well examined [127]. This can be seen as a model of two consecutive junctions on a single TASEP segment. In literature, a network of m incoming and n outgoing segments connected via a junction has been labelled as $V(m:n)$. Theoretical investigation of $V(2:1)$ has been explored using mean-field approximation and extensive computer simulations [162]. Inspired by real phenomena, the study of junctions was extended for multiple input multiple output systems as well as to multiple junctions [119]. Owing to the extensive body of TASEP, the dynamics of traffic flow on $V(2:2)$ with parallel updating rules has also been studied [99,163–165]. The behaviour of all possible fourfold junctions ($V(2:2)$, $V(1:3)$, $V(3:1)$) has been thoroughly investigated with explicit vertex framework [166] and further extended to $V(m:n)$ with interacting particles. Recently, the aspects of the temporal evolution in the initial particle density of $V(1:2)$ and $V(2:1)$ junctions are studied [167]. Another variant has shown the multiplex structure of the closed networks affects the global traffic flow in a non-trivial way [123,168]. All these studies have focused on the minimal model

[1]The content of this chapter is published in: "Ankita Gupta, Arvind Kumar Gupta. Particle creation and annihilation in an exclusion process on networks. *Journal of Physics A: Mathematical and Theoretical,* 55(10):105001, 2022."

of TASEP adopted random updating rules where particles do not interact with the surrounding environment. Such studies are very well suited for understanding stochastic transport on networks such as vehicles on roads or motor proteins on bio-filaments, etc.

Further, various studies have focused on coupling the exclusion processes to a bulk reservoir where attachment-detachment of particles prevails on bulk sites known as Langmuir kinetics (LK). The importance of studying TASEP with LK (TASEP-LK) lies in its application to intracellular dynamics, where motor proteins exhibit microscopic reversibility between the cytoplasm and the molecular filaments. This inclusion leads to rich stationary behaviour such as non-constant linear density profiles, localized shocks, and continuous phase transitions [45,46,169,170]. Closed networks coupled with LK have been studied comprehensively and it is found that the particle non-conserving dynamics affect the steady-state properties of the system significantly [123].

As discussed earlier, one-segment open systems display several interesting phenomena as compared to closed counterparts, in this work, we explore a network of open TASEP-LK consisting of m incoming segments connected via a junction to n outgoing segments represented as $V(m:n)$. To explore the overall dynamics of the proposed model, we compute theoretical expressions for particle density, phase diagrams, and phase transitions. Our system dynamics encourage us to answer a few essential queries. (i) Does the number of segments regulate the stationary properties of the system? (ii) How do the association-dissociation rates govern the dynamics of the system?

6.2 Network model

To mimic the stochastic transport of particles on a network such as vehicular traffic on a road, the motion of molecular motors along microtubules, etc, the present work explores the collective dynamics over a complex network which comprises of m independent incoming segments interacting with n outgoing segments at a junction. We propose a network $V(m:n)$ of open TASEPs composed of two sub-systems: the left (L) sub-system consists of m incoming segments $L_1, L_2, \ldots, L_m$ and the right (R) sub-system comprises of n outgoing segments $R_1, R_2, \ldots, R_n$ connected via a junction with particle creation and annihilation (see Fig. (6.1)). Each L_k and R_k segment represents a uniform open TASEP consisting of N sites and the complete network can be regarded as a system with $(m+n)N$ sites. The sites $i = 1$ and $i = N$ constitute the boundaries whereas $1 < i < N$ represents the bulk of an individual segment. The system is connected to an infinite reservoir of indistinguishable particles which move in a preferred direction (left to right) following a random sequential update rule. Particles are distributed under the hard-core exclusion principle which ensures that not more than

one particle can occupy a segment site. It is assumed that neither intra-sub-systems nor inter-sub-systems particle-particle interactions are permitted directly and the particles of the two sub-systems are only allowed to interact at the junction.

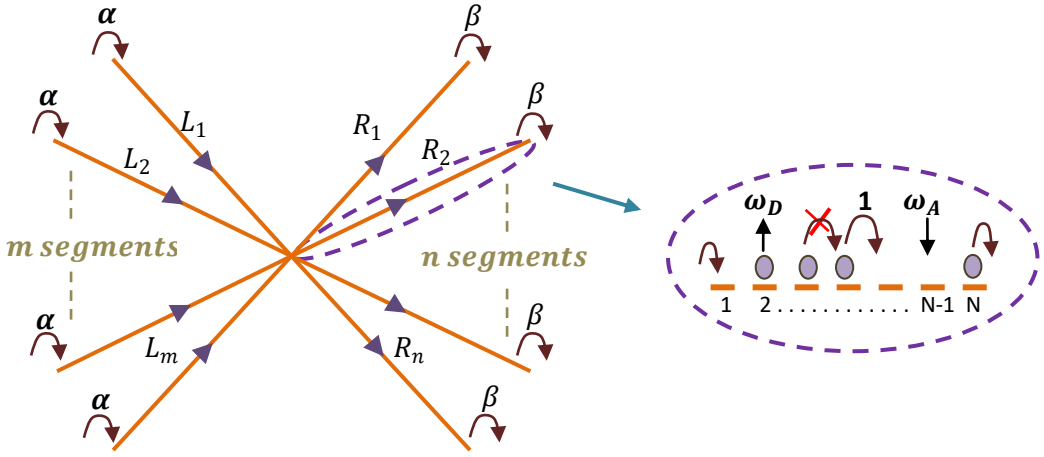

Figure 6.1: Schematic demonstration of the model where m incoming segments and n outgoing segments are connected via a junction. The particle can enter the first vacant site of incoming segments with rate α and exit from the last site of outgoing segments with rate β. To the right, the zoomed version of a segment is shown where attachment(detachment) of particles can occur in the bulk of each segment with rate $\omega_A/(\omega_D)$.

- **Dynamics on an individual segment.** Particles are injected into the system through the first site ($i = 1$) of each L_k segment with a rate α if empty. A particle from this site can hop with a unit rate to the empty neighbouring site. In the bulk, a particle first tries to leave the system with detachment rate ω_D. If it fails, then it attempts to jump to the site $i + 1$ with a unit rate if the target site is empty, obeying the hard-core exclusion principle. Furthermore, if the i^{th} site is vacant, then a particle can enter the system with rate ω_A. A particle finally exits from the last site ($i = N$) of each R_k segment with rate β.

- **Dynamics at the junction.** Particle on the site $i = N$ of any L_k segment, can jump to the vacant site $i = 1$ of each R_k segment with equal rate. In the case of competition, where more than one particle is available to jump across the junction, then they have equal chances of hopping onto the first site of any of the R_k segments.

In the absence of LK dynamics, Ref. [119] can be considered a specific case of our model with $n = 1$ and further for $m = 2$ and $n = 1$, this model reduces to Ref. [167].

6.3 Theoretical description

In the presented network model, all the individual segments are homogeneous and the system dynamics will entirely be governed by the behaviour of each segment at

the steady-state. It is worth here to recall the dynamic properties of a single-segment homogeneous TASEP with open boundaries coupled with LK for random updating rule which has been thoroughly examined in the literature [45,46] and analyzed utilizing a very generic approach known as mean-field Approximation or mean-field theory (MFT). The mean-field approximation assumes that the probability of occupancy of any site is independent of the occupancy of other sites and it also ignores all kinds of interactions in the system.

One-segment TASEP with particle creation and annihilation: To determine the overall state of the system, the master equation for a one-dimensional segment of N sites has been examined at the steady-state [46]. The equation exhibits the temporal evolution of the particle densities on each site of the segment. The continuum limit of this system can be obtained by coarse-graining the discrete lattice with lattice constant $\epsilon = 1/N$ and re-scaling the time as $t' = t/N$. Introduce the re-scaled attachment, detachment rates and the binding constant as $\Omega_A = \omega_A N$, $\Omega_D = \omega_D N$, and $K = \Omega_A/\Omega_D$. The hydrodynamic behaviour is governed by the continuity equation

$$\frac{\partial \rho}{\partial t'} = \partial_x \left(\frac{\epsilon}{2} \partial_x \rho \right) + \rho(1-\rho) + \omega_A(1-\rho) - \omega_D \rho, \tag{6.1}$$

where $x = i/N$, $0 \leq x \leq 1$ denotes the re-scaled position variable and ρ gives the average particle density. We focus on the special case when $\Omega_A = \Omega_D = \Omega$, for which Eq. (6.1) at steady-state reduces to

$$\frac{\epsilon}{2} \frac{d^2\rho}{dx^2} + (2\rho - 1)\frac{d\rho}{dx} + \Omega(1-2\rho) = 0, \tag{6.2}$$

along with the boundary conditions $\rho(0) = \alpha$ and $\rho(1) = 1 - \beta$. In the continuum limit $\epsilon \to 0^+$, it has been predicted [45,46] that the system dynamics is specified by the entrance rate α, exit rate β and the attachment-detachment rate Ω. The obtained density profiles are piece-wise linear and continuously dependent upon Ω. The bulk particle density at the steady-state is given by $\Omega x + C$ where the constant C depends on the boundary condition satisfied. Another solution obtained is $\rho_l(x) = 1/2$ identical to the Langmuir isotherm and also the density of the MC phase of TASEP which remains unaffected by Ω.

For reference, the particle steady-state densities and phase boundaries have been summarized in Table (6.1). In the table, $\rho_\alpha(x) = \Omega x + \alpha$, $\rho_l(x) = 0.5$, and $\rho_\beta(x) = \Omega(x-1) + 1 - \beta$ corresponds to densities of low density phase (LD), maximal current phase (MC) and high density phase (HD), respectively. The points separating the LD phase from the MC phase, and the MC phase from the HD phase are given by $x_\alpha = (1-2\alpha)/2\Omega$ and $x_\beta = (2\beta + 2\Omega - 1)/2\Omega$, respectively. Density discontinuity is located at the point $x_w = (\Omega - \alpha + \beta)/2\Omega$ in shock phase (S), where the currents for

Phase	Phase Boundaries	$\rho(x)$
LD	$\alpha+\Omega<0.5,\ x_w>1$	$\rho_\alpha(x)$
LD-MC	$\beta>0.5,$ $0.5-\Omega<\alpha<0.5$	$\begin{cases}\rho_\alpha(x) & 0\le x\le x_\alpha\\ 0.5 & x_\alpha\le x\le 1\end{cases}$
LD-MC-HD	$\alpha<0.5,\ \beta<0.5,$ $x_\alpha<x_\beta$	$\begin{cases}\rho_\alpha(x) & 0\le x\le x_\alpha\\ 0.5 & x_\alpha\le x\le x_\beta\\ \rho_\beta(x) & x_\beta\le x\le 1\end{cases}$
MC-HD	$\alpha>0.5,$ $0.5-\Omega<\beta<0.5$	$\begin{cases}0.5 & 0\le x\le x_\beta\\ \rho_\beta(x) & x_\beta\le x\le 1\end{cases}$
S	$\alpha<0.5,\ \beta<0.5,$ $x_\alpha>x_\beta, 0<x_w<1$	$\begin{cases}\rho_\alpha(x) & 0\le x\le x_w\\ \rho_\beta(x) & x_w\le x\le 1\end{cases}$
HD	$\beta+\Omega<0.5,\ x_w<0$	$\rho_\beta(x)$
MC	$\alpha>0.5,\ \beta>0.5$	0.5

Table 6.1: Summary of the results for one-dimensional open TASEP coupled with LK.

the left and the right solutions matches, $J_\alpha(x_w)=J_\beta(x_w)$.

6.4 Unconserved $V(m:n)$ network of TASEP

In the proposed network model $V(m:n)$, the absence of inter-segment interactions between $L_k's$, forces all the m incoming segments to behave identically, and thus they have the same phase among the seven possible phases (see Table (6.1)). Similarly, all the n outgoing segments have identical dynamics and hence all of them behave together having the same phase. Thus, the total number of phases cannot be greater than $7^2=49$.

We denote the particle current in any of the incoming segments $L_k's$ ($k\in\{1,2,\cdots,m\}$) by J^{in} whereas in any outgoing segments $R_k's$ ($k\in\{1,2,\cdots,n\}$), the current is denoted by J^{out}. It is assumed that the particles can leave any incoming segments $L_k's$ from the last site with effective exit rate β^{eff}. Similarly, the effective entry rate of particles to the first site of the $R_k's$ segment is taken to be α^{eff}. Since the total current at the steady-state is conserved throughout the system, we have

$$J=\sum_{i=1}^{m}J_{in}=\sum_{i=1}^{n}J_{out}\implies J=mJ_{in}=nJ_{out}, \tag{6.3}$$

where J denotes the overall current of the whole system. Also, the current that leaves the left sub-system is equal to the current across the junction which yields

$$m\beta^{eff}\rho_{in}^{N}=m\rho_{in}^{N}(1-\rho_{out}^{1}), \tag{6.4}$$

where ρ_{in}^{N} and ρ_{out}^{1} denotes the particle density on the last site of $L_k's$ and the first site

of $R_k's$, respectively. Similarly, the current across the junction must be equal to the current entering the right sub-system which gives

$$m\rho_{in}^{N}(1-\rho_{out}^{1}) = n\alpha^{eff}(1-\rho_{out}^{1}). \tag{6.5}$$

From Eqs. (6.3), (6.4), and (6.5), we get

$$J = m\rho_{in}^{N}(1-\rho_{out}^{1}) = m\beta^{eff}\rho_{in}^{N} = n\alpha^{eff}(1-\rho_{out}^{1}). \tag{6.6}$$

Thus, using the above equation, one can obtain the value of effective rates as

$$\alpha^{eff} = \frac{m}{n}\rho_{in}^{N}, \quad \beta^{eff} = 1-\rho_{out}^{1}. \tag{6.7}$$

Utilising the current continuity condition given by Eq. ((6.3)), we have

$$\lim_{x\to 1^{-}} mJ_{in} = \lim_{x\to 0^{+}} nJ_{out}. \tag{6.8}$$

We adopt the effective entrance rate α^{eff} and exit rate β^{eff} for the L_k and R_k segments along with Eq. (6.8) to investigate the possible structures of the system in terms of these rates. Our system has a large number of possible phases, so the dynamics of the whole system can be understood by the phase transitions occurring across the junction. Thus, we categorize the phases into different sub-classes based upon the nature of the phases near the junction. In each sub-class, the methodology will be similar and hence the value of the effective rates, α^{eff} and β^{eff} will remain the same.

Without loss of generality, we restrict our discussion to $m \geq n$. Depending upon how the topology changes near the junction, the phases can be divided into different categories. We designate the notation A $\rightarrow$ B to describe a sub-class which denotes that the region just upstream to the junction in all the incoming segments is in A phase and the region just downstream to the junction of all the outgoing segments is in the B phase.

Among the possible cases, there are certain cases which appear only for a particular relation between the number of segments in the L sub-system and the number of segments in the R sub-system. For example, the cases MC $\rightarrow$ HD, MC $\rightarrow$ LD, and MC $\rightarrow$ MC cannot exist when $m > n$. This is because if MC phase exists just upstream to the junction in L_k segments, then Eq. (6.3) implies that $nJ_{out} = m/4$ which is not possible as $m > n$. Moreover, the MC $\rightarrow$ LD junction does not even exist for $m = n$. In this case, the bulk densities around the junction are given by $\rho_{in} = 0.5$ and $\rho_{out}(x) = \Omega x + \alpha^{eff}$. Plugging these densities into Eq. (6.8) gives $\alpha^{eff} = 0.5$, which violates the existence condition of the phases in this sub-class.

Now, for the case HD $\rightarrow$ LD, $\rho_{in}^{N} = 1-\beta^{eff}$ and $\rho_{out}^{1} = \alpha^{eff}$ and using these in

Eq. (6.7) yields $\alpha^{eff} = 0$ and $\beta^{eff} = 1$, which violates the conditions required for the existence of such phases when $m > n$ ($\beta^{eff} < 1/2$). For $m = n$, Eqs. (6.7) and (6.8) gives $\alpha^{eff} = \beta^{eff} = 0.5$ which is again not possible. Analogous argument gives that LD $\rightarrow$ MC, MC $\rightarrow$ HD and HD $\rightarrow$ MC cannot exist for $m = n$. We use the notation C:D to identify a phase in $V(m:n)$ network, where C and D describe a phase in all the incoming and outgoing segments, respectively. We now discuss the stationary phases and existence conditions in each sub-class, explicitly.

General case: We analyze the sub-classes which exist for all possible values of m and n.

1. **LD $\rightarrow$ LD.** In this case, the region just upstream to the junction as well as the region just downstream to the junction displays LD phase. Since the upstream region to the junction is in LD phase, so the entire incoming segment can exhibit only the low density phase. The possible choices for such phases are LD:LD, LD:LD-HD, LD:LD-MC, and LD:LD-MC-HD. These phases are governed by the following common conditions

$$\Omega + \alpha < min\left\{\beta^{eff}, 0.5\right\}, \quad \alpha^{eff} < 0.5. \tag{6.9}$$

Here, the bulk density in each of the incoming segments is $\rho_{in}(x) = \Omega x + \alpha$ whereas the bulk density in the outgoing segments near the junction is $\rho_{out}(x) = \Omega x + \alpha^{eff}$. To determine the explicit particle densities in such phases, the effective rates can be calculated by utilizing the above expressions of density and Eq. (6.9) in Eq. (6.8), that yields

$$\alpha^{eff} = \begin{cases} \frac{1}{2}\left(1 - \sqrt{1 - \frac{4m(\Omega+\alpha)(1-\Omega-\alpha)}{n}}\right), & \text{if } m > n, \\ \Omega + \alpha, & \text{if } m = n. \end{cases} \tag{6.10}$$

This equation holds only when $\Omega + \alpha \leq \gamma$ where

$$\gamma = \begin{cases} \frac{1}{2}\left(1 - \sqrt{1 - \frac{n}{m}}\right), & \text{if } m > n, \\ \frac{1}{2}, & \text{if } m = n. \end{cases} \tag{6.11}$$

The density at the first site of the R_k segments is $\rho^1_{out} = \alpha^{eff}$ and by Eq. (6.7), $\beta^{eff} = (1 - \alpha^{eff})$. Table 6.2 shows the various phases in this case along with the conditions for the existence of the corresponding dynamic regime.

2. **LD $\rightarrow$ HD.** The only possible phase in this sub-class is LD:HD. This phase occurs when all the L_k segments are in LD phase and all the R_k segments are in HD phase. Such a phase is specified by the conditions,

$$\Omega + \alpha < \min\left\{\beta^{eff}, 0.5\right\}, \quad \beta + \Omega < \min\left\{\alpha^{eff}, 0.5\right\}. \tag{6.12}$$

The corresponding equations for bulk densities are $\rho_{in}(x) = \Omega x + \alpha$ and $\rho_{out}(x) = \Omega(x-1) + 1 - \beta$. Utilising Eq. (6.8), we obtain

$$\beta = \begin{cases} \frac{1}{2}\left(1 - \sqrt{1 - \frac{4m(\Omega+\alpha)(1-\Omega-\alpha)}{n}}\right) - \Omega, & \text{if } m > n, \\ \alpha, & \text{if } m = n. \end{cases} \tag{6.13}$$

The above equation is valid only when

$$\Omega + \alpha \leq \begin{cases} \frac{1}{2}\left(1 - \sqrt{1 - \frac{n}{m}}\right), & \text{if } m > n, \\ \frac{1}{2}, & \text{if } m = n. \end{cases} \tag{6.14}$$

Phase	Phase Boundary
LD:LD	$\Omega + \alpha^{eff} < \min\{\beta, 0.5\}$
LD:S	$\beta - \Omega < \alpha^{eff} < \min\{\beta + \Omega,\ 1 - \beta - \Omega\}$
LD:LD-MC	$\Omega + \alpha < \gamma,\ 0.5 < \Omega + \alpha^{eff},\ 0.5 < \beta$
LD:LD-MC-HD	$\Omega + \alpha < \gamma,\ 1 - \Omega - \alpha_{eff} < \beta < 0.5$

Table 6.2: Phases with LD to LD (LD $\rightarrow$ LD) transition at the junction.

3. **HD $\rightarrow$ HD.** Here, all the segments L_k as well as R_k portray HD phase. The phases that fall under this category are HD:HD, MC-HD:HD, LD-MC-HD:HD, and LD-HD:HD phase. The HD phase in the outgoing segments can exist when

$$\Omega + \beta < min\left\{\alpha^{eff}, 0.5\right\}. \tag{6.15}$$

By Eq. (6.8), the boundary parameters must satisfy

$$\beta^{eff} = \begin{cases} \frac{1}{2}\left(1 - \sqrt{1 - \frac{4n(\Omega+\beta)(1-\Omega-\beta)}{m}}\right), & \text{if } m > n, \\ \Omega + \beta, & \text{if } m = n. \end{cases} \tag{6.16}$$

Moreover, $\rho_{in}^{L} = 1 - \beta^{eff}$ and utilizing Eq. (6.7) to obtain the value of $\alpha^{eff} = \frac{m}{n}(1 - \beta^{eff})$. All the desirable phases of this case with the parameter ranges are summarized in Table 6.3.

Special cases: Now we will discuss the possibility of the existence of the phases which exist for specific relation between the number of incoming and the number of outgoing segments. The sub-classes LD $\rightarrow$ MC and HD $\rightarrow$ MC exist only when $m > n$ whereas

Phase	Phase Boundary	
	$m > n$	$m = n$
LD-MC-HD:HD	$1 - \beta^{eff} - \Omega < \alpha < 0.5,\ \beta < 0.5 - \Omega$	
S:HD	$\alpha - \Omega < \beta^{eff} < \Omega + \alpha$	
	$\beta < 0.5 - \Omega$	$\beta^{eff} < 1 - \Omega - \alpha$
MC-HD:HD	$0.5 < \alpha$ $\beta < 0.5 - \Omega$	$0.5 < \alpha$ $\beta < 0.5 - \Omega < \beta^{eff}$
HD:HD	$\Omega + \beta^{eff} < \alpha$ $\Omega + \beta < 0.5$	$\Omega + \beta^{eff} < \min\{\alpha, 0.5\}$

Table 6.3: Phases with HD to HD (HD $\rightarrow$ HD) transition at the junction.

the sub-class MC $\rightarrow$ MC prevail only for $m = n$. We explore the existence conditions and phase boundaries for these sub-classes.

1. **LD $\rightarrow$ MC.** As discussed earlier this case only exists when $m > n$. We assume that all the L_k segments are in low density phase whereas the R_k segments show maximum current phase at the upstream boundary provided the boundary parameters satisfy the following common relations,

$$\Omega + \alpha < \min\left\{\beta_{eff},\ 0.5\right\},\ \alpha_{eff} > 0.5. \tag{6.17}$$

The feasible choices for phases, in this case, are LD:MC and LD:MC-HD. The

Phase	Phase Boundary
LD:MC	$\Omega + \alpha = \frac{1}{2}\left(1 - \sqrt{1 - \frac{n}{m}}\right),\ \beta > \frac{1}{2}$
LD:MC-HD	$\Omega + \alpha = \frac{1}{2}\left(1 - \sqrt{1 - \frac{n}{m}}\right),\ \frac{1}{2} - \Omega < \beta < \frac{1}{2}$

Table 6.4: Phases with LD to MC (LD$\rightarrow$MC) transition at the junction for $m > n$.

particle densities near the junction are given by $\rho_{in}(x) = \Omega x + \alpha$ and $\rho_{out}(x) = 0.5$. By current continuity condition Eq. (6.8), we get

$$\Omega + \alpha = \frac{1}{2}\left(1 - \sqrt{1 - \frac{n}{m}}\right). \tag{6.18}$$

The various phases in this case for $m > n$ are shown in Table 6.4 along with the conditions for the existence of the corresponding dynamic regime.

2. **HD $\rightarrow$ MC.** As mentioned earlier, this sub-class does not exist for $m = n$. Here, the downstream part of all the L_k segments are exit-dominated and the upstream portion of the R_k segments manifests maximal current. So, the possible phases in this category are HD:MC, LD-HD:MC, MC-HD:MC, LD-MC-HD:MC, LD-HD:MC-HD,

Phase	Phase Boundary
HD:MC	$\Omega + \beta_{eff} < \alpha,\ \beta > 0.5$
S:MC	$\alpha - \Omega < \beta_{eff} < \Omega + \alpha,\ \beta > 0.5$
S:MC-HD	$\alpha - \Omega < \beta_{eff} < \Omega + \alpha$ $0.5 - \Omega < \beta < 0.5$
HD:MC-HD	$\Omega + \beta_{eff} < \alpha,\ 0.5 - \Omega < \beta < 0.5$
MC-HD:MC-HD	$0.5 - \Omega < \beta < 0.5,\ \alpha < 0.5$
MC-HD:MC	$\beta > 0.5,\ \alpha > 0.5$
LD-MC-HD:MC	$1 - \beta^{eff} - \Omega < \alpha < 0.5,\ \beta > 0.5$
LD-MC-HD:MC-HD	$1 - \beta^{eff} - \Omega < \alpha < 0.5$ $0.5 - \Omega < \beta < 0.5$

Table 6.5: Phases with HD to MC (HD→MC) transition at the junction for $m > n$.

HD:MC-HD, MC-HD:MC-HD, and LD-MC-HD:MC-HD. The density of particle in the bulk around the junction in each incoming segment is $\rho_{in}(x) = \Omega(x-1) + 1 - \beta$ and in that of outgoing segments is $\rho_{out}(x) = 0.5$. The effective rates α^{eff} and β^{eff} can be determined by substituting the above values of particle densities in Eq. (6.8) to obtain

$$\beta^{eff} = \frac{1}{2}\left(1 - \sqrt{1 - \frac{n}{m}}\right). \tag{6.19}$$

Furthermore, in this case, $\rho_{in}^{N} = 1 - \beta^{eff}$ and by Eq. (6.7), $\alpha^{eff} = \frac{m}{n}\left(1 - \beta^{eff}\right)$. Summary of all the desirable phases of this case with the parameter ranges for $m > n$ is given in Table 6.5.

As the maximal current phase can exist both upstream and downstream to the junction only when $m = n$, so MC → MC phase transition occurs only for an equal number of incoming and outgoing segments.

1. **MC → MC.** In this phase, the downstream boundaries of all the $L_k's$ and the upstream boundaries of all the $R_k's$ are in maximal current phase. The probable phases here can be LD-MC:MC, MC:MC, LD-MC:MC-HD, and MC:MC-HD. Table 6.6 summarises all the desirable phases of this case with the parameter ranges for $m = n$.

Phase	Phase Boundary
LD-MC:MC	$0.5 - \Omega < \alpha < 0.5,\ \beta > 0.5$
MC:MC	$\alpha > 0.5,\ \beta > 0.5$
LD-MC:MC-HD	$0.5 - \Omega < \alpha < 0.5,\ 0.5 - \Omega < \beta < 0.5$
MC:MC-HD	$\alpha > 0.5,\ 0.5 - \Omega < \beta < 0.5$

Table 6.6: Phases with MC to MC (MC → MC) transition at the junction.

The theoretical observations based upon the mean-field argument predict that out of the 49 possible phases, 30 phases are not realized in the system and for the remaining 19 phases the existing conditions have been thoroughly discussed above for $m > n$. When the number of segments in both sub-systems is equal i.e., $m = n$, the number of admissible phases is reduced to 13 and the remaining 37 phases cease to exist.

6.5 Results and discussions

In this section, we exploit the general conditions of existence discussed in the previous section to address the behaviour of the system in the $\alpha - \beta$ plane. Our main aim is to explore the effect of the LK rates on the stationary properties of the system. Furthermore, we intend to investigate the effect of the number of segments in each sub-system on the topology of the phase diagram. The theoretical outcomes have been extensively validated through Monte Carlo simulations (MCs). We have adopted the random-sequential updating rule and the number of sites in each segment is considered to be $N = 1000$. To ensure the occurrence of a steady-state, the first 5% of the time steps are discarded and the average density of particles is computed over an interval of $10N$. The phase boundaries are computed within an estimated error of less than 2%. For the thorough discussion, we analyze the system dynamics for two different categories: (i) when the number of segments in both sub-systems is equal ($m = n$) and (ii) when the number of segments in both sub-systems is different ($m \neq n$).

6.5.1 Equal number of segments: $m = n$

We begin our analysis for the case when the number of segments in each sub-system is equal and investigate the non-trivial effects on the topology of the phase diagram with the governing parameter Ω in the $\alpha - \beta$ plane. For the inspection, we specifically consider $m = n = 2$ which can be generalized for any values of m and n. For the limiting case $\Omega = 0$, the phase diagram consists of only three phases namely, LD:LD, MC:MC, and HD:HD which resembles the phase diagram for single-segment TASEP as illustrated in Fig. (6.2a). As soon as LK dynamics is introduced in the system, the number of feasible phases increases drastically with the emergence of thirteen stationary phases namely, LD:LD, LD:LD-MC-HD, LD:S, LD:HD, S:HD, HD:HD, LD:LD-MC, LD-MC:MC, LD-MC:MC-HD, MC:MC, MC:MC-HD, MC-HD:HD, and LD-MC-HD:HD as shown in Fig. (6.2b) for $\Omega = 0.1$. It is interesting to note that among these phases, the system can sustain maximal current in both the upstream and downstream of the junction as the number of segments in both the L and R sub-systems is equal. With an increase in Ω, only the re-positioning of the phase boundaries takes place till a critical value $\Omega_{c_1} = 0.25$. This value of Ω_{c_1} can be theoretically obtained

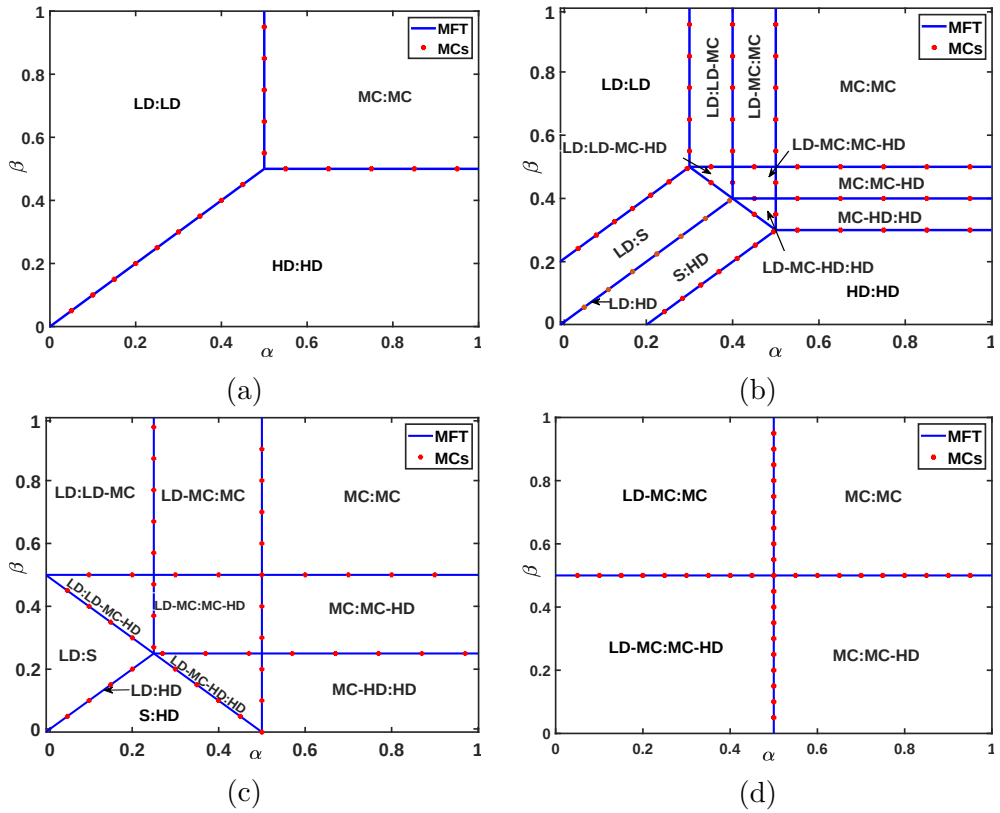

Figure 6.2: Stationary phase diagrams for different value of Ω: (a) $\Omega = 0$, (b) $\Omega = 0.1$, (c) $\Omega = 0.25$, and (d) $\Omega = 0.5$ for $m = n = 2$. Note that, the phase diagrams as well as the density profiles will remain unaffected for any values of m ($n = m$). The phase transformations are continuous for boundaries between all observed phases. Solid blue lines represent theoretical results and dotted red symbols correspond to Monte Carlo simulation.

from Eq. (6.9) and after this value LD:LD and HD:HD no longer persist in the system as shown in Fig. (6.2c) for $\Omega = 0.25$. The remaining eleven phases continue to persists until a critical value $\Omega_{C_2} = 0.5$, as evident from Eq. (6.18). Beyond this critical value, the topology of the phase diagram becomes most simplified where only four phases are realized namely, LD-MC:MC, MC:MC, LD-MC:MC-HD, and MC:MC-HD as illustrated in Fig. (6.2d) for $\Omega = 0.5$. Now, as $\Omega \to \infty$, LK rates dominate the overall dynamics of the system and only these four phases continue to exist.

To understand how the phase transitions occur with an increase in Ω, we have plotted the density profiles keeping fixed the boundary-controlling parameters $\alpha = 0.2$ and $\beta = 0.35$ (see Fig. (6.3)). For these values of α and β, the system exhibits LD:LD phase for $\Omega = 0$. With an increase in Ω, the density profile transits from LD:LD to LD:S then to LD:LD-MC-HD and finally to LD-MC:MC-HD. This can be explained by the following arguments. With an increase in Ω, the value of α^{eff} increases whereas β^{eff} decreases. The system is governed by the LK dynamics leading to the accumulation of particles in the outgoing segments and hence LD:S phase is observed. At $\Omega = 0.225$,

the density in the outgoing segments becomes a simple linear profile, continuously matching the density induced by α^{eff} and β. Consequently, the shock phase vanishes and LD-MC-HD phase emerges in the outgoing segments. As Ω is increased until 0.3, $\alpha^{eff} \to 0.5^{-}$ and $\beta^{eff} \to 0.5^{+}$, thus maximal current is observed around the junction and the system manifest LD-MC:MC-HD phase.

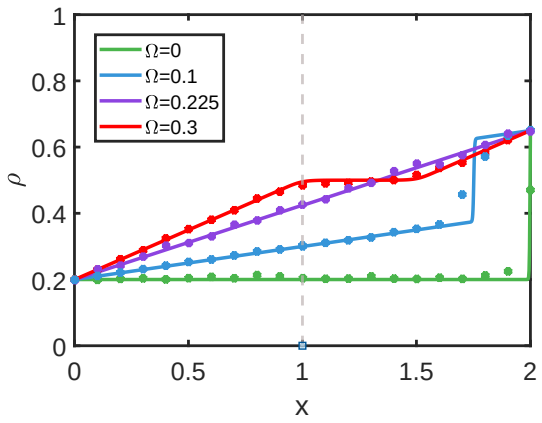

Figure 6.3: Density profiles for different value of Ω when $m = n = 2$. The vertical line at $x = 1$ shows the position of the junction.

Though we have provided the results for $m = n = 2$ but the findings will remain unaffected for any values of m and n $(m = n)$. This is because of the reason that all the phase boundaries are independent of the number of incoming segments and the outgoing segments. Attributable to this fact the topology of the phase diagram obtained for $V(m : m)$ network closely resembles that of a single-segment TASEP-LK model. This can be easily verified by considering the following phase boundary transformations.

$$\text{V(m:m) network} \leftrightarrow \text{Single-segment TASEP-LK}$$
$$\Omega + \alpha^{eff} = \min\{\beta, 0.5\} \leftrightarrow \Omega + \alpha = \min\{\beta, 0.5\}$$
$$\alpha = 0.5 \leftrightarrow \alpha = 0.5$$
$$2\Omega + \beta + \alpha = 1 \leftrightarrow \Omega + \beta + \alpha = 1$$
$$\Omega + \beta^{eff} = \min\{\alpha, 0.5\} \leftrightarrow \Omega + \beta = \min\{\alpha, 0.5\}$$
$$\beta = 0.5 \leftrightarrow \beta = 0.5$$

whereas, for the phases

$$\text{LD:LD} \leftrightarrow \text{LD}$$
$$\left.\begin{matrix}\text{LD:LD-MC}\\ \text{LD-MC:MC}\end{matrix}\right\} \leftrightarrow \text{LD-MC}$$

$$\left.\begin{matrix}\text{MC:MC-HD}\\ \text{MC-HD:HD}\end{matrix}\right\} \leftrightarrow \text{MC-HD}$$

$$\left.\begin{matrix}\text{LD:S}\\ \text{S:HD}\\ \text{LD:HD}\end{matrix}\right\} \leftrightarrow \text{LD-HD}$$

$$\left.\begin{matrix}\text{LD:LD-MC-HD}\\ \text{LD-MC:MC-HD}\\ \text{LD-MC-HD:HD}\end{matrix}\right\} \leftrightarrow \text{LD-MC-HD}$$

$$\text{HD:HD} \leftrightarrow \text{HD}$$

$$\text{MC:MC} \leftrightarrow \text{MC}.$$

6.5.2 Unequal incoming and outgoing segments: $m \neq n$

Now let us investigate the case when the number of segments in each sub-system is unequal and for simplicity, we choose $m = 2$ and $n = 1$ which can be generalized for other values of m and n ($m > n$). In the absence of the non-conserving dynamics ($\Omega = 0$), this case has been well studied [162] and for the sake of completeness, we have reproduced its phase diagram as presented in Fig. (6.4a). The phase diagram exhibits 5 distinct stationary phases, namely, LD:LD, LD:HD, LD:MC, HD:MC, and HD:HD. To investigate the effect of LK dynamics on the network, we study the phase diagram by varying Ω in the parameter space of $\alpha - \beta$. As soon as LK dynamics is introduced in the system, even for a very small value of Ω, the phase composition of the stationary phase diagram is strongly modified. Eight new phases emanate in the system: LD:S, S:HD, LD:LD-MC-HD, S:MC-HD, HD:MC-HD, LD:LD-MC, LD:MC-HD, and S:MC along with the five pre-existing phases. For convenience, we have shown the phase diagram for $\Omega = 0.1$ capturing these thirteen phases in Fig. (6.4b).

Further increasing Ω from 0.1, results in the shrinkage of LD:LD, LD:S, and LD:HD phase and the expansion of S:MC, S:MC-HD, and S-HD phases. Besides, no significant change is observed in the topology of the phase diagram till a critical value $\Omega_{C_3} = 1 - \sqrt{3}/2$, as computed from Eq. (6.9) at which LD:LD phase disappears. To demonstrate the phase schema at this critical value, we have plotted the phase diagram as shown in Fig. (6.4c) for $\Omega_{C_3} = 1 - \sqrt{3}/2$.

With the increase in the value of Ω from Ω_{C_3}, the phase boundary of LD:MC phase approaches the β axis and at a critical value $\Omega_{C_4} = (1/2)(1 - 1/\sqrt{2})$, the feasibility of LD phase in all the incoming segments is disrupted. As a consequence, the possibility of the phases LD:LD-MC, LD:MC, LD:LD-MC-HD, LD:MC-HD, LD:S, and LD:HD completely vanishes. Now, the phase diagram becomes simplified and consists of only six phases namely, S:MC, S:MC-HD, S:HD, HD:MC, HD:MC-HD, and HD:HD as shown

in Fig. (6.4d) for $\Omega_{C_4} = (1/2)(1 - 1/\sqrt{2})$.

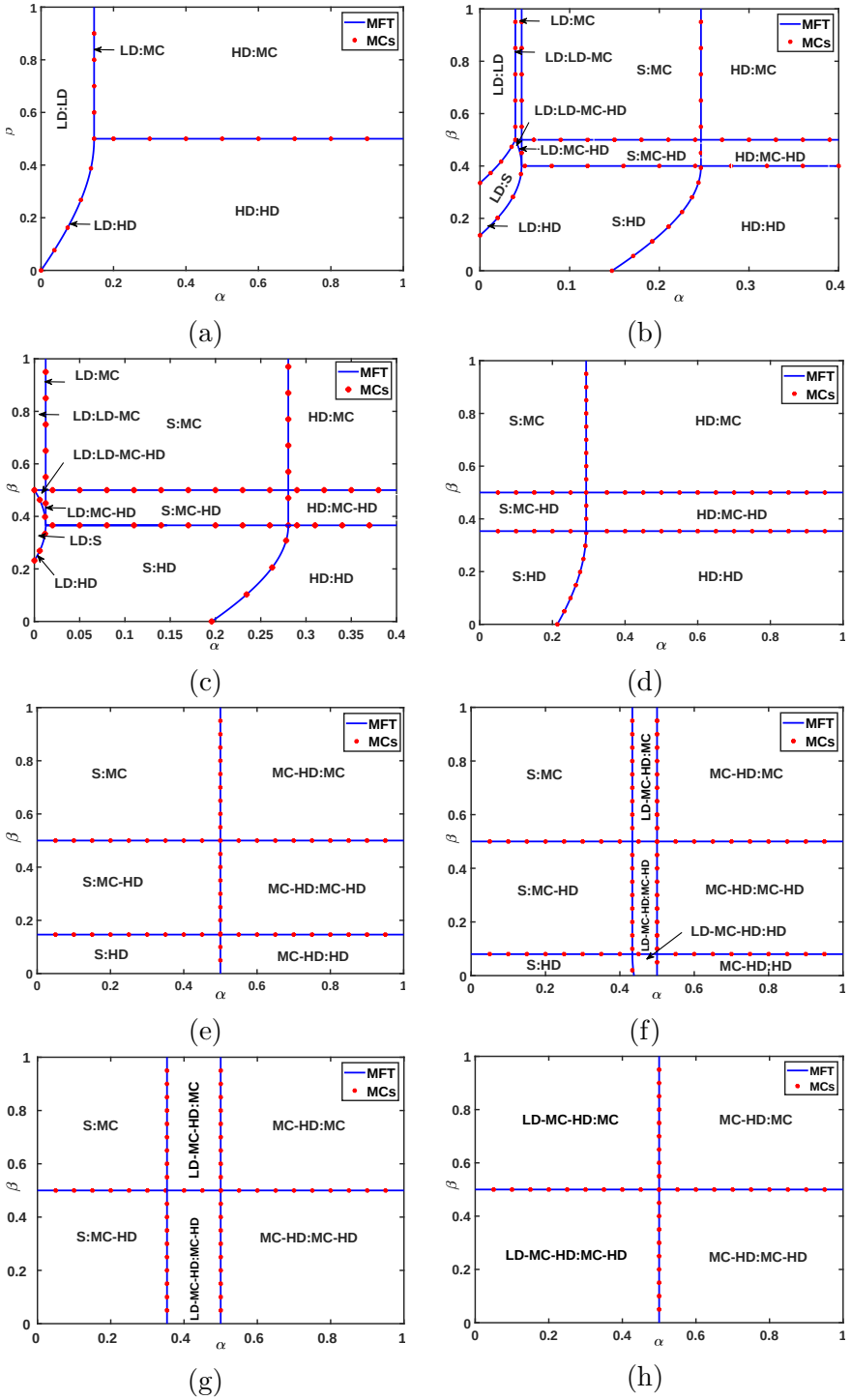

Figure 6.4: Stationary phase diagrams for different value of Ω: (a) $\Omega = 0$, (b) $\Omega = 0.1$, (c) $\Omega = 1 - \frac{\sqrt{3}}{2}$, (d) $\Omega = \frac{1}{2}\left(1 - \frac{1}{\sqrt{2}}\right)$, (e) $\Omega = \frac{1}{2\sqrt{2}}$, (f) $\Omega = 0.42$, (g) $\Omega = 0.5$, and (h) $\Omega = \frac{1}{2}\left(1 + \frac{1}{\sqrt{2}}\right)$ for $m = 2$ and $n = 1$. The phase transformations are continuous for boundaries between all observed phases. Solid blue lines represents theoretical results and dotted red symbols correspond to Monte Carlo simulation.

Considering the further increase in Ω from Ω_{C_4} to $\Omega_{C_5} = 1/2\sqrt{2}$, the phases with

HD $\rightarrow$ MC phase transition at the junction no longer exists. The existence of such phases requires $\Omega + \beta^{eff} < 0.5$ which is only valid when $\Omega < \Omega_{C_5}$. As a result, the LK dynamics dominates and the HD $\rightarrow$ MC phase transition changes to MC-HD $\rightarrow$ MC phase transition i.e., HD:MC, HD:MC-HD, and HD:HD phases transform to MC-HD:MC, MC-HD:MC-HD, and MC-HD:HD in the system as presented in Fig. (6.4e) for $\Omega_{C5} = 1/(2\sqrt{2})$.

Beyond Ω_{C_5}, the three-phase coexistence region LD-MC-HD in all the incoming segments is observed in the system. Three new phases LD-MC-HD:MC, LD-MC-HD:MC-HD, and LD-MC-HD:HD emanate in the system as illustrated in Fig. (6.4f) for $\Omega = 0.42$. As Ω reaches the value $\Omega_{C_6} = 0.5$, the HD phase is no longer observed in all the R_k segments as the phase boundaries of S:HD, LD-MC-HD:HD, and MC-HD:HD phases tends to the line $\beta = 0$. The phase diagram at the critical value $\Omega_{C_6} = 0.5$ is shown in Fig. (6.4g). Now the region for LD-MC-HD:MC and LD-MC-HD:MC-HD phases expand and as a result the phases S:MC and S:MC-HD perishes at the value $\Omega_{C_7} = (1 + \sqrt{2}/2)/2$, as plotted in Fig. (6.4h). Finally, after this critical value Ω_{C_7}, an increase in Ω does not produce any topological change in the phase boundaries nor the phase diagram and it remains unaltered even for $\Omega \rightarrow \infty$. Hence, the phase diagram remains invariant and portrays only four phases namely, LD-MC-HD:MC, LD-MC-HD:MC-HD, MC-HD:MC, and MC-HD:MC-HD. Clearly, the stationary phase diagrams show non-monotonic behaviour with respect to the equal attachment-detachment rate Ω on the number of phases in the $V(2,1)$ network.

Now, we analyze the possible phase transitions that occur for a fixed Ω and study the phase diagram for $\Omega = 0.1$. Choosing fixed $\beta \in (\alpha^{eff} - \Omega, \alpha^{eff} + \Omega)$, where α^{eff} is given by Eq. (6.10) depending upon α and Ω, we can clearly visualize that when α is increased, the phase changes from LD:S to LD:HD then to S:HD and finally to HD:HD (see Fig. (6.4b)). This behaviour can be easily understood by the following arguments. With an increment in α, α^{eff} increases and, hence the influx of particles increases in the outgoing segments. Consequently, the shock vanishes from all the outgoing segments and HD phase emerges in all these segments. Further, increasing α, the values of α^{eff} and β^{eff} (Eq. (6.16)) no longer vary which means that the system dynamics will now be governed by only varying parameter α in L sub-system and thus, S:HD phase emerges in the system. This is because, with the increase in the entry rate, the junction-induced shock absorbs the incoming particles and travels towards the left side in all the incoming segments. Finally, with a further increase in the entry rate, the HD phase is observed in all the segments of the network. Similarly, for any fixed $\beta \in (0,1)$ and varying α, an analogous argument holds for the phase transitions in the system.

In the above discussion, our analysis was restricted to the case when the number of segments in the L sub-system is greater than the number of segments in the R sub-system ($m > n$). For $m < n$, the phase transitions occurring at the junction and

Phase Transition at the junction	$m > n$	$m = n$	$m < n$
LD $\rightarrow$ LD	$\surd$	$\surd$	$\surd$
LD $\rightarrow$ MC	$\surd$	$\times$	$\times$
LD $\rightarrow$ HD	$\surd$	$\surd$	$\surd$
MC$\rightarrow$ LD	$\times$	$\times$	$\surd$
MC $\rightarrow$ MC	$\times$	$\surd$	$\times$
MC $\rightarrow$ HD	$\times$	$\times$	$\surd$
HD $\rightarrow$ LD	$\times$	$\times$	$\times$
HD $\rightarrow$ MC	$\surd$	$\times$	$\times$
HD $\rightarrow$ HD	$\surd$	$\surd$	$\surd$

Table 6.7: The possible phase transitions that can occur across the junction for different values of m and n.

the corresponding phase diagram can be examined on similar lines. Moreover, the phase regimes that exist for different values of m and n are described in tabular form in Table (6.7).

6.6 Conclusion

To summarize, we have presented a detailed study of a $V(m:n)$ network consisting of m incoming segments and n outgoing segments connected via a junction. This network is equipped with an additional feature of particle creation and annihilation where a particle can bind to an empty site or unbind from an occupied one with given rates. Our theoretical method is based on the idea that each segment can be viewed as a one-dimensional TASEP incorporated with LK. This allows us to implement the simple mean-field approximation to investigate the crucial steady-state properties of the system such as density profiles, phase diagrams and phase transitions. In support of mathematical investigations, the theoretical outcomes are obtained for all the observed phases for equal attachment-detachment rates. Our findings are theoretically examined for the different numbers of the incoming and the outgoing segments and numerically by extensive Monte Carlo simulations.

We specifically consider two distinct scenarios for the system dynamics: when the number of segments in both the sub-systems is different and when these values are the same. The study reports the explicit expressions for the phase boundaries of all the possible feasible phases and also provides valid arguments for the non-existence of certain phases in the system. Among the 49 possible phases, 19 different stationary phases have been observed in the system for varied values of Ω when $m \neq n$. For the case when $m = n$, the number of perceived phases reduces to 13. The analysis found that the system displays a large number of stationary phases, so for a systematic

study, the potential phases have been divided into various sub-classes based upon the dynamics happening at the junction. We observed that when the number of incoming and outgoing segments is equal, the maximal current phase can persist in all the segments.

Further, we study the effects of LK rates and the number of segments in each sub-system on the system dynamics. It has been seen that the effect of Ω on the number of phases is non-monotonic. Introducing the LK dynamics in the system, for $m \neq n$, firstly increases the number of phases from 4 to 13, which reduces to 6, then further rises to 9 and finally decreases to 4 as Ω increases. Whereas for $m = n$, with an increase in Ω, the number of phases escalates from 3 to 13 and then drops to 4 phases. After a certain value of Ω, the topology of the phase diagram remains unaltered and the phases boundaries, as well as the observed phases, are no longer modified and hence, the number of observed phases remains 4 as $\Omega \to \infty$. The critical values of Ω are computed where the appearance or disappearance of phases is observed. We also found that when the number of incoming and outgoing segments are equal, the obtained phase diagram is the analogue of a single-segment TASEP-LK model [45,46].

The proposed model is an attempt to provide an intrinsic means to interpret the steady-state properties of transport phenomenon on roads, molecular filaments, etc under the influence of LK dynamics. A further extension of this study can deal with the scenario where particle exchange is permitted in both sub-systems. Our results can also be extended to networks with various junctions.

Chapter 7

Non-equilibrium processes in an unconserved network model with limited resources

In the preceding chapter, we explored complex collective phenomena resembling transport in both man-made and natural systems. This exploration involved an examination of an open network junction model of TASEP with the inclusion of bulk particle attachment and detachment. Driven by the necessity to thoroughly scrutinize more realistic scenarios within the contexts of biological transportation and traffic flow, the current chapter[1] seeks to explore a network featuring a non-conserved TASEP model coupled with a finite pool of resources.

7.1 Introduction

In recent years, many generalizations of TASEP have been contemplated wherein the particles are injected from a limited source of particles [110]. Such phenomenon effectively embraces many physical and biological systems such as parking garage problems, protein synthesis and vehicular traffic [64,65,67]. Incorporating the real-time dynamics invoked by the limited availability of resources, TASEP studies have been conducted on a single-lane as well as to network models with multiple lanes [64,92,99,105,109,110]. These extensions reveal the regulatory effects of the finite reservoir of motor proteins on the onset of jams and other traffic features. However, the literature on limited resources is still deprived of the study of finite resources on a network junction model.

Motivated by the non-trivial effect of limited resources on the system properties, we wish to explore a network of non-conserved TASEP model coupled with a finite pool of resources. Our model corresponds to a modified version of Ref. [171], where the entrance and attachment rates are independent of the reservoir density. Firstly, we consider a non-conserved one-dimensional TASEP lane with limited resources. The method of

[1]The content of this chapter is published in: "Ankita Gupta, Arvind Kumar Gupta. Non-equilibrium processes in an unconserved network model with limited resources. *The European Physical Journal Plus,* 138(2):108, 2023."

characteristics along with the mean-field framework is adopted to theoretically analyze the transient solution of the particle densities and the corresponding phase boundaries. Further, the consequences of supplying limited resources in our network model and its interplay with the LK dynamics are explored. Several results and discussions based on significant parameters such as the number of lanes downstream and upstream to the junction and the total number of particles in the system, based on theoretical and numerical computation are presented.

7.2 Model and dynamic rules

We characterize the transport trails: biological networks, highways, etc., as lanes/lattices and entities advancing along these lanes as particles. In particular, assuming individual road or bio filaments as independent lanes, we consider a $m \times n$ network model of open TASEPs. The network consists of two subsystems: Left (L) and Right (R), involving m and n lanes, denoted by $L_1, L_2, \ldots, L_m$ and $R_1, R_2, \ldots, R_n$, respectively, each with N sites. Following the hard-core exclusion principle, which prevents more than one particle from occupying a single site, the particles drift unidirectionally from the leftmost site in a lane to the rightmost site (see Fig.(7.1)). The network is coupled to a single reservoir having a finite number of identical particles denoted by N_r. The dynamical conduct of the proposed system can be expressed in terms of the permissible movements of the particles as per the following dynamical rules.

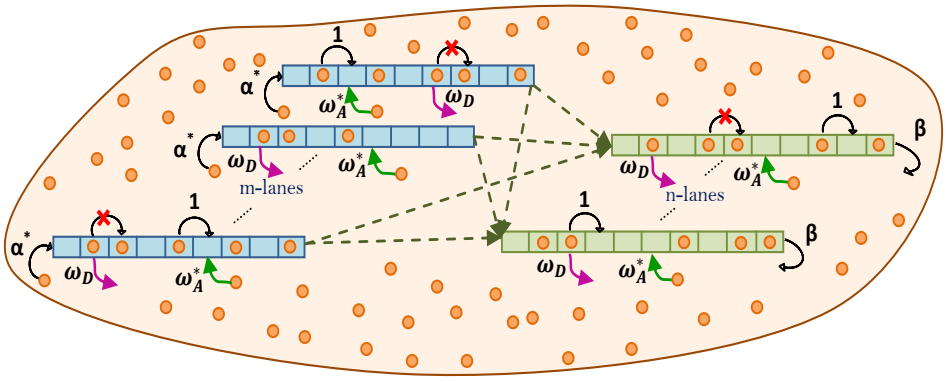

Figure 7.1: Illustration of $m \times n$ network model with LK. Arrows (crosses) indicate the allowed (prohibited) hopping. Here, α^{eff} and β correspond to injection and removal rates whereas ω_A^{eff} and ω_D are attachment and detachment rates, respectively.

(i) For lanes L_i, $1 \leq i \leq m$, a particle is allowed to enter the left end (site $k = 1$) from the reservoir with an effective entrance rate α^{eff} provided the target site is empty.
(ii) In the bulk of any lane, a particle present on the site k ($1 < k < N$), firstly seeks to detach itself with the rate ω_D. In case of unsuccessful detachment, it attempts to jump forward to the vacant site $i + 1$ with unit rate. Moreover, a particle attaches from the

reservoir R to any empty bulk site with an effective attachment rate ω_A^{eff}.
(iii) A particle located at the Nth site of any L_i lattice can jump to the first site in either of the R_j, $1 \leq j \leq n$ lattice with equal probability and will then continue its one-dimensional dynamics along the new lane.
(iv) At the exit site N of each R_j lane, a particle escapes with the constant rate β to the reservoir R, where it is free to rejoin any of the lattices.

It is to be noted that in our model, particles move in a random-sequential manner and explicit lane changing of particles is forbidden. Such an assumption allows obtaining an explicit description of the dynamic properties of the system. This model has been adopted to study a network $V(m:n)$ with infinite resources to analyze physical as well as biological transport systems [171].

Since the total number of particles N_t are conserved in the system at any instance of time

$$N_t = N_r(t) + \sum_{i=1}^{m} N_{L_i}(t) + \sum_{j=1}^{n} N_{R_j}(t),$$

where N_{L_i}(t) and N_{R_j}(t) denotes the number of particles on lattices $L_i(1 \leq i \leq m)$ and $R_j(1 \leq j \leq n)$, respectively. Furthermore, we define the effective entrance and attachment rates to be controlled by the reservoir density N_r/N_t, as follows

$$\alpha^{eff} = \alpha \frac{N_r}{N_t}, \quad \omega_A^{eff} = \omega_A \frac{N_r}{N_t}, \tag{7.1}$$

where α and ω_A are the intrinsic entry and attachment rates, respectively [110]. This relationship indicates that the entrance rate of particles is directly proportional to the particle concentration in the reservoir. If there are no particles in the reservoir, then α^{eff} takes the value zero and for a large number of particles in the reservoir, $N_r/N_t \to 1$ and α^{eff} tends to α. Furthermore, we retrieve $N_r \approx N_t$, resulting in a network system containing a single junction having a constant entrance and attachment rates as α and ω_A, respectively [171].

7.3 Single-lane TASEP-LK with limited resources

To successfully analyze the role of the network conformation and the presence of limited resources, it is necessary to thoroughly investigate the dynamical properties of a one-dimensional TASEP coupled to a reservoir with a finite number of particles. Firstly, we will discuss the non-stationary bulk properties which depend on the controlling parameters, entry rate (α), exit rate (β), attachment rate (ω_A), detachment rate (ω_D), and the reservoir density (N_r). The micro-state of each site is characterized by a set of occupation numbers τ^k, each of which is either '0' (vacant site) or '1' (occupied site). The evolution of the bulk particle densities ($1 < k < N$) in terms of the average

occupation number is governed by

$$\frac{d\langle\tau^k\rangle}{dt} = \langle\tau^{k-1}(1-\tau^k)\rangle + \omega_A^{eff}\langle 1-\tau^k\rangle - \langle\tau^k(1-\tau^{k+1})\rangle - \omega_D\langle\tau^k\rangle. \tag{7.2}$$

Here, $\langle\cdots\rangle$ denotes the statistical average whereas the positive and the negative terms on the right side of the equation depict the gain and loss terms, respectively, arising from the incorporated dynamic rules. Further for the boundaries, the particle densities evolve according to the following equations

$$\frac{d\langle\tau^1\rangle}{dt} = \alpha^{eff}\langle(1-\tau^1)\rangle - \langle\tau^1(1-\tau^2)\rangle, \qquad \frac{d\langle\tau^N\rangle}{dt} = \langle\tau^{N-1}(1-\tau^N)\rangle - \beta\langle\tau^N\rangle,$$

where α^{eff} and β denote the effective injection rate and the exit rate, respectively. Similarly, the master equation for the reservoir density r can be computed as

$$\frac{dr}{dt} = \omega_D\Big(\langle\tau^2\rangle + \langle\tau^3\rangle + \cdots\langle\tau^{N-1}\rangle\Big) + \beta\langle\tau^N\rangle - \alpha^{eff}\langle 1-\tau^1\rangle \\ - \omega_A^{eff}\Big(\langle 1-\tau^2\rangle + \langle 1-\tau^3\rangle + \cdots\langle 1-\tau^{N-1}\rangle\Big). \tag{7.3}$$

Ignoring all particle spatial correlations and factorizing the corresponding correlation function as a product of their averages utilizing the mean-field approximation, we have $\langle\tau^i\tau^j\rangle = \langle\tau^i\rangle\langle\tau^j\rangle$.

The continuum limit of this model can be obtained under the mean-field limit by coarse-graining the discrete lattice with lattice constant $\epsilon = 1/N$ and re-scaling the time as $t' = t/N$. Besides, to observe competition between boundary and the bulk dynamics, we re-scale ω_A and ω_D such that they decrease with the increasing system size N [45,46]. Therefore, we consider $\Omega_A = \omega_A N$ and $\Omega_D = \omega_D N$. Defining the reservoir density by $r = N_r/N$, the filling factor $\mu = N_t/N$, and utilizing Eq. (7.1), the effective entrance and the attachment rates are given by, $\alpha^{eff} = \alpha\frac{r}{\mu}$ and $\Omega_A* = \Omega_A\frac{r}{\mu}$.

Based on the spatial homogeneity in the system, we replace $\langle\tau^k\rangle$ with the continuous variable $\rho(x)$. On expanding the average density $\rho(x)$ in powers of ϵ and retaining the terms up to the second order, we get

$$\frac{\partial\rho}{\partial t'} + \frac{\partial}{\partial x}\left(-\frac{\epsilon}{2}\frac{\partial\rho}{\partial x} + \rho(1-\rho)\right) = \Omega_A^{eff}(1-\rho) - \Omega_D\rho. \tag{7.4}$$

Without loss of generality, we denote t' by t and in the continuum limit $\epsilon \to 0^+$, Eq. (7.4) reduced to

$$\frac{\partial\rho}{\partial t} + \frac{\partial J}{\partial x} = \Omega_D(Kz - (1+Kz)\rho), \tag{7.5}$$

where the bulk current J is given by $\rho(1-\rho)$, $K = \Omega_A/\Omega_D$ is the binding constant, and

$z = r/\mu$. Similarly, Eq. (7.3) is equivalent to

$$\frac{dr}{dt} = \beta(1-\beta) + \Omega_D(\mu - r) - \alpha z\,(1-\alpha z) - \Omega_A z(1-\mu+r). \tag{7.6}$$

7.3.1 Transient solution

We now investigate the evolution in particle density by analyzing the master equation as stated in Eq. (7.5) and further utilize it to acquire the corresponding steady-state solution. A comprehensive study on the transient solution is presented in Appendix (7.7). Here, we briefly summarize the discussion on these solutions. We begin by examining the characteristic equations concerning Eq. (7.5) and an initial density step comprising of a single discontinuity. To completely scrutinize the possible density solutions, a re-scaled density given by

$$\sigma = \frac{(Kz+1)(2\rho-1)}{Kz-1} - 1, \tag{7.7}$$

is defined which does not exist at $Kz = 1$. Therefore, further study is categorized based on the value of Kz. For $Kz = 1$, the acquired density solution is a piecewise linear continuous function. For $Kz \neq 1$, the thorough investigation yields that the density solution is given by the various branches of the Lambert-W function chosen suitably.

7.3.2 Steady-state solution

The steady-state solution for a non-conserved one-dimensional TASEP model with finite resources can be obtained by applying $t \to \infty$ in all the results of the previous subsections. We first consider the case $Kz = 1$ which admits the linear solutions for the density profiles and then for $Kz \neq 1$, where the density profiles are recognized by the various branches of the Lambert W function.

(a) **Kz=1**. As $t \to \infty$, $\rho_I(x,t) \to 1/2$, whereas the relative positions $x_\alpha \to (1 - 2\alpha^{eff})/(2\Omega_D)$ and $x_\beta \to (2\beta + 2\Omega - 1)/(2\Omega_D)$, respectively, whose methodology is detailed in Appendix (7.7). Utilizing these relative positions, we discuss the possible stationary phases that emerge for the density profiles. It is evident from the discussion outlined in Appendix (7.7) that the lattice can exhibit seven possible stationary states: low density (LD), high density (HD), maximal current (MC), two-phase coexistence phases (shock (S), LD-MC, and MC-HD) and a three-phase coexistence (LD-MC-HD) [45,46] as already summarized in Table. (6.1).

(b) **Kz $\neq$ 1**. With the advancement of time, the solution $\rho_I(x,t)$ approaches ρ_l, which is the constant density of the Langmuir isotherm. At steady-state, the solutions $\rho_\alpha(x)$ and $\rho_\beta(x)$ being independent of t, do not modify.

Further, the density profiles are attained depending upon the matching of the two solutions $\rho_\alpha(x)$ and $\rho_\beta(x)$, respectively. For this, we utilize the current continuity principle and obtain the position $x_w \in [0,1]$ at which the discontinuity in the density profile appears given by $\rho_\alpha(x_w) = 1 - \rho_\beta(x_w)$ and whose details can be found in Appendix (7.7). We now evaluate the solutions in the various regimes of the parameter space (α, β) of the phase diagram for $Kz > 1$. The corresponding results for $Kz < 1$ can be obtained from particle-hole symmetry.

1. $\alpha^{\mathbf{eff}} < \mathbf{1/2}$ **and** $\beta < \mathbf{1/2}$. For lower values of α^{eff} and β, one can expect either LD, S, or HD phase. In low density phase (LD), the density profile is purely expressed in terms of $\rho_\alpha(x)$ whereas, for high density(HD), the entire density profile is given by $\rho_\beta(x)$. When $x_w \in (0,1)$, the density is prescribed by a section of density $\rho_\alpha(x)$ on the left and $\rho_\beta(x)$ on the right distinguished at the position x_w.

   The transition line between different phases is given by the sign of $1 - \rho_\alpha(x) - \rho_\beta(x)$. Any shock will be driven out if the system satisfies $\rho_\alpha(1) < 1 - \rho_\beta(1)$ and the system will be dominated by the solution corresponding to the left boundary. Thus, the transition line between LD and S phase is obtained by employing the condition $\rho_\alpha(1) = 1 - \rho_\beta(1) = \beta$ which yields

$$\frac{1}{\Omega_D(1+Kz)}\left(2(\beta-\overline{\alpha}) + \frac{Kz-1}{Kz+1}\ln\left|\frac{Kz-(1+Kz)\beta}{Kz-(1+Kz)\overline{\alpha}}\right|\right) = 1. \tag{7.8}$$

   Similarly, the system is in high density phase if $\rho_\alpha(0) > 1 - \rho_\beta(0)$ and we deduce

$$\frac{1}{\Omega_D(1+Kz)}\left(2(\alpha^{eff}-\bar{\beta}) + \frac{Kz-1}{Kz+1}\ln\left|\frac{Kz-(1+Kz)(1-\bar{\beta})}{Kz-(1+Kz)(1-\alpha^{eff})}\right|\right) = 1, \tag{7.9}$$

   as the phase boundary between S and HD phases.

2. $\alpha^{\mathbf{eff}} > \mathbf{1/2}$ **and** $\beta < \mathbf{1/2}$. In this region, the lattice remains in the high density phase only.

3. $\alpha^{\mathbf{eff}} < \mathbf{1/2}$ **and** $\beta > \mathbf{1/2}$. Here, one can have LD, S, or HD phase based upon x_w. In HD phase, the particle density is independent of the boundary parameters α^{eff} and β, and the density is solely given by $\rho_\beta(x)$ for $\beta = 1/2$. This phase is also recognized as the Meissner (M) phase [46]. When the lattice is in the shock phase, the solution corresponding to the right boundary is given by $\rho_\beta(x)$ with the value of $\beta = 1/2$, which is independent of the rate β.

4. $\alpha^{\mathbf{eff}} > \mathbf{1/2}$ **and** $\beta > \mathbf{1/2}$. The lattice remains in the MC phase and the particle density is given by setting $\beta = 1/2$ in $\rho_\beta(x)$.

Note that a particular scenario of a TASEP-LK model on a single lane with constrained resources has been examined in Ref. [109] where α is taken to be 0.

7.4 Network model

Now, we generalize the results acquired in the Section (7.3) for single-lane TASEP-LK model with limited resources to thoroughly explore the $m \times n$ network model. The fundamental aspect of our approach is that we have partitioned the network model into two subsystems specifically lattices $L_i's$ $(1 \leq i \leq m)$ and $R_j's$ $(1 \leq j \leq n)$ connected directly through the last sites of $L_i's$ and the first site of each R_j. A particle present at the last site of any of the L_i lattice exits with an effective rate β^L. Similarly, the particles can enter the lattices $R_j's$ with an effective entry rate α^R.

Following the mean-field approach, we introduce ρ_{L_i} and ρ_{R_j} as the particle densities of each lattice in both the subsystems and ignoring all spatial correlations to obtain

$$J_{L_i} = \rho_{L_i}(1 - \rho_{L_i}), \quad J_{R_j} = \rho_{R_j}(1 - \rho_{R_j}), \tag{7.10}$$

where J_{L_i} $(i \in \{1, 2, \ldots, m\})$ denotes the steady-state bulk current for any L_i lattice and J_{R_j} $(j \in \{1, 2, \ldots, n\})$ corresponds to the steady-state bulk current in a R_j lattice. Along with these equations, the current at the boundaries is given by

$$\begin{aligned} J_{L_i}(0) &= \alpha^{eff}(1 - \rho_{L_i}(0)), \quad J_{L_i}(1) = \beta^L \rho_{L_i}(1), \\ J_{R_j}(0) &= \alpha^R(1 - \rho_{R_j}(0)), \quad J_{R_j}(1) = \beta \rho_{R_j}(1). \end{aligned}$$

The presence of uniform rates in all the homogeneous lattices $L_i's$ forces all of them to behave identically. So, we have $J_{L_1} = J_{L_2} = \cdots = J_{L_m} = J_L$. Analogously, the particle current in all the right lanes is equal and we denote the corresponding current by J_R. Now the conservation of current in the steady-state throughout the system yields the total current J as

$$J = \sum_{i=1}^{m} J_{L_i} = \sum_{j=1}^{n} J_{R_j}, \tag{7.11}$$

which gives $J = mJ_L = nJ_R$.

In the system, the condition of current continuity suggests that the exit current from lattices $L_i's$ is equal to the current passing across the junction, given by

$$m\beta^L \rho_L(1) = m\rho_L(1)\big(1 - \rho_R(0)\big), \tag{7.12}$$

which results in

$$\beta^L = 1 - \rho_R(0), \tag{7.13}$$

where ρ_L and ρ_R signifies average bulk density in any of the lane L_i and R_j, respectively. Analogously, the current passing from Nth site of any lattice in the L subsystem to the

first site in the R subsystem is equal to the current entering the R_j lattices in the R subsystem, which can be written as

$$m\rho_L(1)\big(1-\rho_R(0)\big) = n\alpha^R\big(1-\rho_R(0)\big), \tag{7.14}$$

that leads to

$$\alpha^R = \frac{m}{n}\rho_L(1). \tag{7.15}$$

Now, we discuss the conditions for the existence of different phase regimes in the (α, β) plane for the proposed network model. The particle densities and the phase boundaries are theoretically obtained utilizing the framework adopted in Section (7.3) along with the procured expressions and the concept of current continuity discussed above. A possible phase in the network model is labelled as P:Q where P and Q describe a phase in all the lanes of the L and the R subsystem, respectively. In addition, a phase transition across the junction is characterized by the notation C $\rightarrow$ D, where C and D represent a phase just upstream and downstream of the junction.

For further discussion, we denote the particle density in each L_i lane by $\rho_L^l(x)$ and $\rho_L^r(x)$ corresponding to the boundary conditions $\rho_L(0) = \alpha^{eff}$ and $\rho_L(1) = 1-\beta^L$. Also, in the right subsystem, $\rho_R^l(x)$ and $\rho_R^r(x)$ describe the solution agreeing with the boundary conditions $\rho_R(0) = \alpha^R$ and $\rho_R(1) = 1-\beta$, respectively. Moreover, we fix the notation $\alpha^L = \min\{\alpha^{eff}, 0.5\}$ and $\beta^R = \min\{\beta, 0.5\}$ which will be used throughout the rest of the chapter. Also, note that for this network junction model, the filling factor gets modified to

$$\mu = \frac{N_t}{(m+n)N}. \tag{7.16}$$

As already discussed in Section (7.3), the presence of a phase in a lane is specified by the value of Kz which is controlled by the reservoir density r and the filling factor μ. Therefore, we break down our further analysis of the network model according to the value of Kz.

7.4.1 $Kz \neq 1$

In this section, the theoretical calculations for $Kz \neq 1$ are performed and we provide expressions for the density profiles as well as the phase boundaries by utilizing the discussion outlined in Appendix (7.7).

1. **LD $\rightarrow$ LD transition.**
   We assume the lattices in the left subsystem as well as the left end of the lattices $R_j's$ exhibit LD phase. The possible choices for such scenarios are LD:LD and LD:S (see Appendix (7.7.2)). For these phases, the particle density in all $L_i's$ lattices corresponds to ρ_L^l and is calculated by setting $\overline{\alpha} = \alpha^L$ in Eq. (7.38). Now to find

$\rho_L^l(1)$, set $x = 1$ and $\overline{\alpha} = \alpha^L$ in Eq. (7.38) which gives

$$\frac{1}{\Omega_D(1+Kz)}\left\{2(\rho_L^l(1)-\alpha^L)+\frac{Kz-1}{Kz+1}\ln\left|\frac{Kz-(1+Kz)\rho_L^l(1)}{Kz-(1+Kz)\alpha^L}\right|\right\}=1. \tag{7.17}$$

The obtained value of $\rho_L^l(1)$ is then utilized to compute α^R from Eq. (7.15). For LD:LD phase, the density $\rho_R^l(x)$ in R_j lattices can be determined by the substitution of $\overline{\alpha} = \alpha^R$ in Eq. (7.38) and the system remains in LD:LD phase until $\rho_R^l(1) < \beta$.

In LD:S phase, the lattices R_j exhibit shock phase i.e., a part of the lattice is in the LD phase and the rest is in the HD phase. The density of the left section, $\rho_R^l(x)$ in any R_j lattice is calculated by setting $\overline{\alpha} = \alpha^R$ in Eq. (7.38) whereas the density of the remaining section ρ_R^r is obtained from Eq. (7.39). The shock position x_w is computed from $\rho_R^l(x_w) = 1 - \rho_R^r(x_w)$. The boundary separating LD:LD and LD:S can be determined from $\rho_R^l(1) = \beta$.

2. **LD → HD transition.**
The only possible phase in this category is LD:HD. Each lattice in the left subsystem exhibits low density, while the lattices in the right subsystem are in the high density phase. The density of particles in the bulk of each L_i is given by $\rho_L^l(x)$ as calculated in the previous case. The densities in each R_j lattice is written as $\rho_R^r(x)$ acquired from Eq. (7.39).

3. **HD → HD transition.**
In this case, we assume that all the region just upstream and downstream of the junction is in high density phase. So, the feasible choices for such scenarios are HD:HD and S:HD. From Eq. (7.39), we obtain the density $\rho_R^r(x)$ in any R_j lane. Also, the current continuity argument near the junction leads to

$$\beta^L(1-\beta^L) = \frac{n}{m}\rho_R^r(0)\big(1-\rho_R^r(0)\big). \tag{7.18}$$

For HD:HD, $L_i's$ are exit dominated and we can calculate the density $\rho_L^r(x)$ from Eq. (7.39) on replacing $\bar{\beta}$ by β^L. The system remains in HD:HD phase for $\rho_L^r(0) > 1-\alpha^{eff}$. For S:HD, the lattices L_i are in the shock phase, i.e., a part of these lattices are in LD phase and the rest is in HD phase. The density to the left of the shock position x_w is given by $\rho_L^l(x)$ calculated from Eq. (7.38) by setting $\overline{\alpha} = \alpha^L$ and to the right, the density is written as $\rho_L^r(x)$ obtained by the substitution of $\bar{\beta} = \beta^L$ in Eq. (7.39). The system must satisfy $\rho_L^r(0) < 1 - \alpha^{eff}$ to remain in S:HD phase. So, the boundary between HD:HD and S:HD phase is determined by $\rho_L^r(0) = 1 - \alpha^{eff}$.

4. **HD → LD transition.**
In each L_i lattice, the particles on the right end are in the high density phase, while,

in R_j lattices, the particles are in the low density phase at the left end. The phases that support the existence of this category are HD:LD, HD:S, S:LD, and S:S. The density profile can be calculated analogously to the previously discussed transition.

7.4.2 $Kz = 1$

In this case, each lane can exhibit any of the seven possible phases, discussed in Section (7.3.2). As stated earlier, the bulk densities in each of the L_i lanes, as well as R_j lanes, remain the same, leading to $7^2 = 49$ feasible phases. It has already been exposed in Ref. [171] that, for $m \neq n$, out of these 49 phases, the perceived number of phases is only 19 and for $m = n$, the number of observed phases reduced to 13. The stationary particle density and the corresponding phase boundaries can be discovered from Ref. [171].

7.5 Results and discussions

To explore the effect of finite resources on the stationary system properties, we exploit the theoretical results discussed in Section (7.4) to study the emerging dynamics for specific values of μ and K in the parameter space (α, β). To validate our theoretical outcomes we perform Monte Carlo simulations for system size $N = 500$ following a random sequential updating rule. The density profiles, phase boundaries, and shock positions computed utilizing the mean-field approach very well agree with the simulations. The phase boundaries are calculated within an estimated error of less than 1%. We would like to mention that the notation A_q is adopted in the phase diagrams where A represents the corresponding phase in a lane and the subscript $q \in \{l, r\}$ indicates the presence of a boundary layer at the left /right end of the stationary density profile. Since our focus is mainly on the inspection of the stationary bulk particle density, this notation is not employed in the text, rather it is restricted to the phase diagrams. Additionally, we have used the symbol M for the Meissner phase in the phase diagram to represent a phase independent of both the boundary controlling parameters α^{eff} and β.

As the number of lanes in both subsystems will significantly affect the stationary system properties, we analyze the system dynamics in two categories, namely, $m \neq n$ and $m = n$.

7.5.1 Equal number of lanes in both the subsystems ($m = n$)

Now we analyze the effect of the finite supply of particles on the topology of the phase diagram when the number of lanes in both subsystems is equal. The phase

diagram is derived for different values of μ and K in the parameter space α and β. To commence, we consider the intrinsic attachment and detachment rates to be equal, i.e., $K = 1$.

For a very small value of μ, the number of particles in the system is scarce and only one phase namely LD:LD appears in the entire phase regime. This behaviour can easily be understood as follows: due to the deficiency of particles in the reservoir, the effective entrance and attachment rates are very low and hence leading to the occurrence of only low density in each lane. The phase diagram exhibits only this phase till $\mu_{C_1} = 0.01$. This critical value μ_{C_1} complies with the condition that the existence of LD phase in the right subsystem requires $\rho_R^l(1) < \beta$. With an increase in μ, for lower values of β, the exit of particles is hindered leading to an accumulation of particles in the right subsystem, and thus, the emergence of LD:S phase is observed. As we keep on increasing μ, the value of α^{eff} and Ω_A^{eff} keeps on increasing which results in more particles being fed onto the lanes. In addition to this, for smaller values of β, the boundary induced shock in LD:S phase absorbs the incoming particles and travels toward the junction. Therefore, a new phase LD:HD emerges in the system at the critical value $\mu_{C_2} \approx 0.59$, near to LD:S phase. This LD:HD phase is confined only to a curve. On further increasing μ, the junction induced shock enters the left lanes, and S phase arises in all these lanes as prescribed in Fig. (7.2b) for $\mu = 0.75$. The LD:HD phase acts as a boundary separating LD:S and S:HD regions. No significant changes are observed in the phase diagram till μ_{C_3}, except the expansion of S:HD and the shrinking of LD:LD phase region. From Eq. (7.9), the existence of S phase in the left subsystem requires the boundary controlling parameters to satisfy $\rho_L^r(0) < 1 - \alpha^{eff}$, which yields the critical value of $\mu_{C_3} \approx 1.14$. At this critical value, the junction induced shock on the L_i lattices shifts towards the left boundary resulting in the HD phase in all the lanes of the system. Till now the phase diagram comprises of only five phases namely, LD:LD, LD:S, LD:HD, S:HD, and HD:HD as shown in Fig. (7.2c).

Now, the particle density in the system continues to increase with μ and it achieves the value ρ_l which is the Langmuir isotherm given by $\rho_l = z/(z+1)$. As $\mu \to \infty$, the Langmuir isotherm reaches the value 0.5 and the region corresponding to the density 0.5 is renamed with the MC phase. Hence, seven new phases emanate in the system namely, LD-MC-HD:HD, MC-HD:HD, LD:LD-MC-HD, LD-MC:MC-HD, MC:MC-HD, LD:LD-MC, LD-MC:MC, and MC:MC as depicted in Fig. (7.2d) for $\mu = 200$. In the limit, $\mu \to \infty$, the topology of the phase diagram remains preserved, and as expected, the phase diagram for the $m \times n$ network model with unlimited resources for $m = n$ has been retrieved [171].

To further inspect, we examine the scenario when the ratio of intrinsic attachment and detachment rates is not equal to 1 ($K \neq 1$). In particular, for $K < 1$, only two phases namely LD:LD and LD:S are observed in the phase diagram for $\mu < 1$. With

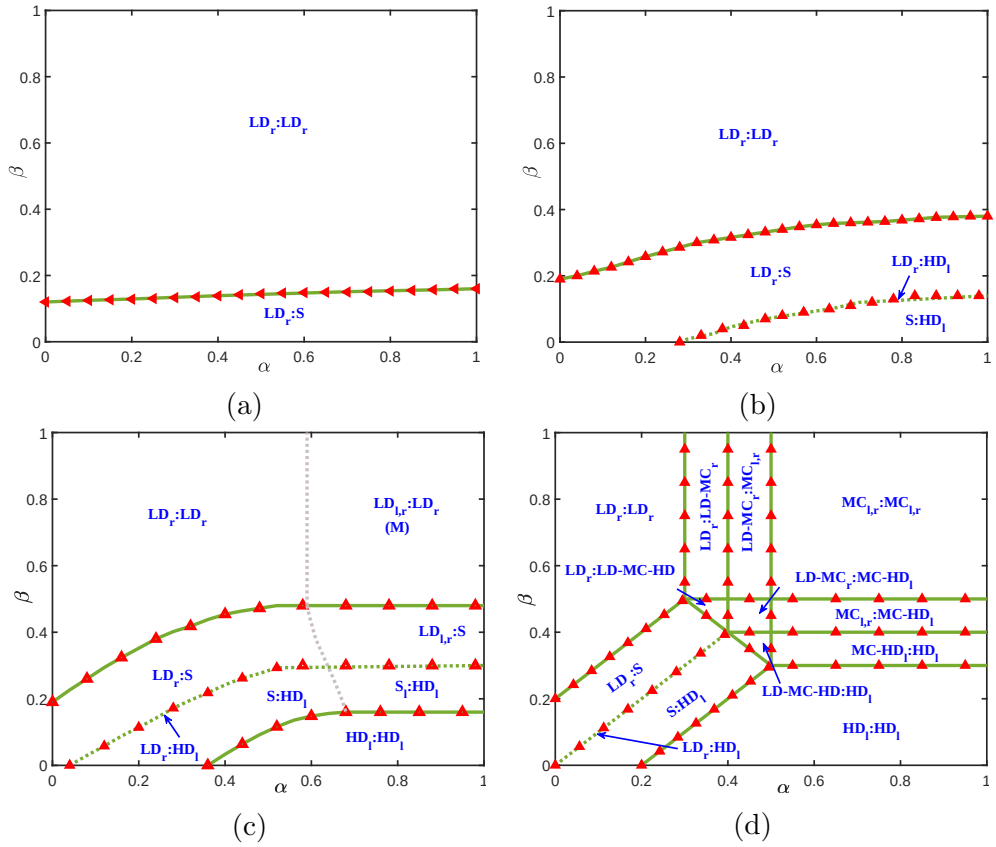

Figure 7.2: Stationary phase diagrams for different value of μ: (a) $\mu = 0.2$, (b) $\mu = 0.75$, (c) $\mu = 2.5$, and (d) $\mu = 200$ for $m = n$, $K = 1$ and $\Omega_D = 0.1$. Note that, the phase diagrams will remain unaffected for any values of m, $(m = n)$. Green solid/dotted lines represent mean-field results and red symbols correspond to the Monte Carlo simulations. The subscripts 'l' and 'r' signify the presence of a boundary layer forming in the density profile at the left and the right end respectively. M represents the Meissner phase where the bulk density is independent of the boundary parameters.

an increase in the filling factor μ, LD:HD, S:HD and HD:HD phases gradually enter the phase diagram. Unlike the case when $K = 1$, here no MC phase is encountered, neither in any section nor the complete lattice of the system. Mathematically, the MC phase is achieved when Kz reaches the value 1, which is impossible as $K < 1$. Hence, as $\mu \to \infty$ the phase diagram remains invariant and portrays only five phases namely, LD:LD, LD:S, LD:HD, S:HD, and HD:HD, respectively. Moreover, the phase diagrams obtained for $K = 1$ qualitative remain unaffected for $K < 1$. Also, all lines represent continuous transitions between different regions of the phase diagram.

Though in the above discussion, our analysis was restricted to the case when the intrinsic attachment rate is greater than the detachment rate ($K < 1$). For $K > 1$, the phase diagrams, as well as the phase transitions, can be examined utilizing the particle-hole symmetry. It is worthwhile to note that, when the number of lanes in both subsystems is taken to be identical, the network system behaves as a one-dimensional TASEP-LK model. The findings will remain unaffected for any values of m and n

$(m = n)$. This is because of the reason that all the phase boundaries are independent of the number of lanes in the left and the right subsystem.

7.5.2 Number of lanes in both the subsystems are different $(m \neq n)$

In this section, we aim to discuss a special case when the number of lanes in the left subsystem is different from the number of lanes in the right subsystem. For simplicity, we fix $m = 2$ and $n = 1$, which can be easily generalized for other values of m and n $(m > n)$. To investigate the effect of limited resources on the phase schema, we begin by studying the phase diagram for the varying parameter μ keeping fix $\Omega_D = \Omega_A = 0.1$, i.e., $K = 1$ in the parameter space of $\alpha - \beta$. As soon as μ is increased from 0, due to the availability of a very less number of particles in the system, only two phases LD:LD and LD:S appear in the phase diagram. The LD:LD region contracts and LD:S region expands with increasing μ. This continues till $\mu \approx 0.29$ where two new phases namely S:S and S:LD emerge in the system (see Fig. (7.3a)).

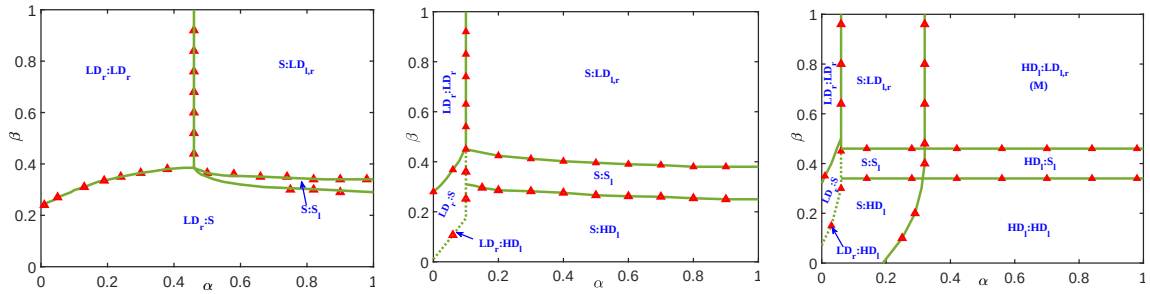

(a) (b) (c)

Figure 7.3: Stationary phase diagrams for different value of μ: (a) $\mu = 0.33$, (b) $\mu = 0.67$, and (c) $\mu = 3.33$ for $m = 2, n = 1$, $K = 1$ and $\Omega_D = 0.1$. Dotted green line denotes LD:HD phase. Green solid/dotted lines represent mean-field results and red symbols correspond to the Monte Carlo simulations. The subscripts 'l' and 'r' signify the presence of a boundary layer forming in the density profile at the left and the right end, respectively. M represents the Meissner phase where the bulk density is independent of the boundary parameters.

Afar $\mu \approx 0.36$, LD:HD and S:HD phase appears in the phase diagram along with the existence of LD:LD, LD:S, S:LD, and S:S phases, as evident from Fig. (7.3b). Observe that LD:HD phase acts as a boundary separating LD:S and S:HD region. To analyze the possible phase transition, we study the phase diagram (see Fig. (7.3b)) for a value of β. One can visualize that with an increase in α, as more particles are fed into the system through the left end, particles start accumulating in the right lanes and the boundary induced shock in LD:S phase travels towards the junction. Consequently, the shock completely vanishes from the right lanes as it reaches the junction leading

to LD:HD phase. On further, increasing α, the junction induced shock absorbs the incoming particles and hence, S phase is observed in the left system.

With further increase μ, at a critical value $\mu \approx 1.08$, three new phases HD:HD, HD:S and HD:LD appear to alter the phase diagram due to the expansion and contraction of the existing phases. Now, the phase diagram consists of nine phases as shown in Fig. (7.3c). It can be observed that for $\beta > 0.5$, the right lanes demonstrate low density phases while for $\beta < 0.5$, these lanes are either in shock or high density phase. Studying the phase transition that occurs in the left subsystem, with an increase in α, the density changes from low density to shock phase and finally to high density phase. The topology of the phase diagram remains preserved with a further increase in the parameter μ. In the limiting case of a large number of particles, i.e., $\mu \to \infty$, we retrieve the phase diagram obtained for the network junction model for $m \neq n$ with infinite resources [172].

According to the analysis revealed in Section (7.3), the number of feasible phases in each lane strongly depends on the value of Kz. For $K \leq 1$, the value of Kz always remains less than 1. So, the phase diagrams for $K < 1$ will be qualitatively analogous to that for $K = 1$. While considering the case when $K > 1$, clearly the attachment rate Ω_A will be greater than the detachment rate Ω_D and the value of decisive parameter Kz can attain any value in $(0, K)$. To investigate the phase diagram in this case, we fix $K = 3$ and $\Omega_D = 0.01$, respectively.

As discussed above, for $\mu < 1$, only two phases namely LD:LD and LD:S are observed in the entire phase diagram. We encounter only these phases until the critical value $\mu_{C_1} \approx 0.31$, where a new phase S:LD appears along with the existing phases. This critical value is calculated in accordance with the condition that the existence of LD phase in the left subsystem requires $\rho_L^l(1) < \beta^L$. Further, after this critical value, as can be seen from Fig. (7.4a), both qualitative and quantitative changes are viewed with the emergence of S:S phase in the phase diagram, leading to the shrinking of LD:LD region and expansion of S:LD region. At the critical value $\mu_{C_2} \approx 0.4$, LD:HD and S:HD phases enter the phase schema whereas the S:S phase remains confined only to a curve (see Fig. (7.4b)). Apart from shifting of phase boundaries, no significant changes are discovered until μ reaches the value $\mu_{C_3} \approx 1$. At this critical value, the phase diagram comprises a total of nine phases. For $\alpha < 0.5$ the phases LD:LD, LD:S, LD:HD, and S:HD continue to appear whereas for $\alpha > 0.5$, the S:HD and S:LD regions shrink and the arrival of three new phases namely, HD:LD, HD:S, and HD:HD phases is observed as displayed in Fig. (7.4c). After the critical value $\mu_{C_4} \approx 1.07$, the phases S:LD, HD:LD, S:S, and HD:S vanish resulting in the expansion of HD:HD phase and contraction of S:HD phase. Additionally, it is notable that HD:HD region appears for a significant range of β, as evident from Fig. (7.4d). As expected, in the limit of $\mu \to \infty$, the phase diagram for a standard nonconserved network junction model has been recovered [172].

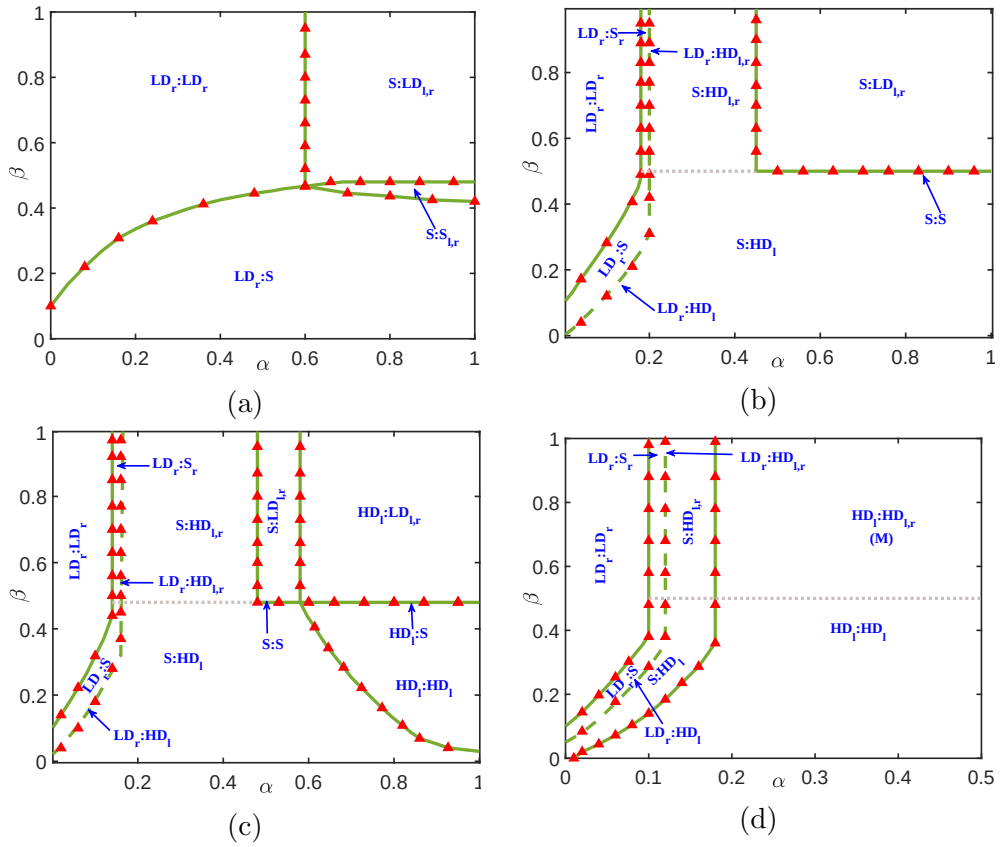

Figure 7.4: Stationary phase diagrams for different value of μ: (a) $\mu = 0.33$, (b) $\mu = 0.67$, (c) $\mu = 1$, and (d) $\mu = 3.33$ for $m = 2, n = 1$, $K = 3$ and $\Omega_D = 0.01$. Dashed green line denotes LD:HD phase. Green solid/dashed lines represent mean-field results and red symbols correspond to Monte Carlo simulations. The subscripts 'l' and 'r' signify the presence of a boundary layer forming in the density profile at the left and the right end respectively. M represents a region where the bulk density is independent of the boundary parameters.

The above analysis divulges that for $K > 1$, a maximum of nine phases are observed in the entire phase diagram with varied values of the filling factor. The complexity of the phase diagram concerning the number of phases reveals non-monotonic behaviour with an increase in the total number of particles. Initially, there exist only two phases and when the total number of particles is equal to the total number of sites in the system, i.e., $\mu = 1$, the dynamics become complex and the system can exhibit all the possible nine phases observed for $K \neq 1$. To study the unusual topology of the phase diagram revealed in Fig. (7.4c), we observe the change in the value of the reservoir density r with respect to an increase in α for a fixed β. As α increases, more particles are fed into the system through the left end, which in turn decreases the reservoir density and Kz remains greater than 1. With further increase in α, the reservoir density goes on decreasing and Kz becomes less than 1, hence, a different topology of the phase diagram is identified.

In a one-lane TASEP-LK system with infinite resources, it has been observed that

the particle-hole symmetry leads to invariance between the situations $K > 1$ and $K < 1$ [45,46]. However, in this model, as already discussed above, the results obtained of $K < 1$ are quantitatively different from those of $K > 1$. Nevertheless, the particle-hole symmetry can be utilized to investigate the phase diagram for $m < n$ from those of $m > n$ with the simultaneous exchanges, $m \leftrightarrow n$, $\alpha^{eff} \leftrightarrow \beta$, $\rho \leftrightarrow 1-\rho$, and $\omega_A^{eff} \leftrightarrow \omega_D$, respectively. Furthermore, all the phase transitions involved in the phase diagrams are of second order. We have included various density profiles corresponding to different phases observed for the model in Appendix (7.8).

7.6 Conclusion

In this chapter, we have studied a specific variant of the network TASEP model consisting of m lanes in the left subsystem interacting at a junction with n lanes in the right subsystem. A reservoir with a limited number of particles is connected to the left end of the m lanes and the right end of the n lanes. Particles are allowed to attach in the bulk from the reservoir and can unbind from a lane to rejoin the reservoir. Due to the presence of limited resources, the attachment and entrance rates are regulated by the occupancy of the reservoir and the filling factor. Interactions at the junction are dealt with by considering suitable effective rates upstream and downstream of the junction. Even though the particle interacts at the junction, mean-field approximation works well to investigate the crucial stationary state properties such as density profiles, phase diagrams, and phase boundaries.

By inspecting the characteristics of the mean-field equations, the steady-state density is studied utilizing the time-dependent density solutions. The stationary densities are computed by two distinct methods: first, by integrating the characteristics to obtain implicit solutions and then, by applying an appropriate transformation to determine the explicit solution in terms of the Lambert-W function. These approaches have been used alternately to trace and carefully examine the phase diagram's attributes.

We observed that the stationary phase diagram exhibits quite different topologies in the case of equal and unequal numbers of lanes in each subsystem. It is found that if the number of lanes is equal in both subsystems, there exists a maximum of thirteen phases when the intrinsic attachment and detachment rates are equal. On the contrary, when these rates are different, the phase diagram is established to attain a simpler structure with only five phases. The MC phase can prevail in the system only when intrinsic attachment rate and the detachment rate are equal. When the number of lanes in both subsystems is different, the maximum number of observed phases is nine. The study reports that in the presence of very few particles, only LD:LD and

LD:S are realized whereas for any value of the filling factor, LD:HD phase is confined to a curve in the phase plane. In the case of $m = n$, it can be observed from the phase diagrams that LD:LD phase covers most of the region when limited resources are available. Furthermore, the complexity of the phase diagram shows monotonic behaviour with increasing values of μ for $m = n$. For $m \neq n$ and $K \leq 1$, the decisive parameter Kz always remains less than 1, leading to a monotonic increase in the number of phases with respect to μ. However, when $K > 1$, the number of phases first increases from two to nine and then reduces to five. Due to the complex calculations involved, the critical values of μ where new phases appear are numerically determined. Considering the phase diagram for larger values of μ, our results converge to the limiting case of infinite resources. Also, we describe the phase transitions as more particles are allowed to enter, by monitoring the movement of shock in each subsystem. All the findings have been supported with intuitive observations of finite resources as well as examined through theoretically computed phase boundaries and Monte Carlo simulations.

7.7 Appendix A

Here, we investigate the transient solution i.e., the evolution in particle density by analyzing the master equation as stated in Eq. (7.5) and further utilize it to acquire the corresponding steady-state solution. To completely understand the first order differential equation in Eq. (7.5), one needs to study its characteristics which are given by

$$\frac{d\rho}{dt} = \Omega_D[Kz - (1 + Kz)\rho], \tag{7.19}$$

$$\frac{d\rho}{dx} = \frac{\Omega_D[Kz - (1 + Kz)\rho]}{1 - 2\rho}, \tag{7.20}$$

where $Kz = \Omega_A^{eff}/\Omega_D$. We consider the density profile $\rho(x, t)$ that develops for an initial density step

$$\rho_0(x, 0) = \begin{cases} \alpha^{eff}, & \text{if } 0 \leq x < 0.5, \\ 1 - \beta, & \text{if } 0.5 < x \leq 1, \end{cases} \tag{7.21}$$

where the left ($x = 0$) and the right ($x = 1$) boundaries are fixed at α^{eff} and $1 - \beta$, respectively. Integrating Eq. (7.19) and utilizing the initial density profile given by Eq. (7.21), we obtain the solution $\rho_I(x, t)$ given by

$$\rho_I(x, t) = \frac{Kz - \left(\Big(Kz - (1 + Kz)\rho_0(x, 0)\Big)e^{-\Omega_D(1+Kz)t}\right)}{1 + Kz}. \tag{7.22}$$

For the study of Eq. (7.20), we introduce a re-scaled density of the form

$$\sigma = \frac{(Kz+1)(2\rho-1)}{Kz-1} - 1, \tag{7.23}$$

where Langmuir isotherm $\rho_l = Kz/(Kz+1)$ eventuate for $\sigma = 0$ and is similar to that in Ref. [46] . It is evident that the above equation is not defined for $Kz = 1$. Depending upon the values of Kz, different scenarios are possible. Therefore, we categorize our analysis into two cases, i) $Kz = 1$ and ii) $Kz \neq 1$.

7.7.1 $Kz = 1$

Let us first discuss the case when $Kz = 1$, for which Eqs. (7.19) and (7.20) simplify considerably and lead to

$$\frac{d\rho}{dt} = \Omega_D(1-2\rho), \quad \frac{d\rho}{dx} = \Omega_D. \tag{7.24}$$

Solving the above equations, we obtain the general solution of Eq. (7.5) as

$$(1-2\rho)e^{2\Omega_D t} = f(\rho - \Omega_D x), \tag{7.25}$$

where f is an arbitrary function to be calculated. Utilizing the initial and boundary conditions, we obtain three solutions

$$\begin{aligned}
\rho_\alpha(x) &= \Omega_D x + \alpha^{eff}, \\
\rho_I(x,t) &= \frac{1-(1-2\rho_0)e^{-2\Omega_D t}}{2}, \\
\rho_\beta(x) &= \Omega_D(x-1) + 1 - \beta,
\end{aligned}$$

where $\rho_\alpha(x)$ and $\rho_\beta(x)$ denote the solutions satisfying the left and the right boundary conditions, respectively. Depending upon how $\rho_\alpha(x)$, $\rho_I(x,t)$, and $\rho_\beta(x)$ can be matched, different scenarios for the density profile occur [46]. The density profile $\rho_\alpha(x)$ is separated from $\rho_I(x,t)$ at x_α and $\rho_I(x,t)$ is separated from $\rho_\beta(x)$ at x_β whose values are given by

$$x_\alpha = \frac{1-(1-2\rho_0)e^{-2\Omega_D t} - 2\alpha^{eff}}{2\Omega_d}, \quad x_\beta = \frac{1-(1-2\rho_0)e^{-2\Omega_D t} - 2(1-\beta)}{2\Omega_d} + 1. \tag{7.26}$$

According to the relative positions of x_α and x_β, the density profile is obtained as follows:

1. When $x_\alpha > x_\beta$, there is necessarily a density discontinued at the point x_w where the currents corresponding to $\rho_\alpha(x)$ and $\rho_\beta(x)$ matches. The density profile is expressed

as

$$\rho(x,t) = \begin{cases} \Omega_D x + \alpha^{eff}, & \text{if } 0 \le x \le x_w, \\ \Omega_D(x-1) + 1 - \beta, & \text{if } x_w \le x \le 1, \end{cases} \tag{7.27}$$

where $x_w = (\Omega_d - \gamma + \beta)/(2\Omega_D)$.

2. When $x_\alpha \le x_\beta$, the density profile is given by

$$\rho(x,t) = \begin{cases} \Omega_D x + \alpha^{eff}, & \text{if } 0 \le x \le x_\alpha, \\ \dfrac{1-(1-2\rho_0)e^{-2\Omega_D t}}{2}, & \text{if } x_\alpha \le x \le x_\beta, \\ \Omega_D(x-1) + 1 - \beta, & \text{if } x_\beta \le x \le 1. \end{cases} \tag{7.28}$$

7.7.2 $Kz \neq 1$

In this case, the transformation given by Eq. (7.23) is well defined and Eq. (7.20) in the re-scaled form reduces to

$$\left(\frac{\sigma+1}{\sigma}\right)\frac{\partial\sigma}{\partial x} = \frac{\Omega_D(Kz+1)^2}{Kz-1}. \tag{7.29}$$

Integrating the above equation yields

$$|\sigma(x)|\exp(\sigma(x)) = Y(x), \tag{7.30}$$

where $Y(x)$ is

$$Y(x) = |\sigma(x_0)|\ \exp\left\{\Omega_D \frac{(Kz+1)^2}{Kz-1}(x-x_0) + \sigma(x_0)\right\}, \tag{7.31}$$

and x_0 is the reference point. In particular, x_0 can take the values 0 and 1 corresponding to the two boundaries. The re-scaled Eq. (7.30) is known to have an explicit solution in the form of a special function known as Lambert-W function [45,46,173] and can be written as

$$\sigma(x) = \begin{cases} W_{-1}(-Y(x)), & \text{if } \sigma(x) < -1, \\ W_0(-Y(x)), & \text{if } -1 \le \sigma(x) < 0, \\ W_0(Y(x)), & \text{if } 0 < \sigma(x). \end{cases} \tag{7.32}$$

Using the properties of the Lambert-W function and the values of α^{eff} and β, a specific branch of the Lambert-W function can be chosen to obtain the solution to Eq. (7.30). The re-scaled solution satisfying the left boundary condition is the left re-scaled solution denoted by $\sigma_\alpha(x)$, while the one obeying the right boundary condition is represented by $\sigma_\beta(x)$ called as the right re-scaled solution. Therefore, the particle densities $\rho_\alpha(x)$ and

$\rho_\beta(x)$ can be obtained by substituting back $\sigma_\alpha(x)$ and $\sigma_\beta(x)$ in Eq. (7.23). Employing the suitable solution to $\sigma_\alpha(x)$ and $\sigma_\beta(x)$, the complete solution is constructed from the possible combination of the three solutions, i.e.,

$$\rho(x,t) = \begin{cases} \rho_\alpha(x), & \text{if } 0 \le x \le x_\alpha, \\ \rho_I(x,t), & \text{if } x_\alpha \le x \le x_\beta, \\ \rho_\beta(x), & \text{if } x_\beta \le x \le 1, \end{cases} \tag{7.33}$$

where $\rho_I(x,t)$ is given by Eq. (7.22). The two solutions $\rho_\alpha(x)$ and $\rho_I(x,t)$ are matches at the position x_α for which the current for both the solutions is equal. Similarly, the currents for $\rho_I(x,t)$ and $\rho_\beta(x)$ are equated to calculate the value of x_β.

7.7.3 Explicit solution

Analogous to the homogeneous single-lattice TASEP model with LK coupled to an infinite reservoir [45,46], the solution $\rho_\alpha(x)$ corresponding to the left boundary condition is stable only if $\alpha^{eff} \le 0.5$. The entry rate $0 \le \alpha^{eff} \le 0.5$ implies that $0 \le \rho_\alpha(x) \le 0.5$. Utilizing re-scaled density Eq. (7.23), one has $\sigma_\alpha \in [-2Kz/(Kz-1), -1]$ for $Kz > 1$ and $\sigma_\alpha \in [-1, -2Kz/(Kz-1)]$ for $Kz < 1$. Hence, the left re-scaled solution is given as follows:

(a) If $Kz > 1$, then $\sigma_\alpha(x) = W_{-1}(-Y_\alpha(x))$.

(b) If $Kz < 1$, then

$$\sigma_\alpha(x) = \begin{cases} W_0(Y_\alpha(x)), & \text{if } 0 \le \alpha \le \rho_l, \\ 0, & \text{if } \alpha = \rho_l, \\ W_0(-Y_\alpha(x)), & \text{if } \rho_l \le \alpha \le 0.5. \end{cases} \tag{7.34}$$

Similarly, the solution $\rho_\beta(x)$ matching the right boundary is stable only for $\beta \le 0.5$ and is always in high density regime ($\rho_\beta(x) \ge 0.5$). For the right re-scaled solution $\sigma_\beta(x)$, employing $\beta \le 0.5$ and $\rho_\beta(x) \ge 0.5$ transforms to $\sigma_\beta(x) \in [-1, 2/(Kz-1)]$, if $Kz > 1$ and $\sigma_\beta(x) \in [2/(Kz-1), -1]$ for $Kz < 1$. Hence, by choosing the suitable branch of the Lambert W-function, one obtains

(a) If $Kz > 1$, then

$$\sigma_\beta(x) = \begin{cases} W_0(Y_\beta(x)), & \text{if } 0 \le \beta \le 1-\rho_l, \\ 0, & \text{if } \beta = 1-\rho_l, \\ W_0(-Y_\beta(x)), & \text{if } 1-\rho_l \le \beta \le 0.5, \end{cases} \tag{7.35}$$

where ρ_l is the Langmuir isotherm.

(b) If $Kz < 1$, then $\sigma_\beta(x) = W_{-1}(-Y_\beta(x))$.

For thorough exploration, it is essential to perceive the phase boundaries separating the different phases in the phase diagram, in addition to the particle densities. The following section supplies a different method to calculate the density profiles as well as the phase boundaries.

7.7.4 Implicit solution

An alternative method for obtaining the particle densities $\rho_\alpha(x)$ and $\rho_\beta(x)$ is through direct integration of Eq. (7.20). This equation can be rewritten as

$$dx = \frac{1-2\rho}{\Omega_D[Kz-(1+Kz)\rho]}d\rho. \tag{7.36}$$

Upon integration, we have

$$\frac{1}{\Omega_D(1+Kz)}\left(2\rho + \frac{Kz-1}{Kz+1}\ln|Kz-(1+Kz)\rho|\right) = x + const. \tag{7.37}$$

In the low density situation, the density of the left end α^{eff} is employed, to find the profile $\rho_\alpha(x)$ through

$$\frac{1}{\Omega_D(1+Kz)}\left(2(\rho_\alpha - \overline{\alpha}) + \frac{Kz-1}{Kz+1}ln\left|\frac{Kz-(1+Kz)\rho_\alpha}{Kz-(1+Kz)\overline{\alpha}}\right|\right) = x, \tag{7.38}$$

where $\overline{\alpha} = \min\{\alpha^{eff}, 0.5\}$. The high density solution $\rho_\beta(x)$ corresponding to the right boundary condition is obtained from

$$\frac{1}{\Omega_D(1+Kz)}\left(2(1-\bar{\beta}-\rho_\beta) + \frac{Kz-1}{Kz+1}\ln\left|\frac{Kz-(1+Kz)(1-\bar{\beta})}{Kz-(1+Kz)\rho_\beta}\right|\right) = 1-x, \tag{7.39}$$

for $\bar{\beta} = \min\{\beta, 0.5\}$.

Now, the solutions procured for the densities $\rho_\alpha(x)$ and $\rho_\beta(x)$ in the Section (7.7) can be deployed in Eq. (7.33) to finally compute the overall density of the lattice. Both the implicit and the explicit solutions are equivalent and can be used interchangeably. For the sake of completeness, we will be utilizing the explicit solutions to calculate the density profiles while the implicit solution will provide the phase boundaries.

7.8 Appendix B

Density profiles corresponding to different phases of the phase diagrams are depicted in Fig. (7.5).

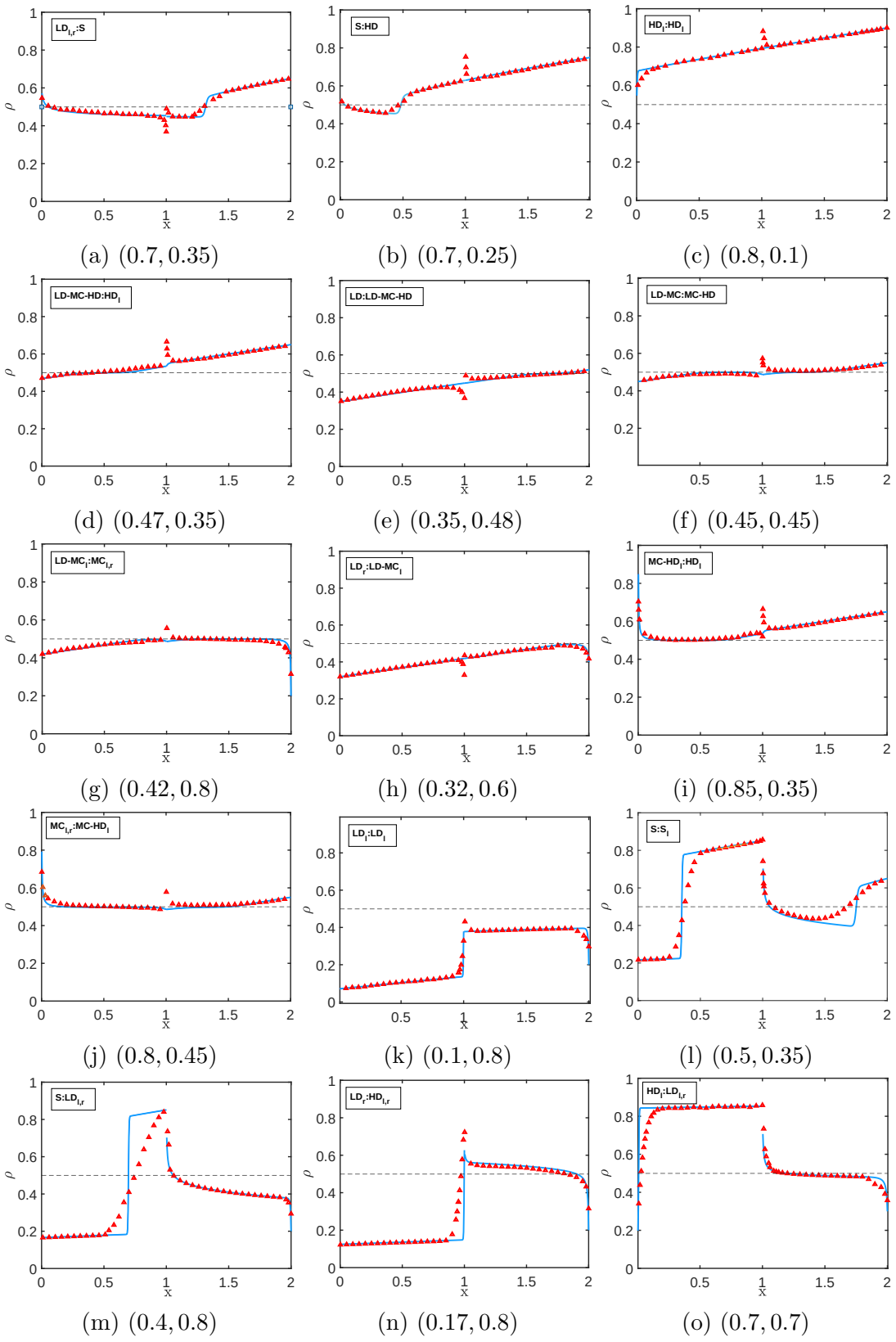

(a) $(0.7, 0.35)$ (b) $(0.7, 0.25)$ (c) $(0.8, 0.1)$

(d) $(0.47, 0.35)$ (e) $(0.35, 0.48)$ (f) $(0.45, 0.45)$

(g) $(0.42, 0.8)$ (h) $(0.32, 0.6)$ (i) $(0.85, 0.35)$

(j) $(0.8, 0.45)$ (k) $(0.1, 0.8)$ (l) $(0.5, 0.35)$

(m) $(0.4, 0.8)$ (n) $(0.17, 0.8)$ (o) $(0.7, 0.7)$

Figure 7.5: Typical density profiles for $m = n,\ K = 1,\ \Omega_D = 0.1$ ((a)-(c) with $\mu = 2.5$ and (d)-(j) with $\mu = 200$), $m = 2,\ n = 1,\ K = 1,\ \Omega_D = 0.1$ ((k)-(m) with $\mu = 1$) and $m = 2,\ n = 1,\ K = 3,\ \Omega_D = 0.01$ ((n)-(o) with $\mu = 1$). Solid blue curves and red symbols denote mean-field and Monte Carlo simulations respectively.

Chapter 8

Conclusion and future outlook

This thesis primarily centres on exploring the collective behaviour of particles navigating single, multiple, or network topologies. The research questions tackled in this work draw inspiration mainly from the intracellular transport of motor proteins along microtubules and vehicular traffic. To model these driven diffusive systems, we employ a well-established class of non-equilibrium models, specifically the Totally Asymmetric Simple Exclusion Process (TASEP), to investigate the dynamic properties of the system. Various forms of the mean-field approximation are adopted to establish a theoretical basis for the addressed problems. Subsequently, thorough numerical validation is conducted through finite difference schemes and stochastic approaches, utilizing Monte Carlo simulations in conjunction with the Gillespie algorithm. The content of the thesis is categorized systematically into six chapters (excluding the introduction and the conclusive chapter) based on the nature of the problem.

8.1 Summary of the results

In the first problem presented as chapter 2 of the thesis, we examine a theoretical model capturing bidirectional particle movement along a one-dimensional track, reflecting phenomena such as cargo vesicle transport by motor proteins on microtubules and vehicular traffic on narrow roads. This track is coupled with distinct finite particle reservoirs corresponding to each species. Utilizing mean-field theory, we explore the system's impact on steady-state properties like phase diagrams, density profiles, boundaries, and transitions. Monte Carlo simulations validate our theoretical findings. Considering scenarios with equal and unequal filling factors, we observe up to five stationary phases in the symmetric case and up to sixteen phases in the asymmetric case, revealing non-monotonic trends. Notably, our model introduces new phases, such as the shock-low density and maximal current phase, and features concave downward phase boundaries, distinguishing it from previous studies.

Continuing our exploration further on bidirectional transport in the second problem, we investigate a distinctive variant of the exclusion model centred on roundabouts, featuring two bridge lanes in the middle with particles moving in opposing directions. These bridge lanes intricately connect to bidirectional TASEP lanes on each side, introducing system inhomogeneity addressed through effective entrance and exit rates.

Our main objective is to explore the influence of coupling the system to a finite pool on spontaneous symmetry-breaking. Increasing particle count brings qualitative and quantitative changes to the phase diagram, with the complexity being highly sensitive to the filling factor. The phase diagram exhibits non-monotonic variation, featuring congested phases, a back-and-forth phase transition, and boundary- and bulk-induced shocks. Explicit calculations for phase boundaries, phase transitions and density profiles are presented and are explained by giving physical arguments. Theoretical groundwork is laid through mean-field approximations, and is subsequently verified via simulations utilizing the Gillespie Algorithm.

The third problem deals with the non-equilibrium dynamics of a two-lane TASEP model with dynamic disorder, where particles moving in opposite directions interact solely at the boundaries. The dynamic disorder is introduced through stochastic appearance and disappearance of defects at each site, slowing down particle movement when present. Reservoir crowding regulates particle entry and exit, while for defects, only the entry rate is affected. The model is inspired by intracellular transport processes and traffic situations with dynamic obstacles. Employing the continuum mean-field framework, we reduce the parameters associated with defect dynamics to a single scaling factor, simplifying mathematical treatment. Effective entrance definitions address narrow entrances at entry-exit sites, yielding explicit expressions for particle densities, currents, and phase boundaries. Spontaneous symmetry-breaking occurs despite symmetry in lane dynamics. Reservoir crowding introduces a back-and-forth transition and sustains a localized domain wall in density profiles. Monte Carlo simulations validate computational outcomes, demonstrating agreement with numerical and analytical results.

The problem in chapter 5 is based on a two-lane exclusion model with distinct particle attachment and detachment characteristics. The system operates in a constrained resource environment, regulated by the filling factor determining the particle count. Employing a vertical cluster mean-field technique and singular perturbation theory, we derive theoretical insights into bulk stationary properties for each lane. Kinetic Monte Carlo simulations and numerical approaches validate our analytical findings. Investigating the impact of limited particle resources, we unveil distinct phases characterized by zero or maximum particle density in each lane. The phase diagram exhibits non-monotonic trends with varying particle counts, featuring up to ten phases before stabilizing at seven for infinite resources. Moreover, the study uncovers the emergence of both upward and downward shocks in the system.

The sixth chapter covers a general network comprising of m incoming segments and n outgoing segments connected through a junction, featuring particle creation and annihilation with specified rates. We adopt a theoretical approach considering

each segment as a one-dimensional TASEP with LK, enabling the application of a simple mean-field approximation to investigate steady-state properties like density profiles, phase diagrams, and phase transitions. Theoretical outcomes, supported by mathematical analyses, cover all observed phases for equal attachment-detachment rates. Two distinct scenarios are explored: when the number of segments in both subsystems is different and when they are the same. The study identifies explicit expressions for phase boundaries, provides valid arguments for the non-existence of certain phases, and classifies potential phases into sub-classes based on junction dynamics. The influence of LK rates and the number of segments in each subsystem on system dynamics is examined. Moreover, when the number of incoming and outgoing segments is equal, the phase diagram aligns with a single-segment TASEP-LK model.

Finally, the sixth problem expands on the prior model by introducing a constraint on particle resources, quantified through the filling factor. Mean-field approximation effectively investigates stationary state properties like density profiles, phase diagrams, and boundaries at the junction. We explore steady-state density using time-dependent solutions, obtaining implicit and explicit solutions employing Lambert-W function transformations. Distinct topologies emerge in the stationary phase diagram for equal and unequal lane numbers in each subsystem. Equal lane numbers result in a maximum of thirteen phases with equal attachment and detachment rates, reduced to five when rates differ. The study reveals unique phase occurrences for specific conditions and explores the impact of critical parameters on phase diagram complexity. Theoretical calculations and Monte Carlo simulations support the phase boundaries and shock dynamics, offering a comprehensive insight into the impact of finite resources on the system.

8.2 Future scope

While this thesis tries to comprehend essential physical phenomena in various lattice-based transport systems, it represents a preliminary effort. Recognizing that the proposed models are not exhaustive, there is considerable room for further exploration. Nevertheless, our aim is to explore distinctive aspects of the field, addressing important concerns for researchers in this domain. There are numerous potential directions for further exploration of the discussed model. These may involve aspects like examining the lattice's flexibility, exploring the coupling between lanes, investigating site-dependent hopping rates, studying interactions among neighboring particles, and considering the dynamic length of the lattice, among other possible features.

Traditionally, TASEP assumes a uniform particle speed, simplifying the analysis and facilitating the derivation of key properties. However, considering variable particle

speeds introduces a dynamic dimension to the system, allowing for a more realistic representation of particle behaviour in diverse scenarios. It would be interesting to incorporate site-depending hopping rates in the models investigated in this thesis.

The issue explored in the thesis assumes a fixed lattice length, but in reality, the situation differs. Take microtubules, for instance, composed of thirteen tubulin protein subunits that undergo polymerization and depolymerization at their ends—a phenomenon known as dynamic instability. This length regulation, coupled with particles exhibiting Langmuir kinetics, has been observed to exhibit bistability under specific parameter values. Though it is very challenging, one can explore dynamic length effects in network junction models which is incorporated with Langmuir kinetics. Moreover, this flexible length of the lane can also be investigated in case of one-dimensional bidirectional transport.

We have broadened the scope of investigation from a single-lane Totally Asymmetric Simple Exclusion Process (TASEP) to a more intricate two-lane system featuring a dynamic lane-changing mechanism. It's noteworthy that this lane-changing attribute is not limited to the two-lane setup alone; but can also be included in the network junction model as well. One can expect novel phases, both qualitatively and quantitatively.

Extending the Markovian Totally Asymmetric Simple Exclusion Process (TASEP) to a non-Markovian framework represents a compelling frontier in research. While traditional Markovian models assume memory-less transitions between states, the non Markovian TASEP introduces a more nuanced perspective by considering the influence of past events and history on the system's dynamics. This extension allows for a richer representation of real-world scenarios where memory effects play a crucial role in governing particle movements.

Lastly, we would like to integrate data-driven tools into addressing the underlying problems, as these tools are expected to deliver more effective solutions.

References

[1] Chapin Korosec and Nancy R Forde. Engineering nanoscale biological molecular motors. *arXiv preprint arXiv:1701.01776*, 2017.

[2] Michael Schreckenberg, Andreas Schadschneider, Kai Nagel, and Nobuyasu Ito. Discrete stochastic models for traffic flow. *Physical Review E*, 51(4):2939, 1995.

[3] Tobias Kretz, Anna Grünebohm, Maike Kaufman, Florian Mazur, and Michael Schreckenberg. Experimental study of pedestrian counterflow in a corridor. *Journal of Statistical Mechanics: Theory and Experiment*, 2006(10):P10001, 2006.

[4] B Holldobler and EO Wilson. The ants harvard university press. *Cambridge, Mass*, 1990.

[5] Debashish Chowdhury, Ludger Santen, and Andreas Schadschneider. Statistical physics of vehicular traffic and some related systems. *Physics Reports*, 329(4-6):199–329, 2000.

[6] Tom Chou and Greg Lakatos. Clustered bottlenecks in mrna translation and protein synthesis. *Physical review letters*, 93(19):198101, 2004.

[7] JW Gibbs. Elementary principles in statistical mechanics; courier corporation: North chelmsford, ma, usa. *Google Scholar*, 2014.

[8] David Chandler. Introduction to modern statistical. *Mechanics. Oxford University Press, Oxford, UK*, 5:449, 1987.

[9] Edwin T Jaynes. Gibbs vs boltzmann entropies. *American Journal of Physics*, 33(5):391–398, 1965.

[10] Andreas Schadschneider, Debashish Chowdhury, and Katsuhiro Nishinari. *Stochastic transport in complex systems: from molecules to vehicles*. Elsevier, 2010.

[11] Vladimir Privman. *Nonequilibrium statistical mechanics in one dimension*. Cambridge University Press, 1997.

[12] Debashish Chowdhury, Andreas Schadschneider, and Katsuhiro Nishinari. Physics of transport and traffic phenomena in biology: from molecular motors and cells to organisms. *Physics of Life reviews*, 2(4):318–352, 2005.

[13] Shriniwas S Arkatkar. Traffic operations and capacity analysis in india, 2018.

[14] Harvey F Lodish. *Molecular cell biology*. Macmillan, 2008.

[15] Manfred Schliwa and Günther Woehlke. Molecular motors. *Nature*, 422(6933):759–765, 2003.

[16] Cécile Appert-Rolland, Maximilian Ebbinghaus, and Ludger Santen. Intracellular transport driven by cytoskeletal motors: General mechanisms and defects. *Physics Reports*, 593:1–59, 2015.

[17] Erel Levine, Yariv Kafri, and David Mukamel. Ordering dynamics of the driven lattice-gas model. *Physical Review E*, 64(2):026105, 2001.

[18] Sheldon Katz, Joel L Lebowitz, and Herbert Spohn. Nonequilibrium steady states of stochastic lattice gas models of fast ionic conductors. *Journal of statistical physics*, 34(3-4):497–537, 1984.

[19] Carolyn T MacDonald, Julian H Gibbs, and Allen C Pipkin. Kinetics of biopolymerization on nucleic acid templates. *Biopolymers: Original Research on Biomolecules*, 6(1):1–25, 1968.

[20] Tom Chou, Kirone Mallick, and Royce KP Zia. Non-equilibrium statistical mechanics: from a paradigmatic model to biological transport. *Reports on progress in physics*, 74(11):116601, 2011.

[21] Debashish Chowdhury. Stochastic mechano-chemical kinetics of molecular motors: a multidisciplinary enterprise from a physicist's perspective. *Physics Reports*, 529(1):1–197, 2013.

[22] Denis Chretien, Frédéric Metoz, Fulvia Verde, Eric Karsenti, and Richard H Wade. Lattice defects in microtubules: protofilament numbers vary within individual microtubules. *The Journal of cell biology*, 117(5):1031–1040, 1992.

[23] Kai Nagel. Particle hopping models and traffic flow theory. *Physical review E*, 53(5):4655, 1996.

[24] Stefan Klumpp and Reinhard Lipowsky. Traffic of molecular motors through tube-like compartments. *Journal of Statistical Physics*, 113:233–268, 2003.

[25] HJ Hilhorst and C Appert-Rolland. A multi-lane tasep model for crossing pedestrian traffic flows. *Journal of Statistical Mechanics: Theory and Experiment*, 2012(06):P06009, 2012.

[26] B Widom, JL Viovy, and AD Defontaines. Repton model of gel electrophoresis and diffusion. *Journal de Physique I*, 1(12):1759–1784, 1991.

[27] Joachim Krug. Boundary-induced phase transitions in driven diffusive systems. *Physical review letters*, 67(14):1882, 1991.

[28] Gunter Schütz and Eytan Domany. Phase transitions in an exactly soluble one-dimensional exclusion process. *Journal of statistical physics*, 72(1):277–296, 1993.

[29] Vladislav Popkov and Gunter M Schütz. Steady-state selection in driven diffusive systems with open boundaries. *EPL (Europhysics Letters)*, 48(3):257, 1999.

[30] Anatoly B Kolomeisky, Gunter M Schütz, Eugene B Kolomeisky, and Joseph P Straley. Phase diagram of one-dimensional driven lattice gases with open boundaries. *Journal of Physics A: Mathematical and General*, 31(33):6911–6919, aug 1998.

[31] Bernard Derrida, Eytan Domany, and David Mukamel. An exact solution of a one-dimensional asymmetric exclusion model with open boundaries. *Journal of statistical physics*, 69(3):667–687, 1992.

[32] Bernard Derrida, Martin R Evans, Vincent Hakim, and Vincent Pasquier. Exact solution of a 1d asymmetric exclusion model using a matrix formulation. *Journal of Physics A: Mathematical and General*, 26(7):1493, 1993.

[33] Bernard Derrida. The asymmetric exclusion model: exact results through a matrix approach, 1997.

[34] Martin R Evans, Damein P Foster, Claude Godrèche, and David Mukamel. Asymmetric exclusion model with two species: spontaneous symmetry breaking. *Journal of statistical physics*, 80(1):69–102, 1995.

[35] Nikolaus Rajewsky, Ludger Santen, Andreas Schadschneider, and Michael Schreckenberg. The asymmetric exclusion process: Comparison of update procedures. *Journal of statistical physics*, 92(1):151–194, 1998.

[36] Bernard Derrida and MR Evans. Bethe ansatz solution for a defect particle in the asymmetric exclusion process. *Journal of Physics A: Mathematical and General*, 32(26):4833, 1999.

[37] Kurt Binder. Monte carlo simulations in statistical physics. In *Statistical and Nonlinear Physics*, pages 85–97. Springer, 2022.

[38] Daniel T Gillespie. Exact stochastic simulation of coupled chemical reactions. *The journal of physical chemistry*, 81(25):2340–2361, 1977.

[39] Pierre Curie. *Propriétés magnétiques des corps a diverses températures.* Number 4. Gauthier-Villars et fils, 1895.

[40] Richard A Blythe and Martin R Evans. Nonequilibrium steady states of matrix-product form: a solver's guide. *Journal of Physics A: Mathematical and Theoretical*, 40(46):R333, 2007.

[41] Michael James Lighthill and Gerald Beresford Whitham. On kinematic waves ii. a theory of traffic flow on long crowded roads. *Proceedings of the royal society of london. series a. mathematical and physical sciences*, 229(1178):317–345, 1955.

[42] Paul I Richards. Shock waves on the highway. *Operations research*, 4(1):42–51, 1956.

[43] Ankita Gupta, Bipasha Pal, Akriti Jindal, Nikhil Bhatia, and Arvind Kumar Gupta. Modelling of transport processes: Theory and simulations. *MethodsX*, 10:101966, 2023.

[44] Jonathon Howard. Mechanics of motor proteins. In *Physics of bio-molecules and cells. Physique des biomolécules et des cellules: session LXXV. 2–27 July 2001*, pages 69–94. Springer, 2002.

[45] Andrea Parmeggiani, Thomas Franosch, and Erwin Frey. Phase coexistence in driven one-dimensional transport. *Physical review letters*, 90(8):086601, 2003.

[46] Andrea Parmeggiani, Thomas Franosch, and Erwin Frey. Totally asymmetric simple exclusion process with langmuir kinetics. *Physical Review E*, 70(4):046101, 2004.

[47] RD Willmann, GM Schütz, and Damien Challet. Exact hurst exponent and crossover behavior in a limit order market model. *Physica A: Statistical Mechanics and its Applications*, 316(1-4):430–440, 2002.

[48] Nikolay Mirin and Anatoly B Kolomeisky. Effect of detachments in asymmetric simple exclusion processes. *Journal of statistical physics*, 110:811–823, 2003.

[49] Virupakshi Soppina, Arpan Kumar Rai, Avin Jayesh Ramaiya, Pradeep Barak, and Roop Mallik. Tug-of-war between dissimilar teams of microtubule motors regulates transport and fission of endosomes. *Proceedings of the National Academy of Sciences*, 106(46):19381–19386, 2009.

[50] William O Hancock. Bidirectional cargo transport: moving beyond tug of war. *Nature reviews Molecular cell biology*, 15(9):615–628, 2014.

[51] William HK Lam, Jodie Lee, and CY Cheung. A study of the bi-directional pedestrian flow characteristics at hong kong signalized crosswalk facilities. *Transportation*, 29(2):169–192, 2002.

[52] David W Erickson, Gunnar Pruessner, Beate Schmittmann, and Royce KP Zia. Spurious phase in a model for traffic on a bridge. *Journal of Physics A: Mathematical and General*, 38(41):L659, 2005.

[53] Martin R Evans, Damien P Foster, Claude Godrèche, and David Mukamel. Spontaneous symmetry breaking in a one dimensional driven diffusive system. *Physical review letters*, 74(2):208, 1995.

[54] Peter F Arndt, Thomas Heinzel, and Vladimir Rittenberg. First-order phase transitions in one-dimensional steady states. *Journal of statistical physics*, 90(3):783–815, 1998.

[55] M Clincy, MR Evans, and David Mukamel. Symmetry breaking through a sequence of transitions in a driven diffusive system. *Journal of Physics A: Mathematical and General*, 34(47):9923, 2001.

[56] Vladislav Popkov, Martin R Evans, and David Mukamel. Spontaneous symmetry breaking in a bridge model fed by junctions. *Journal of Physics A: Mathematical and Theoretical*, 41(43):432002, 2008.

[57] Sudipto Muhuri and Ignacio Pagonabarraga. Phase segregation and transport in a two-species multi-lane system. *Journal of Statistical Mechanics: Theory and Experiment*, 2011(11):P11011, 2011.

[58] Bipasha Pal and Arvind Kumar Gupta. Persistence of spontaneous symmetry breaking in bidirectional transport system with reservoir crowding. *Journal of Physics A: Mathematical and Theoretical*, 54(40):405002, 2021.

[59] Erel Levine and RD Willmann. Spontaneous symmetry breaking in a non-conserving two-species driven model. *Journal of Physics A: Mathematical and General*, 37(10):3333, 2004.

[60] Ekaterina Pronina and Anatoly B Kolomeisky. Spontaneous symmetry breaking in two-channel asymmetric exclusion processes with narrow entrances. *Journal of Physics A: Mathematical and Theoretical*, 40(10):2275, 2007.

[61] B Alberts, A Johnson, P Walter, J Lewis, M Raff, and K Roberts. Molecular cell biology. *New York: Garland Science*, 2008.

[62] Anna Akhmanova and Michel O Steinmetz. Tracking the ends: a dynamic protein network controls the fate of microtubule tips. *Nature reviews Molecular cell biology*, 9(4):309–322, 2008.

[63] Andrea Grafmüller and Gregory A Voth. Intrinsic bending of microtubule protofilaments. *Structure*, 19(3):409–417, 2011.

[64] DA Adams, B Schmittmann, and RKP Zia. Far-from-equilibrium transport with constrained resources. *Journal of Statistical Mechanics: Theory and Experiment*, 2008(06):P06009, 2008.

[65] T Lynne Blasius, Nathan Reed, Boris M Slepchenko, and Kristen J Verhey. Recycling of kinesin-1 motors by diffusion after transport. *PloS one*, 8(9):e76081, 2013.

[66] L Jonathan Cook and RKP Zia. Feedback and fluctuations in a totally asymmetric simple exclusion process with finite resources. *Journal of Statistical Mechanics: Theory and Experiment*, 2009(02):P02012, 2009.

[67] Meesoon Ha and Marcel Den Nijs. Macroscopic car condensation in a parking garage. *Physical Review E*, 66(3):036118, 2002.

[68] Chris A Brackley, M Carmen Romano, and Marco Thiel. The dynamics of supply and demand in mrna translation. *PLoS Computational Biology*, 7(10):e1002203, 2011.

[69] Astik Haldar, Parna Roy, and Abhik Basu. Asymmetric exclusion processes with fixed resources: Reservoir crowding and steady states. *Physical Review E*, 104(3):034106, 2021.

[70] Bipasha Pal and Arvind Kumar Gupta. Reservoir crowding in a resource-constrained exclusion process with a dynamic defect. *Physical Review E*, 106(4):044130, 2022.

[71] Bruce Alberts. *Molecular biology of the cell*. Garland science, 2017.

[72] Mustansir Barma. Driven diffusive systems with disorder. *Physica A: Statistical Mechanics and its Applications*, 372(1):22–33, 2006.

[73] Chikashi Arita, M Ebrahim Foulaadvand, and Ludger Santen. Signal optimization in urban transport: A totally asymmetric simple exclusion process with traffic lights. *Physical Review E*, 95(3):032108, 2017.

[74] Francesco Turci, Andrea Parmeggiani, Estelle Pitard, M Carmen Romano, and Luca Ciandrini. Transport on a lattice with dynamical defects. *Physical Review E*, 87(1):012705, 2013.

[75] Richard J Harris and RB Stinchcombe. Ideal and disordered two-lane traffic models. *Physica A: statistical mechanics and its applications*, 354:582–596, 2005.

[76] Tobias Reichenbach, Erwin Frey, and Thomas Franosch. Traffic jams induced by rare switching events in two-lane transport. *New Journal of Physics*, 9(6):159, 2007.

[77] Song Xiao, Xiaoyu Chen, Lin Qi, and Yanna Liu. Totally asymmetric simple exclusion process with two consecutive ramps. In *Journal of Physics: Conference Series*, volume 1324, page 012059. IOP Publishing, 2019.

[78] Ankita Gupta and Arvind Kumar Gupta. Reservoir crowding in a dynamically disordered bidirectional system with narrow entrances. *Chaos, Solitons & Fractals*, 178:114318, 2024.

[79] Debashish Chowdhury, Ashok Garai, and Jian-Sheng Wang. Traffic of single-headed motor proteins kif1a: effects of lane changing. *Physical Review E*, 77(5):050902, 2008.

[80] Smriti Pradhan, Swayamshree Patra, Yasar Efe Dai, Andreas Schadschneider, and Debashish Chowdhury. Flux-density relation for traffic of army ants in a 3-lane bi-directional trail. *Physica A: Statistical Mechanics and its Applications*, 567:125664, 2021.

[81] Ekaterina Pronina and Anatoly B Kolomeisky. Asymmetric coupling in two-channel simple exclusion processes. *Physica A: Statistical Mechanics and its Applications*, 372(1):12–21, 2006.

[82] Ekaterina Pronina and Anatoly B Kolomeisky. Two-channel totally asymmetric simple exclusion processes. *Journal of Physics A: Mathematical and General*, 37(42):9907, 2004.

[83] Qi-Hong Shi, Rui Jiang, Mao-Bin Hu, and Qing-Song Wu. Strong asymmetric coupling of two parallel exclusion processes. *J. Stat. Phys.*, 142(3):616–626, 2011.

[84] K. Tsekouras and A. B. Kolomeisky. Parallel coupling of symmetric and asymmetric exclusion processes. *J. Phys. A*, 41(46):465001, 15, 2008.

[85] Arvind Kumar Gupta and Isha Dhiman. Coupling of two asymmetric exclusion processes with open boundaries. *Physica A: Statistical Mechanics and its Applications*, 392(24):6314–6329, 2013.

[86] Song Xiao, Peng Dong, Yingjie Zhang, and Yanna Liu. Strong asymmetric coupling of two parallel exclusion processes: effect of unequal injection rates. *International Journal of Theoretical Physics*, 55:1642–1651, 2016.

[87] Rui Jiang, Mao-Bin Hu, Yong-Hong Wu, and Qing-Song Wu. Weak and strong coupling in a two-lane asymmetric exclusion process. *Physical Review E*, 77(4):041128, 2008.

[88] Atri Goswami, Utsa Dey, and Sudip Mukherjee. Nonequilibrium steady states in coupled asymmetric and symmetric exclusion processes. *arXiv preprint arXiv:2306.14651*, 2023.

[89] Qi-Hong Shi, Rui Jiang, Mao-Bin Hu, and Qing-Song Wu. Strong asymmetric coupling of multilane paseps. *Physics Letters A*, 376(40-41):2640–2644, 2012.

[90] Zhong-Pan Cai, Yao-Ming Yuan, Rui Jiang, Mao-Bin Hu, Qing-Song Wu, and Yong-Hong Wu. Asymmetric coupling in multi-channel simple exclusion processes. *Journal of Statistical Mechanics: Theory and Experiment*, 2008(07):P07016, 2008.

[91] Rui Jiang, Mao-Bin Hu, Katsuhiro Nishinari, Ruili Wang, and Qing-Song Wu. Shock formation in the periodic exclusion process with asymmetric coupling. *Journal of Statistical Mechanics: Theory and Experiment*, 2010(07):P07003, 2010.

[92] Atul Kumar Verma and Arvind Kumar Gupta. Limited resources in multi-lane stochastic transport system. *Journal of Physics Communications*, 2(4):045020, 2018.

[93] S Tamizhazhagan and Atul Kumar Verma. Role of extended coupling in bidirectional transport system. *Physical Review E*, 106(1):014120, 2022.

[94] S Tamizhazhagan and Atul Kumar Verma. Multiple reentrance transitions in exclusion process with finite reservoir. *Physical Review E*, 107(4):044133, 2023.

[95] Atul Kumar Verma et al. Asymmetric coupling induces two-directional reentrance transition in three-lane exclusion process. *Physical Review E*, 107(4):044104, 2023.

[96] Isha Dhiman and Arvind Kumar Gupta. Effect of coupling strength on a two-lane partially asymmetric coupled totally asymmetric simple exclusion process with langmuir kinetics. *Physical Review E*, 90(1):012114, 2014.

[97] Arvind Kumar Gupta and Isha Dhiman. Asymmetric coupling in two-lane simple exclusion processes with langmuir kinetics: Phase diagrams and boundary layers. *Physical Review E*, 89(2):022131, 2014.

[98] Isha Dhiman and Arvind Kumar Gupta. Collective dynamics of an inhomogeneous two-channel exclusion process: Theory and monte carlo simulations. *Journal of Computational Physics*, 309:227–240, 2016.

[99] Akriti Jindal and Arvind Kumar Gupta. Exclusion process on two intersecting lanes with constrained resources: symmetry breaking and shock dynamics. *Physical Review E*, 104(1):014138, 2021.

[100] Natasha Sharma and AK Gupta. Phase segregation and spontaneous symmetry breaking in a bidirectional two-channel non-conserving model with narrow entrances. *Journal of Statistical Mechanics: Theory and Experiment*, 2017(4):043211, 2017.

[101] Vladislav Popkov and Ingo Peschel. Symmetry breaking and phase coexistence in a driven diffusive two-channel system. *Physical Review E*, 64(2):026126, 2001.

[102] Atul Kumar Verma, Natasha Sharma, and Arvind Kumar Gupta. Far-from-equilibrium bidirectional transport system with constrained entrances competing for pool of limited resources. *Physical Review E*, 97(2):022105, 2018.

[103] Akriti Jindal, Anatoly B Kolomeisky, and Arvind Kumar Gupta. Effect of local dissociations in bidirectional transport of driven particles. *Journal of Statistical Mechanics: Theory and Experiment*, 2020(11):113202, 2020.

[104] Akriti Jindal and Arvind Kumar Gupta. Effect of local dissociation on symmetry breaking in exclusion model constituted by bridge lane and input-output taseps. *Chaos, Solitons & Fractals*, 152:111354, 2021.

[105] L Jonathan Cook, RKP Zia, and B Schmittmann. Competition between multiple totally asymmetric simple exclusion processes for a finite pool of resources. *Physical Review E*, 80(3):031142, 2009.

[106] L Jonathan Cook, JJ Dong, and Alexander LaFleur. Interplay between finite resources and a local defect in an asymmetric simple exclusion process. *Physical Review E*, 88(4):042127, 2013.

[107] Chris A Brackley, Luca Ciandrini, and M Carmen Romano. Multiple phase transitions in a system of exclusion processes with limited reservoirs of particles and fuel carriers. *Journal of Statistical Mechanics: Theory and Experiment*, 2012(03):P03002, 2012.

[108] Atul Kumar Verma and Arvind Kumar Gupta. Stochastic transport on flexible lattice under limited resources. *Journal of Statistical Mechanics: Theory and Experiment*, 2019(10):103210, 2019.

[109] Luca Ciandrini, Izaak Neri, Jean Charles Walter, Olivier Dauloudet, and Andrea Parmeggiani. Motor protein traffic regulation by supply-demand balance of resources. *Physical biology*, 11(5):056006, 2014.

[110] Philip Greulich, Luca Ciandrini, Rosalind J Allen, and M Carmen Romano. Mixed population of competing totally asymmetric simple exclusion processes with a shared reservoir of particles. *Physical Review E*, 85(1):011142, 2012.

[111] Joachim Krug. Phase separation in disordered exclusion models. *Brazilian Journal of Physics*, 30:97–104, 2000.

[112] Wipsar Sunu Brams Dwandaru. Numerical study of the totally asymmetric simple exclusion process that consists of only a single site for modeling the dynamics of coulomb blockade in 2d quantum dot. In *AIP Conference Proceedings*, volume 1788, page 030070. AIP Publishing LLC, 2017.

[113] Alexander John, Andreas Schadschneider, Debashish Chowdhury, and Katsuhiro Nishinari. Traffic like collective movement of ants on trails: Absence of a jammed phase. *Physical review letters*, 102(10):108001, 2009.

[114] Ambarish Kunwar, Alexander John, Katsuhiro Nishinari, Andreas Schadschneider, and Debashish Chowdhury. Collective traffic-like movement of ants on a trail: dynamical phases and phase transitions. *Journal of the Physical Society of Japan*, 73(11):2979–2985, 2004.

[115] Beate Schmittmann and Royce KP Zia. Statistical mechanics of driven diffusive systems. *Phase transitions and critical phenomena*, 17:3–214, 1995.

[116] B Schmittmann and RKP Zia. Driven diffusive systems. an introduction and recent developments. *Physics reports*, 301(1-3):45–64, 1998.

[117] Tom Chou and Detlef Lohse. Entropy-driven pumping in zeolites and biological channels. *Physical review letters*, 82(17):3552, 1999.

[118] M Ebrahim Foulaadvand and Philipp Maass. Phase transitions and optimal transport in stochastic roundabout traffic. *Physical Review E*, 94(1):012304, 2016.

[119] Ruili Wang, Mingzhe Liu, and Rui Jiang. Theoretical investigation of synchronous totally asymmetric exclusion processes on lattices with multiple-input–single-output junctions. *Physical Review E*, 77(5):051108, 2008.

[120] Nina Christova Pesheva and Jordan Georgiev Brankov. Position-induced phase change in a tasep with a double-chain section (a model of biological transport). *Biomath*, 1(2):ID–1211211, 2012.

[121] N Zh Bunzarova, NC Pesheva, and JG Brankov. On the appearance of traffic jams in a long chain with a shortcut in the bulk. *Physica A: Statistical Mechanics and its Applications*, 438:645–656, 2015.

[122] Izaak Neri, Norbert Kern, and Andrea Parmeggiani. Totally asymmetric simple exclusion process on networks. *Physical review letters*, 107(6):068702, 2011.

[123] Izaak Neri, Norbert Kern, and Andrea Parmeggiani. Exclusion processes on networks as models for cytoskeletal transport. *New Journal of Physics*, 15(8):085005, 2013.

[124] Izaak Neri, Norbert Kern, and Andrea Parmeggiani. Modeling cytoskeletal traffic: an interplay between passive diffusion and active transport. *Physical review letters*, 110(9):098102, 2013.

[125] M Ebrahim Fouladvand, Zeinab Sadjadi, and M Reza Shaebani. Characteristics of vehicular traffic flow at a roundabout. *Physical Review E*, 70(4):046132, 2004.

[126] B Ray and SN Bhattacharyya. Formation of density waves in traffic flow through intersecting roads. *Physical Review E*, 73(3):036101, 2006.

[127] Jordan Brankov, Nina Pesheva, and Nadezhda Bunzarova. Totally asymmetric exclusion process on chains with a double-chain section in the middle: Computer simulations and a simple theory. *Physical Review E*, 69(6):066128, 2004.

[128] NC Pesheva and JG Brankov. Position dependence of the particle density in a double-chain section of a linear network in a totally asymmetric simple exclusion process. *Physical Review E*, 87(6):062116, 2013.

[129] Hiroki Yamamoto, Daichi Yanagisawa, and Katsuhiro Nishinari. Metastability due to a branching-merging structure in a simple network of an exclusion process. *Physical Review E*, 108(4):044121, 2023.

[130] Lawrence SB Goldstein. Kinesin molecular motors: transport pathways, receptors, and human disease. *Proceedings of the National Academy of Sciences*, 98(13):6999–7003, 2001.

[131] Daryl D Hurd and William M Saxton. Kinesin mutations cause motor neuron disease phenotypes by disrupting fast axonal transport in drosophila. *Genetics*, 144(3):1075–1085, 1996.

[132] Ankita Gupta, Bipasha Pal, and Arvind Kumar Gupta. Interplay of reservoirs in a bidirectional system. *Physical Review E*, 107(3):034103, 2023.

[133] Anatoly B Kolomeisky, Gunter M Schütz, Eugene B Kolomeisky, and Joseph P Straley. Phase diagram of one-dimensional driven lattice gases with open boundaries. *Journal of Physics A: Mathematical and General*, 31(33):6911, 1998.

[134] Tirthankar Banerjee and Abhik Basu. Smooth or shock: Universality in closed inhomogeneous driven single file motions. *Physical Review Research*, 2(1):013025, 2020.

[135] Olivier Dauloudet, Izaak Neri, Jean-Charles Walter, Jérôme Dorignac, Frédéric Geniet, and Andrea Parmeggiani. Modelling the effect of ribosome mobility on the rate of protein synthesis. *The European Physical Journal E*, 44:1–15, 2021.

[136] Tom Chou. Ribosome recycling, diffusion, and mrna loop formation in translational regulation. *Biophysical Journal*, 85(2):755–773, 2003.

[137] Isha Dhiman and Arvind Kumar Gupta. Steady-state dynamics of an inhomogeneous two-channel tasep with langmuir kinetics. *International Journal of Modern Physics C*, 29(04):1850037, 2018.

[138] Anatoly B Kolomeisky. Asymmetric simple exclusion model with local inhomogeneity. *Journal of Physics A: Mathematical and General*, 31(4):1153, 1998.

[139] Róbert Juhász, Ludger Santen, and Ferenc Iglói. Partially asymmetric exclusion processes with sitewise disorder. *Physical Review E*, 74(6):061101, 2006.

[140] Goutam Tripathy and Mustansir Barma. Steady state and dynamics of driven diffusive systems with quenched disorder. *Physical review letters*, 78(16):3039, 1997.

[141] Philip Greulich and Andreas Schadschneider. Phase diagram and edge effects in the asep with bottlenecks. *Physica A: Statistical Mechanics and its Applications*, 387(8-9):1972–1986, 2008.

[142] Philip Greulich and Andreas Schadschneider. Single-bottleneck approximation for driven lattice gases with disorder and open boundary conditions. *Journal of Statistical Mechanics: Theory and Experiment*, 2008(04):P04009, 2008.

[143] M Ebrahim Foulaadvand, Anatoly B Kolomeisky, and Hamid Teymouri. Asymmetric exclusion processes with disorder: Effect of correlations. *Physical Review E*, 78(6):061116, 2008.

[144] S Tamizhazhagan and Atul Kumar Verma. Reentrance transition in two lane bidirectional transport system with bottlenecks. *Chaos, Solitons & Fractals*, 165:112780, 2022.

[145] Bipasha Pal and Arvind Kumar Gupta. Non-conserving exclusion process with a dynamic obstacle. *Chaos, Solitons & Fractals*, 162:112471, 2022.

[146] Mamata Sahoo, Jiajia Dong, and Stefan Klumpp. Dynamic blockage in an exclusion process. *Journal of Physics A: Mathematical and Theoretical*, 48(1):015007, 2014.

[147] Akriti Jindal, Anatoly B Kolomeisky, and Arvind Kumar Gupta. The role of dynamic defects in transport of interacting molecular motors. *Journal of Statistical Mechanics: Theory and Experiment*, 2020(4):043206, 2020.

[148] Leah B Shaw, Anatoly B Kolomeisky, and Kelvin H Lee. Local inhomogeneity in asymmetric simple exclusion processes with extended objects. *Journal of Physics A: Mathematical and General*, 37(6):2105, 2004.

[149] Shaweta Garg and Isha Dhiman. Particle creation and annihilation in a dynamically disordered totally asymmetric simple exclusion process. *Physical Review E*, 103(5):052120, 2021.

[150] Kang Qiu, Xianqing Yang, Wei Zhang, Dapeng Sun, and Yuemin Zhao. Density profiles in the totally asymmetric exclusion processes with both local inhomogeneity and langmuir kinetics. *Physica A: Statistical Mechanics and its Applications*, 373:1–10, 2007.

[151] Paolo Pierobon, Mauro Mobilia, Roger Kouyos, and Erwin Frey. Bottleneck-induced transitions in a minimal model for intracellular transport. *Physical Review E*, 74(3):031906, 2006.

[152] Ruili Wang, Mingzhe Liu, and Rui Jiang. Local inhomogeneity in two-lane asymmetric simple exclusion processes coupled with langmuir kinetics. *Physica A: Statistical Mechanics and its Applications*, 387(2-3):457–466, 2008.

[153] Bartlomiej Waclaw, Justyna Cholewa-Waclaw, and Philip Greulich. Totally asymmetric exclusion process with site-wise dynamic disorder. *Journal of Physics A: Mathematical and Theoretical*, 52(6):065002, 2019.

[154] Juraj Szavits-Nossan and Bartlomiej Waclaw. Current-density relation in the exclusion process with dynamic obstacles. *Physical Review E*, 102(4):042117, 2020.

[155] Nikhil Bhatia and Arvind Kumar Gupta. Role of site-wise dynamic defects in a resource-constrained exclusion process. *Chaos, Solitons & Fractals*, 167:113109, 2023.

[156] Shaweta Garg and Isha Dhiman. Two-channel totally asymmetric simple exclusion process with site-wise dynamic disorder. *Physica A: Statistical Mechanics and its Applications*, 545:123356, 2020.

[157] Shaweta Garg and Dr Isha Dhiman. Vertical cluster mean-field analysis for a two-lane exclusion process with site-wise dynamic disorder. *Available at SSRN 4141261*, 2022.

[158] Nikhil Bhatia and Arvind K. Gupta. Far from equilibrium transport on tasep with pockets. *The European Physical Journal Plus*, 137(8):892, 2022.

[159] D. Ben-Avraham and J. Köhler. Mean-field (n, m)-cluster approximation for lattice models. *Physical Review A*, 45(12):8358, 1992.

[160] Julian D Cole and Lawrence E Levine. Perturbation methods in applied mathematics. *IEEE Transactions on Systems, Man, and Cybernetics*, (6):647–648, 1973.

[161] Sutapa Mukherji and Vivek Mishra. Bulk and surface transitions in asymmetric simple exclusion process: Impact on boundary layers. *Physical Review E*, 74(1):011116, 2006.

[162] Ekaterina Pronina and Anatoly B Kolomeisky. Theoretical investigation of totally asymmetric exclusion processes on lattices with junctions. *Journal of Statistical Mechanics: Theory and Experiment*, 2005(07):P07010, 2005.

[163] Minoru Fukui and Yoshihiro Ishibashi. Traffic flow in 1d cellular automaton model including cars moving with high speed. *Journal of the Physical Society of Japan*, 65(6):1868–1870, 1996.

[164] Yoshihiro Ishibashi and Minoru Fukui. Phase diagrams for traffics on the crossroad: Ii. the cases of different velocities. *Journal of the Physical Society of Japan*, 70(12):3747–3750, 2001.

[165] Yoshihiro Ishibashi and Minoru Fukui. Phase diagrams for traffics on the crossroad. *Journal of the Physical Society of Japan*, 70(9):2793–2799, 2001.

[166] Ben Embley, Andrea Parmeggiani, and Norbert Kern. Understanding totally asymmetric simple-exclusion-process transport on networks: Generic analysis via effective rates and explicit vertices. *Physical Review E*, 80(4):041128, 2009.

[167] Keming Zhang, PL Krapivsky, and S Redner. Exclusion in junction geometries. *Physical Review E*, 99(5):052133, 2019.

[168] Guojiang Shen, Xinye Fan, and Zhongyuan Ruan. Totally asymmetric simple exclusion process on multiplex networks. *Chaos: An Interdisciplinary Journal of Nonlinear Science*, 30(2), 2020.

[169] Vladislav Popkov, Attila Rákos, Richard D Willmann, Anatoly B Kolomeisky, and Gunter M Schütz. Localization of shocks in driven diffusive systems without particle number conservation. *Physical Review E*, 67(6):066117, 2003.

[170] Martin R Evans, Róbert Juhász, and Ludger Santen. Shock formation in an exclusion process with creation and annihilation. *Physical Review E*, 68(2):026117, 2003.

[171] Ankita Gupta and Arvind Kumar Gupta. Particle creation and annihilation in an exclusion process on networks. *Journal of Physics A: Mathematical and Theoretical*, 55(10):105001, 2022.

[172] Zhong-Pan Cai, Yao-Ming Yuan, Rui Jiang, Katsuhiro Nishinari, and Qing-Song Wu. The effect of attachment and detachment on totally asymmetric exclusion processes with junctions. *Journal of Statistical Mechanics: Theory and Experiment*, 2009(02):P02050, 2009.

[173] Robert M Corless, Gaston H Gonnet, David EG Hare, David J Jeffrey, and Donald E Knuth. On the lambert w function. *Advances in Computational mathematics*, 5:329–359, 1996.

List of Publications

1. Ankita Gupta, Arvind Kumar Gupta. Particle creation and annihilation in an exclusion process on networks. *Journal of Physics A: Mathematical and Theoretical,* 55(10):105001, 2022.

2. Ankita Gupta, Arvind Kumar Gupta. Non-equilibrium processes in an unconserved network model with limited resources. *The European Physical Journal Plus,* 138(2):108, 2023.

3. Ankita Gupta, Bipasha Pal, Akriti Jindal, Nikhil Bhatia, Arvind Kumar Gupta. Modelling of transport processes: Theory and simulations. *MethodsX,* 10:101966, 2023.

4. Ankita Gupta, Bipasha Pal, Arvind Kumar Gupta. Interplay of reservoirs in a bidirectional system. *Physical Review E,* 107(3):034103, 2023.

5. Ankita Gupta, Arvind Kumar Gupta. Reservoir crowding in a dynamically disordered bidirectional system with narrow entrances. *Chaos, Solitons & Fractals,* 178:114318, 2024.

6. Ankita Gupta, Arvind Kumar Gupta. Exclusion process on roundabout traffic model with constraint resources. *Physical Review E,* 108(6):064116, 2023.

7. Ankita Gupta, Arvind Kumar Gupta. Competition for resources in an exclusion model with biased lane-changing mechanism. *Physical Review E,* 109(3):034132, 2024.

Ankita Gupta

Department of Mathematics
Indian Institute of Technology Ropar
Nangal Road, Rupnagar
Punjab-140001, India

Phone: (+91) 7376106815
Email: gupta.ankita1995@gmail.com

Education

† *Indicates expected*

2019–2024 †	Ph.D. Mathematics
	Indian Institute Of Technology, Ropar, Punjab, India
	Supervisior- Dr. Arvind Kumar Gupta
2016–2018	M.Sc. Mathematics
	Indian Institute Of Technology, Kanpur, Uttar Pradesh, India
2013–2016	B.Sc. Mathematics Hons
	Keshav Mahavidyalaya, University of Delhi, Delhi, India

Appointments

2021–2023	Senior research fellow (SRF), Department of Mathematics, Indian Institute of Technology, Ropar
2019–2021	Junior research fellow (JRF), Department of Mathematics, Indian Institute of Technology, Ropar

Awards and achievements

2023	Recieved Travel Support to attend STATPHYS28, University of Tokyo, Japan
2019	Awarded CSIR fellowship 2019-2023
2018	Qualified IIT-GATE-2018 in MA (Mathematics)
2017	Qualified CSIR-UGC NET-JRF Dec-2017 in Mathematical Sciences
2016	Qualified IIT-JAM-2016 in MA (Mathematics)
2012	Qualified International Informatics Olympiad-2012 with All India Rank- 21

Academic events attended

Workshops/Schools

[1] Attended school on Stochastic Thermodynamics in Biology at IIT Bombay during Nov 28-Dec 02, 2022

[2] Attended GIAN program on "Motor Proteins and Molecular Motors" held at IIT Ropar from Feb 4-8, 2019

Conferences/Symposiums

[1] Participated in "Youth in High-Dimensions: Recent Progress in Machine Learning, High-Dimensional Statistics and Inference | (smr 3719)" organized by International Center for Theoretical Physics, Italy during June 27-30, 2022 (Online)

[2] Delivered a talk titled "Particle creation and annihilation in an exclusion process on networks" in the International Conference on Advances in Mechanics, Modelling, Computing and Statistics (ICAMMCS-2022), BITS Pilani during March 19-21, 2022

[3] Participated in "International Symposium on Recent Advances in Computational Analysis and Modeling", IIT Roorkee during June 20-24, 2022

[4] Presented a poster titled "Dynamics in an unconserved junction model" in the annual research day, Cynosure-2022 & National Symposium on Advances in Mathematics held at IIT Ropar on Dec 10, 2022

[5] Participated in "International Symposium on Interdisciplinary and Transdisciplinary Modeling tools for Particulate Systems" organized by IIT, Ropar and Hamburg University of Technology, from Feb 22-24, 2023

[6] Presented a poster titled "Dynamics in an unconserved junction model" in Steady state phenomena in soft matter, active and biological systems, held at S N bose, Kolkata from March 16-18, 2023

[7] Presented a poster titled "Interplay of reservoirs in a bidirectional system." in STATPHYS28, held at University of Tokyo, Japan from August 7-11, 2023

[8] Delivered a contributed talk titled "Interplay of finite reservoirs in a bidirectional system." in ICIAM 2023, held at Waseda University, Japan from August 20-25, 2023

Teaching assistant

2019	MA101, Calculus	Indian Institute Of Technology, Ropar
2019	MA203, Probability and Stochastic Processes	Indian Institute Of Technology, Ropar
2020	MA201, Differential Equations	Indian Institute Of Technology, Ropar
2020	MA-202, Probability and Statistics	Indian Institute Of Technology, Ropar
2021	MA102, Linear Algebra, Integral Transforms and Special Functions	Indian Institute Of Technology, Ropar
2022	MA703, Computational Partial Differential Equations	Indian Institute Of Technology, Ropar
2023	MA101, Calculus	Indian Institute Of Technology, Ropar